

SYNTHESIS AND CHARACTERIZATION OF TRANSITION METAL CHALCOGENIDES FOR HIGH PERFORMANCE SUPERCAPACITORS

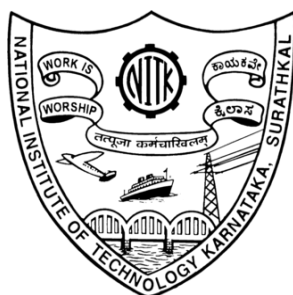
Thesis

Submitted in partial fulfilment of the requirements for the degree
of

DOCTOR OF PHILOSOPHY

by

FIONA JOYLINE MASCARENHAS



DEPARTMENT OF CHEMISTRY

NATIONAL INSTITUTE OF TECHNOLOGY KARNATAKA

SURATHKAL, MANGALORE – 575025

OCTOBER, 2024

DECLARATION

I hereby declare that the Research Thesis entitled **Synthesis and Characterisation of Transition Metal Chalcogenides for High Performance Supercapacitors** which is being submitted to the **National Institute of Technology Karnataka, Surathkal** in partial fulfilment of the requirements for the award of the Degree of **Doctor of Philosophy in Chemistry** is a bonafide report of the research work carried out by me. The material contained in this Research Thesis has not been submitted to any University or Institution for the award of any degree.



Fiona Joyline Mascarenhas

Reg. No.: 197001CY001

Department of Chemistry

Place: NITK, Surathkal

Date: 30/10/2024

C E R T I F I C A T E

This is to certify that the Research Thesis entitled **Synthesis and Characterisation of Transition Metal Chalcogenides for High Performance Supercapacitors** submitted by **Fiona Joyline Mascarenhas (Register Number: 197001CY001)** as the record of the research work carried out by her, is accepted as the Research Thesis submission in partial fulfilment of the requirements for the award of degree of **Doctor of Philosophy**.



Dr. B. RAMACHANDRA BHAT

Professor

Department of Chemistry

National Institute of Technology Karnataka

Surathkal, Srinivasanagar, Mangaluru-575 025

Research Guide

Place: NITK, Surathkal

Date: 30.10.2024



Chairman - DRPC

विभागाध्यक्ष / H.O.D.

रसायन शास्त्र विभाग/ Chemistry Dept.
राष्ट्रीय प्रौद्योगिकी संस्थान कर्नाटक, सुरत्कल

NITK SURATHKAL

मंगलूरु-५७५ ०२५, कर्नाटक

MANGALURU-575 025, KARNATAKA

ACKNOWLEDGEMENT

I want to express my heartfelt gratitude to my research guide, Prof. B. Ramachandra Bhat, for accepting me as his student and believing in me. His invaluable support, guidance, patience, and encouragement throughout the duration of this research have been pivotal in making me capable at the end of this Ph.D. journey. His expertise, insight, and patience have been instrumental in shaping this work, and his unwavering belief in my abilities has inspired me to strive for excellence. His kindness and remarkable character have not only made this challenging journey manageable but also profoundly enriching. I am profoundly grateful for the numerous discussions and feedback sessions that have significantly enhanced the quality of this thesis. I am forever indebted to him for his mentorship and for helping me realize my potential.

I am grateful to my RPAC members Dr. Beneesh P. B, Dept. of Chemistry, Prof. Nagaraja H.S, Dept. of Physics. Their encouragement, perceptive comments, and fruitful discussions throughout the progress of my research work have been success driving factors towards accomplishment of my objectives.

I would like to thank Prof. Arun M Isloor and Prof. Udaya Kumar D, and Prof. Darshak R Trivedi who have extended administrative facility for my Ph.D. work in their tenure as the Head of the Department of Chemistry.

I am thankful to the National Institute of Technology Karnataka, Surathkal for providing an opportunity to conduct my research work and faculty members of the chemistry department for their good wishes.

I am thankful to the kind assistance of Sprint Mumbai, JNCASR Bengaluru, SRMIST Chennai, Satyabhama university Chennai, Alagappa University Kozhikode, Dept. of Physics, NITK and CRF NITK for extending their sophisticated experimental and characterization facilities.

I am grateful to the all the non-teaching staff of the Dept. of Chemistry, NITK Surathkal for extending their kind assistance, care and help in all the official matter without fail. I extend my appreciation to all the non-teaching staff of the Chemistry Department, namely, Mrs. Rashmi, Ms. Vikhitha, Mr. Santhosh, Mr. Prashanth, Mrs. Sharmila, Mr. Pradeep, Mr. Harish, Mrs. Deepa, Mrs. Divya and Mrs. Ashvija for their support in the department.

The research period can be overwhelming, but it becomes bearable with an inspiring and energetic group of lab colleagues who lift your spirits when you stumble and help you get back on track. I want to recognize a very supportive group of fellow researchers: Dr. Praveen Mishra, Dr. Anuma Saroja, Dr. Madhukar Nimalbakar, Mrs. Lavanya Rao, Mr. Shreeganesh Hegde, Ms. Sushmitha S and Mr. Mahesh Nayak, for their camaraderie and constant support throughout my Ph.D. journey. A heartfelt appreciation goes out to our collaborator, Dr. John D Rodney who has been instrumental in guiding me through every step of this journey and instilling belief in my research. His mentorship has pushed me to work diligently, and his assistance in crafting research papers has been invaluable. A sincere thank you to him for his support and guidance. A special thanks to Mrs. Lavanya Rao my colleague, who embarked on this journey alongside me, has been an unwavering pillar of support. She has been my confidante, offering invaluable advice, steadfast encouragement, and unwavering emotional support. Without her by my side, this journey would have been infinitely more challenging, if not impossible.

I would like to express my heartfelt gratitude to my family for their unwavering support and encouragement throughout this journey. To my mother, whose endless love and belief in me has been my greatest source of strength. Your wisdom and guidance have shaped me into the person I am today. To my father, whose steadfast support and confidence in my abilities have been a constant source of motivation. Your faith in me has driven me to pursue my dreams with determination. To my husband, whose unwavering patience, love, and support have been my rock. You have sacrificed so much without ever complaining, always listening to each and every step I have taken in my PhD journey. Your dedication and involvement mean that you now know everything about my work, and your encouragement and sacrifices have made this accomplishment possible. Finally, to my brother, for always being there with a listening ear and a kind word. Your camaraderie and understanding have been invaluable. Thank you all for being my pillars of strength. This achievement is as much yours as it is mine.

I cannot leave to thank my supportive friends Mrs. Aarabhi Putti, Ms. Archana Seshachala and Mrs. Sammitha Hebbar and few more for being there for all the thick and thins. Lastly, I extend my heartfelt gratitude to everyone who has assisted me, both directly and indirectly, in making this dissertation possible.

Fiona Joyline Mascarenhas

TABLE OF CONTENTS

CHAPTER 1	1
INTRODUCTION AND LITERATURE REVIEW	1
1 INTRODUCTION	1
1.1 Importance of electrochemical capacitors	1
1.2 LITERATURE REVIEW	3
1.2.1 Energy storage mechanism for supercapacitors	3
1.2.2 Types of supercapacitors	6
1.2.2.1 Electric Double layer Capacitors (EDLCs)	6
1.2.2.2 Pseudocapacitors	8
1.2.2.3 Hybrid pseudocapacitors	8
1.2.3 Electrode material	9
1.2.3.1 Electric double layer capacitor (EDLC) electrode materials: Activated carbon	10
1.2.3.2 Carbon nanotubes (CNTs)	12
1.2.3.3 Graphene.....	14
1.2.3.4 Pseudocapacitor electrode materials: Conducting polymers (CPs).....	16
1.2.3.5 Transition metal oxides and their composites.....	18
1.2.3.6 Transition metal chalcogenides (TMCs): Transition metal sulfides (TMSs) .	23
1.2.3.7 Transition metal selenides (TMSes)	29
1.2.3.8 Transition metal tellurides	34
1.2.4 Electrolytes.....	35
1.2.4.1 Aqueous electrolytes.....	36
1.2.4.2 Organic electrolytes.....	37
1.2.4.3 Ionic liquids (ILs)	37
1.2.5 Separator.....	38
1.2.6 Current collector.....	39
1.2.7 Experimental assessment techniques for supercapacitor electrodes	39
1.2.7.1 Cyclic Voltammetry (CV)	40
1.2.7.2 Galvanostatic charge discharge (GCD)	42
1.2.7.3 Electrochemical Impedance Spectroscopy (EIS)	44
1.2.8 Summary	45
1.2.9 Research gap	45
1.2.10 Objectives of the work	46

CHAPTER 2	49
SYNTHESIS OF A NOVEL Cu ₂ Se-GO NANOCOMPOSITE FOR SUPERCAPACITORS.....	49
2.1 INTRODUCTION	51
2.2 EXPERIMENTAL	53
2.2.1 Materials.....	53
2.2.2 Synthesis of GO	53
2.2.3 Synthesis of Cu ₂ Se and Cu ₂ Se-GO composites	54
2.2.4 Fabrication of electrode material.....	54
2.2.5 Materials Characterization Techniques	54
2.2.6 Electrochemical characterisation.....	55
2.3 RESULTS AND DISCUSSIONS	56
2.3.1 XRD and Raman analysis	56
2.3.2 FESEM and EDAX analysis	57
2.3.3 BET analysis	59
2.3.4 EIS analysis.....	60
2.3.5 CV and GCD analysis	62
2.3.6 XPS analysis.....	63
2.3.7 TEM analysis.....	64
2.3.8 Electrochemical performance of Cu ₂ Se-5GO	65
2.3.9 Post cycling characterisation.....	68
2.4 CONCLUSIONS.....	69
CHAPTER 3	71
SIGNIFICANCE OF TRANSITION METAL (Co, Ni, AND Zn) DOPING ON THE MnSe FOR HIGH-PERFORMANCE SUPERCAPACITOR ELECTRODE	71
3.1 INTRODUCTION	73
3.2. EXPERIMENTAL	74
3.2.1 Materials.....	74
3.2.2 Synthesis of M _x Mn _{1-x} Se (M= Co / Ni / Zn); (x = 0.0 , 0.01 , 0.02, 0.03)	74
3.2.3 Electrode fabrication	75
3.2.4 Material characterisation.....	75
3.2.5 Electrochemical characterization	75
3.3 RESULTS AND DISCUSSIONS	77
3.3.1 XRD analysis.....	77
3.3.2 CV and GCD analysis	78

3.3.3 Raman analysis.....	80
3.3.4 ECSA and EIS analysis	81
3.3.5 FESEM analysis	83
3.3.6 TEM analysis.....	84
3.3.7 XPS analysis.....	86
3.3.8 Electrochemical performance of $\text{Co}_{0.01}\text{Mn}_{0.99}\text{Se}$	87
3.3.9 Post-Cyclic Stability Characterization	91
3.3.10 Electrochemical performance of symmetric supercapacitor	94
3.4 CONCLUSIONS.....	96
CHAPTER 4	97
TWO STEP ELECTRODEPOSITION SYNTHESIS OF $\text{CoMnS/NiCo}_2\text{S}_4$ NANOCOMPOSITE FOR HIGH PERFORMANCE SYMMETRIC SUPERCAPACITOR.....	97
4.1 INTRODUCTION	99
4.2 EXPERIMENTAL	101
4.2.1 Materials.....	101
4.2.2 Electrodeposition of CoMnS (CMS)/NF	101
4.2.3 Electrodeposition of $\text{NiCo}_2\text{S}_4 \text{ (NCS) on CoMnS (CMS)/NF}$	102
4.2.4 Materials Characterization Techniques	102
4.2.5 Electrochemical characterisation.....	103
4.3 RESULTS AND DISCUSSIONS	104
4.3.1 XRD analysis.....	104
4.3.2 ECSA and EIS analysis	105
4.3.3 CV and GCD analysis	106
4.3.4 FESEM and EDS analysis.....	108
4.3.5 TEM analysis.....	110
4.3.6 XPS analysis.....	111
4.3.7 Electrochemical performance of CMS/NCS/NF	113
4.3.8 Electrochemical performance of a symmetric supercapacitor	118
4.4 CONCLUSIONS.....	120
CHAPTER 5	121
IRON DECORATED COBALT MANGANESE SULPHIDE NANOFLOWERS AS A BATTERY TYPE ELECTRODE MATERIAL FOR HIGH PERFORMANCE SUPERCAPACITOR.....	121
5.1 INTRODUCTION	123
5.2 EXPERIMENTAL	125

5.2.1 Materials.....	125
5.2.2 Synthesis of CoMnS.....	125
5.2.3 Synthesis of FeCoMnS.....	126
5.2.4 Electrode fabrication	127
5.2.5 Material characterisation	127
5.2.6 Electrochemical characterization	127
5.3. RESULTS AND DISCUSSIONS	128
5.3.1 XRD analysis.....	128
5.3.2 ECSA and EIS analysis	129
5.3.3 CV and GCD analysis	131
5.3.4 FESEM and EDS analysis.....	132
5.3.5 HRTEM analysis	134
5.3.6 XPS analysis.....	135
5.3.7 Electrochemical performance of FeCoMnS.....	137
5.3.8 Post cycling characterization.....	141
5.3.9 Electrochemical performance of FeCoMnS FeCoMnS.....	143
5.4 CONCLUSIONS.....	144
CHAPTER 6	145
SUMMARY AND CONCLUSIONS.....	145
6.1 SUMMARY	147
6.2 CONCLUSIONS.....	148
6.3 FUTURE WORK	149
REFERENCES	151
LIST OF PUBLICATIONS.....	196
LIST OF CONFERENCES AND WORKSHOPS.....	196
CURRICULUM VITAE	198

NOMENCLATURE

AC	Activated carbon
ACN	Acetonitrile
ASC	Asymmetric supercapacitor
CBD	Chemical bath deposition
CNFs	Carbon nanofibers
CNTs	Carbon nanotubes
CP	Conducting Polymers
CPs	Conducting polymers
CV	Cyclic Voltammetry
CVD	Chemical Vapour Deposition
CMS	Cobalt Manganese Sulphide
ECSA	Electrochemical Active Surface Area
EDAX	Energy-dispersive X-ray analysis
EDL	Electric double layer
EDLC	Electric double layer capacitor
EDS	Energy Dispersive spectroscopy
EIS	Electrochemical Impedance Spectroscopy
EMI	Electromagnetic interference
ESR	Equivalent series resistance
FESEM	Field Emission Scanning Electron Microscopy
GCD	Galvanostatic Charge-Discharge
GNP	Graphene nanoplatelets
GO	Graphene oxide
HRTEM	High-Resolution transmission electron microscopy
HSC	Hybrid supercapacitor
IHP	Inner Helmholtz plane
ILs	Ionic liquids
LDHs	Layered double hydroxides

MOFs	Metal-organic frameworks
MOs	Metal oxides
MSCs	Micro-supercapacitors
MWCNTs	Multi-walled carbon nanotubes
NF	Nickel Foam
NCS	Nickel Cobalt Sulphide
PANI	Polyaniline
PC	Propylene carbonate
PANI	Polyaniline
PEDOT	Poly 3,4-ethylenedioxythiophene
PIND	Polyindole
PPy	Polypyrrole
PTh	Polythiophene
PVA	Poly vinyl alcohol
PVDF	Polyvinylidene fluoride
rGO	Reduced graphene oxide
R_s	Solution resistance
R_{ct}	Charge transfer resistance
SAED	Selected area electron diffraction
SSC	Solid-state supercapacitor
SWCNTs	Single-walled carbon nanotubes
TMCs	Transition metal chalcogenides
TMOs	Transition metal oxides
TMSes	Transition metal selenides
TMSs	Transition metal sulfides
XPS	X-ray Photoelectron Spectroscopy
XRD	X-ray diffraction

CHAPTER 1

INTRODUCTION AND LITERATURE REVIEW

***Abstract:** This chapter introduces the significance of energy storage solutions, highlighting the advantages of supercapacitors. This overview establishes the foundational role of supercapacitors in modern energy storage.*

1 INTRODUCTION

Over the past few decades, there has been significant dependence on fossil fuel resources due to their ability to fulfil a wide range of energy needs. Although fossil fuels are advantageous, they are non-renewable and mitigating (Libich et al. 2018). Also, The surge in energy demand, driven by both the advancement of lifestyle standards and the growth of the global population, is expected to lead to a significant increase in energy consumption over the next two decades (Chakraborty and N. L. 2022; Forouzandeh et al. 2020b). In response to this mounting challenge, researchers have directed substantial efforts towards the exploration of novel techniques aimed at harnessing and storing energy in a sustainable manner. Because of which it is imperative to develop clean energy sources to safeguard natural resources, manage burgeoning global energy consumption (Aravinda et al. 2016a; Mascarenhas et al. 2023). Notably, energy storage facilitates the seamless transition from fossil fuels to sustainable alternatives while affording the capacity to store surplus energy for subsequent release as per demand dynamics. This synergy between renewable energy sources and energy storage technologies holds significant promise in shaping a more sustainable energy paradigm for the future. Renewable energy sources like solar, wind, hydropower, and biomass are crucial for meeting our energy needs (Kalair et al. 2021). However, they can be expensive, and their efficiency and suitability vary depending on the circumstances. Also, they exhibit intermittent availability, the integration of energy storage devices presents a viable mechanism for mitigating these inherent challenges. The selection of appropriate energy storage technologies is pivotal, with a diverse array of options available across chemical or electrochemical, mechanical, electromagnetic, and thermal storage domains. Notably, batteries, capacitors, and supercapacitors have garnered recognition as highly efficient solutions in this context, offering promising avenues for addressing the exigencies of contemporary energy landscapes (Liu et al. 2018a).

1.1 Importance of electrochemical capacitors

Supercapacitors have attracted considerable attention among different unconventional electric-power gadgets, such as batteries and fuel cells. They are utilized across various sectors including hybrid vehicles, electric public transportation systems, and handheld

electronic gadgets. Notably, supercapacitors exhibit outstanding electrochemical properties, such as high specific power, prolonged cycling life, and rapid charging and discharging rates (Kim et al. 2015a). An electrolyte, a conductor for electric current, and electrodes featuring an extensive specific surface area form the core supercapacitor configuration, boosting capacitance ten thousand times greater than standard capacitors (Forouzandeh et al. 2020a). The storage of energy in supercapacitors relies on the charge-discharge mechanism occurring at the interface between the electrode and electrolyte. While this process bears some resemblance to that observed in conventional capacitors, it distinguishes itself by its markedly rapid rate of charge and discharge (Lakshmi and Vedhanarayanan 2023).

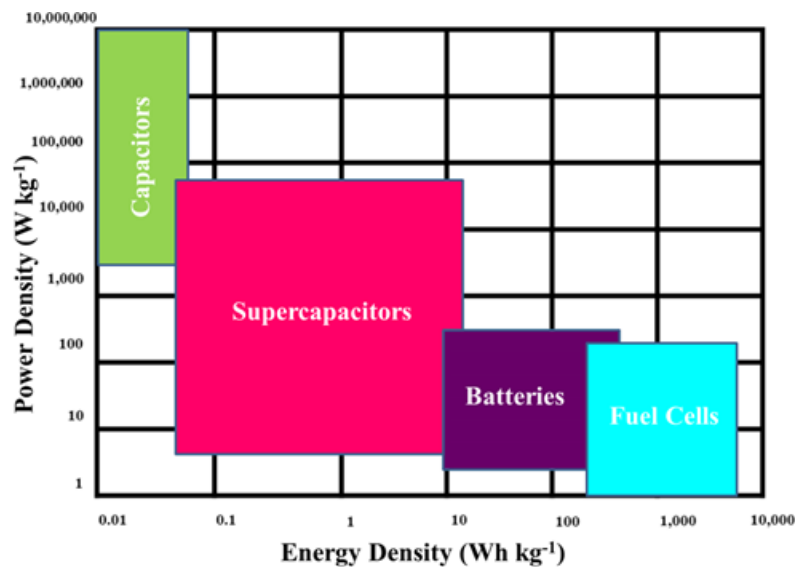


Figure 1.1. Ragone plots for various energy storage and conversion devices (Chakraborty and N. L. 2022).

Although supercapacitors offer significantly higher power density, ranging from hundreds to many thousands of times that of batteries in the same volume, they fall short in terms of charge storage capacity, typically being 3–30 times lower. This limitation positions supercapacitors as optimal solutions for applications requiring intense power bursts but not necessarily extensive energy storage. While supercapacitors boast lower power output compared to electrolytic capacitors, they can achieve approximately power density of 10 kW/kg (González et al. 2016a). On the other hand, their unique energy capacity is significantly higher compared to that of conventional capacitors. As a result, these gadgets close the distance between aluminium electrolytic capacitors and batteries, offering an interesting solution. Notably, supercapacitors not only discharge rapidly but can also

recharge within a brief timeframe, a crucial advantage for energy recovery systems (Chatterjee and Nandi 2021a). Supercapacitors occupy an intermediate position between capacitors and batteries in terms of both specific power and energy. This can be illustrated through a Ragone plot, as depicted in Fig 1.1 (Chakraborty and N. L. 2022), where the energy and power densities of diverse energy storage conversion devices are represented on the horizontal and vertical axes, respectively (Chatterjee and Nandi 2021).

1.2 LITERATURE REVIEW

1.2.1 Energy storage mechanism for supercapacitors

Understanding the mechanisms by which supercapacitors store charges is crucial. These devices utilize two primary methods for charge storage: one occurs at the interfaces of electrode-electrolyte, while the other takes place within the active sites of the electroactive materials.

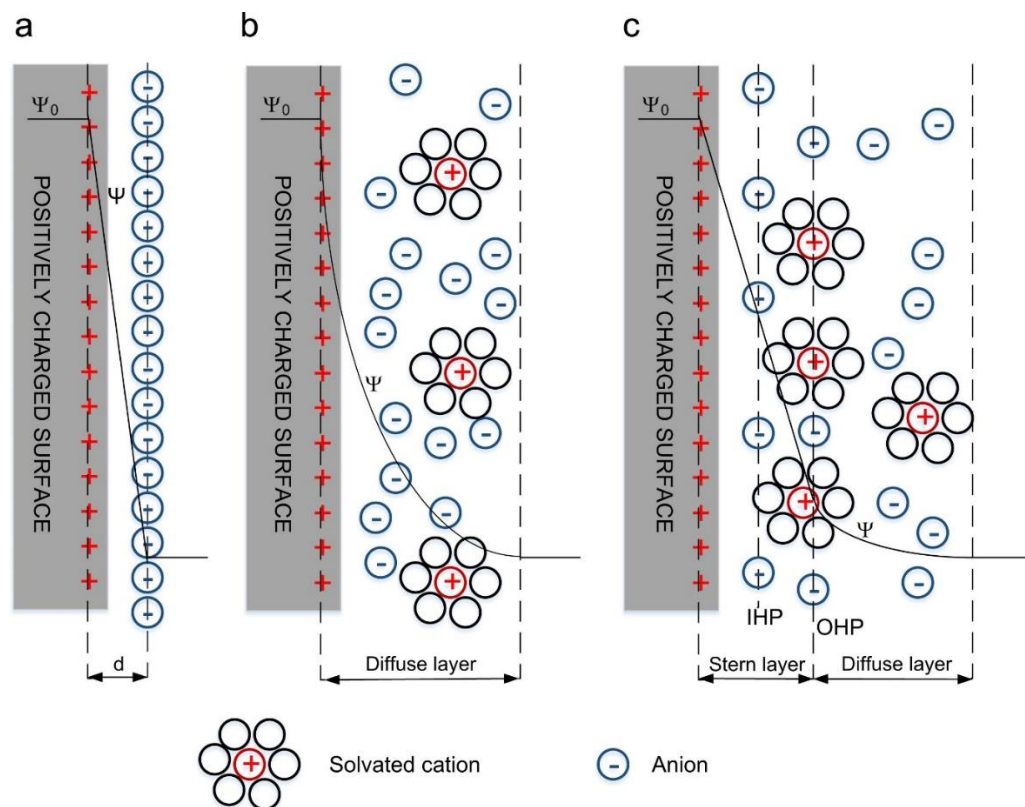


Figure 1.2. (a) Helmholtz model, (b) Gouy–Chapman model, and (c) Stern model (González et al. 2016a)

The storage of charge at interfaces is referred to as the electric double layer capacitance mechanism. Alternatively, the charge storage phenomenon within the electroactive sites

follows the pseudocapacitive mechanism, involving redox transition and intercalation processes (Iro et al. 2016; Miller 2018). Electric double layer capacitors (EDLCs) store electric charge by electrostatically adsorbing and then releasing electrolyte ions at the interface between the electrode and the electrolyte. The concept is controlled by the Electric double layer (EDL) model, which was first developed by von Helmholtz in the 1800s (Helmholtz 1853). This theory offers a simple structure for estimating the spatial charge arrangement at interfaces of double layers. According to this theory, the charge of a solid electronic conductor is neutralized by ions of opposite charge, which are located at a distance 'd' from the surface of the solid to the centre of the ions. Additionally, the theory accommodates the existence of rigid layers that offset the charges originating from the solid (Bagotsky 2005; Endo et al. 2001) (Fig 1.2(a)). Gouy suggested that when a solid becomes charged, an equal and opposite ionic charge emerges in the surrounding liquid, considering the arrangement of electrolyte ions in the electrolyte. These ions diffuse into the liquid until their departure creates a counter potential, limiting further diffusion (Fig 1.2(b)). Gouy and Chapman developed theories on this diffuse layer, suggesting ion concentration near the surface follows the Boltzmann distribution. However, this model falls short for highly charged double layers, as experimental observations show measured thickness exceeds calculated thickness (Guo et al. 2015a; Zhang et al. 2018). Stern made a significant discovery in comprehending the double layer mechanism by combining elements of the Helmholtz and Gouy-Chapman theories. He separated the ion distribution close to the charged surface into two sections: the dense Stern layer near the surface and the spread-out layer extending away from it. In the Stern layer, hydrated ions adhere to the electrode, comprising specific and non-specific ions, as well as counter ions. These ions are classified into inner Helmholtz plane (IHP) and outer Helmholtz planes (OHP) (Fig 1.2(c)). Meanwhile, the diffuse layer maintains its properties as described by Gouy and Chapman (Eftekhari 2018a; Snook et al. 2009). This combined model helps calculate the EDL capacitance (C_{dl}) by considering the capacitances of both layers.

Under these circumstances, the capacitance of the EDL is determined by adding together the capacitance of the diffusion layer (C_{diff}) and the Stern layer (C_H). This can be represented by the equation:

$$\frac{1}{C_{dl}} = \frac{1}{C_H} + \frac{1}{C_{diff}} \quad (1.1)$$

The characteristics of EDL are determined by aspects like the characteristics of the electrode's surface, the variety of ions in the electrolyte, the choice of solvent, and the prevailing environmental settings. These elements collectively determine charge distribution and ion interactions at the solid-liquid interface, crucial in electrochemical processes (Zhang and Zhao 2009). The capacitance of an EDLC closely mirrors that of a capacitor with parallel plates. As a result, its specific capacitance can be articulated as (Breitkopf and Swider-Lyons 2017; Yu et al. 2013):

$$C = \frac{\epsilon_0 \epsilon_r A}{d} \quad (1.2)$$

where ϵ_r signifies the dielectric constant of the electrolyte solution, ϵ_0 denotes the permittivity of free space, A stands for the surface area, and d represents the Debye length which essentially measures the effective distance between ions and the electrode surface. In theory, a larger surface area should yield a greater capacitance, implying a direct correlation. Nonetheless, the actual relationship is not straightforward because solvated ions struggle to access micropores at small sizes, hindering double layer formation. Besides surface area, high conductivity is crucial for achieving substantial capacitance (Fan et al. 2010; Guo and Li 2011; Hulicova-Jurcakova et al. 2009). Consequently, carbon-based materials with extensive surface areas are commonly employed in EDLCs. Given the absence of faradaic processes, these materials exhibit prolonged cycle life as they are not prone to destruction from phase changes or swelling.

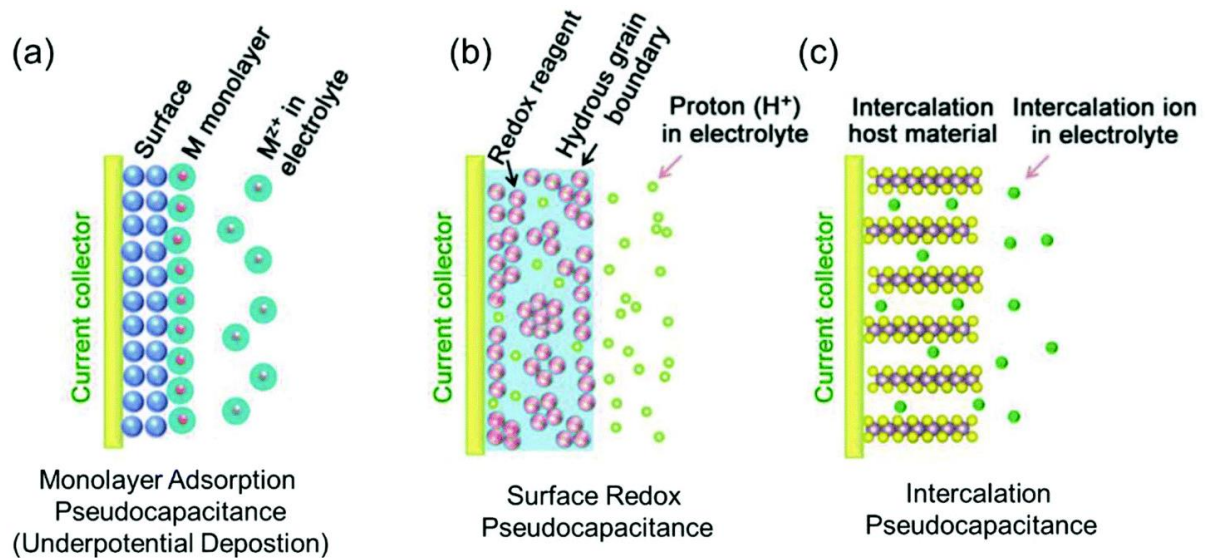


Figure 1.3. (a) Underpotential deposition; (b) Redox pseudocapacitance; (c) Intercalation pseudocapacitance (Huang and Niederberger 2019)

Pseudocapacitors differ from EDLCs in the way they store energy. Energy storage in pseudocapacitors involves fast and reversible reactions between the electrolyte and certain materials on the surface of the electrode, happening at specific energy levels. Ions from the electrolyte pass through a barrier and contact the surface atoms of the electrode. Fig 1.3 shows three distinct redox mechanisms capable of generating pseudocapacitance (Augustyn et al. 2014): (a) underpotential deposition, (b) redox pseudocapacitance, and (c) intercalation pseudocapacitance.

(a) Underpotential deposition: Underpotential deposition is a phenomenon that occurs in electrochemistry where metal cations are reduced on the surface of a different metal at a potential that is less negative than their own redox potential. An example of this process is the formation of a monolayer of lead on a gold surface. This occurs when metal ions from the bulk electrolyte are reversibly adsorbed onto the surface, forming an adsorbed monolayer above their redox potential (Liu et al. 2018b). This category encompasses underpotential deposition of lead on a gold electrode (Fig 1.3(a)).

(b) Redox pseudocapacitance: Pseudocapacitors operate by facilitating redox transitions triggered by the electrochemical adsorption of ions onto or in close proximity to the surface of the electrode material. This is succeeded by faradaic processes (Fig 1.3(b)). For example, transition metal oxides like Ruthenium oxide undergo redox reactions (Raza et al. 2018a).

(c) Intercalation pseudocapacitance: In this process, ions pass through the layers or tunnels of a material or species that can undergo a faradaic transition, while retaining its original crystal structure (Liu et al. 2018b). An example of this phenomenon can be seen in Nb_2O_5 when it is placed in a lithium electrolyte (Fig 1.3(c)).

1.2.2 Types of supercapacitors

Supercapacitors are classified as Electric Double layer Capacitors (EDLCs), pseudocapacitors, and hybrid capacitors based on their storage mechanism and cell structure.

1.2.2.1 Electric Double layer Capacitors (EDLCs)

Electric Double layer Capacitors EDLCs function differently from traditional capacitors. EDLCs utilize the boundary between the electrode and the electrolyte for energy storage rather than storing charges within the dielectric layer (González et al. 2016b). When voltage is applied to the electrodes, ions migrate to the surface of the double layer, charging the

capacitor. During discharge, ions migrate through the electrolyte and enter the pores of oppositely charged electrodes (Kötz and Carlen 2000). The electrode prevents the recombination of positive and negative charges, generating charge on both electrodes as shown in Fig 1.4 (a). This connection of dual layers enhances the available area and minimizes the gap between electrodes, enabling supercapacitors to attain greater energy storage capacity compared to traditional capacitors (Sharma and Kumar 2020). Additionally, EDLCs benefit from a larger electrode/electrolyte interface, leading to increased capacitance. The electrolyte has excellent electrical conductivity, reducing internal resistance, and good wettability, facilitating ion mobility into the electrode pores, further enhancing capacitive performance. The choice of a supercapacitor depends heavily on the choice of electrolyte, with aqueous and organic electrolytes being common options. The selection depends on the electrodes and charge collectors used. Activated carbon, a category of abundant and affordable carbon, is commonly used in commercial EDLCs, offering specific capacitance values of 100-120 F/g in organic electrolytes (Simon and Gogotsi 2008). Advanced carbon structures like ordered mesoporous carbon, carbon nanotubes, carbon aerogels and graphene have been developed to enhance the capacitance of EDLC.

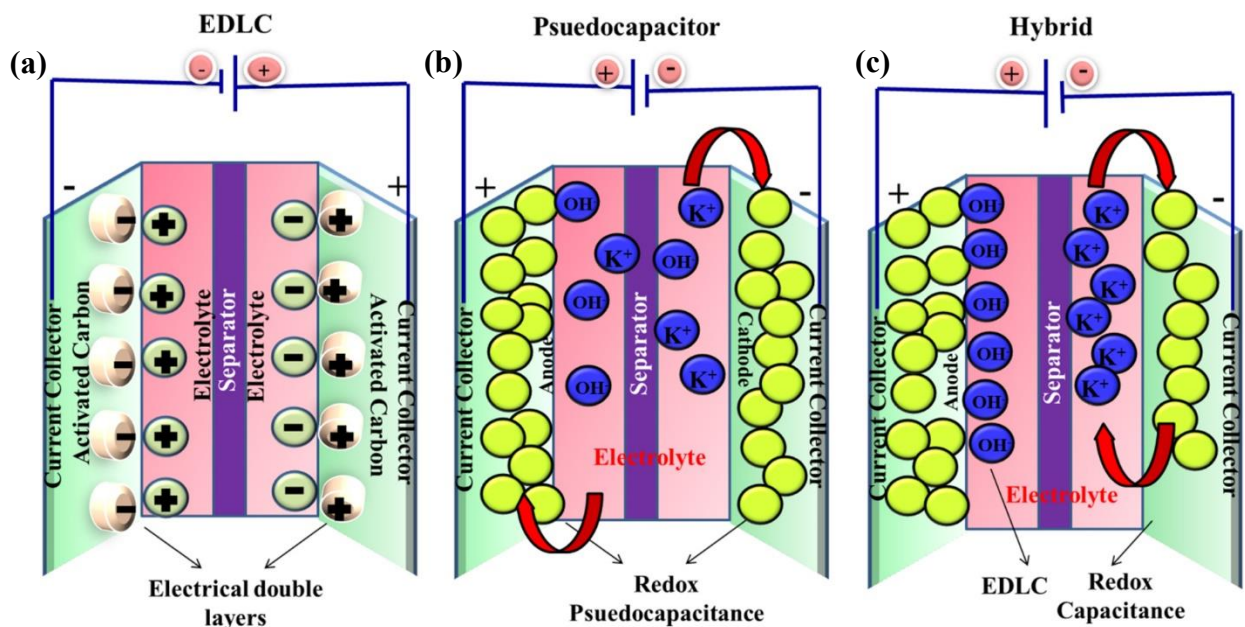


Figure 1.4. (a) Electric Double Layer Capacitor; Pseudocapacitor; (c) Hybrid supercapacitor (Chakraborty and N. L. 2022)

1.2.2.2 Pseudocapacitors

Pseudocapacitors store charge through the transfer of charge between the electrode and electrolyte, unlike EDLCs, which store charge electrostatically (Mohapatra et al. 2012). The Fig 1.4(b) represents the schematic illustration of a pseudocapacitor. In these capacitors, electrons are emitted in redox reactions and move between the electrode-electrolyte interface, ensuing a transfer of charge. The chemical changes that take place in the electrodes should ideally be reversible for achieving a higher cycle life. By utilizing these electrode materials, it is possible to create higher energy density supercapacitors. Pseudocapacitors offer superior energy densities compared to electrochemical double-layer capacitors, but at the cost of reduced rates and shorter cycle lifetimes (Lokhande et al. 2011; Stoller et al. 2008). When a voltage is applied to a pseudocapacitor, the movement of charge through the double layer causes reduction and oxidation reactions on the electrode material, leading to a flow of faradic current through the supercapacitor cell. Due to their faradic nature, which involves a reduction-oxidation cycle similar to that of batteries, pseudocapacitors exhibit lower power density and cycling degradation (Jiang and Liu 2019). Ruthenium oxide, a valuable material for pseudocapacitors due to its multiple redox phases, offers high capacitance in proton-rich environments like sulfuric acid (Zhang and Zhao 2009). However, its toxicity, cost, and scarcity limit practical application, leading research towards alternatives like cobalt oxide, nickel oxide, cobalt selenide, manganese selenide and conductive polymers (Wang et al. 2011b, 2015c; Xuan et al. 2021a). The theoretical pseudocapacitance can be calculated using the formula (Zhi et al. 2013):

$$C = \frac{n \times F}{M \times V} \quad (1.3)$$

The number of electrons transferred during the process is denoted by n , the molar mass of the metal oxide used is represented by M , the Faraday constant is denoted by F , and the operating voltage window is represented by V .

1.2.2.3 Hybrid pseudocapacitors

Hybrid supercapacitors integrate electrostatic and pseudocapacitive charge storage mechanisms, offering advantages surpassing those of individual EDLC and pseudocapacitor systems as shown in Fig 1.4(c). These hybrids boast high specific capacitance and enhanced specific energy, coupled with excellent power density and cycle stability (Chen et al. 2017b). Electrodes in hybrid systems are categorized based on material composition. Asymmetric hybrid supercapacitors feature one EDLC electrode and one

pseudocapacitor electrode, typically comprising carbon-based and pseudocapacitive materials, respectively (Mei et al. 2019; Patil et al. 2020). Battery-type hybrid supercapacitors incorporate one battery electrode and one supercapacitor electrode, providing high energy density and rapid recharging, alongside exceptional power density and extended cycle life (Halper and Ellenbogen 2006). Composite electrodes blend conducting polymers, metal oxides, and carbon-based materials, optimizing characteristics like capacitance, operational potential window, and cycle stability. Carbon-based materials foster a capacitive charge layer and facilitate increased contact between electrolyte and pseudocapacitive materials, enhancing overall performance. Supercapacitors that are hybrid can have a symmetric or asymmetric configuration. (Baptista et al. 2019; Kunwar et al. 2019). Symmetric systems employ identical pseudocapacitive and EDLC materials for both electrodes, while asymmetric configurations utilize dissimilar materials. Asymmetric supercapacitors offer superior energy and power densities, though with greater complexity and cost compared to symmetric counterparts. Understanding the interplay between electrode materials and overall system performance is crucial, particularly in asymmetric designs where each electrode significantly influences supercapacitor behavior. This overview provides insight into the diverse configurations and potential applications of hybrid supercapacitors in energy storage solutions (Wang et al. 2019b).

1.2.3 Electrode material

Supercapacitors use two energy storage mechanisms depending on the electrode materials. EDLCs store charges statically within porous carbonaceous electrodes, while pseudocapacitive supercapacitors use transitional metal oxides, metal chalcogenides, nitrides and conducting polymers to store energy through rapid and reversible electrochemical redox reactions. Both mechanisms require suitable materials in electrodes, selected based on shared criteria.

1. Ample surface area and porosity
2. Excellent surface wettability
3. Superior electrical conductivity
4. Prolonged cycle stability (over 10^5 cycles)
5. Easy adjustment of morphology (such as pore sizes, distribution, and particle dimensions)

6. Thermodynamic stability across a broad operational potential range (Kim et al. 2015a).

1.2.3.1 Electric double layer capacitor (EDLC) electrode materials: Activated carbon

Carbon is the material widely used for EDLC electrodes. This is because it has several ideal characteristics such as low manufacturing cost, abundance, large surface area, controllable morphology, and high electrical conductivity. Modified carbon can be classified into three types, namely Activated carbon, Carbon nanotubes, and Graphene. Activated carbon (AC) is often chosen as the material for EDLC electrodes because of its reasonable cost. Their structure is complex and contains tiny pores, medium-sized pores, and large pores, which results in a substantial specific surface area (Pandolfo and Hollenkamp 2006; Syarif et al. 2012). Although their electrical conductivity is lower, they are still suitable for supercapacitors. AC can be manufactured from different carbon-dense organic sources like fossil fuels, coal, synthetic polymers, lumber, and coconut husks (Zhang and Zhao 2009). To produce non-crystalline carbon, the carbonization process includes subjecting precursors to oxidizing gases like CO₂, steam, and air at high temperatures in an inert atmosphere. In contrast, activation occurs at lower temperatures. Activating agents such as carbonates, alkalis, chlorides, or specific acids are necessary for chemical activation. These substances assist in developing a porous structure within the carbon particles (Simon and Burke 2008).

The activated carbon electrodes in aqueous electrolytes exhibit specific capacitance values ranging from 100 to 300 F/g, which are higher than those in organic solutions, typically below 150 F/g. This difference is mainly attributed to the smaller ion size in aqueous systems. (Ali et al. 2013). The increase in specific surface area (SSA) of activated carbon from 621 m²/g to 2685 m²/g has been demonstrated to raise the specific capacitance of electrodes from 17.68 F/g to 171.2 F/g (Wang et al. 2015a). It's crucial to select an appropriate pore size; for instance, a pore size of 0.8 nm is appropriate for organic electrolytes, while 0.4 or 0.7 nm pore sizes are beneficial for aqueous electrolytes (Raymundo-Piñero et al. 2006). Surface functionalization of carbon material enhances faradaic redox reactions, resulting in a capacitance increase of about 5 to 10 %. Achieving maximum specific capacitance hinges on the harmonization between pore size and ion size (Zhong et al. 2015).

The development of hybrid lithium-ion supercapacitors (HSCs) has recently utilized agar-derived AC as the cathode material. This takes advantage of the EDL capacitance behavior

for charge storage. HSCs offer a combination of high-power density similar to capacitors and high energy density similar to lithium batteries. The AC being utilized possesses an ideal pore volume and a tight distribution of pore sizes, leading to a considerable specific surface area of over 1672 m²/g and a specific capacitance of 210.4 F/g (Zhang et al. 2020a). Different approaches can improve the electrochemical capabilities of ACs, such as adjusting the Fermi level position through the use of ultrasonic radiation (Bordun et al. 2017), and oxidizing the surface (Grishchenko et al. 2020), introduction of sulfur and oxygen functionalities (Raj et al. 2020), composite fabrication with other carbon nanomaterials like carbon nanotubes and carbon nanofibers (CNFs). Cheng et al. (Cheng et al. 2020a) introduced a novel nanocomposite electrode by combining conventional ACs with carbon black, carbon nanotubes, and CNFs. The resulting electrode exhibited superior electrochemical performance compared to pure AC electrodes, attributed to synergistic effects among the composite constituents.

This quaternary nanocomposite electrode demonstrated excellent capacitance retention, with 91.4 % / 30,000 cycles. Wang et al. (Wang et al. 2024b) developed a composite material called CCV, made of cellulose nanofibers (CNFs), carbon nanotubes, and vinasse activated carbon (VAC), with a multi-layer framework. CNFs form the main skeleton, carbon nanotubes provide fast electron transfer and electromagnetic wave loss, and VAC enhances double layer performance. This synergy results in excellent energy storage and electromagnetic interference (EMI) shielding capabilities. By adding a vitrimer polymer, Wang et al. tailored CCV's shape and performance. Overall, CCV shows promising potential for energy storage and EMI shielding applications due to its stable performance and integration. Thillaikkarasi et al. (Thillaikkarasi et al. 2023) studied novel electrode materials for supercapacitors, including activated carbon and multiwalled carbon nanotubes. They found that the AC-MWCNTs (25:75) nickel foam electrode showed high specific capacitance and energy/power densities, outperforming the stainless-steel counterpart. Teak sawdust-derived porous carbon (TPC) and activated carbon *Mangifera indica* leaves was prepared using a cost-effective method, showcasing a high surface area and enhanced storage capacity by Hegde et al. (Hegde and Bhat 2024a). In tests, TPC-850 displayed a capacitance of 572 F/g at 0.5 A/g in 6 M KOH, and retained 95.83 % capacity after 4500 cycles at 500 mV/s scan rate. The activated carbon from *mangifera indica* depicted a high specific capacitance of 521.65 F/g at a current density of 0.5 A/g. It also achieved an energy density of 17.04 Wh/kg at a power density of 242.50 W/kg in a 6 M

KOH electrolyte. In the same way, Hegde et al. (Hegde and Bhat 2024b) highlighted a study on carbon derived from *Cocos nucifera* trunk sawdust. The study demonstrated that this material exhibited exceptional performance as an electrode material. The researchers found that the material showed optimal performance at a 6 M KOH electrolyte concentration, with high specific capacitance of 559 F/g at 0.5 A/g, good cyclic stability, and high energy density.

1.2.3.2 Carbon nanotubes (CNTs)

Electrodes crafted from carbon nanotubes (CNTs) have emerged owing to their distinctive characteristics. Their wide external structure includes a high SSA, a unique inner framework of mesopores, strong chemical and heat resistance, improved electrical conductivity, and low mass densities. Additionally, the pliability of CNTs and their interconnected lattice facilitate improved integration with active materials, ensuring a seamless distribution for heightened utilization of the SSA (Isacfranklin et al. 2023). The mesoporous structure of CNT networks leads to CNT electrodes possessing a lower equivalent series resistance (ESR) and enhanced power relative to ACs, facilitating quicker and more efficient diffusion of electrolyte ions (Cheng et al. 2011a). Du et al. reduced electrode ESR using highly concentrated colloidal CNT films (Du et al. 2005). Various fabrication methods can be employed for CNTs. Shi et al. (Rui et al. 2011) emphasized the impact of synthesis method on electrode performance. They grew CNTs on porous nickel foam using the Chemical Vapour Deposition (CVD) method, resulting in superior capacitive performance but limited specific surface area remains a challenge for CNT applications in high-performance supercapacitors. CNTs are typically categorized into two main types: single-walled carbon nanotubes (SWCNTs) and multi-walled carbon nanotubes (MWCNTs) (Boddula et al. 2019). CNTs are typically produced by catalytically decomposing certain hydrocarbons. It is possible to control different factors, such as crystalline structure, in order to create different types of CNTs, including SWCNTs and MWCNTs (Pandolfo and Hollenkamp 2006). SWCNTs tend to clump together in bundles, which reduces their surface area and makes only the external layer available to electrolyte ions (Cheng et al. 2011a). The effectiveness of SWCNTs is significantly influenced by the availability of electrode materials and the dimensions of the electrolyte ions (Li et al. 2010). The SSA of SWCNTs is around 1315 m²/g, while MWCNTs have a smaller SSA than ACs. This leads to reduced electrical capacitance for CNTs compared to ACs. The mesoporous structure of MWCNTs allows for easier ion migration, but frequent intercalation and

depletion can weaken their mechanical strength (Dillon 2010). The shape and purity of the resulting CNT material are crucial in determining the specific capacitance of the electrodes. For example, MWCNT sheet electrodes with a diameter of 80 Å and a SSA of 430 m²/g showed a maximum specific capacitance of 104 F/g (Niu et al. 1997). By treating with acid, the specific capacitance can be increased by about 50 F/g by adding oxygen-containing groups to the surface of MWCNTs (Peng et al. 2007).

CNT materials are directly used on conductive substrates, providing support to enhance electron transport and lower the contact resistance among current collectors and active substances. Furthermore, different materials and composites have been employed to coat CNTs, with the goal of enhancing the electrode's electrochemical properties (Liu et al. 2020a). For example, Aravinda et al. (Aravinda et al. 2016b) developed an eco-friendly titanium dioxide/functionalized multiwalled carbon nanotube (TiO₂/FMWCNT) composite electrode for supercapacitors with a specific capacitance of 90 F/g using reactive magnetron sputtering. A new method decorates carbon nanotubes with ZnO for supercapacitor electrodes, achieving a specific capacitance of 48 F/g and an energy density of 13.1 Wh/kg (Aravinda et al. 2013c). Liu et al. (Liu et al. 2020a) developed flexible supercapacitors with high-performance fibrous electrodes using a composite of MnO₂ nanorods loaded onto MXene nanosheets and coated onto carbon nanotube fibers. The resulting supercapacitors showed excellent capacitance retention after 5000 cycles and superior flexibility. They have garnered attention as electrode materials for supercapacitors, often employed in composite form alongside various materials including graphene, metal oxides (MOs), polymers, MXene, and their composites. Kaushik et al. (Kaushik et al. 2023) studied the effects of adding CNTs to Fe₂O₃ nanoparticles on the electrochemical properties of the composite. They synthesized Fe₂O₃-CNT composites by hydrothermal treatment of ferricyanide, sodium dodecylbenzene sulfonate, and commercially available CNTs. By adjusting the concentrations of CNTs and Fe₂O₃, they achieved Fe₂O₃:CNT ratios of 1:1, 1:1.5, and 1:2.5. The 1:1.5 ratio showed the highest pseudocapacitance due to improved conductivity from the added CNTs and optimized Fe concentration.

The synergistic behavior of a graphene nanoplatelets (GNP)/CNT composite as an electrode material was systematically demonstrated by Pandit et al. (Pandit et al. 2023). The restacking of GNP sheets is effectively inhibited by the uniform dispersion of CNTs, resulting in enhanced SSA, porosity, and conductivity. As a result, a specific capacitance of up to 143 F/g at 5 mV/s is exhibited by the GNP composite with 1.0 wt % MWCNTs,

representing a 150 % improvement compared to pristine GNPs. Xu et al.(Xu et al. 2023) have developed an ultralight and durable MXene/CNT aerogel with excellent electrical conductivity and mechanical properties. It can withstand 70 % compressive strain and retains 85 % of its initial strain over 1000 cycles. Integrated into a supercapacitor, it achieves 410.7 mF/cm² at a current density of 0.8 mA/cm² and can effectively power an LED when four devices are connected in series.

1.2.3.3 Graphene

Graphene is a widely recognized substance comprising a single-atom-thick layer with a two-dimensional monolayer structure. The material consists of carbon atoms with all-sp² hybridization in a polyaromatic crystal lattice, and it has a honeycomb structure. Graphene showcases several fascinating qualities, such as a significant surface area compared to its volume, superior thermal and electrical conductance, adaptable structural properties, a highly adjustable surface area (reaching up to 2675 m²/g), minimal diffusion length owing to its slimness, robust chemical resilience, formidable mechanical durability, and an extensive range of potential applications (Booth et al. 2008; Lee et al. 2008; Wu et al. 2012; Xia et al. 2009). It benefits from a large surface area and open pore system, making it ideal for high-performance electronics, energy storage systems, and sustainable energy generation devices (Brownson et al. 2011; Liang et al. 2009, 2011; Wu et al. 2012). Graphene is typically obtained by oxidizing graphite to produce graphite oxide, followed by the exfoliation of graphite oxide to produce graphene oxide (GO) sheets, which can be further reduced to obtain chemically derived graphene (Chen et al. 2013b).

Several graphene production techniques include Chemical Vapour Deposition (CVD), micromechanical exfoliation, arc discharge, electrochemical methods, epitaxial growth on silicon carbide, chemical reduction of exfoliated graphene oxide, and unzipping carbon nanotubes (Kuilla et al. 2010). The hydrothermal technique allows for the creation of GO nanostructures in various forms, including single layers, few layers, and 3D porous configurations. Modifying the Ni²⁺ concentration during the process enables control over these forms. Notably, the 3D porous configuration stands out for achieving a specific capacitance of 352 F/g at 5 mV/s (Li et al. 2014).

Ogata et al. (Ogata et al. 2016) devised a novel device incorporating reduced graphene oxide (rGO) and GO that served dual functions as both a supercapacitor and a battery. The device demonstrated supercapacitor behaviour up to an operating voltage of approximately

1.2 V, transitioning to battery-like characteristics beyond 1.5 V. This innovative design capitalizes on the unique properties of graphene-based materials to fulfil multiple energy storage roles within a single device. Furthermore, Liu et al. (Liu et al. 2010a) developed a mesoporous graphene network tailored for use with ionic liquid electrolytes. This network exhibited remarkable performance, capable of operating at voltages up to 4 V. At elevated temperatures of 80 °C, the device achieved impressive energy densities of 136 Wh/kg, while maintaining a respectable energy density of 90 Wh/kg at room temperature. Such advancements underscore the capabilities of materials derived from graphene in facilitating superior energy storage systems across various operating conditions.

Graphene layers often face the challenge of readily creating unchangeable clusters and returning to their graphite form due to restacking. The issue of restacking leads to a permanent loss in battery capacity and reduces the efficiency of its initial charge-discharge cycle. Van der Waals interactions between adjacent sheets reduce the material's energy density by decreasing its surface area (Dubey and Guruviah 2019). To address restacking, researchers have developed composite nanofibers of graphene nanoribbons (GNR/C) through electrospinning of polyacrylonitrile (PAN) containing graphene oxide nanoribbons (GONRs), followed by twisting and carbonization (Matsumoto et al. 2013). The PAN-containing GONR nanocomposites exhibited high orientation during electrospinning and were transformed into all-carbon materials GNR/CNF after carbonization (Zhang et al. 2014b). Also, several approaches can mitigate this challenge, including template-assisted growth (Karnan et al. 2017), integration of spacers (Shabangoli et al. 2019; Wang et al. 2012a) and crumpling the graphene layers (Casiraghi et al. 2007). For instance, Wang et al. (Wang et al. 2012a) expanded the separation between graphene layers by incorporating pillared carbon black nanoparticles as spacers. This modification enhanced the electrochemical characteristics of flexible graphene papers by creating an open structure, thereby facilitating charge storage and ion transfer.

Another way to prevent graphene sheet restacking is by blending it with other materials to form a composite or nanocomposite. The main objective is to enhance the material's charge storage capacity by incorporating redox-active materials (Ul Hoque et al. 2024). Li and colleagues (Li et al. 2024) developed an eco-friendly method to create a graphene-based nanomaterial called graphene/amorphous carbon/Mn₃O₄. They used a special type of polymer to help form thin layers of graphene during the manufacturing process. This improved how well the graphene and Mn₃O₄ materials stuck together with excellent

performance. Beemaroo et al. (Beemaroo et al. 2023) developed a NiS₂@C-rGO hybrid network with a porous core-shell structure through hydrothermal synthesis for superior supercapacitors. This nanocomposite exhibited high capacitance values and showed outstanding endurance during cycling tests. It has the potential for advanced supercapacitor applications. Ghasemi et al. (Ghasemi et al. 2023) synthesized a novel ternary nanocomposite between polyaniline (PANI), GO and Copper ferrite (CuFe₂O₄) for hybrid supercapacitors using a two-step technique. Various electrochemical techniques were employed to assess the electrochemical properties, revealing superior performance of the ternary PANI/GO/CuFe₂O₄ electrode compared to single and binary samples.

1.2.3.4 Pseudocapacitor electrode materials: Conducting polymers (CPs)

Conducting polymers (CPs) have emerged as promising materials for pseudocapacitive electrodes due to their distinct advantages. These polymers offer high capacitance, adjustable redox activity, excellent conductivity, wide voltage ranges, easy manufacturing, minimal environmental impact, and cost-effectiveness. These attributes collectively make CPs a highly sought-after choice for energy storage applications (Gupta and Miura 2006; Kalaji et al. 1999; Wang et al. 2009). CPs excel at charge storage within their bulk, as their charge/discharge mechanism does not involve structural alterations like phase changes. This unique property enables CPs to deliver elevated capacitance due to their large surface areas and the ability to store energy through redox reactions (Ramya et al. 2013; Ryu et al. 2003; Shirakawa et al. 1977). Compared to other carbon-based materials, CPs provide greater conductivity, capacitance, and reduced equivalent series resistance (Halper and Ellenbogen 2006; Snook et al. 2011). Their specific capacitance arises from rapid, reversible redox reactions along π -conjugated polymer chains. However, the redox processes in CPs can lead to mechanical stress, limiting stability over numerous cycles, and they exhibit low power densities due to sluggish ion diffusion rates (Cheng et al. 2011b; Sharma and Bhatti 2010).

CPs are synthesized through various methods, primarily by oxidizing monomers chemically or electrochemically (Lokhande et al. 2016). These polymers feature a positively charged backbone and high electronic conductivity (ranging from 1 to 100 Scm⁻¹), typically existing in oxidized or "p-doped" states (Rudge et al. 1994). Currently, researchers are focusing on p-dopable polymers due to their consistent performance compared to non-dopable ones (Ryu et al. 2003). CP-based supercapacitors employ

electrodes arranged in three main configurations: (a) p-p type, comprising two p-doped CPs with differing electroactivities; (b) n-p type, with one p-doped and one negatively charged electrode of the same polymer; and (c) p-doped and p-p⁰, featuring two distinct p-doped CPs with varying electroactivities. The n-p type arrangement enables better energy density and power density (Cameron 2017; Meng et al. 2017; Sivaraman et al. 2006; Wang et al. 2010). Commonly used CPs for supercapacitors encompass a range of types, such as PANI, poly 3,4-ethylenedioxythiophene (PEDOT), polypyrrole (PPy), polyfurane, polyindole (PIND), poly(p-phenylenevinylene), polythiophene (PTh), and poly(p-phenylene).

Indeed, conducting polymers have garnered significant attention from research groups lately. Yang et al. introduce a novel method employing macromolecular interaction to fabricate self-standing hydrogels comprising PANI and PEDOT. These hydrogels, benefiting from high electrochemical activity of PANI and PEDOT's high electronic conductivity, exhibit robust mechanical properties and excellent electronic/electrochemical performances (Yang et al. 2020b). Lignin/polypyrrole composites were formed by coating water-insoluble kraft lignin with polypyrrole in a single-step process, as detailed by Bober et al. (Bober et al. 2018). Pyrrole polymerization, with or without methyl orange, yielded two types of polypyrrole films on the lignin surface: globular and nanotubular. These composites were converted into double-carbon composites via pyrolysis in a nitrogen atmosphere at 650 °C. The resulting materials were characterized using various techniques such as FTIR spectroscopy, XPS, EPR, SEM, specific surface area, and electrical conductivity measurements. Electrochemical properties were evaluated, focusing on capacitive behavior in acidic, neutral, and alkaline solutions.

Expansion and contraction issues during the charging/discharging process present a major challenge for conductive polymers, resulting in physical damage and reduced electrical efficiency through repeated use. For instance, PPy electrodes experienced a 50 % initial capacitance loss within the first 1000 cycles (Sharma et al. 2008). Similarly, Zhu et al. noted a 29.5 % reduction in performance for a PANI after 1000 cycles in a 1 M H₂SO₄ solution (Zhu et al. 2011). To address this stability issue, researchers have proposed two primary approaches: designing appropriate microstructures and creating composite electrodes. Wang et al. introduced a durable nanocellulose combined with PPy@GO nanocomposites (Wang et al. 2015d). After 16,000 cycles at this voltage, the electrode showed excellent stability, retaining over 85 % capacitance, and achieving a high volumetric capacitance of 198 F/cm³.

The addition of graphene, metal oxides, or other nanomaterials can greatly improve the effectiveness of CPs. Additionally, modifying the morphology or nanostructure of conducting polymers through techniques like nanostructuring, templating, or intercalation can also improve their activity and stability. Furthermore, exploring novel synthesis methods, such as electrochemical deposition, CVD, or templated polymerization, can lead to conducting polymer materials with tailored properties optimized for specific applications (Tundwal et al. 2024). In this context Pan et al. (Pan and Dong 2024) developed a method for constructing flexible, freestanding, three-dimensional hierarchical electrodes comprising graphene-encapsulated one-dimensional conducting PANi@MnO₂ coaxial nanowires grown on electrospun carbon nanofibers (G-PANi@MnO₂/ECNFs). Electrochemical experiments demonstrated outstanding results, exhibiting a high specific capacitance (1364.3 F/g at 0.3 A/g) and impressive cycling durability (89.2 % retention after 2000 cycles) in a 1 M Na₂SO₄ solution. Shehzad et al. (Shehzad et al. 2024) developed a hierarchical porous biocarbon by carbonizing sugar at 700 °C, then functionalized it with molybdenum disulfide nanosheets to create SC/MoS₂. They electrodeposited polypyrrole onto this composite on a nickel foam substrate. The composites showed high specific capacitance and improved mesopore volume.

1.2.3.5 Transition metal oxides and their composites

Metal oxides belong to a category of materials known as pseudocapacitance materials, which rely on the redox pseudocapacitive charge storage mechanism. Electrode materials have been extensively researched, focusing on transition metal oxides (TMOs) and their composites, including MnO₂, ZnO, Fe₂O₃, Co₃O₄, as well as layered double hydroxides (LDHs) such as CoAl LDH and NiCo LDH. The distinct qualities of TMOs, such as their ability to have different valence states that enable ion and electron intercalation into the structure of metallic compounds, add to their significant natural stability (Jing et al. 2020b; a, 2021; Li et al. 2017b). Metal oxides provide supercapacitors with greater energy density than traditional carbon materials and superior electrochemical stability compared to CPs. They enable the occurrence of faradaic electrochemical interactions between ions and electrode materials within certain potential limits, comparable to the behavior of electrostatic carbon materials. Investigations into surface enhancements have aimed to increase both the hydrophilicity and the capacitive capabilities of carbon-based materials. The application of metal oxide/hydroxide particles, including RuO₂, MnO₂, Co₃O₄, NiO, or mixed metals, markedly boosts the electrodes' capacitance by inducing swift faradaic

pseudocapacitance effects. Improving the electrical conductivity of electrodes is vital for maximizing the capacitive properties of carbon capacitors, especially when incorporating metals (Wiston and Ashok 2019).

Different TMOs including RuO₂, Fe₃O₄, MnO₂, NiO, Co₃O₄, IrO₂, V₂O₅, and CuO demonstrate faradaic behavior during their charge storage process (Zhang et al. 2020b) that exhibit faradaic behavior in their charge storage mechanism. Additionally, there are mixed metal oxides like CuO@NiO (Guo et al. 2015b), CuO/Cu₂O (Hu et al. 2013), Cu/Cu₂O@TiO₂ (Mondal and Pal 2016), Fe₂O₃@TiO₂ (Dekrafft et al. 2012), ZnO@Co₃O₄ (Huang et al. 2014a), Fe₂O₃/Co₃O₄ (Kaneti et al. 2014), Fe₂O₃/NiCo₂O₄ (Huang et al. 2014a), Co₃O₄/ZnFe₂O₄ (Zhou et al. 2015), Co₃O₄/NiCo₂O₄ (Hu et al. 2015), ZnO/ZnFe₂O₄ (Hou et al. 2015; Yang et al. 2017), where By enhancing the surface area and incorporating multiple functionalities into metal-organic frameworks (MOFs), they can be fabricated into electrodes for supercapacitors, offering high-performance capabilities.

Ruthenium oxide (RuO₂) has attracted significant attention for its use in supercapacitor electrodes due to its remarkable properties. These properties include superior chemical and thermal robustness, outstanding electrical conductivity, a broad potential window of 1.2 V, easily reversible redox reactions, prolonged cycle life, a high theoretical capacitance ranging from 1200 to 2200 F/g, and strong rate capability (Lokhande et al. 2016). RuO₂ substances are costly, possibly restricting their widespread use. To create affordable substances, RuO₂ combinations are linked with other pseudocapacitive or carbon-based materials to decrease the quantity of RuO₂ without affecting efficiency (Hwang et al. 2015).

MnO₂ stands out as a favorable choice for electrode materials because of its affordability (Chen et al. 2010b; Toupin et al. 2004; Zhang et al. 2014a), along with its advantageous properties such as a wide electrochemical potential window, low toxicity, and high theoretical specific capacitance (1370 F/g), position it as a promising alternative for electrode materials (Wang et al. 2015b; Zhu et al. 2012). In their study, Devi et al. (Devi et al. 2023) investigated the potential of MnO₂ as a significant material for energy storage because of its technological importance and potential in pseudocapacitance.as a promising material for power storage due to its technological significance and potential in pseudocapacitance. They synthesized different phases of MnO₂ (α , β , and γ) with distinct morphologies using a hydrothermal route and evaluated their electrochemical performance in aqueous sodium sulfate. Characterization techniques, including X-ray diffraction and

electron microscopy, revealed the material's structure and morphology. The direct band gaps of α -, β -, and γ - MnO_2 were found to enhance electrochemical performance. The specific capacitance of α - MnO_2 reached a peak of 138 F/g at 1 A/g. Utilizing a method known as free dealloying, a composite electrode comprising $\text{Ni}(\text{OH})_2$ nanopetals network, Ni-based metallic glass matrix and Ni nanofoam interlayer ($\text{Ni}(\text{OH})_2/\text{Ni-NF/MG}$) was precisely engineered. The creation process involved an HF solution with a high oxygen content. Remarkably, this self-standing electrode achieved 966.4 F/cm³ of volume-specific capacitance at 0.5 A/cm³. Its durability is further highlighted by maintaining around 92 % of its original capacitance after 6000 usage cycles, indicating superior cyclic stability (Zheng et al. 2019a).

The exfoliation of crystalline α - V_2O_5 powders into V_2O_5 nanoribbons was carried out using an innovative microwave heating method. These nanoribbons were then used to develop a hybrid material composed of V_2O_5 and rGO. This was achieved through a mechanism of self-assembly, facilitated by cations, and was followed by a process of thermal annealing. The produced nanoribbons showed a remarkable energy and power density. Furthermore, the specific capacitance stayed almost unchanged after going through 1800 cycles, showing excellent durability in cycling (Chen et al. 2020b). In a separate study, researchers successfully fabricated a $\text{V}_2\text{O}_5/\text{PANI}$ through a single-step chemical process. This composite exhibited impressive properties, including an energy density of 54.62 Wh/kg, a specific capacitance of 273 F/g, and a power density of 1636.5 W/kg at a current density of 1 A/g. Supercapacitors, both symmetric and asymmetric, utilizing V_2O_5 -based composites as electrodes, demonstrated high energy density and a wide voltage window, making them strong contenders against conventional batteries (Chen et al. 2019a).

Zhai et al. (Zhai et al. 2020) developed a versatile electrode termed pCcZC, which integrates porous carbonized cotton, ZnO nanoparticles, and CuS microspheres. This innovative composite material demonstrates potential for advanced applications in energy storage technologies. It also enabled the creation of binder-free and wearable electrodes. The flexible symmetrical supercapacitor using pCcZC electrodes demonstrated superior energy density and successfully powered an LED, showing potential for portable and wearable energy storage applications.

The electrochemical properties of Co_3O_4 are significantly influenced by its structure and the electronic configuration of the metal ions. In 2014, a team led by Guoxing Wang (Huang

et al. 2014b) synthesized nanoporous graphene embedded with Co_3O_4 nanocrystals. This resulted in three-dimensional nanoarchitectures that exhibited a high supercapacitance of 424.2 F/g. Supercapacitors with high specific capacitance can benefit from the use of battery-type materials. Phosphorous-doped Co_3O_4 (P- Co_3O_4) nanomaterial was synthesized by incorporating it within carbon nanowires co-doped with phosphorous and nitrogen (P, N-C). The structure prevents agglomeration of active materials, resulting in a large accessible surface area and efficient transfer of electrolyte ions. The P- Co_3O_4 and N-C structure delivers a high specific capacity of 669 mC/cm^2 at 1 mA/cm^2 and an ultralong cycle life with only a 4.8 % loss over 5000 cycles at 30 mA/cm^2 (Liu et al. 2020b).

Fe_2O_3 , renowned for its abundance, affordability, and high capacity, holds promise for various applications. Micro-supercapacitors (MSCs) are emerging as key components in portable and wearable electronic devices, given their high potential for energy storage. A novel $\text{Fe}_2\text{O}_3/\text{graphene}/\text{Ag}$ ink is utilized to fabricate MSC electrodes via 3D printing. This approach results in solid-state MSC devices with exceptional capacitance, energy density, and retention over 5000 cycles. Additionally, the 3D printed MSC demonstrates reliable flexibility, offering an efficient solution for advanced electrochemical energy storage (Tang et al. 2020b).

The $\alpha\text{-MoO}_3$ structure boasts the highest theoretical specific capacitance among intercalation pseudocapacitive materials (Yao et al. 2016). $\text{MoO}_3/\text{MWCNT}$ composites were synthesized using magnetron sputtering, offering an eco-friendly option for supercapacitor electrodes. The composite demonstrated a specific capacitance of 93 F/g and an energy density of 7.28 Wh/kg in a non-aqueous electrolyte, indicating its potential as an energy storage material for consumer electronics (Aravinda et al. 2013b). Hollow structures such as $\text{MoO}_2@\text{N}$ doped C nanofibers and CuCo_2S_4 tubular nanostructures are emerging as promising components for energy storage devices, exhibiting outstanding electrical storage capabilities (Chen et al. 2016b). A supercapacitor constructed from these materials showcased an ultrahigh energy density of 65.1 Wh/kg at a power density of 800 W/kg, alongside good electrochemical cycling stability. These findings underscore the potential of tube-like nanostructures for supercapacitors (Liu et al. 2018c). A nano CeO_2/AC composite electrode was prepared using a solvent and binder-free scalable technique. It exhibited an area capacitance of 162 F/g and excellent cycle stability, with an energy density of 4.86 Wh/kg and a power density of 3500 W/kg even at high current density. (Aravinda et al. 2013a).

Spinel nickel oxide offers several advantages, such as affordability, accessibility, and eco-friendliness, making it an attractive and scalable alternative among other metal oxides. Moreover, spinel nickel cobaltite (NiCo_2O_4) shows significantly enhanced electrochemical performance compared to single counterparts (Wang et al. 2011a). The researchers created flexible solid-state supercapacitors using $\text{NiCo}_2\text{O}_4 @ \text{NiMoO}_4$ deposited along PANI on carbon cloth. The carbon cloth-based electrodes exhibited a specific areal capacitance of 2.38 F/cm^2 and maintained 92.36 % capacitance even after 5000 cycles, making them suitable for use in flexible and wearable devices (Shen et al. 2019). The research explores the utilization of NiMn_2O_4 incorporated on rGO as an electrode material for supercapacitor applications. Synthesized via a one-pot hydrothermal technique, the nanocomposites, namely $\text{rNiMn}_2\text{O}_4\text{-10}$ and $\text{rNiMn}_2\text{O}_4\text{-20}$, were examined and found that the $\text{rNiMn}_2\text{O}_4\text{-20}$ nanocomposite exhibited outstanding electrochemical performance. It exhibited 1248 F/g of specific capacitance 1 A/g while maintaining long-term stability of 91.6 % even after 5000 cycles at 3 A/g . (Britto et al. 2024).

The combination of CP and metal oxides to develop nanocomposites has garnered significant interest due to their ability to integrate the advantages of both materials at the nanoscale. Nanocomposites, characterized by their nanoscale structure, enhance the macroscopic properties of products. These substances provide distinct mechanical characteristics, enhanced barrier attributes, decreased weight, and improved long-term resilience against heat, wear, and scratches. In a study conducted by Shahabuddin et al., (Shahabuddin et al. 2022) CP was doped with metal oxides to synthesize a nanocomposite. This synthesized material demonstrated superior performance in both supercapacitor applications and photocatalysis compared to bare CP. Similarly, in an experiment by Raza et al., metal oxides and CPs were combined as composites to mitigate each other's limitations, resulting in a potential composite material with promising prospects for supercapacitor applications (Raza et al. 2022). A novel PANI- Co_3O_4 supercapacitor electrode with foamed nickel substrate was synthesized by Fan et al. (Fan et al. 2021) using hydrothermal and in situ polymerization methods. The composite exhibited notably elevated specific capacitance of 3105 F/g along with dependable cycle stability. Moreover, it showcased a substantial energy density, underscoring its promising prospects for advanced energy storage equipment.

1.2.3.6 Transition metal chalcogenides (TMCs): Transition metal sulfides (TMSs)

Transition metal chalcogenides (TMCs) represent a class of stable crystalline compounds formed by the combination of transition metals (elements belonging to groups 3 to 12) and chalcogenides (elements from group 16, particularly sulphides, selenides, and tellurides) (Simon and Gogotsi 2008; Wang et al. 2012b). With their adjustable structures, varying band gaps, and diverse stoichiometries, TMCs exhibit a wide range of material properties, rendering them highly appealing for numerous applications, notably in energy conversion and storage technologies. Their suitability for supercapacitor utilization stems from a host of advantageous characteristics, including abundant electrochemically active sites, favorable flexibility, moderate conductivity, short diffusion pathways, diverse morphologies, and the manifestation of quantum effects (Theerthagiri et al. 2018b). TMCs have garnered significant interest due to their ability to deliver high specific power, extended stability and life cycles, and enhanced safety profiles compared to conventional battery systems. Consequently, they find applications across a spectrum of fields, including consumer electronics, power buffering systems, electric tools, and hybrid electronic vehicles. Furthermore, TMCs have become integral components in cutting-edge energy technologies, serving purposes in fuel cells, LEDs, sensors, lithium-ion batteries, electrocatalysts, and memory storage units (Gao et al. 2013). The exceptional properties of TMCs, such as improved longevity, flexibility, additional reactive sites, catalytic activity, enhanced conductivity, reduced internal resistance, minimized ohmic losses, shortened electron transport pathways, and quantum size effects, underscore their versatility and promise in addressing a myriad of technological challenges and advancing sustainable energy solutions (Han et al. 2018).

Nanostructured transition metal sulfides (TMSs) have become pivotal electrode materials in electrochemical supercapacitors due to their outstanding features. They possess superior electrical conductivity, high specific capacity, low electronegativity, unique crystal structures, and heightened redox activity. Remarkably, TMSs demonstrate improved performance in contrast to TMOs, primarily due to the replacement of oxygen atoms with sulfur atoms within their lattice (Geng et al. 2018; Liu et al. 2018f; Yu and Lou 2018).

Recent investigations into electrode materials based on nickel sulfide (NiS) have primarily focused on their application in supercapacitors. This concentration stems from the distinctive chemical and physical properties inherent to NiS, facilitating efficient ionic

transport pathways across the electrode surface via Faradaic processes. Chen et al. (Chen et al. 2017a) employed a two-step process to synthesize Ni₃S₂ nanosheet clusters for a high-performance supercapacitor where 2-methylimidazole (2-MI) guided the formation of α -Ni(OH)₂ nanosheet clusters, which were then sulfidized hydrothermally to produce pure Ni₃S₂. The resultant supercapacitor exhibited remarkable characteristics, attaining a specific capacitance of around 1000 F/g at 50 A/g even after undergoing 20,000 cycles in a 1 M NaOH electrolyte. This underscores its exceptional performance and enduring stability. Chen et al. (Chen et al. 2019b) successfully created a composite between NiS and Ni₃S₄ through a single step hydrothermal process. This composite featured interconnected 2D nanosheets supporting the formation of 3D microspheres. With an impressive specific capacitance of 1,796 F/g, these results underscore the promise of interconnected NiS/Ni₃S₄ composites as electrode materials for supercapacitors.

A hydrothermal method introduced phosphorus doping in copper sulfides. The P-doped copper sulfide achieved 656 F/g specific capacitance at 1 A/g with 80 % retention over 800 cycles. In an asymmetric supercapacitor, it yielded 28.537 Wh/kg energy density and 642.08 W/kg power density at 2 A/g (Samdhyan et al. 2023). Ahmad et al. (Ahmad et al. 2023) synthesized ZnS, CuSe₂, and ZnS–CuSe₂ nanocomposites using a cost-effective sonochemical method. The ZnS–CuSe₂ composite showed a specific capacitance of 640 F/g at 1 A/g, outperforming ZnS (501 F/g) and CuSe₂ (450 F/g). It also maintained 81.8 % capacitance over 8000 cycles at 5 A/g discharge current.

Various CoS₂ and CoS₂-based composites with diverse nanostructures are now utilized as electrode materials for advanced supercapacitors. Porous quadruple-shelled hollow CoS₂ dodecahedrons were synthesized employing ZIF-67 as a template. These formations exhibited excellent supercapacitive behavior, showcasing a specific capacitance of 375.2 F/g at a current density of 1 A/g. Moreover, the material retained 92.1 % of its original capacitance following 10,000 cycles in a 2 M KOH electrolyte (Jia et al. 2019). Wang et al. (Wang et al. 2017a) employed a one-step hydrothermal method to grow CoS₂ and MoS₂/CoS₂ nanotube arrays on Ti substrates, using Co(OH)₂ nanorod array templates. The composite electrode exhibited a specific capacitance of 142.5 mF/cm² at 1 mA/cm² in a 1 M KCl electrolyte, surpassing that of pure CoS₂ (3.13 mF/cm²) and MoS₂ (84 mF/cm²) electrodes. Furthermore, the MoS₂/CoS₂ electrode retained 92.7 % of its capacitance over 1,000 cycles, demonstrating notable long-term stability.

The affordability, remarkable conductivity, and abundance of electrochemically active sites of FeS₂ have rendered it a favored option for supercapacitor electrodes. Diverse morphologies of FeS₂-based composites have been devised for this application (Pham et al. 2018; Yu et al. 2018; Zhao et al. 2017a). Zardkhoshoui et al. (Zardkhoshoui et al. 2019) synthesized petal-like FeS₂ on nickel foam via hydrothermal synthesis for supercapacitor electrodes. It exhibited a maximum specific capacitance of 321.30 F/g at 2 A/g in a 6 M KOH electrolyte and retained 47 % at 20 A/g, showing excellent rate capability. Stability was good, with a 19.10 % loss after 5,000 cycles at 4 A/g. They also created a flexible, asymmetric, all-solid-state supercapacitor using graphene-coated NiCo₂Se₄ as the positive electrode and petal-like FeS₂ as the negative electrode, achieving a specific capacitance of 221.30 F/g at 1 A/g and an energy density of 78.68 Wh/kg, offering a promising route for flexible, high-performance supercapacitor electrodes. Sun et al. (Sun et al. 2019) synthesized FeS₂ nanoellipsoids for supercapacitors using a microwave-based technique. The FeS₂ electrode exhibited notable specific capacities of 515 C/g at 1 A/g and 355 C/g at 20 A/g in a 2 M KOH electrolyte, indicating outstanding rate performance. The resultant supercapacitor demonstrated a high energy density of 64 Wh/kg at a power density of 271.2 W/kg and retained 91 % of its initial capacity after 5,000 cycles, showcasing the promise of FeS₂ nanoellipsoids for energy storage applications. A FeS₂ and nitrogen-sulfur-doped graphene (FeS₂/NSG) composite was synthesized via a swift microwave technique for supercapacitor electrodes. In a 6 M KOH electrolyte, the FeS₂/NSG composite attained a peak specific capacitance of 528.7 F/g at 1 A/g. It also displayed commendable cycling stability, preserving 89 % of its capacitance after 10,000 cycles at 10 A/g (Wang et al. 2018)

Research has particularly emphasized the use of MoS₂ and its composites as electrode materials for supercapacitors due to their promising electrochemical properties (Chen et al. 2018; Hongtao et al. 2019; Liu et al. 2016). Kandula et al. (Kandula et al. 2018) fabricated Co₉S₈/α-MnS@N-C@MoS₂ nanowires through a hydrothermal sulfurization process for supercapacitor electrodes. The electrode attained a peak specific capacitance of 1,938 F/g at 1 A/g in a 2 M KOH electrolyte and exhibited robust cycling stability, preserving 86.9 % of its initial capacitance after 10,000 cycles at 10 A/g. An asymmetric supercapacitor incorporating this electrode demonstrated high energy densities of 64.2 Wh/kg and 23.5 Wh/kg at power densities of 729.2 W/kg and 11,300 W/kg, respectively, underscoring its potential for large-scale energy storage applications. Liu et al. (Liu et al. 2019b) introduced a MoS₂/N-doped three-dimensional graphene amalgamation for supercapacitors. The

electrode demonstrated a distinct capacitance of 301.2 F/g at 0.2 A/g in a 1 M Na₂SO₄ electrolyte and maintained 82 % of its capacitance post 1,000 cycles at 1 A/g.

Manganese sulfide (MnS) has recently attracted interest due to its diverse valence states, abundant occurrence, and enhanced electronic conductivity relative to its oxide counterparts (Palaniyandy et al. 2019). A nanocomposite of MnS hybrid supported on graphene nanosheets (GNS-MnS) was produced using a hydrothermal process. This composite demonstrated a maximum specific capacitance of 792 F/g at 2 A/g (Palaniyandy et al. 2019). Mixed metal sulfides represent a promising class of materials for supercapacitors, offering high specific capacitance, enhanced conductivity, and chemical stability. Their tunable properties allow for optimization based on specific application needs, while their abundance and relatively low cost make them economically viable for large-scale production. With ongoing research focused on improving synthesis methods and material designs, they hold significant potential for advancing the development of high-performance supercapacitors capable of meeting the demands of various energy storage applications (Ali et al. 2023). Kim et al. (Kim et al. 2017) produced a NiCo₂S₄ film on stainless steel foil using a chemical bath deposition process for supercapacitor applications. The NiCo₂S₄ nanosheets exhibited excellent electrochemical performance, achieving a specific capacitance of 1,155 F/g at 10 mV/s in a 1 M KOH electrolyte. Furthermore, they demonstrated good cycling stability, retaining 95 % of their original capacitance after 2,000 cycles. Research on cobalt, copper, and manganese sulfide composites for supercapacitor electrodes is limited despite their promising potential. In this regard Iqbal et al. (Iqbal et al. 2020a) utilized a simple one-step electrodeposition technique to grow CuMnS and CoMnS directly on a Ni substrate. CuMnS and CoMnS electrodes displayed maximum specific capacitances of 1691 F/g and 2290 F/g, respectively, at 10 A/g current density. Asymmetric supercapacitor devices with CoMnS//AC exhibited superior energy density compared to CuMnS//AC. Both devices showed ~94 % capacitance retention after 2500 cycles. Dunn's model was employed to scrutinize the charge storage phenomenon, revealing the potential of co-electrodeposited transition metal sulfides as effective electrode materials for supercapacitors. Another study describes a one-step electrodeposition method to tailor the morphology and structure of CoMnS nanomaterials by adjusting the amount of CS₂. This results in the preparation of CoMnS nanomaterials with unique flower-like structures, which facilitate electron transfer and improve electrochemical behavior. Notably, when the CS₂ amount is 4 mmol, CoMnS-4 exhibits a specific capacitance of 3469.5 F/g at 1 A/g,

maintaining 2830.5 F/g (81.56 %) even at a high current density of 20 A/g. After 10,000 cycles, it demonstrates excellent cycle stability, retaining 95.78% capacitance at 20 A/g. Furthermore, the CoMnS-4//AC asymmetric supercapacitor device achieves an outstanding energy density of 85.91 Wh/kg at 800 W/kg, showcasing its significant application potential (Hu et al. 2020a). Hu et al. (Hu et al. 2020b) introduced a non-polluting, simple electrodeposition method to fabricate ternary iron cobalt transition metal sulfide (FeCoS) nanosheet arrays on Ni foam, serving as cathode materials for asymmetric supercapacitors. FeCoS-15 nanosheet arrays exhibit a specific capacitance of 3741.03 F/g at 1 A/g and maintain 92.84 % capacitance retention at 20 A/g for 10,000 cycles. Asymmetric supercapacitors using FeCoS-15 nanosheets as positive electrodes and AC as negative electrodes demonstrate remarkable electrochemical performance, achieving an energy density of 54.08 Wh/kg at 800 W/kg with 85.64 % cycling retention over 10,000 cycles. These findings highlight the promising application potential of FeCoS nanosheet arrays for high-performance asymmetric supercapacitors. Zhao et al. (Zhao et al. 2021) aimed to enhance the electrochemical performance of TMSs commonly used in supercapacitors. They devised a novel approach using a Zn–Co-ZIF template to fabricate Ni–Zn–Co–S hollow nanocages, achieving a remarkable specific capacitance of 1930.9 F/g at 1 A/g. This innovative design strategy aimed to overcome limitations by optimizing the structure and composition of the electrode material. Miah et al. (Miah et al. 2023) synthesized the composite rGO/FeNiS₂, which demonstrated a specific capacitance of 1013 F/g at 2 A/g and displayed enhanced rate capability, indicating its potential for high-performance supercapacitor applications. Chandraraj et al. (Chandraraj and Xavier 2023) investigated cobalt sulphide, nickel sulphide, and graphene oxide nanocomposites for a supercapacitor using electroanalytical techniques and found that the CoS/NiS/GO electrode exhibited lower impedance compared to graphene oxide. The electrode showed a specific capacitance of 1114 mAh/g at 5 A/g and retained 80 % capacity after 8000 cycles. This highlights the potential of CoS/NiS/GO for practical supercapacitor use. Guo et al. (Guo et al. 2023) used a simple electrodeposition method to create iron-cobalt bimetallic sulfide nanospheres on nickel foam. This improved its capacitive performance, resulting in high specific capacitance, long-term stability, and good rate capability. FeCo₂S₄/NF and AC were used to build an asymmetric supercapacitor (ASC), achieving a maximum energy density of 29.4 Wh/kg at 800 W/kg.

In supercapacitor applications, the composite of nickel cobalt sulfide (NiCo_2S_4) and nickel cobalt oxide (NiCo_2O_4) with metal sulfides offers a promising solution for enhancing energy storage performance. The composite material, by merging the high specific capacitance characteristic of metal sulfides with the conductivity and stability of NiCo_2S_4 , demonstrates enhanced capacitance, charge/discharge rates, and cycling stability. Synergistic effects between the components further enhance overall performance, while the cost-effectiveness and versatility of the composite make it a competitive option for various supercapacitor applications, promising advancements in energy storage technology (Chen et al. 2020a).

Shinde et al. (Shinde et al. 2019) synthesized NiCo_2S_4 thin films for supercapacitors using the SILAR method on Ni mesh with different Ni and Co ratios. The films showed superior supercapacitance performance with a specific capacitance of 1427 F/g at a scan rate of 20 mV/s, indicating their effectiveness compared to other metal oxides and sulfides. In this study by Raman et al., (Raman et al. 2019) the use of TMCs, particularly manganese selenide (MnSe), is explored for enhancing supercapacitor electrodes. MnSe 's multiple oxidation states and high electrical conductivity make it promising compared to transition metal oxides. Electrodeposited MnSe and a $\text{MnSe}/\text{NiCo}_2\text{O}_4$ heterostructure were synthesized and evaluated. Both showed impressive specific capacitances: 184.92 F/g and 450.75 F/g, respectively, at 0.1 A/g. The $\text{MnSe}(20)/\text{NiCo}_2\text{O}_4$ cell displayed a specific capacitance of 45.78 F/g and excellent cycling stability over 5000 cycles, retaining 86 % of its capacitance. This research highlights MnSe and $\text{MnSe}/\text{NiCo}_2\text{O}_4$ as potential high-performance supercapacitor electrode materials, advancing energy storage technology. Zhao et al. (Zhao et al. 2022) developed a core-shell heterostructure, $\text{R-NiCo}_2\text{S}_4@\text{CuCo}_2\text{S}_4$, with sulfur vacancies to enhance supercapacitor electrodes. This material displayed remarkable performance: 2922.9 F/g capacity at 0.5 A/g, 68 % retention from 0.5 A/g to 10 A/g, and 99.92 % capacitance retention after 10,000 cycles at 30 A/g, highlighting its potential for efficient electrochemical energy storage.

In a study, a $\text{NiCo}_2\text{S}_4/\text{MoS}_x/\text{NF}$ electrode material was created and showed improved electrochemical performance compared to single-component MoS_x/NF or $\text{NiCo}_2\text{S}_4/\text{NF}$. The $\text{NiCo}_2\text{S}_4/\text{MoS}_x/\text{NF}$ electrode demonstrated superior cyclic stability and coulomb efficiency. When used in a supercapacitor, it achieved an energy density of 32.54 Wh/kg and power density of 285.72 W/kg, and powered an LED for 6 minutes. These findings highlight its capability for supercapacitor electrodes in energy systems (Wang et al. 2023). Kong et al.

(Kong et al. 2023) investigated morphology and structure's impact on nanomaterials' cycle stability and rate performance. They developed $\text{MnCo}_2\text{S}_4/\text{NiCo}_2\text{S}_4$ (MCS/NCS) composites with a three-dimensional network structure, showing superior capacitive and conductive properties. Among them, MCS/NCS-6 demonstrated exceptional specific capacity (920 C/g at 1 A/g) and cycling stability. The assembled asymmetric supercapacitor, MCS/NCS//AC, displayed high energy density (45.6 Wh/kg at 800 W/kg) and robust cycle life (75.6 % capacitance retention over 10,000 cycles). The research led by Liao et al. (Liao et al. 2024) resulted in the successful synthesis of a composite material, $\text{NiCo}_2\text{O}_4@\text{MnS}$, with remarkable electrochemical properties. It attained 2100 F/g of specific capacitance at 2 A/g and retained 76 % of its capacitance after 10,000 cycles at 10 A/g. When incorporated into a $\text{NiCo}_2\text{O}_4@\text{MnS}/\text{AC}$ device at a current density of 1 A/g, it showed a specific capacitance of 203 F/g and an energy density of 55 Wh/kg at a power density of 697 W/kg. These enhancements were attributed to the unique hierarchical structure of $\text{NiCo}_2\text{O}_4@\text{MnS}$, which facilitated ion diffusion, increased specific surface area, and improved electronic conductivity.

1.2.3.7 Transition metal selenides (TMSes)

Transition metal selenides (TMSes) have attracted considerable interest as efficient electrode materials for supercapacitors among TMCs. This interest is primarily due to their high electronic conductivity (1×10^{-3} S/m), extensive surface area, and robust electrochemical performance (Gopi et al. 2018; Zhai et al. 2018). The electrodes based on selenide are particularly noteworthy for their ability to retain cycling stability, as they avoid the formation of polyselenide intermediates when undergoing repeated charge and discharge cycles (Ko et al. 2016). In recent years, a diverse array of TMSes, including single-metal (Kirubasankar et al. 2018), binary-metal (Zhai et al. 2018), multinary-metal (Hosseini and Shahrokhian 2019), and composite/hybrid/integrated forms (Wang et al. 2019c), have been investigated for SC applications. The increasing volume of recent publications on metal selenide electrode materials, underscores the growing research interest in this area, suggesting continued and expanded development in the near future. Nickel selenide has been extensively researched as an electrode material for supercapacitors due to its similarities with nickel sulfide in chemistry (Sivanantham and Shanmugam 2017; Tang et al. 2015a). In a single-step hydrothermal process, (Du et al. 2017) produced honeycomb-shaped arrays of electrically conductive $\text{Ni}_{0.85}\text{Se}$ nanosheets on NF with a low band gap. Subhadarshini et al. (Subhadarshini et al. 2020) documented

the formation of NiSe-Se nanotubes on NF through chemical bath deposition (CBD) method. These nanotubes demonstrated a significant capacitance of 2447.46 F/g at 1 A/g, attributed to their expansive surface area, abundant active sites, structure free of binders, and the hollow nature that serves as ion reservoirs. Tang et al. (Tang et al. 2015a) fabricated NiSe nanowire films on NF via a hydrothermal method. These electrodes showed a specific capacitance of 1790 F/g at 5 A/g and retained 70% of their initial capacitance after 1000 cycles. Various nanostructures of nickel selenide have been reported as advanced electrode materials for supercapacitors. These include nanoparticles (Wu et al. 2019), microspheres (Guo et al. 2016), nanorods (Yu et al. 2020), nanosheets (Chang et al. 2018a), leaf-like structures (Chang et al. 2018a), and nanoarrays (Gu et al. 2020).

The superior conductivity and electrochemical properties of copper selenide make it a highly effective electrode material when compared to its oxide counterparts. For example, Liu et al. (Liu et al. 2021) experimented with different microwave power levels (600, 800, and 1000 W for 90 seconds) and reaction durations (60, 90, and 120 seconds at 1000 W) to synthesize CoSe₂ with porous nature. The best electrode, made at 1000 W for 90 seconds, showed superior cyclic durability (100.97% /25,000). Furthermore, an asymmetric supercapacitor (ASC) using CoSe₂ as the anode and AC as the cathode achieved a highest energy density of 18.9 Wh/kg. Li et al. (Li et al. 2023) have developed hollow CoSe₂ nanospheres enveloped with reduced graphene oxide (rGO) nanosheets using a self-templated method in combination with electrostatic self-assembly and heat treatment. The rGO nanosheets served as separators and structural protectors, preventing aggregation and reducing nanoparticle size while preserving structural integrity. This encapsulation enhanced electrical conductivity and decreased OH⁻ adsorption energy at the CoSe₂/rGO interface. The resulting hollow CoSe₂/rGO nanocomposites demonstrated high specific capacities. When paired with a nitrogen-doped carbon nanotube negative electrode, the hybrid supercapacitor device achieved an energy density of 50.1 Wh/kg at 800 W/kg and maintained 94% capacity after 5000 cycles.

Cu₃Se₂ is grown on Cu foil by immersion in a sodium selenosulfate solution for the first time. The self-supported copper selenide electrode material exhibits superior electrochemical properties and a flexible ASC was fabricated using Cu₃Se₂@Cu and AC, delivering an energy density of 30.8 Wh/kg at 461 W/kg (Li et al. 2023). Cu₃Se₂ thin film was deposited on a stainless steel substrate using the chemical bath deposition method (Malavekar et al. 2020). This electrode demonstrates excellent specific capacitance of

1285 F/g and cycling stability of 92 % after 3000 cycles. The solid-state symmetric supercapacitor made with this electrode achieves 132 F/g and shows notable stability.

There is a scarcity of discussions regarding the applicability of zinc selenide (ZnSe) alone in supercapacitors. Typically, ZnSe often struggles with poor electronic conductivity and a tendency to clump together during electrochemical processes. These issues reduce its effectiveness as electrodes. (Mohammadi Zardkhoshoui et al. 2020). To tackle these issues, researchers have turned to utilizing ZnSe in combination with bimetallic selenides or composite materials, aiming to enhance its performance by integrating combined characteristics and configurations. For instance, Cheng et al. (Cheng et al. 2020b) synthesized ZnSe using a hydrothermal method. To address its limitations, ZnSe has been incorporated into zinc-cobalt bimetallic selenide, resulting in improved electrode activity. In another similar work by Vidhya et al. (Sangeetha Vidhya et al. 2022) the ZnSe@MoSe₂ electrode shows its outstanding potential in supercapacitor application with good stability over 2000 cycles at 10 A/g. Its flower-like structure facilitated ion transport and electron mobility. When assembled in a full-cell configuration with AC, it achieved an energy density of 43 Wh/kg at 740 W/kg with over 99.3 % retention capacity. When connected in series, the full cell powered multiple LEDs, demonstrating its potential for practical supercapacitor applications. The hydrothermal technique was used to synthesize ZnSe, MnSe, and a composite of ZnSe/MnSe. The specific capacitance values obtained were 536 F/g for ZnSe, 733 F/g for MnSe, and notably 1439.89 F/g for the ZnSe/MnSe composite at 1 A/g. The MnSe/ZnSe composite demonstrated excellent specific power and energy values. Also, it was found that the material was stable even after 5000 cycles, and impedance spectroscopy results showed a low charge transfer resistance (R_{ct}) value of 0.35 Ω compared to 0.51 Ω for ZnSe and 0.46 Ω for MnSe (Hussain et al. 2024).

Santhoshkumar et al. (Santhoshkumar et al. 2020) synthesized FeSe₂ which possess flower like morphology. Consequently, the electrode material delivered 95 % capacitance retention after 500 cycles. The synthesis of the Fe₂O₃@FeSe₂ heterostructure represents a significant advancement in the field of supercapacitors. With a specific capacitance of 524 mF/cm² at 1 mA/cm², this structure demonstrates exceptional energy storage capability and efficiency. Moreover, when incorporated into the MnO₂//Fe₂O₃@FeSe₂ device configuration, a specific capacitance of 155 mF/cm² was achieved (Liu et al. 2024a).

Furthermore, Javed et al. (Javed et al. 2020a) synthesized α -MnSe microflowers on flexible carbon textile substrates for solid-state supercapacitor (SSC) devices. The SSC device maintained a high level of performance over time (97.17 % /5000). This was because of the synthesis procedure behind α -MnSe nanostructure and the construction of SSC device. Duan et al. (Duan et al. 2023) introduced a new method for designing and synthesizing MnSe electrodes for energy storage devices. These electrodes exhibit a unique flower-like morphology and demonstrate a specific capacitance of 423.1 F/g at a current density of 1 A/g, with exceptional cyclic stability over 3000 cycles. This highlights the potential of MnSe electrodes in advancing high-performance supercapacitors and energy storage technologies.

Researchers have discovered that single metal selenides have limited capacity due to having only one metal available for potential redox reactions. To address this limitation, they have started exploring mixed metal selenides. These compounds contain different metal ions, which create synergistic effects that lead to stronger chemical bonds, a broader range of redox reactions, and ultimately, enhanced capacity. This shift towards using mixed metal selenides shows promise in overcoming the drawbacks of single metal selenides and represents a strategic direction for improving the performance and functionality of energy storage devices (Hussain et al. 2022).

Cheng et al. (Cheng et al. 2020b) observed the development of needle-like Zn-CoSe, created via a hydrothermal process and then selenization. The nanomaterial exhibited characteristics similar to a battery with a respectable specific capacity of 1419 C/g at 2 A/g. Hollow nanospheres of Co-Mo-Se were produced using the gas bubble template method. These empty spherical structures were made from many extremely thin layers, creating a special design with plenty of active surfaces and many pathways for quick energy storage and transfer. The optimized Co-Mo-Se hollow nanospheres exhibited outstanding electrochemical performance, maintaining a cycling stability of 94.2% after 2000 cycles (Ma et al. 2020b). This study highlights the potential of mixed metal selenide-based nanostructures in addressing the challenges of energy storage and paving the way for advancements in next-generation rechargeable battery technologies. In 2020, Cu-Co-Se with nanosphere morphology was developed by Zardkhoshoui et al. (Zardkhoshoui and Davarani 2020a). The battery type electrode material exhibited excellent electrochemical properties and confirming its potential for high-performance energy storage applications. Nanoarchitectures consisting of CuSe polyhedra/CoSe₂ nanorods@GO hybrids were

created, showcasing an impressive surface area of 83.11 m²/g. These structures displayed exceptional electrochemical performance, with an asymmetric cell delivering a superior capacitance of 192.8 F/g at 1 A/g. Additionally, the hybrid system achieved the highest energy and power densities on record at 54.6 W/kg and 700 Wh/kg, respectively (Karuppasamy et al. 2022b). The hydrothermal process successfully synthesized bimetallic NiCo₂Se₄/Fe₂CoSe₄ micro-flowers. The resulting NiCo₂Se₄/Fe₂CoSe₄ composite exhibited an activity of 323.66 mAh/g at 1 A/g and retained 91.08 % of original capacity over 10,000 GCD cycles. Furthermore, when used in a NiCo₂Se₄/Fe₂CoSe₄//AC configuration, the system achieved an impressive energy density of 51.83 Wh/kg at 1 A/g (Panah et al. 2024).

Moreover, doping transition metal selenides for supercapacitors enhances conductivity, increases electrochemical surface area, improves stability, and allows for tuning of electronic properties, offering a promising route to tailor material properties and optimize electrode performance. In this context Sreehari et al. (Sreehari et al. 2024) investigated transition metal-doped CoSe₂ for superior supercapacitor applications via density functional theory. Fe and Cu doping boosts structural stability and electron states near the Fermi level. Fe-doping, more effective than Cu, yields more redox active sites due to its lower potential. Optimized Co_{0.5}Fe_{0.5}Se₂ exhibits maximum quantum capacitance (~1154 μF/cm²) versus CoSe₂ (~906 μF/cm²) at -0.6 V, ideal for asymmetric supercapacitors. The effect of adding niobium to NiSe nanostructures on their capacitive properties was investigated by Alshammari et al (Alshammari et al. 2024). The best-performing Nb_{0.06}NS showed 1482 F/g of C_s at 1 A/g, surpassing other doped materials. This improved performance is attributed to its morphology which helps in fast charge transfer inside nanomaterial.

A straightforward hydrothermal process combined with a universal ion exchange reaction by Liu et al. (Liu et al. 2024b) to produce transition-metal-doped Ni_{0.85-x}Se and NiSe nanoflowers using Co, Cu, and Zn ions. Various characterization techniques are employed to analyze the phases, morphologies, and compositions of the synthesized materials. This doping enhances the supercapacitor properties of Ni_{0.85}Se and NiSe, with Co_xNi_{1-x}Se delivering the best specific capacitances among the tested electrodes. Overall, this work provides valuable insights for producing desired nickel selenides for supercapacitors and offers a straightforward approach for designing other cation-doped transition-metal selenides for energy storage applications.

Combinations of metal selenides and carbonaceous materials have unique properties suitable for energy-related applications. Metal selenides face challenges such as poor conductivity and stability, which can be improved by combining them with carbonaceous materials. This combination enhances conductivity and mechanical strength. These composite materials show promise in batteries, solar cells, and catalytic processes due to their synergistic effects. Moosavifard et al. (Moosavifard et al. 2021a) developed a simple self-template method for preparing hollow cobalt-copper selenide microspheres wrapped on rGO with porous nature which may increase the surface area and conductivity of metal selenides. The synthesized electrode exhibited significant capacity retention of 91.5% after 6000 charge cycles, with excellent specific capacitance. Additionally, in an asymmetric two electrode assembly the corroborative effect of rGO and metal selenide gives a remarkable electrochemical output. The composite between carbon sphere and nickel cobalt selenide (C-20@ $(\text{Ni}, \text{Co})_{0.85}\text{Se}$) composite features a core-shell heterostructure and demonstrates exceptional electrochemical performance, making it ideal for advanced energy storage systems. It has a C_s of 960 F/g at 1 A/g, with exemplary energy and power density making it suitable for high-power applications. Additionally, it exhibits remarkable stability, retaining 81.5 % capacity after 5000 cycles at 10 A/g (Wu et al. 2021a). $\text{MnSe}_2/\text{CoSe}_2/\text{rGO}$ composites, synthesized using an ion-exchange strategy, show promising electrochemical properties (Xuan et al. 2021b). The optimized electrode exhibits 1138 C/g specific capacity, indicating efficient charge storage. The composites maintain a high-rate capability of 80 % even with a 50-fold increase in current density, making them suitable for high-power applications. The assembled hybrid supercapacitor (HSC) demonstrates a desirable energy density, highlighting their potential for efficient energy storage solutions. In one of the studies, the composition transferred from NiSe_2 to $\text{Ni}_{0.85}\text{Se}$ by adjusting the potential in a pulse-reversal electrodeposition technique (Su et al. 2024). The NiSe_2 electrode achieved 125.4 mAh/g at 2 A/g and retained 81.2 % capacity at 16 A/g. The hybrid supercapacitor reached 42 mAh/g at 1 A/g and 33.6 Wh/kg at 800 W/kg. This method shows great promise for practical applications in energy storage and conversion.

1.2.3.8 Transition metal tellurides

Transition metal tellurides, a class of compounds composed of metal cations bonded with tellurium anions are attracting attention for their diverse properties and potential uses. These compounds exhibit a broad spectrum of electronic, magnetic, and structural behaviors, making them intriguing subjects for both fundamental research and practical

utilization. From semiconducting behavior to superconductivity, metal tellurides offer a rich playground for exploring the interplay between structure, composition, and functionality. Their versatile nature has influenced supercapacitor technology also extends their relevance across various fields including electronics, thermoelectrics, and catalysis.

Manikandan et al. (Xuan et al. 2021b) used a hydrothermal method to form cobalt telluride nanorods for supercapacitor use. The CoTe NR electrode showed 170 C/g of specific capacity at 0.5 A/g and maintained 85 % of its initial capacity after 10,000 cycles at 30 A/g. An asymmetric supercapacitor using CoTe NRs achieved admirable energy and power density. Shi et al. (Shi et al. 2022a) synthesized CF@CoTe₂-NiTe₂, with 261.4 mAh/g of Cs at 1 A/g. Achieved an energy density of 41 Wh/kg at 750 W/kg and retained 87.6% of its capacitance after 5000 cycles when a hybrid supercapacitor was built. Rathore et al. (Rathore et al. 2022) synthesized a new material for supercapacitors. They used a simple chemical process to make a mix of vanadium telluride and carbon. They found that this mix had lots of micro and mesopores confirmed using BET isotherm analysis and could store a lot of electric charge. They also tested the material and found that it could keep working well even after being charged and discharged 5000 times. Furthermore, Farashah et al. (Farashah et al. 2023) introduces a self-templating approach to synthesize hollow FeNiCoTe nanocubes for hybrid supercapacitor electrodes. The optimized surface morphology and tellurium ion incorporation enhance electrochemical performance. Electrochemical analysis reveals exhibit a capacity of 1402 C/g at 1 A/g and 92.65% charge retention after 7500 cycles. The hybrid device (FeNiCoTe|| AC) shows high energy density (62.9 Wh/kg), power density (806.4 W/kg), and 89.6% capacity retention after 7500 cycles. These results highlight the potential of telluride-based chalcogenides for future energy storage devices. Meanwhile, an all-solid-state supercapacitor was created using tellurium nanotubes decorated with cobalt magnesium telluride microtubes on nickel foam. This unique structure enhances energy storage performance and delivers a lifespan of up to 15,000 cycles. The fabricated device exhibits a maximum energy density of 42.2 Wh kg/kg and maintains robust performance at various bending angles, demonstrating potential for future flexible applications (Bhol et al. 2024).

1.2.4 Electrolytes

The performance of a supercapacitor is intricately tied to the characteristics of its electrolyte, alongside its electrodes. The electrolyte plays a pivotal role in determining

operational voltage, resistance, and overall efficiency. Energy density, directly influenced by the voltage window, increases with the square of the operational voltage, while ionic resistivity inversely affects the supercapacitor's power capability (Burke 2007). Consequently, factors such as temperature coefficient, conductivity, and equivalent series resistance (ESR) are vital considerations in electrolyte selection, as they directly impact supercapacitor performance. A wide voltage window, high electrochemical stability, elevated ionic concentration, low solvated ionic radius, low viscosity, minimal volatility, low toxicity, cost-effectiveness, and high purity availability are key attributes sought in electrolytes. Given their critical role, the choice of electrolyte profoundly influences the construction of high-performance supercapacitors (Wang et al. 2012b). Currently, three primary types of electrolytes are employed in supercapacitors: aqueous, organic, and ionic liquids. Each type presents distinct advantages and challenges, necessitating careful consideration to match the electrolyte with the specific requirements and performance targets of the supercapacitor system.

1.2.4.1 Aqueous electrolytes

Aqueous electrolytes are favoured in supercapacitors due to their advantageous characteristics, including easy handling and high conductivity, which effectively reduce ESR and enhance device power density. Additionally, they are cost-effective and readily available. However, their operational range is constrained by the decomposition of water, limiting the voltage window within which they can function. Moreover, their temperature tolerance is bounded by the boiling and freezing points of water. Variations in aqueous electrolytes, spanning acid, base, and neutral compositions, offer researchers ample opportunities to optimize performance. For instance, transitioning from H_2SO_4 to KOH for nickel oxide electrodes has been shown to significantly boost specific capacitance, from 16 to 155 F/g, by facilitating Faradaic reactions in an OH^- ion-rich environment (Srinivasan and Weidner 2000). Aqueous electrolytes can be categorized into neutral (e.g., Na_2SO_4), alkaline (e.g., KOH), or acidic (e.g., H_2SO_4) solutions. The maximum cell voltage reported for acid and alkaline electrolytes is 1.3 V, while for neutral electrolytes, it extends to 2.2 V (Zhong et al. 2015). These insights underscore the versatility and potential for optimization offered by aqueous electrolytes in supercapacitor design and performance enhancement.

1.2.4.2 Organic electrolytes

Organic electrolytes are widely used in commercial applications due to their expansive potential window. This window spans from 0 to 2.2–2.7 V, which aligns with the energy density requirements of commercial demands. This broad voltage range enhances energy density significantly to meet industry standards. Acetonitrile (ACN) and propylene carbonate (PC) are the most commonly used solvents among organic electrolytes (Chakraborty and N. L. 2022). Acetonitrile has advantages over PC due to its lower ionic resistivity, which presents a more conducive environment for supercapacitor performance. However, safety concerns regarding acetonitrile's toxicity and flammability pose challenges (Kim et al. 2015c). Both solvents share common drawbacks, including higher costs, decreased conductivity and specific capacitance, and safety risks associated with volatility, toxicity, and flammability. Additionally, their purification and fabrication processes are complex, necessitating controlled environments devoid of water. Furthermore, organic electrolytes contribute to the aging, or degradation, of carbon electrodes (Kovalska and Kocabas 2016). Decomposition of the organic electrolyte occludes electrode pores, thereby diminishing capacitive performance and cyclic stability (Azaïs et al. 2007). Despite their benefits, these challenges underscore the need for ongoing research and development efforts to address safety concerns and optimize the performance of supercapacitors utilizing organic electrolytes.

1.2.4.3 Ionic liquids (ILs)

Ionic liquids (ILs) are a type of low-temperature molten salts made up of large organic cations and organic or inorganic anions. They are chosen as supercapacitor electrolytes because they are non-flammable and provide excellent electrochemical, thermal, and chemical resistance, along with low volatility (Galiński et al. 2006). This makes them ideal for high-temperature applications. One of the primary benefits of ILs is their capacity for customization through the combination of cations and anions, allowing for the fine-tuning of their properties to meet specific device needs (Armand et al. 2009; Liu et al. 2010b). Common cations for ILs include ammonium, imidazolium, pyrrolidinium, sulfonium, and phosphonium. Common anions, hexafluorophosphate (PF_6^-), include tetrafluoroborate (BF_4^-) and dicyanamide (DCA^-). ILs can withstand temperatures up to 300°C without evaporating (Burke 2007). However, ILs have a drawback in their relatively low ionic conductivity compared to other types of electrolytes. While conductivity can be improved

by heating ILs to 125°C, this method presents additional design challenges. El-Kady et al. (2012) demonstrated the superior performance of laser-scribed graphene (LSG) supercapacitors using IL electrolytes compared to aqueous and organic alternatives with higher energy density and power density. Despite their promising performance, the commercial viability of ILs for supercapacitor applications faces several challenges, including high costs, high viscosity, and inadequate ionic conductivity. Addressing these challenges is critical to realizing the full potential of IL-based supercapacitors in practical applications (Ortega et al. 2020).

1.2.5 Separator

In a supercapacitor cell, a separator plays a critical role by physically separating the two electrodes. The separator must resist chemical reactions with the electrodes, ensuring long-term performance. Additionally, it needs to maintain a thin profile to facilitate swift transfer of ionic charges, minimizing electrical resistance (Kim et al. 2015c). The separator is immersed in the electrolyte solution, acting as a barrier that prevents direct electrical contact between the electrodes. To achieve efficient operation, the separator material needs to allow the flow of ions, facilitating the movement of ionic charge, while also maintaining high electrical resistance, high ionic conductance, and low thickness (Dubal et al. 2017; Shown et al. 2015). The separator's critical attributes include its regulated porosity and robust mechanical and electrical characteristics, which ensure effective isolation of the electrodes while facilitating unimpeded electrolyte flow. By managing porosity, the separator can modulate ion flow, optimizing device performance. Furthermore, separators are engineered to prevent unwanted materials like gases, air, and humidity from infiltrating the internal environment of the supercapacitor, guaranteeing long-term stability and reliability (Liivand et al. 2015; SUN et al. 2014). Depending on the type of electrolyte used, different materials are employed for separators. For supercapacitors utilizing organic electrolytes, polymer or paper separators are commonly employed. Conversely, ceramic or glass fiber separators are preferred for supercapacitors operating with aqueous electrolytes (Sharma and Bhatti 2010). In summary, the separator in a supercapacitor is a critical component that ensures efficient charge transport while maintaining the integrity of the device. Its design and material properties directly impact the performance, stability, and longevity of the supercapacitor system.

1.2.6 Current collector

Current collectors serve a crucial function in supercapacitors by establishing the electrical connection between the active material and the current source. They facilitate the flow of electric current during charging and discharging processes, ensuring efficient energy transfer. Consequently, they must possess high electronic conductivity and withstand chemical reactions induced by electrolytes (Liu et al. 2019a). Materials commonly employed for current collectors include copper, aluminium, stainless steel, iron, and various alloys. Coating active materials directly onto current collectors promotes strong molecular contact, thereby reducing interfacial resistance between active layers and current collectors (Wu et al. 2009). This enhancement in performance is attributed to the improved electrical contact. However, over repeated cycles, the active material may degrade, leading to deterioration of both the electrode and current collector. This degradation results in increased resistance within the supercapacitor, ultimately reducing specific capacitance over its cycle life. To address this issue, polymeric binding materials such as nafion, polyvinylidene fluoride, and polytetrafluoroethylene are incorporated with active materials. These binding materials ensure prolonged attachment of the active material to the current collector, thereby enhancing the durability and longevity of the supercapacitor (Kumagai et al. 2015).

1.2.7 Experimental assessment techniques for supercapacitor electrodes

Supercapacitor devices undergo meticulous assessment, evaluating their efficacy through sophisticated programs reliant on the interplay of voltage, current, and time. Predominantly employed methodologies encompass Cyclic Voltammetry (CV), Galvanostatic Charge-Discharge (GCD), and Electrochemical Impedance Spectroscopy (EIS) (Conway and Conway 1999). In scrutinizing the attributes of electrode materials or devices, researchers commonly opt for either three-electrode or two-electrode configurations (Kim et al. 2015a). These configurations facilitate a comprehensive exploration of the electrochemical performance, offering insights into the intricate dynamics governing supercapacitor functionality.

In a three-electrode configuration, electrical current traverses both the counter and working electrodes. The process of voltage measurement or modulation is executed between the reference electrode and the working electrode. Selecting a reference electrode characterized by optimal non-polarizable properties is imperative for maintaining voltage stability across

a spectrum of current densities. This meticulous selection is pivotal in preserving the precision of electrochemical measurements. Such accuracy is indispensable for elucidating the intricate dynamics within supercapacitor systems (Kim et al. 2015a).

A two-electrode system involves the device voltage being represented by the measured voltage. In this arrangement, the reference electrode and counter electrode are linked together, acting as the positive and negative electrodes for the device (Kim et al. 2015a). This arrangement simplifies the assessment process, offering a direct glimpse into the operational characteristics of the supercapacitor system, while maintaining precision and reliability in voltage measurements.

1.2.7.1 Cyclic Voltammetry (CV)

Cyclic Voltammetry stands out as a preeminent electrochemical technique, widely revered for its versatility and depth of insight. Typically, CV offers a profound understanding of electrode reaction kinetics, unveiling intricate details regarding both heterogeneous and homogeneous electron-transfer phenomena, alongside coupled chemical reactions (Heinze 1984).

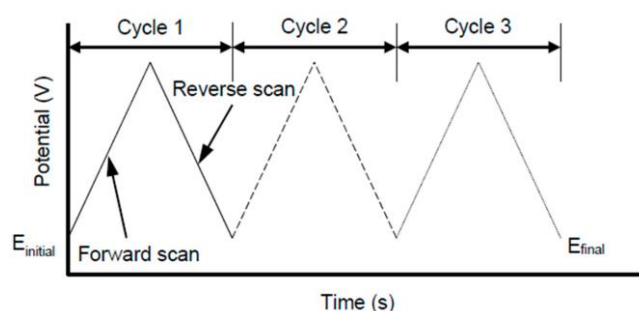


Figure 1.5. Cyclic voltammetry wave form (Hui et al. 2019).

Moreover, CV affords the scrutiny of reaction reversibility, intermediates, and phase adsorption, elevating it beyond mere data collection to a realm where mechanistic intricacies are meticulously probed. In CV measurements, a stationary working electrode is placed in an electrolyte solution, and a linear potential ramp is applied. The scan rate is a critical factor, ranging from several to hundreds of mV/s. The applied potential follows a triangular waveform over time. (Fig. 1.5). The current response is plotted against the applied potential, and this yields characteristic CV curves. The current response indicates the magnitude of charge transfer (Bard and Faulkner 2001). The current reaches a maximum value before gradually decreasing. This process is mirrored in the reverse

potential direction, reflecting the dynamic interplay between electrochemical processes and surface phenomena as shown in a typical cyclic voltammogram (Fig 1.6).

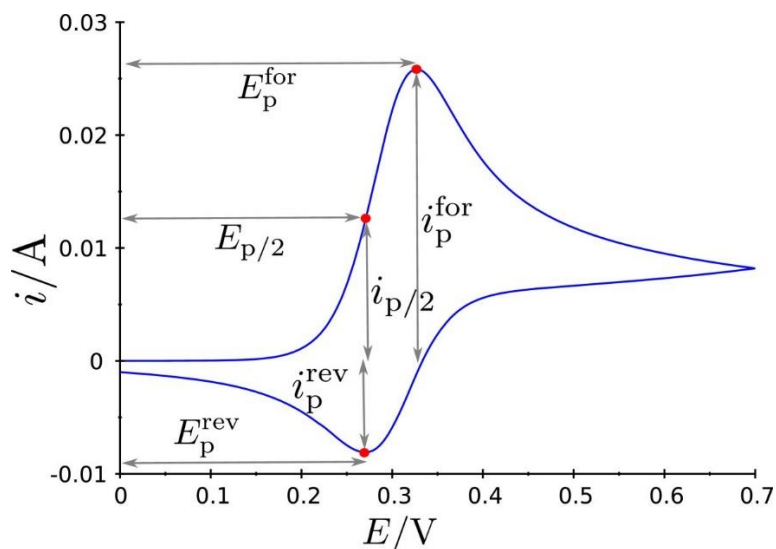


Figure 1.6. A typical cyclic voltammogram (Bogdan et al. 2014)

CV also is a fundamental electrochemical technique that plays a crucial role in characterizing the redox activity within an experimental potential window. Measuring the oxidation and reduction peaks of an analyte requires both anodic and cathodic scans. The potential window for CV measurements is determined by the mix of salt and solvent in the electrolyte, as well as the active material in the working electrode (Kim et al. 2015b). The amount of charge accumulated at the electrode surface is calculated by integrating the electric current over time. The specific capacitance of the three and two electrode configuration can be calculated from the CV studies using the following equations respectively (Joyline et al. 2024):

$$C_s = \frac{A}{m \times \Delta t \times v} \quad (1.4)$$

$$C_s = \frac{4 \times A}{m \times \Delta t \times v} \quad (1.5)$$

Where A is the area beneath the CV graph, m (g) is the mass of the material coated on the electrode, ΔV (V) is the potential window, and v (V/s) is the scan rate applied. Supercapacitors and batteries exhibit different charge storage mechanisms, as seen in their CV curves. The CV curve of a supercapacitor is rectangular, indicating its characteristic charge-discharge behaviour, while the CV curve of a battery displays cathodic and anodic peaks, suggesting redox reactions at specific potentials as shown in Fig 1.7 (a&b). Charge storage in a supercapacitor is largely independent of potential, unlike in a battery where

potential strongly influences peak behaviour. Therefore, selecting the potential range for studying device behaviour is critical when using cyclic voltammetry.

1.2.7.2 Galvanostatic charge discharge (GCD)

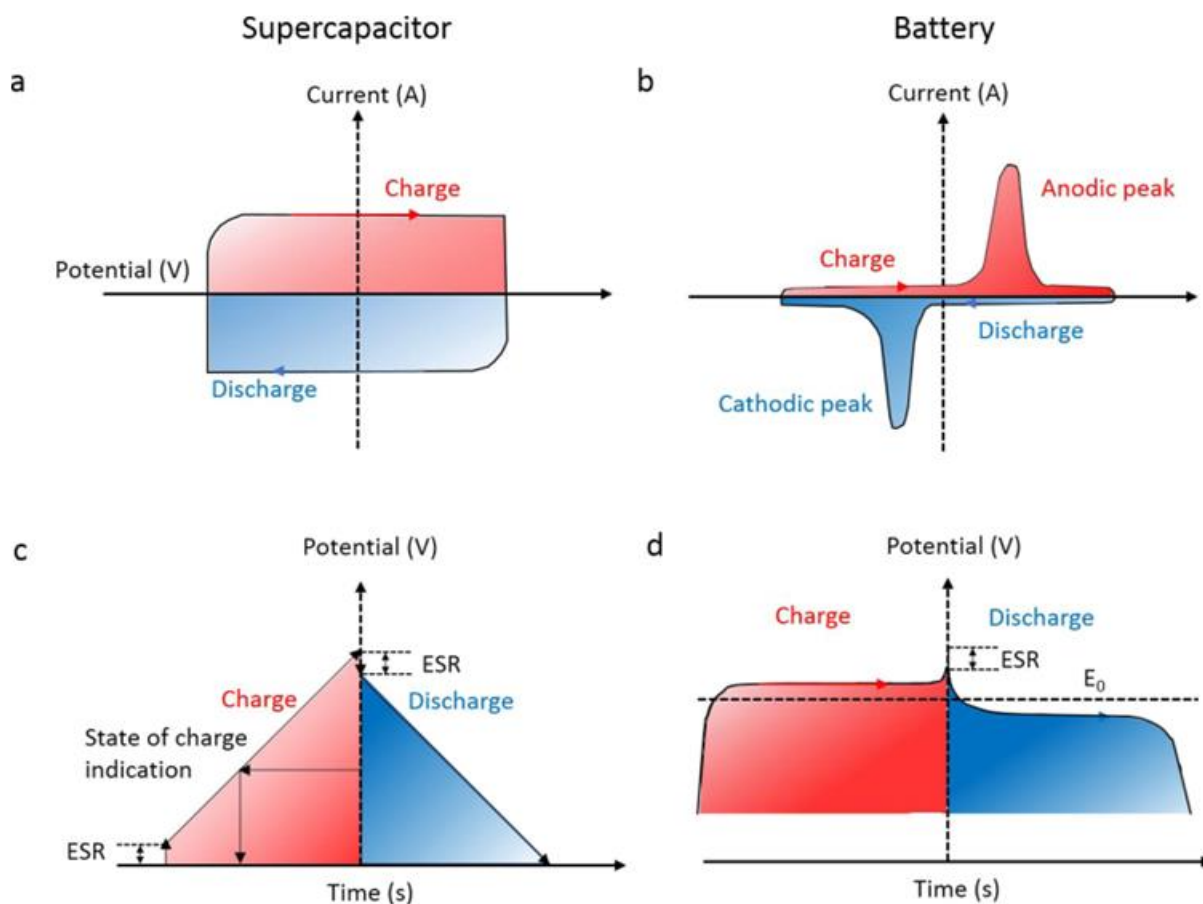


Figure 1.7. a and b cyclic voltammogram curves of a typical supercapacitor and a typical battery and c and d galvanostatic charge–discharge curves of a typical supercapacitor and a typical battery (Shao et al. 2018)

The Galvanostatic charge discharge (GCD) method stands out as a highly efficient technique for evaluating the performance of energy storage materials, particularly concerning their cycling stability and specific capacitance. This method contrasts with the CV approach; in GCD, voltage variations are monitored over time while maintaining a constant current. In the GCD process, a consistent current is applied to the working electrode, and the potential is monitored as time progresses. In a typical test scenario, the electrode undergoes an initial charging phase until the potential reaches a predetermined set point. Subsequently, the current is abruptly switched to the opposite direction, maintaining the same magnitude, initiating the discharge process. When a constant anodic or cathodic current is applied, the reactant undergoes oxidation or reduction at a consistent

rate, resulting in a gradual shift in potential over time due to changes in the reactant concentration at the electrode interface. As the concentration of the reactant at the electrode surface decreases to zero, the ability of the electrode surface to accept electrons provided by the constant current also decreases, leading to a sudden shift in potential towards a more anodic or cathodic direction. For supercapacitors that use EDLC principles, the potential window does not depend on charge storage. On the other hand, for pseudocapacitors that show redox activity or intercalation, the ability to retain charge depends on the specific material's predetermined potential range (Goodenough and Park 2013). Fig 1.7(c & d) show the GCD behaviour for EDL capacitor and batteries respectively. An EDL capacitor exhibits a linear charge-discharge curve, whereas a battery shows charge/discharge plateau at a constant voltage. The initial potential drop in both cases is due to the equivalent series resistance of the device. Moreover, the stability performance underwent analysis through numerous GCD cycles. The specific capacitance of the three and two electrode system can be determined from the discharge curves using the following equations (Joyline et al. 2024):

$$C_s = \frac{I \times \Delta t}{m \times \Delta V} \quad (1.6)$$

$$C_s = \frac{4 \times I \times \Delta t}{m \times \Delta V} \quad (1.7)$$

Where I/m (A/g) is the applied current density, Δt (s) is the total discharge time, and ΔV (V) is the potential window of the discharge curve.

The energy density (E (Wh/kg)) and power density (P (W/kg)) are calculated using the equations (1.8) and (1.9).

$$E = \frac{1}{2} \times C_s \times \Delta V^2 \times \frac{1000}{3600} \quad (1.8)$$

$$P = \frac{E}{t_d} \times 3600 \quad (1.9)$$

where, C_s (F/g) is the specific capacitance, ΔV (V) is the maximum potential window, and t_d (s) is the discharging time.

1.2.7.3 Electrochemical Impedance Spectroscopy (EIS)

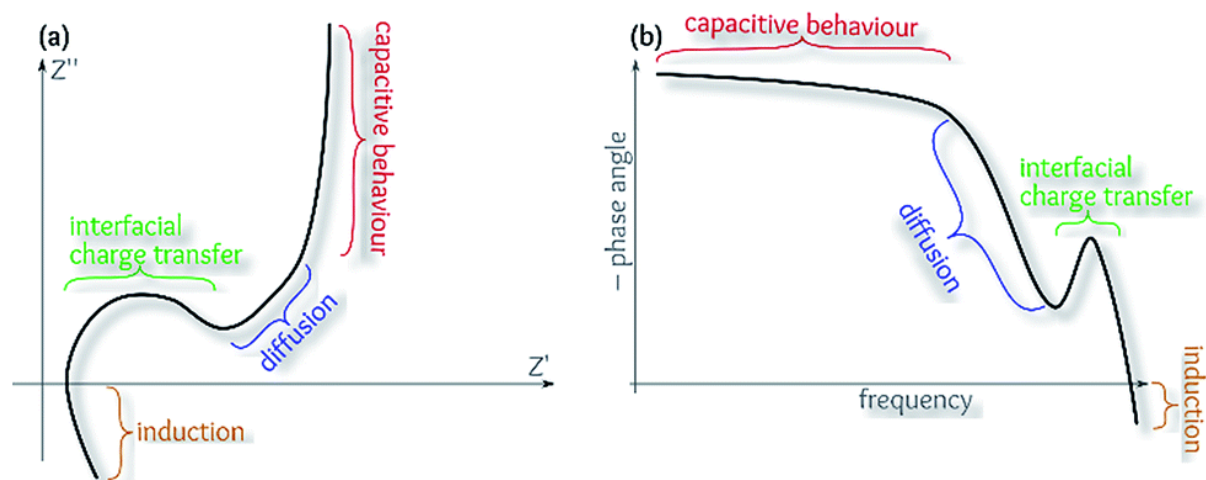


Figure 1.8. Schematic impedance model (a) Nyquist and (b) Bode plots (Eftekhari 2018b).

Electrochemical Impedance Spectroscopy (EIS) which stands for alternating current impedance spectroscopy, is a valuable tool that provides a connection between real-world systems and their theoretical equivalents through an idealized circuit. This circuit includes discrete electrical components such as resistance, impedance, and inductance, arranged in various sequential and concurrent configurations. It offers insights into the behaviour of electrochemical capacitors with polarizable electrodes or electroactive materials. By analyzing responses at different alternating current frequencies, we can determine the intrinsic properties of electrode materials, the pore size distributions in high surface area electrodes, and factors such as electrode material thickness and particle interactions (Conway and Conway 1999). Impedance spectra provide richer insights into capacitive behaviour compared to batteries, as the capacitance component is directly linked to $1/j\omega C$. Frequency response patterns vividly illustrate the role of porous electrodes, enabling us to determine pseudocapacitive behaviour based on real and imaginary impedance components (Conway and Conway 1999). The Nyquist plot, which depicts the response of a real capacitor, includes a semicircle representing the parallel combination of bulk resistance (related to ion migration) and geometric capacitance (related to dielectric polarization of the electrolyte at a given potential). Accurate assessment of the electrochemical profile yields specific capacitance, energy density, and power density, which are pivotal in gauging the electrochemical performance of electrode materials and assembled devices (Muzaffar et al. 2019). Therefore, in Fig 1.8 (a) a schematic depiction of the Nyquist plot is presented,

while Fig 1.8 (b) illustrates the corresponding Bode phase. Fig 1.8 encapsulates the general impedance behaviour, delineating three key regions: a high-frequency semicircle, mid-frequency Warburg impedance, and low-frequency capacitive behaviour (Eftekhari 2018b).

1.2.8 Summary

This chapter includes an introduction to the background of energy storage, emphasizing the importance of energy storage solutions and the unique advantages of supercapacitors among various energy storage devices. It reviews the mechanisms of energy storage, including EDLC and pseudocapacitance, and discusses the types of supercapacitors along with their key components: electrode materials, electrolytes, separators, and current collectors. The chapter thoroughly explores electrochemical techniques such as CV, GCD, and EIS used to assess supercapacitor performance. Significant emphasis on the basis of literature review is placed on transition metal chalcogenides (TMCs) like selenides, sulfides, and tellurides, highlighting their superior redox chemistry, electronic conductivity, and high specific capacitance. TMCs are noted for their cost-effectiveness and versatility, with applications spanning fuel cells, solar cells, sensors, lithium-ion batteries, and more. These materials provide numerous benefits, including improved life cycle, flexibility, enhanced conductivity, and efficient electron transport, positioning them as promising candidates for supercapacitor applications.

1.2.9 Research gap

Despite significant advancements in the development of transition metal chalcogenides (TMCs) for supercapacitor applications, several gaps remain in the existing literature. While TMCs have demonstrated promising electrochemical properties, there is still a need for further exploration and optimization in several key areas. Comprehensive studies on the synthesis methods, structural properties, and electrochemical behaviour of TMCs and their composites are limited. There is a need for a detailed investigation into how different synthesis techniques and composite ratios affect the overall performance of these materials in supercapacitors.

Doping metal chalcogenides with various transition metals has shown potential in improving their electrochemical properties. However, there remains a gap in understanding the optimal doping concentrations and the resulting impacts on supercapacitor performance. Additionally, the potential of doped metal chalcogenides in symmetric supercapacitor devices requires further exploration. A critical challenge that persists for

supercapacitors is their energy density, which remains lower compared to other energy storage devices like batteries. Although TMCs and their composites can enhance the capacitance and power density, achieving higher energy densities is crucial for their broader application. More research is needed to identify and develop materials and configurations that can significantly improve the energy density of supercapacitors. Trimetallic sulfides, which offer the potential for superior electrochemical performance due to their multi-element composition, are still underexplored. The reported studies on these materials are relatively few, and there is a lack of comprehensive research on their synthesis protocols, structural characterization, and electrochemical properties. Further investigation is necessary to establish effective synthesis routes and to thoroughly evaluate the performance of trimetallic sulfides in supercapacitor applications. Similarly, while the combination of different TMCs to form composites holds promise for enhancing electrochemical characteristics, systematic studies on the synthesis, structural properties, and supercapacitor performance of these composites are lacking. Moreover, their application in symmetric supercapacitor devices remains underexplored.

These research gaps highlight the need for a systematic investigation into the synthesis and characterization of various transition metal chalcogenides and their composites. Addressing these gaps will not only advance the understanding of TMC-based materials but also contribute to the development of high-performance supercapacitors. Therefore, this thesis aims to fill these gaps by synthesizing and studying various metal chalcogenides and their composites, focusing on their electrochemical properties and potential applications in supercapacitors and symmetric devices.

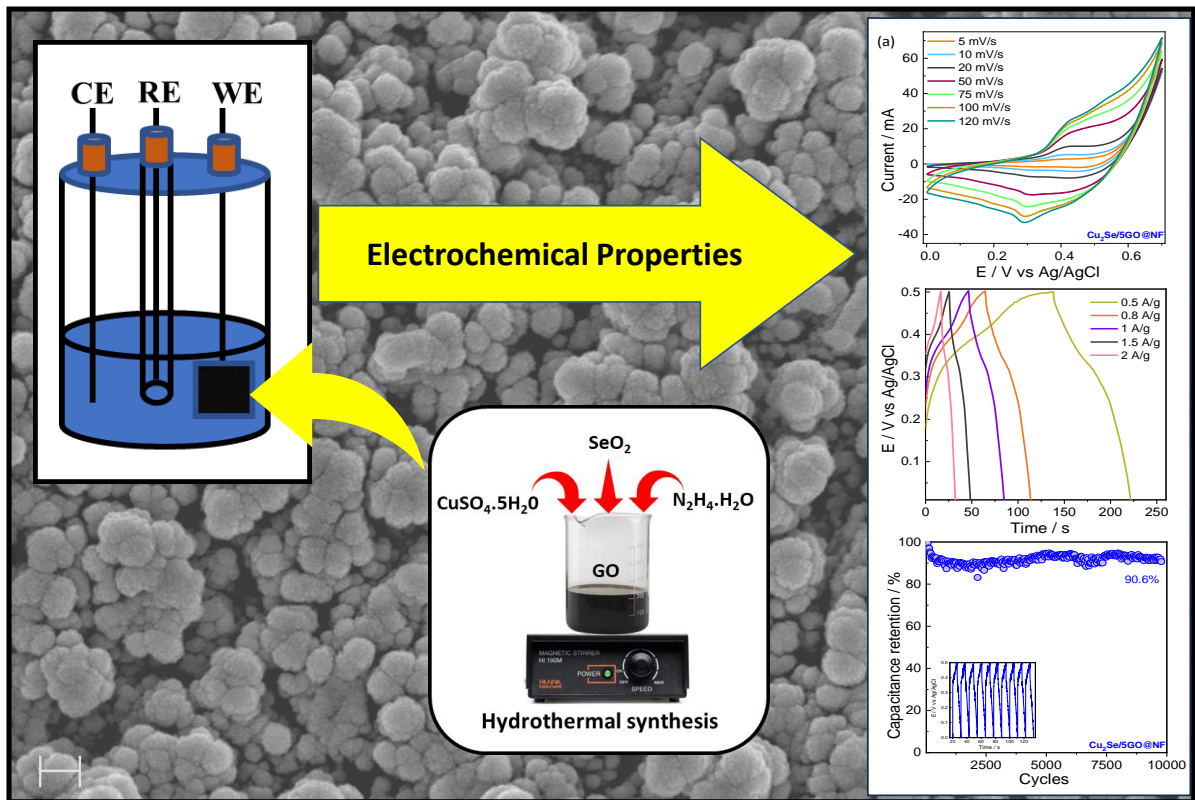
1.2.10 Objectives of the work

1. To synthesize various transition metal chalcogenides using hydrothermal and electrodeposition methods.
2. To characterize the synthesized materials by analyzing their morphology and elemental composition using techniques such as X-ray Diffraction (XRD), Raman Spectroscopy, Field Emission Scanning Electron Microscopy (FESEM), High Resolution Transmission Electron Microscopy (HRTEM), and X-ray Photoelectron Spectroscopy (XPS).
3. To fabricate supercapacitors employing the synthesized transition metal chalcogenide materials.

4. To investigate the electrochemical properties of the fabricated supercapacitors through Cyclic Voltammetry (CV), Galvanostatic Charge Discharge (GCD), and Electrochemical Impedance Spectroscopy (EIS).

CHAPTER 2

SYNTHESIS OF A NOVEL Cu_2Se -GO NANOCOMPOSITE FOR SUPERCAPACITORS



Abstract: This chapter involves the synthesis of Copper selenide-Graphene oxide (Cu₂Se-GO) nanocomposite and its application as a supercapacitor electrode.

2.1 INTRODUCTION

There has been a huge adoption of fossil fuel resources for the last decades since it meets all the energy demands (Armaroli and Balzani 2011). Although fossil fuels are advantageous, they are non-renewable and mitigating. Hence, efforts have been made to replace them with renewable energy sources (Shafiee and Topal 2009; Wang et al. 2022b). Renewable sources like solar, water, and wind are intermittent and encounter challenges in transitioning from fuels to sustainable sources. This issue can be solved by using energy storage devices, which helps in a smooth energy transition without wasting it. Also, it stores extra energy available and releases on demand (Hao et al. 2022; Kalair et al. 2021).

Among energy storage devices, batteries and supercapacitors are two major energy sources that have gained immense value. Especially supercapacitors have gained huge popularity because of their exceptional power density, long cycle life, and large charge storage ability than batteries (Raza et al. 2018b). Concurrently, they are environmentally safe and have a potent thermal operating range (Theerthagiri et al. 2018a; Vangari et al. 2013). Various electrode materials are available for supercapacitors based on their working mechanism, which includes carbon-based materials, metal oxides, metal chalcogenides, and conducting polymers. When compared with carbon-based materials, pseudocapacitive type materials such as metal oxides and metal chalcogenides contribute towards the betterment of supercapacitor activity through oxidation and reduction reactions (Malavekar et al. 2021). Additionally, the commercially available supercapacitors are formulated only from carbonaceous materials, which do not promise ample energy density and specific capacitance (Chen et al. 2010a). In this regard, considerable progress has been accomplished in the pseudocapacitive type of materials, out of which metal chalcogenides comprising selenides, sulfides, and tellurides have grabbed extensive attention and evolved into wonderful performers due to their better redox chemistry, cycle life electronic conductivity, denser active sites, providing higher specific capacitance than their oxide and nitride counterparts (Ahmadi et al. 2020). They are cost-effective and find numerous applications in the field of energy (Lu et al. 2017). Chou et al. (Chou and Lin 2013) synthesized Ni₃S₂ via potentiodynamic deposition method convinces to be the robust supercapacitor electrode material having 91 % capacitance retention. Peng et al. (Peng et

al. 2015) fabricated an asymmetric supercapacitor using $\text{Co}_{0.85}\text{Se}$ as the positive electrode, and nitrogen-doped porous carbon as the negative electrode yielding 93.8 % of capacitance retention with an energy density of 21.1 Wh/kg at a power density of 400 W/kg. Nickel cobalt telluride nanosheets were synthesized on carbon fibers by Shi et al. (Shi et al. 2022b) exhibits capacitance of 261.4 mAh/g at 1A/g and retains 70 % capacitance at 20 A/g.

Transition metal selenides have better electrical conductivity, theoretical capacity, cyclic stability, improved redox chemistry, high specific power than transition metal sulfides. Owing to this nature, though transition metal sulfides are largely studied in energy storage systems transition metal selenides have accomplished the interest of the scientific community and emerged to be an electrode material with high calibre for supercapacitors (Ahmadi et al. 2020; Lu et al. 2017; Theerthagiri et al. 2018a; Wang et al. 2022a; Zou and Zhang 2015).

Recently, many reports can be found on selenides like $\text{Ni}_{10.85}\text{Se}$ (Younas et al. 2022), CuSe (Sajjad et al. 2022), MnCoSe (Miao et al. 2019), NiSe_2 (Wang et al. 2017b), $\text{NiSe}@MoSe_2$ (Peng et al. 2017) etc., which have performed extremely well. However, surplus research on supercapacitors can gravitate towards Cu_2Se since it can be produced in various stoichiometric arrangements such as CuSe , Cu_2Se , CuSe_2 , and Cu_3Se_2 (Raju et al. 2020; Shinde et al. 2017). Also, Cu_2Se is a semiconductor with unique morphology and shows merits in thermoelectrics (Wang et al. 2019a), biomedicine (Ai et al. 2021) and gas sensors (Xu et al. 2009). Despite, the electronic conductivity and mechanical stability of metal selenides can be increased by combining them with carbon-based materials such as graphene oxide, activated carbon, carbon nanotubes, reduced graphene oxide, and other related materials (Vinoth et al. 2021). GO has emerged as an unparalleled material because of its enormous surface area, thermal and electrical conductivity, and mechanical and thermal stability. Moreover, it possesses a layered structure bearing various oxygen functionalities acting as a supportive framework for any material. At the same time, it lowers the agglomeration of particles and controls the volume change during electrochemical studies (Dreyer et al. 2010; Karuppasamy et al. 2022a; Stankovich et al. 2006; Wang et al. 2011b). Considering these advantages, some researchers have combined GO with a few transition metal selenides $\text{CuSe}/\text{CoSe}_2@\text{GO}$ (Karuppasamy et al. 2022a), and FeSe_2/GO (Theerthagiri et al. 2017), and there have been no reports on Cu_2Se -GO composite synthesis through the hydrothermal method.

In this chapter, we report the synthesis of Cu₂Se and GO through one-step hydrothermal and Improved Hummers methods, respectively. Hydrothermal method is advantageous over other synthesis methods as it is simple to perform, saves energy, operates at mild temperatures and environmentally friendly. Besides, this is a one-step synthesis method and has better control over its size and shape of the particles (Yoshimura and Byrappa 2008). Also, we have narrated for the first time the strategy for synthesizing Cu₂Se-GO composite with different weight percentages (wt.%) of GO via a one-step hydrothermal method. Cu₂Se and GO are potential materials; incorporating GO into Cu₂Se will yield a synergistic effect. The electrochemical studies reveal the outstanding performance of the Cu₂Se-GO electrode with high cyclic stability and hence becomes possibly the imminent material for applications in supercapacitors.

2.2 EXPERIMENTAL

2.2.1 Materials

Copper sulphate pentahydrate (CuSO₄.5H₂O), selenium dioxide (SeO₂), hydrazine hydrate (N₂H₄.H₂O), potassium hydroxide (KOH) and carbon black were purchased from Loba. Nickel Foam (NF) was purchased from Global Nanotech, Mumbai, with a thickness of 0.5 mm. Nafion was procured from Sigma. All the solutions were prepared using Ultrapure Milli-Q water (18.2 MΩ). The purchased materials were used with high purity and no further purification is required.

2.2.2 Synthesis of GO

The GO was synthesized using the Improved Hummers method (Marcano et al. 2010). 1.5 g of natural graphite flakes were added to the round bottom flask containing 180 mL of concentrated H₂SO₄ and 20 mL of concentrated H₃PO₄ in an ice bath and stirred for 30 min. Later, 9 g of KMnO₄ is added to the reaction mixture gently and stirred for two hours which was later kept in an oil bath at 50°C for 12 h under stirring. The reaction mixture was poured over 200 mL of ice-cold water, and 1.5 mL of H₂O₂ was slowly added under stirring until the brilliant yellow color was obtained. The obtained residue was washed several times with Milli Q water until neutral pH is obtained, followed by 30 % HCl and ethanol. The residue was dried at 45°C and collected.

2.2.3 Synthesis of Cu₂Se and Cu₂Se-GO composites

In the beginning, a required amount of CuSO₄ · 5H₂O and SeO₂ are weighed and are dissolved in 50 mL Milli Q water under stirring condition. To this 8 mL of hydrazine hydrate has been added and stirred for 30 min. The reaction mixture was then filled in the stainless-steel autoclave heated for 24 h at a temperature of 180°C. The product obtained was cooled and washed with Milli Q water, ethanol, and acetone. Afterward, it was dried at 60°C in the hot air oven, and Cu₂Se was collected (Liu et al. 2009a). To synthesize Cu₂Se-GO composites with 5, 10, and 20 wt % of GO, a calculated amount of GO was dispersed in 50 mL of water and ultrasonicated for 30 min. To this, a required amount of CuSO₄ · 5H₂O and SeO₂ was added under stirring condition. The mixture was further stirred for 30 min. Then, 8 mL of hydrazine hydrate was added to the reaction mixture and stirred for 30 min. The stainless-steel autoclave was then filled with the reaction mixture and heated for 24 h at a temperature of 180°C. The product obtained was cooled and washed with Milli Q water, ethanol, and acetone. Afterward, it was dried at 60°C in the hot air oven, and Cu₂Se-GO was collected. The synthesized composites of 5, 10, and 20 wt % of GO are named Cu₂Se-5GO, Cu₂Se-10GO, and Cu₂Se-20GO respectively.

2.2.4 Fabrication of electrode material

For the preparation of electrochemical supercapacitor electrode, the composite, carbon black, and Nafion binder were mixed in a ratio of 7:2:1 and ground into a slurry using mortar and pestle. The obtained slurry has been drop casted on a previously weighed clean NF with coating area 1×1 area and dried in the hot air oven at 60°C for 15 h. The amount of material being coated is found to be in between 1.89-2.03 mg. The three-electrode setup consisting of a nickel foam coated with the material acts as a working electrode, platinum electrode as a counter electrode, and Ag/AgCl as a reference electrode is employed to carry out electrochemical studies.

2.2.5 Materials Characterization Techniques

The surface morphology and elemental details were tested using Carl Zeiss Model Supra 55 Germany field-emission scanning electron microscope implemented with energy dispersive X-ray spectroscopy (EDAX). Then employed Jeol Model JM 2100 instrument for high-resolution transmission electron microscope (HRTEM). Using Rigaku miniflex 600 powder XRD instrument, various phases and crystalline compositions were obtained

in the range 5° - 90° at a scan rate of 3° per minute using monochromatic Cu- K_{α} radiation of wavelength 0.154 nm. The Raman analysis is examined by using Horiba Japan Xplora Plus. The BET surface area has been found with the help of the instrument Quantachrome Novae 2200. The samples were degassed at 200°C for two hours before analysis. The X-ray photoelectron spectroscopy (XPS) data were obtained using a Thermo Fischer Scientific ESCALAB Xi+ with an Al K-alpha X-ray source (1486.7 eV).

2.2.6 Electrochemical characterisation

Autolab PGSTAT204 electrochemical workstation is used to study the electrochemical properties of the prepared electrodes. For the selection of electrolyte, the CV was performed for copper selenide in 1M NaOH and KOH where the latter clearly showed better activity (Fig. 2.1 (a)). Later CV was run for copper selenide with various concentrations of KOH where it was found that 2M KOH gives good results as shown in Fig 2.1 (b). The CV studies were carried out with a potential range of 0-0.7 V vs Ag/AgCl for all the modified electrodes with different scan rates from 5-120 mV/s. The GCD studies were performed at different current densities from 0.5-2 A/g between the potential window 0-0.45 V. The EIS was carried out with the frequency range of 1-10 kHz at zero-bias voltage. The experiment was carried out without stirring and purging any inert gases. Also, the data obtained here are not iR corrected.

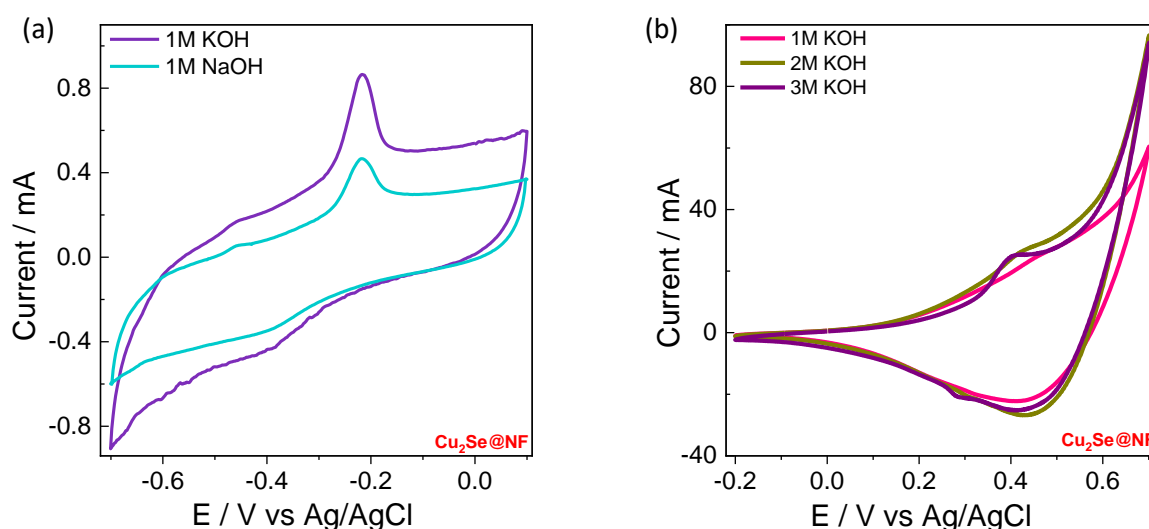


Figure 2.1. a) CV of 1M KOH and 1M NaOH and (b) CV of Cu₂Se in 1M, 2M, and 3M KOH, respectively.

The specific capacitance (C_s) of the electrodes from the CV and GCD curves in a three-electrode system was calculated using equations (1.4) and (1.6) respectively.

2.3 RESULTS AND DISCUSSIONS

2.3.1 XRD and Raman analysis

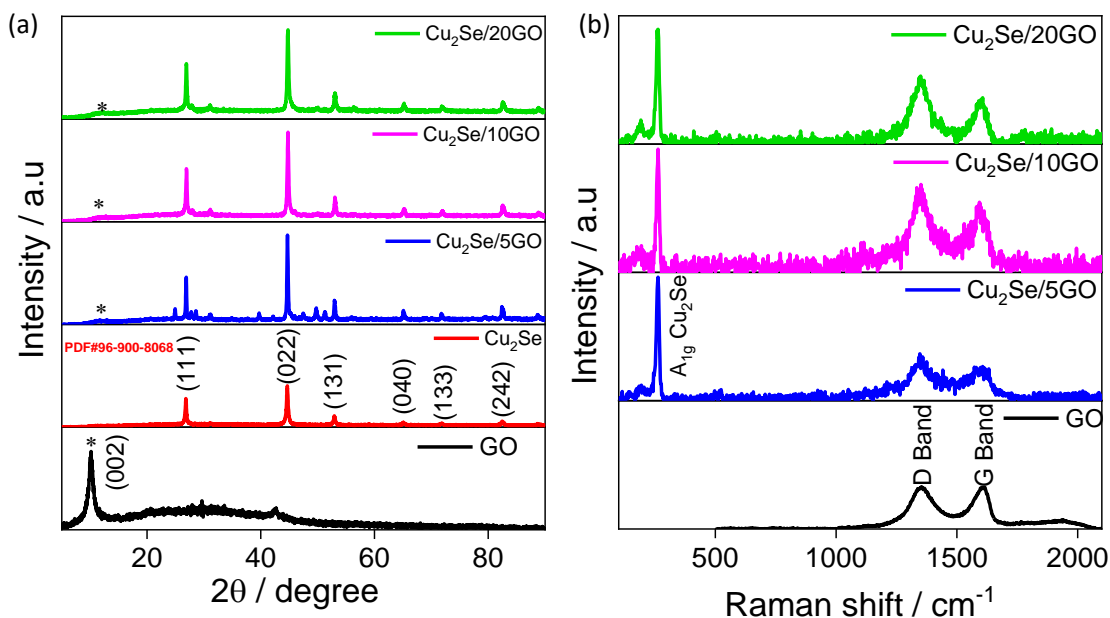


Figure 2.2. *a) Powder XRD diffraction pattern of synthesized samples and (b) Raman spectrum of GO, Cu₂Se-5GO, Cu₂Se-10GO and Cu₂Se-20GO.*

The XRD pattern of GO, Cu₂Se, and Cu₂Se-GO composites is shown in Fig 2.2 (a). In the XRD of GO, a peak at 10.2° analogous to the (002) plane of GO indicates the formation of GO (Khandelwal and Kumar 2015). The XRD pattern of Cu₂Se reveals peaks at 26.83°, 44.65°, 52.9°, 65.02°, 71.86° and 82.46° exactly matching with JCPDS Card. No. 96-900-8068 confirming that it is a cubic system. In the XRD of Cu₂Se-GO composites the GO peak is observed at 11° confirming the formation of Cu₂Se-GO composites. It was found from the spectra that the composites are formed without any impurity peaks.

Table 2.1. *Crystalline size (D) and lattice parameters of Cu₂Se, Cu₂Se-5GO, Cu₂Se-10GO, Cu₂Se-20GO.*

Sample	a=b=c (Å)	D (nm)
Cu ₂ Se	5.726	17.51
Cu ₂ Se-5GO	5.732	29.16
Cu ₂ Se-10GO	5.721	22.03
Cu ₂ Se-20GO	5.725	20.05

The average crystallite size of Cu_2Se , $\text{Cu}_2\text{Se-5GO}$, $\text{Cu}_2\text{Se-10GO}$ and $\text{Cu}_2\text{Se-20GO}$ calculated using Scherrer equation were found to be 17.5, 29.5, 22.03, and 20.05 nm respectively. The calculated lattice parameters for the composites are given in the Table 2.1. The Raman spectra of GO and $\text{Cu}_2\text{Se-GO}$ composites are shown in Fig 2.2 (b). The peak at 1350 cm^{-1} and 1604 cm^{-1} corresponds to the D and G bands in the GO. The in-plane stretching between sp^2 carbon atoms gives rise to the G band, and the D band arises due to the disorderliness of the dangling sp^2 carbon bonds. The characteristic peak of Cu_2Se is observed at 262 cm^{-1} corresponding to A_{1g} mode which arises because of the Cu-Se vibration (Tran et al. 2017). Also, the composites show peaks at 1300 cm^{-1} and 1600 cm^{-1} for the D and G bands of GO confirming the formation of the $\text{Cu}_2\text{Se-GO}$ composites.

2.3.2 FESEM and EDAX analysis

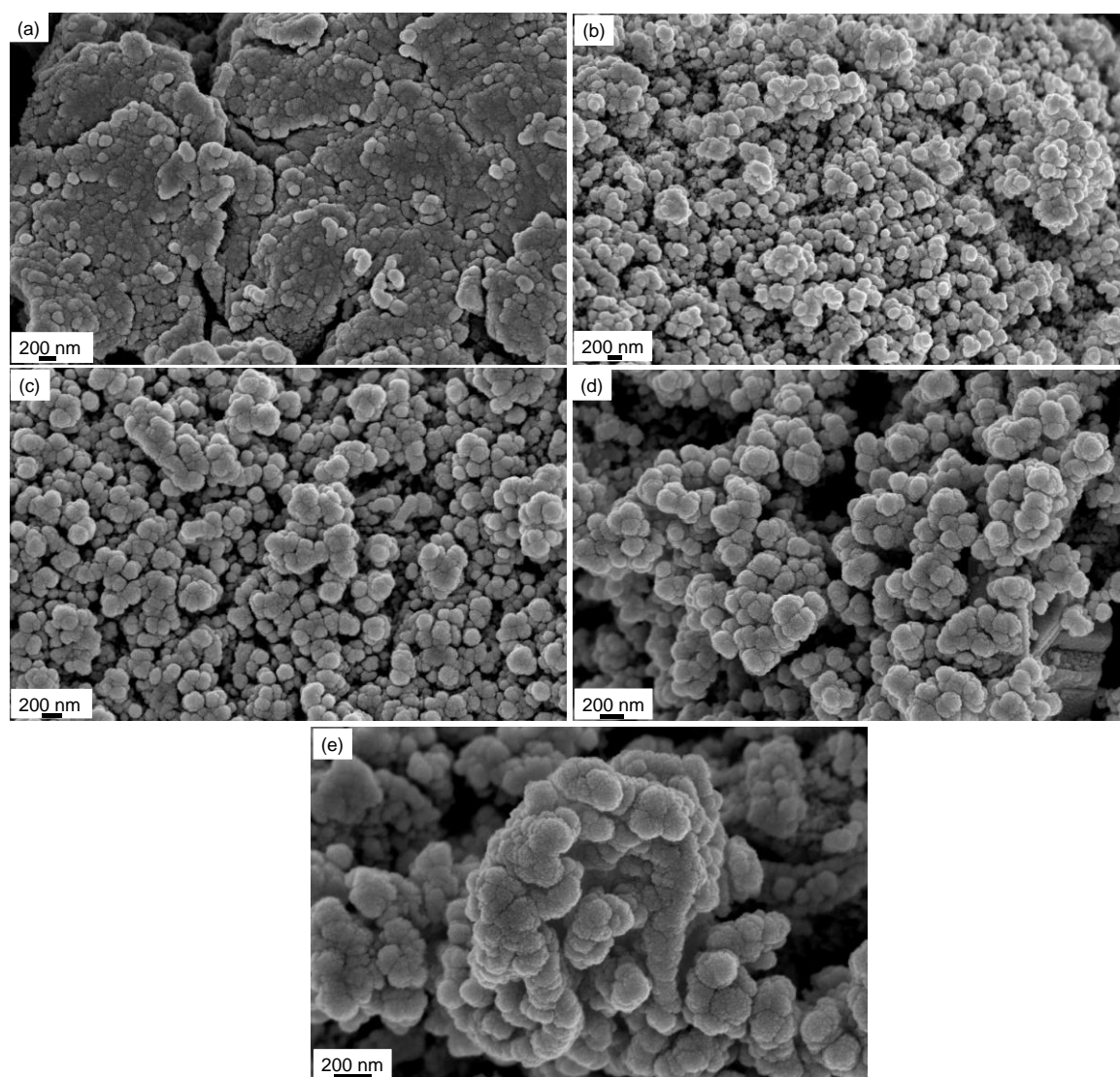


Figure 2.3. FESEM images of (a) GO, (b) Cu_2Se , (c) $\text{Cu}_2\text{Se-5GO}$, (d) $\text{Cu}_2\text{Se-10GO}$, and (e) $\text{Cu}_2\text{Se-20GO}$

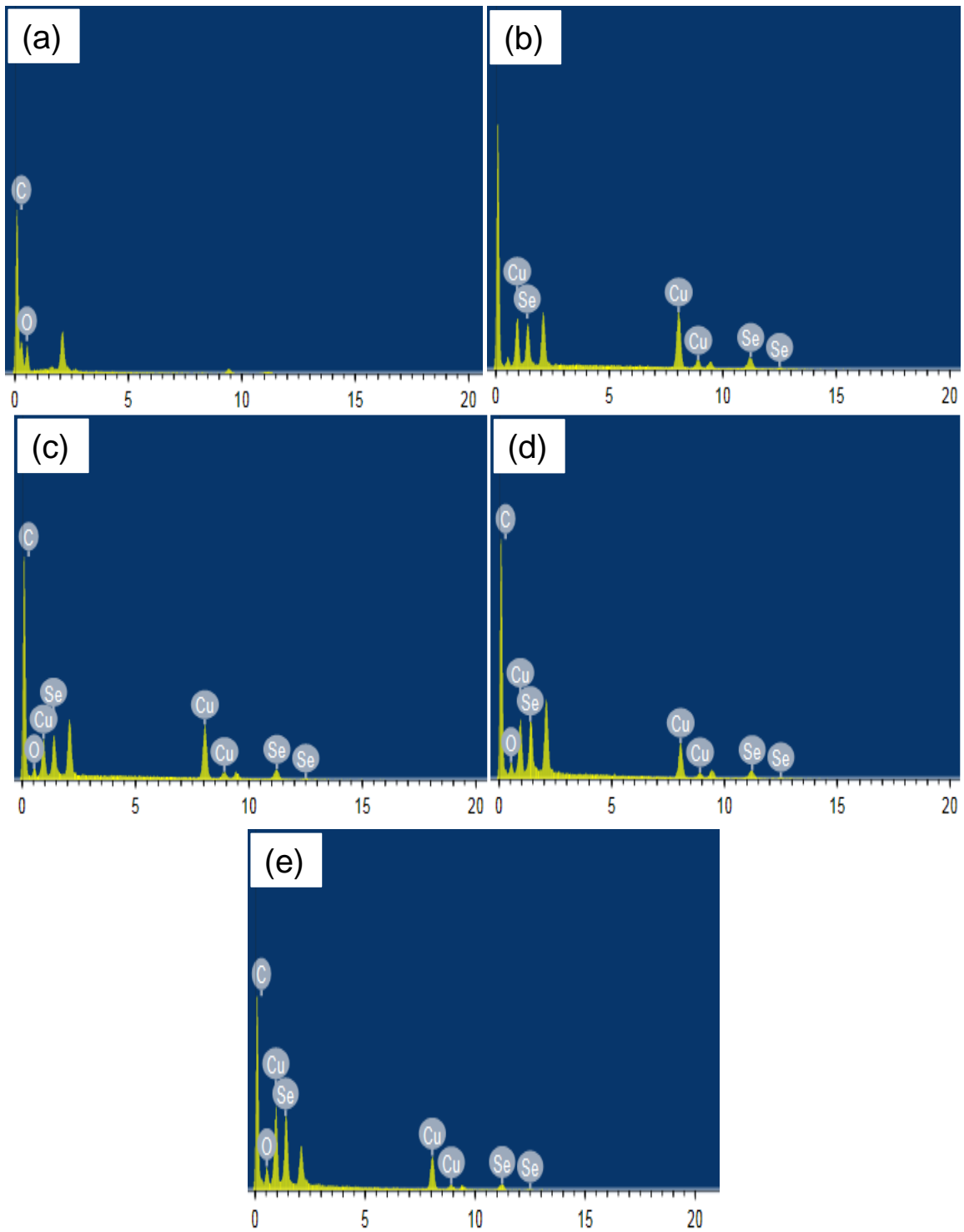


Figure 2.4. EDAX images of (a) GO, (b) Cu_2Se , (c) Cu_2Se -5GO, (d) Cu_2Se -10GO, and (e) Cu_2Se -20GO.

The GO is aggregated and are stacked on one another because of Van der Waals interaction in the reaction system as shown in FESEM image (Fig 2.3 (a)). A cluster of spheres can be seen in the FESEM image of copper selenide (Fig 2.3 (b)). In the FESEM images of composites, we can observe that the copper selenide clusters are spread over GO in a non

uniform way and the size of the clusters gets bulkier and takes the shape of cauliflower florets as the GO composition increases as result of agglomeration of GO due to van der Waals interaction (Yang et al. 2012) (Fig 2.3 (c-e)). Energy Dispersive x-ray Spectroscopy Analysis (EDAX) of GO, Cu₂Se and Cu₂Se GO composites (Fig 2.4 (a-e)) shows the predicted elements, such as Copper, Selenium, Carbon, and Oxygen. No other elements were found, hence confirming the formation of a composite.

2.3.3 BET analysis

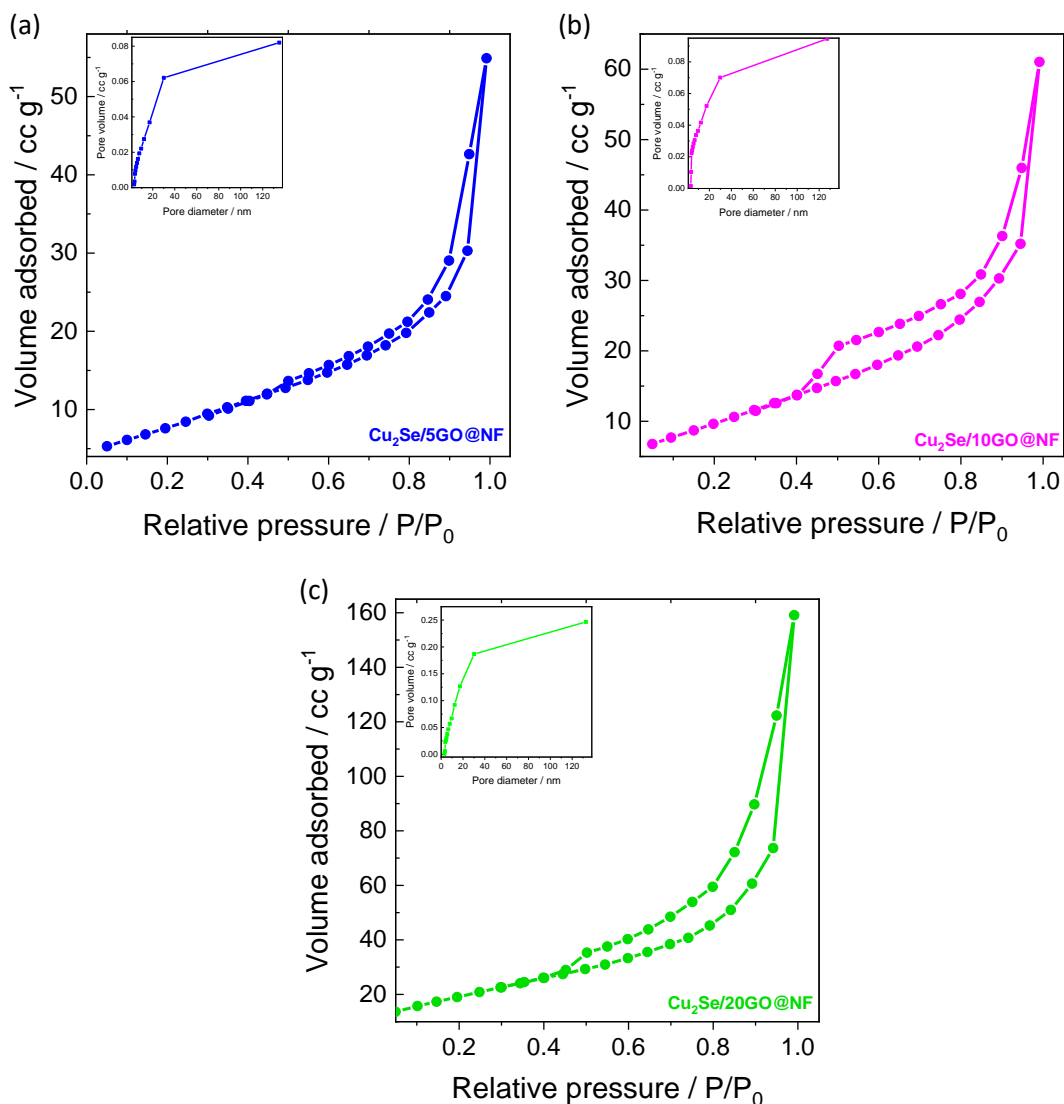


Figure 2.5. (a), (b), and (c) Nitrogen adsorption-desorption isotherm of Cu₂Se-5GO, Cu₂Se-10GO, and Cu₂Se-20GO with inset showing corresponding pore size distribution.

The nitrogen adsorption-desorption isotherms and the corresponding BJH pore size distribution curves of Cu₂Se-5GO, Cu₂Se-10GO, Cu₂Se-20GO is shown in Fig 2.5 (a-c). The nitrogen adsorption-desorption isotherms are of type IV with the hysteresis loops of

type H3. Moreover, the isotherm has a high absorption at relative pressure (P/P_0) range between 0.5-1.0, showing the formation of mesopores. The pore-size distributions (Inset of Fig 2.5) have a pore-size distribution majorly from 3 to 30 nm, which also supports the formation of mesopores (Malavekar et al. 2021).

Tale 2.2. Shows the surface area, pore volume, and pore diameter of Cu_2Se -5GO, Cu_2Se -10GO, and Cu_2Se -20GO.

Material	Surface area / m^2/g	Pore diameter/nm	Pore volume/ $cc\ g^{-1}$
Cu_2Se -5GO	31.739	10.72	0.085
Cu_2Se -10GO	38.257	9.89	0.009
Cu_2Se -20GO	72.613	13.5	0.246

The specific surface area of Cu_2Se -5GO, Cu_2Se -10GO, Cu_2Se -20GO are 31.739, 38.257, and 72.613 m^2/g and their respective pore diameters and pore volume are shown in Table 2.2. As the amount of GO increases the surface area increases from Cu_2Se -5GO to Cu_2Se -20GO and the latter has highest surface area; The BET surface is not exclusive parameter in the capacitance, however the increase in the capacitance may be related to the higher surface area (He et al. 2010). Moreover, Cu_2Se -5GO has the lowest pore volume. Therefore, the highest surface area, lowest pore volume and mesoporous nature of Cu_2Se -5GO altogether may contribute for the higher specific capacitance than other composites.

2.3.4 EIS analysis

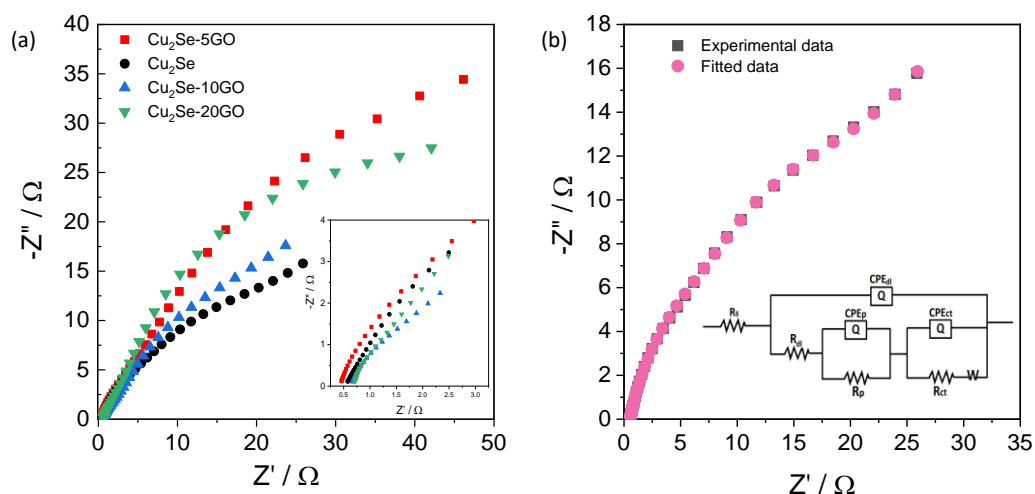


Figure 2.6. Nyquist plot of Cu_2Se , $Cu_2Se/5GO$, $Cu_2Se/10GO$ and $Cu_2Se/20GO$ (b) Fitted Nyquist plot of Cu_2Se (inset shows the fitted equivalent circuit)

The Nyquist plot of Cu₂Se, Cu₂Se-5GO, Cu₂Se-10GO and Cu₂Se-20GO (Fig 2.6 (a)) exhibits a negligibly small semicircle in the high-frequency and a straight line inclined almost at 45° in the lower frequency region. The Nyquist plot has been fitted to the equivalent circuit as shown in Fig 2.6 (b). It consists of solution resistance (R_s) with the double layer resistance (R_{dl}), polarisation resistance (R_p) and charge transfer resistance (R_{ct}), its equivalent constant phase element for double layer capacitance (Q_{dl}) with equivalent capacitance for polarisation (Q_p) and charge transfer (Q_{ct}) respectively as shown in the inset of Fig 2.6 (a). The smaller semicircle and the straight line following in the high-frequency region indicate the good capacitive nature of the material.

Table 2.3. EIS parameters for the fitted circuit

Samples	R_s (Ω)	CPE_{dl} (μF)	R_{dl} (Ω)	CPE_p (μF)	R_p (Ω)	CPE_{ct} (μF)	R_{ct} (Ω)
Cu₂Se	0.54	0.00018	2.04	0.0026	53.67	0.0030	33.81
Cu₂Se-5GO	0.02	0.02×10 ⁻⁷	0.65	0.0024	11.16	0.0004	1.01
Cu₂Se-10GO	0.78	0.0003	1.53	0.0041	64.58	1.02×10 ²²	2.15
Cu₂Se-20GO	0.03	9.5×10 ⁻⁷	0.47	0.0005	3.40	0.0012	407.6

The electrochemically fitted parameters are tabulated in Table 2.3, where we can see that the value of R_s is 0.02 Ω and R_{ct} is 1.01 Ω for Cu₂Se-5GO which is lowest comparing to other synthesized materials and hence it confirms the synergistic effect between Cu₂Se and GO. Therefore, Cu₂Se-5GO has better electron transfer and reduces the internal resistance of the material making it the best active material among the composites (Yang et al. 2020a).

2.3.5 CV and GCD analysis

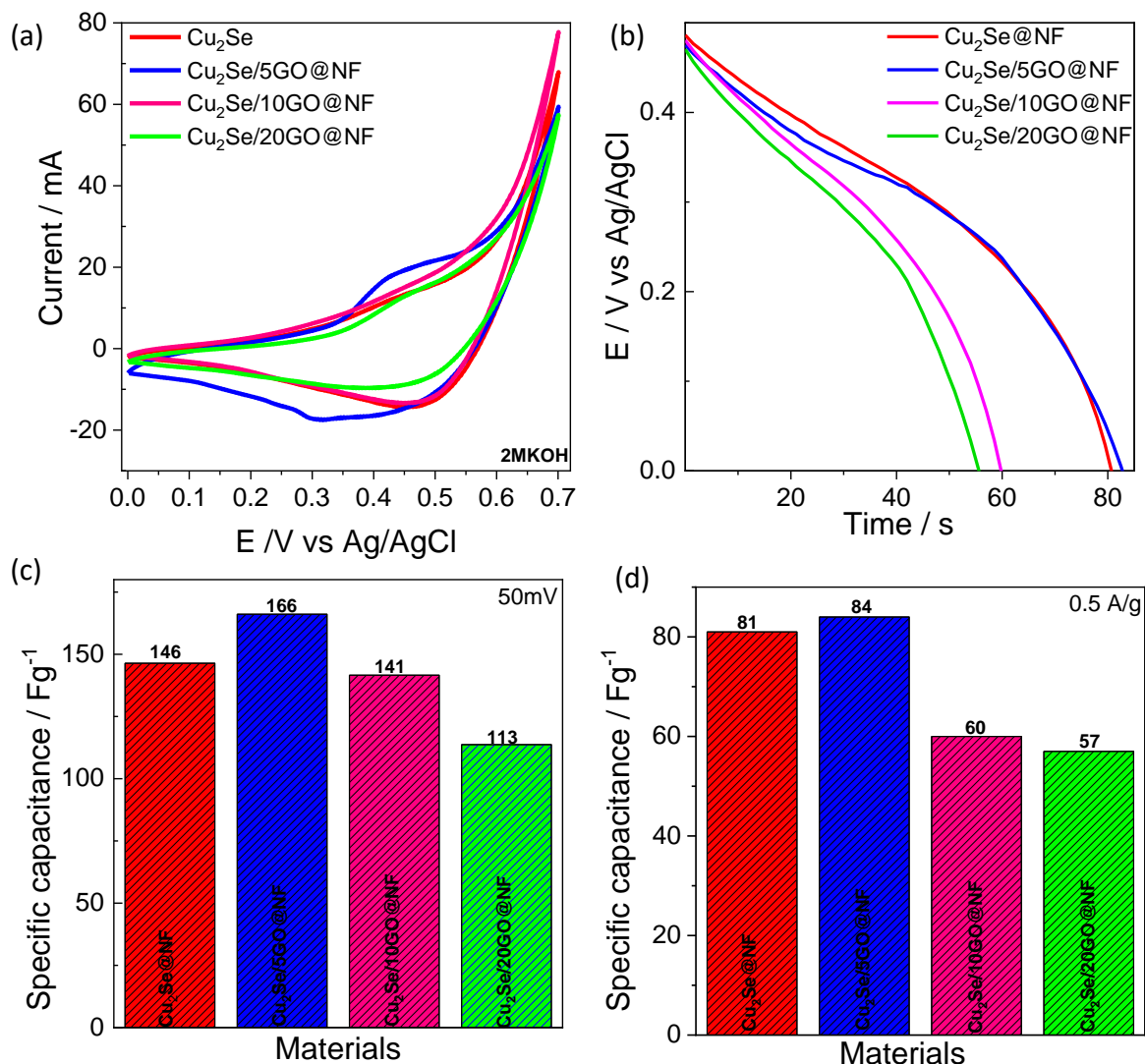


Figure 2.7. (a) CV of Cu₂Se, Cu₂Se-5GO, Cu₂Se-10GO, and Cu₂Se-20GO at 50mV/s; (b) GCD of Cu₂Se, Cu₂Se-5GO, Cu₂Se-10GO, and Cu₂Se-20GO at 0.5 A/g; (c) Specific capacitance values of composites measured using (a) cyclic voltammetry at 50mV/s; (d) Galvanostatic charge discharge analysis at 0.5A/g.

Further, CV and GCD was performed for the synthesized materials such as Cu₂Se, Cu₂Se-5GO, Cu₂Se-10GO, Cu₂Se-20GO as shown in Fig 2.7 (a&b) respectively. The CV study clearly shows that the activity of Cu₂Se-5GO is better compared to Cu₂Se, Cu₂Se-10GO, Cu₂Se-20GO, as the anodic peak and cathodic peak of Cu₂Se-5GO is much higher compared to other materials and in terms of GCD the highest discharge time was obtained for Cu₂Se-5GO when compared to other synthesized materials. The specific capacitance

calculated for Cu₂Se, Cu₂Se-5GO, Cu₂Se-10GO, Cu₂Se-20GO through CV and GCD are 146, 166, 141, 113 F/g and 81, 84, 60, 57 F/g respectively as shown in Fig 2.7 (c&d). Hence, Cu₂Se-5GO shows maximum specific capacitance of 166 F/g at 50 mV/s and 84 F/g at 0.5 A/g in CV and GCD studies respectively. The enhanced specific capacitance of Cu₂Se-5GO can be attributed to the synergistic effect between Cu₂Se and GO. Firstly, GO provides electrochemically active surface area for the adsorption of Cu²⁺ on its surface so that the pseudocapacitance nature of Cu₂Se and double layer capacitance of GO can be fully employed. Further, the symbiotic relation between Cu₂Se and Graphene oxide paves the way for increased electronic conductivity by helping in efficient electron flow. However, as the GO composition increases from Cu₂Se-5GO to Cu₂Se-20GO, results in the agglomeration of GO as shown in Fig 2.3 (c-e). Therefore, the specific capacitance decreases in the same manner and it is shown in Fig 2.7 (c&d) (Yang et al. 2012).

2.3.6 XPS analysis

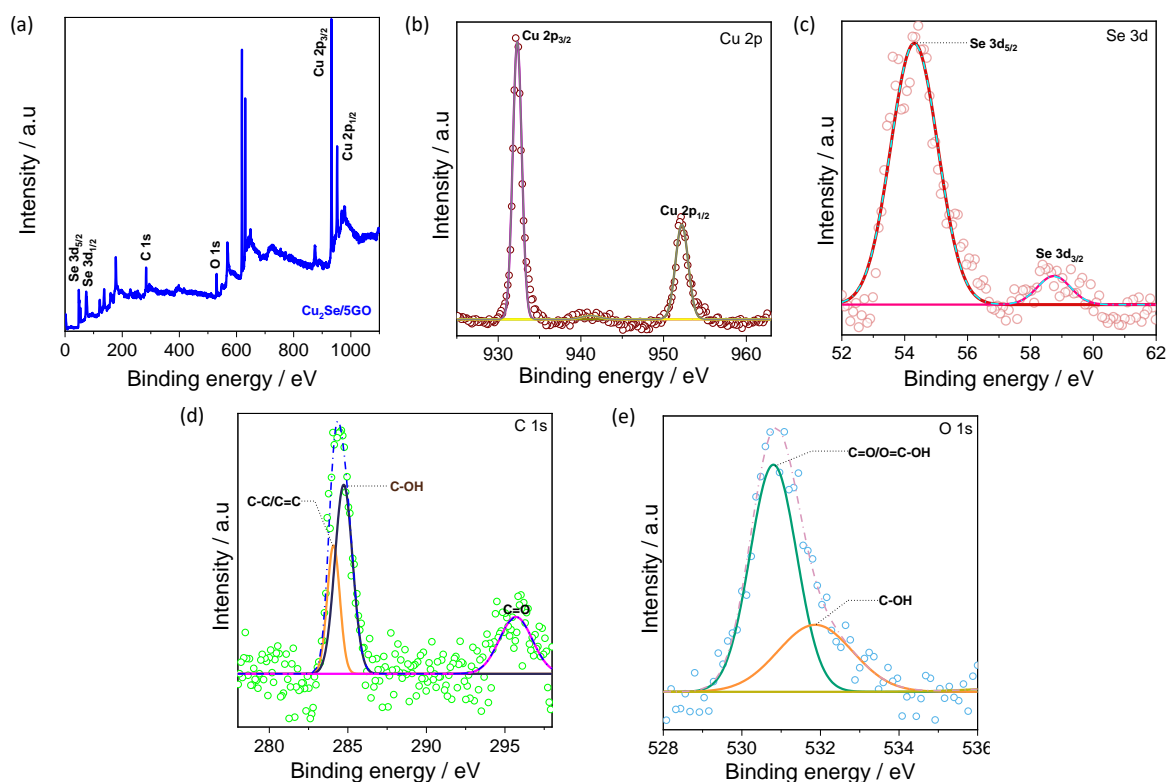


Figure 2.8. (a) XPS spectrum of Cu₂Se-5GO; (b), (c), (d), and (e) are high-resolution XPS spectrum of Cu 2p, Se 3d, C 1s, O 1s, respectively.

Elemental composition and the chemical and electronic state of the atoms within a material can be obtained from XPS, shown in Fig 2.8 (a-e). The survey spectrum of XPS of Cu₂Se-

5GO composite is presented in Fig 2.8 (a), shows the presence of Cu, Se, C, and O. Fig 2.8 (b) displays the XPS spectrum of Cu 2p where the two prominent peaks at 932.25 and 952.17 eV harmonize to Cu 2p_{3/2} and Cu 2p_{1/2}, correspondingly. Also, a small peak at 942.72 eV indicates the paramagnetic chemical state of Cu²⁺ (Zhang et al. 2011). Fig 2.8 (c) is the XPS spectra for Se 3d, confirms the divalent state of Se in the material as the peaks at 54.28 and 58.7 eV correspond to 3d_{5/2} and 3d_{3/2} spin-orbit couple (Balasingam et al. 2016). The spectra for C 1s are shown in Fig 2.8 (d), where the peaks 284, 284.7, and 295.69 represents C-C/C=C, C-OH, and C=O, respectively (Patil et al. 2016). Fig 2.8(e) displays the spectra for O 1s, where 530.8, 531.8 eV indicate the presence of C=O/O=C-OH and C-OH respectively (Torrissi et al. 2020).

2.3.7 TEM analysis

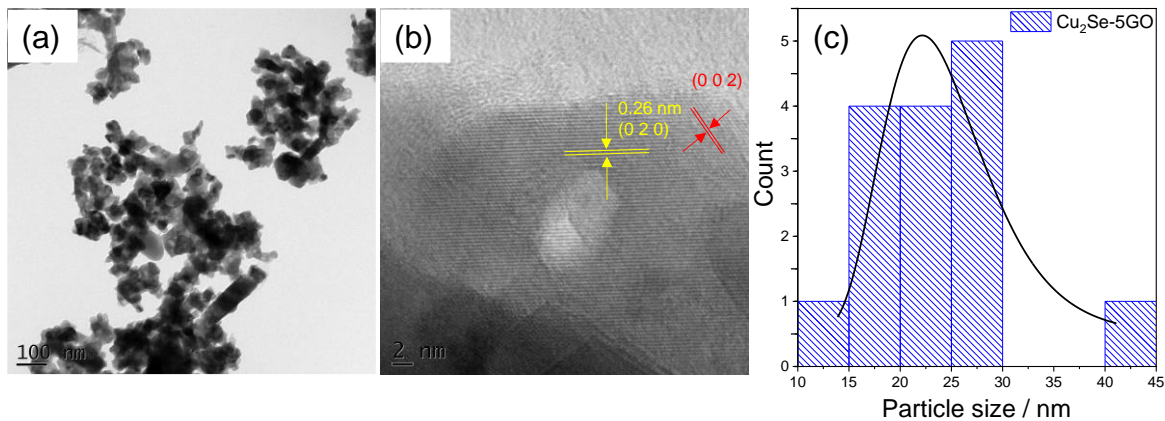


Figure 2.9 (a) TEM image of Cu₂Se-5GO and (b) corresponding HRTEM image (c) Fit distribution curve on the histogram for Cu₂Se-5GO

In the TEM image of the Cu₂Se-5GO (Fig 2.9 (a)) GO has encapsulated Cu₂Se and Fig 2.9 (b) shows the corresponding HRTEM image. The material has mesoporous nature with an irregular shape of particles with the diameter ranging from 13 nm to 40 nm as shown in Fig 2.9 (c). The Fig 2.9(b) shows the (020) plane of Cu₂Se, which corresponds to the interplanar distance d=0.26 nm and (002) plane of GO from XRD results.

2.3.8 Electrochemical performance of Cu₂Se-5GO

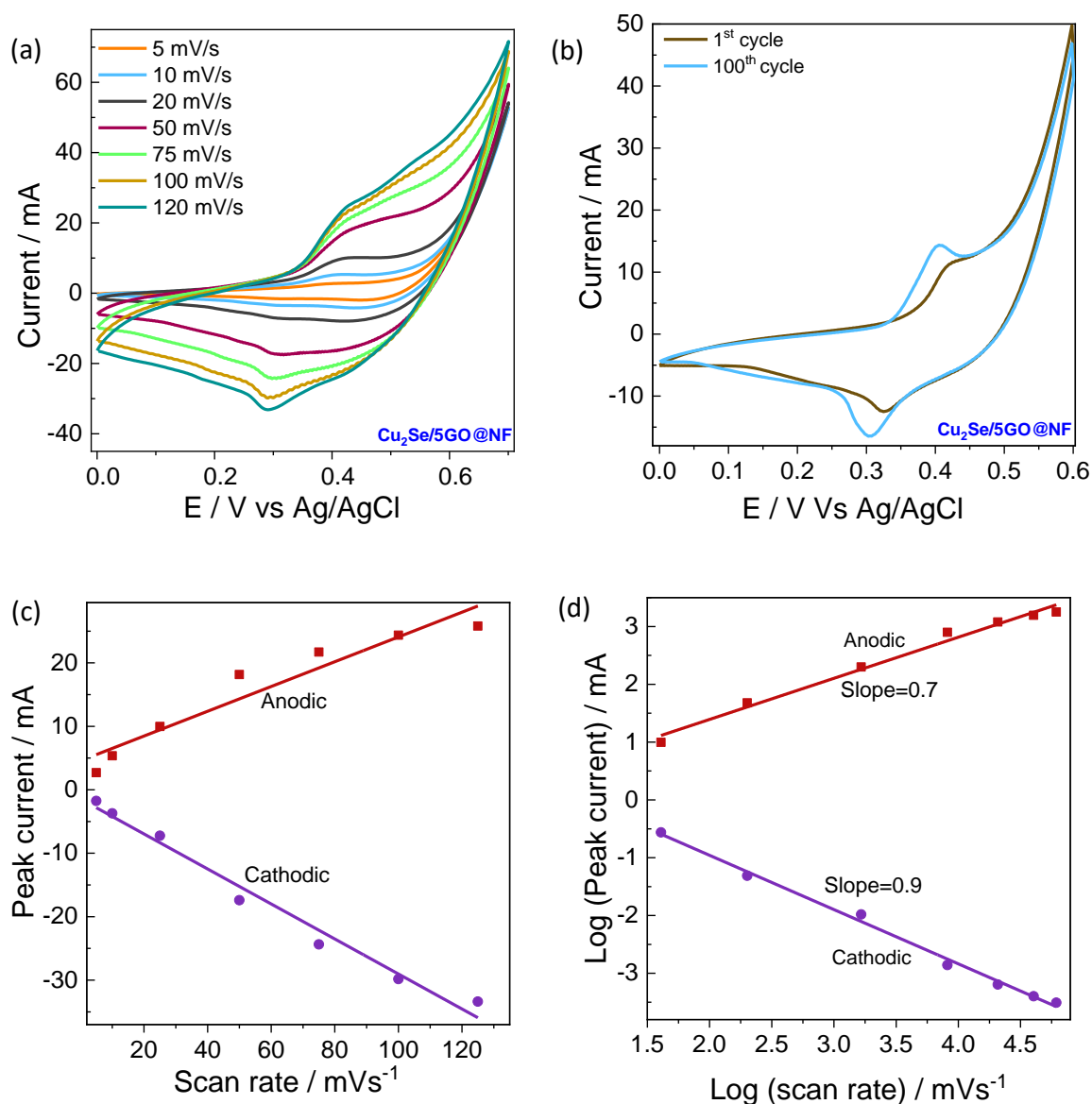


Figure 2.10. (a) CV curves of Cu₂Se-5GO at various scan rates (b) CV of Cu₂Se-5GO after 100 cycles (c) The linear variation graph of peak current as a function of scan rate (d) The linear variation graph of Log (peak current) as a function of Log (scan rate).

The CV curves of Cu₂Se 5GO at various scan rate depicts quasi rectangular curves with the couple of redox peaks which indicates pseudocapacitive nature of the material (Fig 2.10 (a)). At the highest scan rate two couple of redox weak peaks have been observed. All these redox peaks can be attributed to the following reversible reactions (Deka et al. 2019).



The CV curves at all the scan rates are almost similar alongside analogous redox peaks, which confirms the material's refined stability and rate capability. The anodic peak shifted to the positive end of potential and the cathodic peak shifted to the negative end of potential as the scan rate increased as shown in Fig 2.10 (a). Also, the potential difference between oxidation and reduction peak widens as the scan rate increases (Yang et al. 2020a). As the scan rate increases, though the peak current increases, the material do not exhibit higher specific capacitance. The reason behind these observations is due to the retardation of either ion diffusion in an electrolyte or charge transfer in an electrode or because of in-accessible electrodes surface to the electrolyte. Thereby resulting in the decreased specific capacitance with an increase in the scan rate (Singu and Yoon 2019; Zhang et al. 2014c) and when the Cu₂Se-5GO is subjected to 100 cycles of cyclic voltammetry as shown in Fig 2.10 (b), both anodic and cathodic current peaks are much higher than the first cycle there by occupying higher area. This may be attributed to the fact that the material gets activated in the longer run and due to the electrochemical reduction of GO (Aboutalebi et al. 2011). The recorded specific capacitance for Cu₂Se-5GO at the scan rates of 5-120 mV/s are 219, 212, 199, 166, 143, 124, and 66 F/g, respectively. Even at 120 mV/s, the material retains 30.13 % of the specific capacitance at 5 mV/s.

The anodic and the cathodic peak current is in linear relationship with the scan rate as shown in Fig 2.10 (c) which indicates that the redox system depend on a surface-controlled process (Karuppasamy et al. 2022a). This result has been supported by a following relation between peak current (*i*) and scan rate (*v*) (Balakrishna Pillai et al. 2018):

$$i = av^b \quad (2.3)$$

Where *a* and *b* are adjustable parameters varying from 0.5 to 1. The slope of the graph, Log *i* vs Log *v* gives the *b* value (Zardkhoshoui and Davarani 2020b). The parameter *b*= 0.5, implies diffusion-controlled process and *b*=1 corresponds to a surface-controlled process. From Fig 2.10 (d), the value of *b* is found to be 0.7 for anodic peak and 0.9 for cathodic peak. Since both the values are near to 1, it can be concluded that the current in the system is surface controlled (Augustyn et al. 2013).

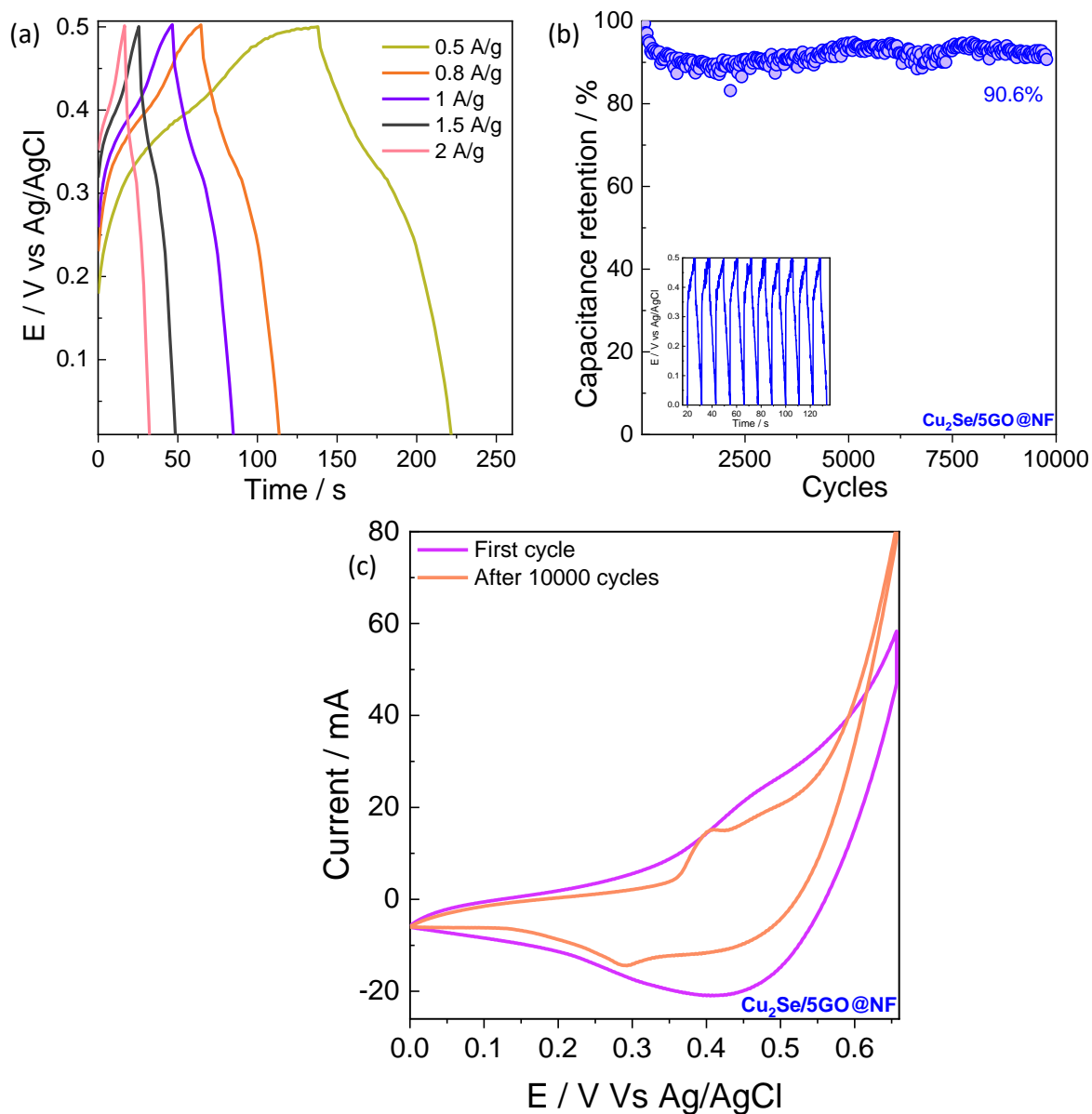


Figure 2.11. (a) GCD of $\text{Cu}_2\text{Se}/5\text{GO}$ at different current densities. (b) Cyclic stability of $\text{Cu}_2\text{Se}/5\text{GO}$ for 10000 cycles at 2 A/g and (c) CV of $\text{Cu}_2\text{Se}/5\text{GO}$ before and after 10000 cycles.

GCD Curves for $\text{Cu}_2\text{Se}/5\text{GO}$ at the current density 0.5, 0.8, 1, 1.5, 2 A/g are demonstrated in Fig 2.11 (a). The specific capacitances measured at 0.5, 0.8, 1, 1.5, 2 A/g are 84, 78.4, 76, 66, 60 A/g respectively. The GCD curves show a similar voltage plateau in the charging and discharging curves as in the CV curve, and do not exhibit ideal triangular shape which focuses on the faradaic type of the material (Li et al. 2018; Yu et al. 2017a). These curves remaining symmetric throughout different current densities implies the reversibility of the material (Zardkhoshoui and Davarani 2020b). Additionally, these non-aligned GCD curves predicts that the charge storage is via redox process. The negligible iR drop indicates that

the material has lower internal resistance and high electrical conductivity (Moosavifard et al. 2021b). The specific capacitances of the Cu₂Se-5GO electrode capacitance decreases with the increasing current density as represented as there occurs insufficient faradaic reactions at a higher current density (Li et al. 2018).

2.3.9 Post cycling characterisation

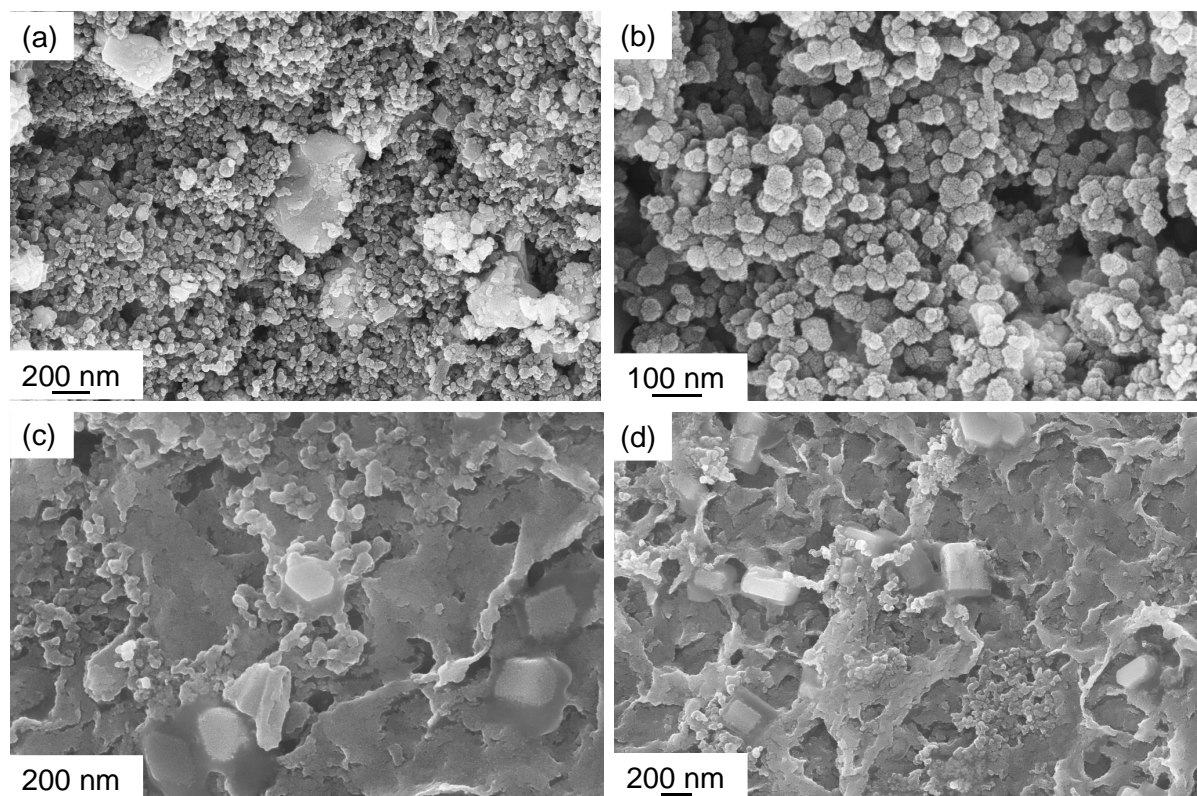


Figure 2.12. FESEM images of Cu₂Se-5GO (a&b) before and (c&d) after 10000 cycles.

Cyclic stability is one of the important applications in supercapacitors. In this case, the Cu₂Se-5GO electrode material was made to run 10,000 cycles at a current density of 2 A/g, and 90.6 % of capacitance was maintained at the end of cycles, as shown in Fig 2.11 (b) where the first ten GCD cycles are shown in the inset. The FESEM images of Cu₂Se-5GO coated on nickel foam before and after 10000 cycles are shown in Fig 2.12. Even though the cauliflower floret morphology has been somewhat flattened and scattered, the original morphology has been preserved (Fig 2.12 (c&d)). The CV was run for Cu₂Se-5GO after 10000 cycles as shown in Fig 2.11 (c) where the anodic and cathodic peaks have been shifted to the negative end of the potential and the anodic and the cathodic peaks are much lower than the first cycle. Hence the overall electrochemical analysis on the Cu₂Se-5GO found that it is a potent material as it exhibits excellent electrochemical properties because

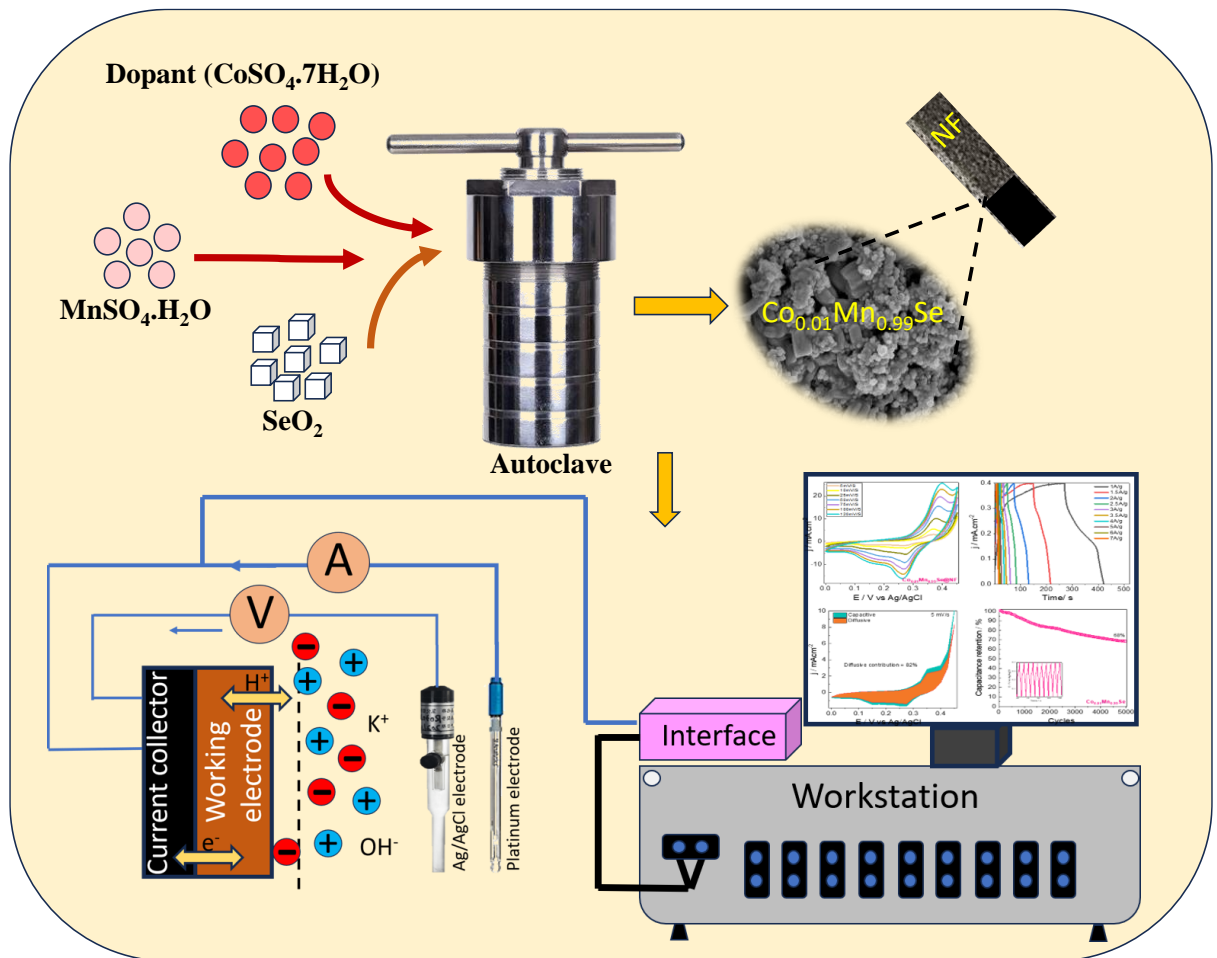
of the combined effect of GO and Cu₂Se. Also, Cu₂Se-5GO electrode has performed comparably well and proved that this method will be attainable and advantageous at the same time.

2.4 CONCLUSIONS

This chapter summarizes the synthesis of nanocomposite of Copper selenide- Graphene oxide in various compositions of Graphene oxide (Cu₂Se-5GO, Cu₂Se-10GO, and Cu₂Se-20GO) through one step hydrothermal method. These composites were comprehensively characterized to ascertain their structures and properties. The electrochemical analysis revealed that the Cu₂Se-5GO performs very well in comparison with other composites as a result of the synergetic effect of Cu₂Se and GO. Therefore, the composite Cu₂Se-5GO delivered maximum specific capacitance of 219 F/g at 5mV/s. Also, it produced high capacitance retention of 90.6 % and proved that the material will be superlative as a supercapacitor electrode.

CHAPTER 3

SIGNIFICANCE OF TRANSITION METAL (Co, Ni, AND Zn) DOPING ON THE MnSe FOR HIGH-PERFORMANCE SUPERCAPACITOR ELECTRODE



Abstract: This chapter provides the synthesis of transition metal doped Manganese selenide and its application as a supercapacitor electrode.

3.1 INTRODUCTION

Recent advancements in supercapacitor electrode materials have mainly focused on increasing energy density. This involves developing electrode materials with high specific capacitance, allowing for operation at higher voltages (Zheng et al. 2019c). The carbonaceous materials employed in commercially available supercapacitors predominantly serve as double-layer capacitor electrodes. However, these materials may not ensure sufficient specific energy and specific capacitance (Chen et al. 2010a). However, pseudocapacitive materials such as conducting polymers, transition metal oxides, transition metal selenides, and transition metal sulfides have been intensively investigated as they provide higher energy density and specific capacity due to the faradaic reactions (Zheng et al. 2019c).

Among the extensively researched pseudocapacitive materials, transition metal selenides have captured the attention of researchers, appearing as high-quality electrode materials for supercapacitors. One of the typical representative of transition metal selenides with acceptable cost is Manganese Selenide (MnSe) that is environment friendly and has uses in oxygen reduction catalysis and lithium storage (Li et al. 2016; Liu et al. 2015). Due to its low electrical resistance and high conductivity, it attracts bounteous research areas for better energy conversion and storage and is thus an attractive electrode material for energy storage (Shah et al. 2023). According to recent studies, adding the right transition metal ions to a catalyst's substance can significantly improve its electrochemical performance (Tigwere et al. 2023). The added dopants generate structural defects and induce active catalytic sites in the host material (Kundu et al. 2019). Xie et al. doped nickel sulfide with cobalt for a supercapacitor and noticed tremendous results in its activity with an energy density of 54.9 Wh/kg (Xie et al. 2018). The morphology of cobalt selenide was modified by doping with nickel to improve the electrochemical properties. The doped electrode exhibited a specific capacitance of 1472 mF/cm² at 1mA/cm² (Sheng et al. 2021).

Considering the significant impact of doping on the energy storage characteristics of nanomaterials, we have reported the synthesis of MnSe doped with three transition metal dopants, Cobalt, Nickel, and Zinc, in various concentrations through the hydrothermal method. The hydrothermal methodology offers several advantages over conventional

synthesis techniques, including ease of usage, low energy consumption, low temperature functionality, and is environment friendly. Additionally, this is a one-step synthesis process with improved control over particle size (Yoshimura and Byrappa 2008). All the synthesized materials are fabricated on the nickel foam (NF) to study electrochemical performance. The best one is further examined as an electrode material for the supercapacitor with various electrochemical techniques. A two-electrode symmetric assembly, using the best active material has been developed to analyse the cell assembly with various electrochemical methods which streamlines experimentation while enabling targeted analysis of device performance under practical conditions.

3.2. EXPERIMENTAL

3.2.1 Materials

Selenium dioxide (SeO_2) and C65 conductive carbon were purchased from Sigma Aldrich. polyvinylidene fluoride (PVDF), N-Methyl 2-pyrrolidone (NMP), manganese sulfate monohydrate ($\text{MnSO}_4 \cdot \text{H}_2\text{O}$), hydrazine hydrate ($\text{N}_2\text{H}_4 \cdot \text{H}_2\text{O}$), cobaltous sulfate heptahydrate ($\text{CoSO}_4 \cdot 7\text{H}_2\text{O}$), nickel sulfate heptahydrate ($\text{NiSO}_4 \cdot 7\text{H}_2\text{O}$) and zinc sulfate heptahydrate ($\text{ZnSO}_4 \cdot 7\text{H}_2\text{O}$) were bought from Loba Chemie. NF was bought from Global Nanotech, Mumbai, India. The preparation of all solutions involved the use of Ultrapure Milli-Q water (18.2 M Ω). All purchased materials were of high purity and were utilized without undergoing additional purification.

3.2.2 Synthesis of $\text{M}_x\text{Mn}_{1-x}\text{Se}$ (M= Co / Ni / Zn); (x = 0.0 , 0.01 , 0.02, 0.03)

$\text{M}_x\text{Mn}_{1-x}\text{Se}$ (M= Co / Ni / Zn, x = 0.0, 0.01, 0.02, 0.03) nanoparticles was synthesized when the dopants, i.e., $\text{CoSO}_4 \cdot 7\text{H}_2\text{O}$, $\text{NiSO}_4 \cdot 7\text{H}_2\text{O}$ or $\text{ZnSO}_4 \cdot 7\text{H}_2\text{O}$ were prepared in the different molar concentrations (i.e., 0.0, 0.01, 0.02 and 0.03) each and dissolved in 70 mL of distilled water. Then, 0.2 M each of $\text{MnSO}_4 \cdot \text{H}_2\text{O}$ (2.36 g) and SeO_2 (1.55 g) was added with stirring. After that 7 mL of hydrazine hydrate ($\text{N}_2\text{H}_4 \cdot \text{H}_2\text{O}$) is added dropwise and stirred well and transferred into autoclave subjected to 24 h treatment at 180°C, as illustrated in Fig 3.1. Following synthesis, the resulting materials underwent a cooling phase and thorough washing with Milli-Q water, ethanol, and acetone. and dried at 60°C (Liu et al. 2009b).



Figure 3.1 A schematic representation for the synthesis of $M_xMn_{1-x}Se$ ($M = Co / Ni / Zn$, $x = 0.0, 0.01, 0.02, 0.03$)

3.2.3 Electrode fabrication

In the formulation of the electrode for the electrochemical supercapacitor, a slurry was prepared by combining the material, C65 conductive carbon and PVDF binder in a proportion of 7:2:1, along with 200 μL of NMP solvent using a mortar and pestle. This resultant slurry was meticulously deposited using a micropipette onto a pre-weighed and cleansed NF, possessing a coating dimension of $1 \times 1 \text{ cm}^2$. The coated assembly was kept in a hot air oven set at 120°C for a duration of 15 h. The quantification of the coated material revealed a mass within the range of $1.5 \pm 0.8 \text{ mg}$.

3.2.4 Material characterisation

The surface morphology and elemental details were tested using Carl Zeiss Model Supra 55 Germany field-emission scanning electron microscope. Then employed Jeol Model JM 2100 instrument for high-resolution transmission electron microscopy. Using Rigaku miniflex 600 powder XRD instrument, various phases and crystalline compositions were obtained in the range 5° - 90° at a scan rate of 3° per minute using monochromatic $\text{Cu-K}\alpha$ radiation of wavelength 0.154 nm. The Raman analysis is examined by using Horiba Japan Xplora Plus. The X-ray photoelectron spectroscopy data were obtained using a Thermo Fischer Scientific ESCALAB Xi+ with an Al K-alpha X-ray source (1486.7 eV).

3.2.5 Electrochemical characterization

The exploration of the electrochemical properties of the prepared electrodes unfolds with the utilization of the Autolab PGSTAT204 electrochemical workstation. Employing a sophisticated three-electrode setup, the designated material coated on a NF act as a working electrode, a platinum electrode as a counter electrode, while Ag/AgCl serves as the

reference electrode. This intricate arrangement forms the foundation for the meticulous execution of electrochemical studies. CV studies on MnSe with electrolytes like 1M NaOH, KOH, Na₂SO₄ revealed that 1M KOH shows the superior activity as illustrated in Fig 3.2 (a). Following this, CV analysis was carried out with different KOH concentrations, and 5 M KOH produced positive results, as shown in Fig 3.2 (b).

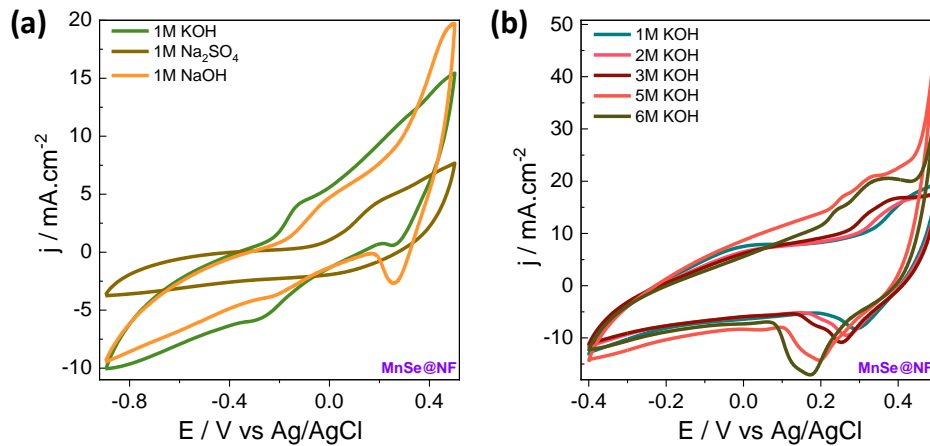


Figure 3.2. (a) CV of MnSe in 1 M KOH, NaOH, and 1 M Na₂SO₄ and (b) CV of MnSe in 1 M, 2 M, 3 M, 4 M, and 5 M KOH, respectively.

The CV studies encompassed a potential range of 0.0-0.45 V vs. Ag/AgCl employing diverse scan rates ranging from 5-120 mV/s. Additionally, GCD studies were executed at various current densities spanning from 1-7 A/g within the potential window of 0.0-0.4 V. The EIS study was accomplished at a frequency range of 1-100 kHz at zero-bias voltage. Electrochemical Active Surface Area (ECSA) was carried out for different scan rates from 5-120 mV/s. The slope of the plot of $\Delta j = j_a - j_c$ vs scan rate gives the value of double layer capacitance ($2C_{dl}$). The surface area is calculated using the following equation

$$ECSA = \frac{C_{dl}}{C_s} \quad (3.1)$$

where C_s is an capacitance of an atomically smooth surface ($40\mu\text{F}/\text{cm}^2$) (Junita et al. 2023; Kim et al. 2020). The specific capacitance (C_s) for the three electrode configuration can be calculated from the CV and GCD studies utilizing equations (1.4) and (1.6) correspondingly (Mascarenhas et al. 2023).

A symmetrical supercapacitor cell was carefully created using the highest performing sample through a three-electrode method. The electrodes were coated using the same procedure used for three-electrode system. The calculated mass of the electrodes was found

to be 2 mg. The cell assembly involved immersing both electrodes in a 5M KOH electrolyte for the electrochemical analysis. To thoroughly examine the electrochemical behaviour of the cell CV experiments were conducted in a potential range of 0-1.5 V at scan rates ranging from 5-120 mV/s. Additionally, GCD studies were performed at varying current densities, ranging from 0.5-2 A/g, within the potential window of 0.0-1.5 V. The specific capacitance (C_s) for two electrode assembly can be calculated from CV and GCD using the equations (1.5) and (1.7) respectively. The energy density (E (Wh/kg)) and power density (P (W/kg)) are calculated using the equations (1.8) and (1.9) (Zheng et al. 2019b).

3.3 RESULTS AND DISCUSSIONS

3.3.1 XRD analysis

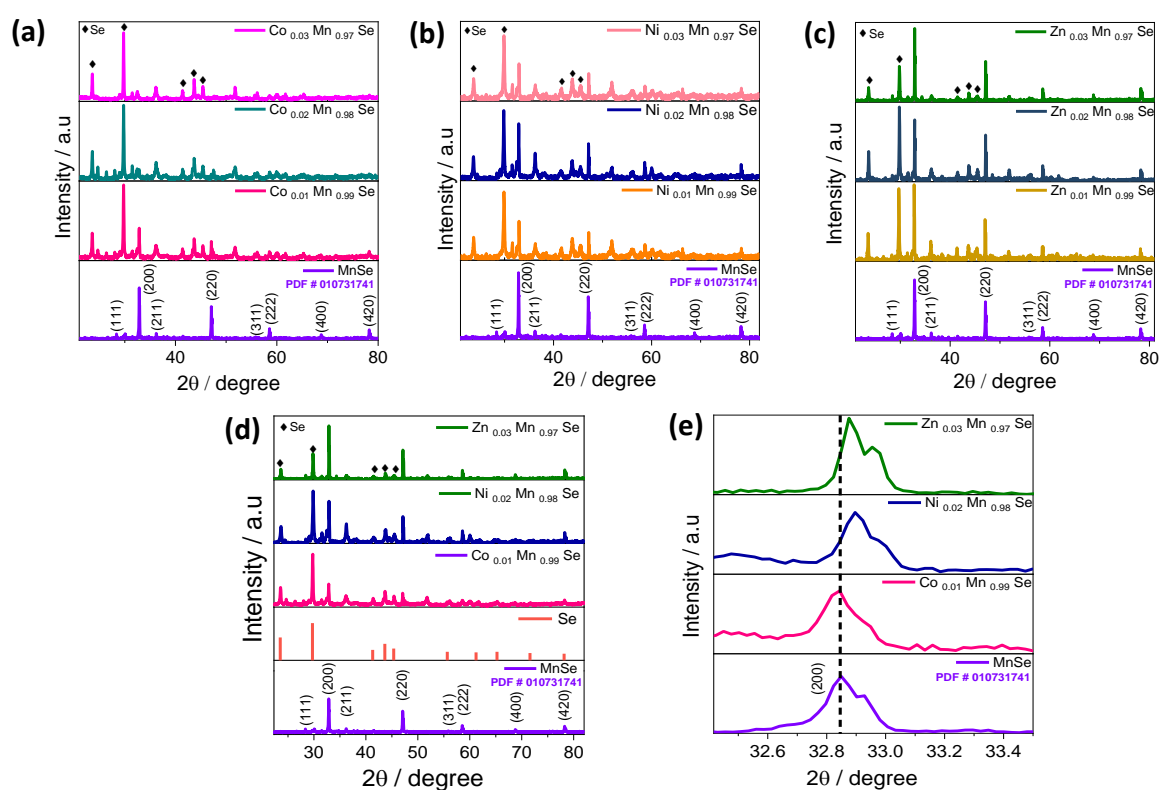


Figure 3.3. XRD of (a) $Co_xMn_{1-x}Se$ (b) $Ni_xMn_{1-x}Se$ (c) $Zn_xMn_{1-x}Se$ ($x = 0, 0.01, 0.02$ and 0.03); (d) XRD pattern of $MnSe$, $Co_{0.01}Mn_{0.99}Se$, $Ni_{0.02}Mn_{0.98}Se$ and $Zn_{0.03}Mn_{0.97}Se$; (e) XRD peak shifting towards higher diffraction angle with different dopants.

The XRD pattern of $M_xMn_{1-x}Se$ ($M = Co / Ni / Zn$, $x = 0.0, 0.01, 0.02, 0.03$) is as shown in Fig 3.3 (a-c). In $MnSe$, the observed peaks corresponding to the cubic phase of $MnSe$, can be successfully matched with JCPDS card no. 01-073-1741. In $Co_xMn_{1-x}Se$, $Ni_xMn_{1-x}Se$ and $Zn_xMn_{1-x}Se$, small peaks seen in addition to the $MnSe$ which are associated

with the JCPDS card for Se (00-006-0362) (Jevtovic et al. 2023). It can be observed that the phases of all the $\text{Co}_x\text{Mn}_{1-x}\text{Se}$, $\text{Ni}_x\text{Mn}_{1-x}\text{Se}$ and $\text{Zn}_x\text{Mn}_{1-x}\text{Se}$ are unchanged compared to pure MnSe implying the incorporation of Co, Ni or Zn ions into MnSe without any disparity in the structural composition.

3.3.2 CV and GCD analysis

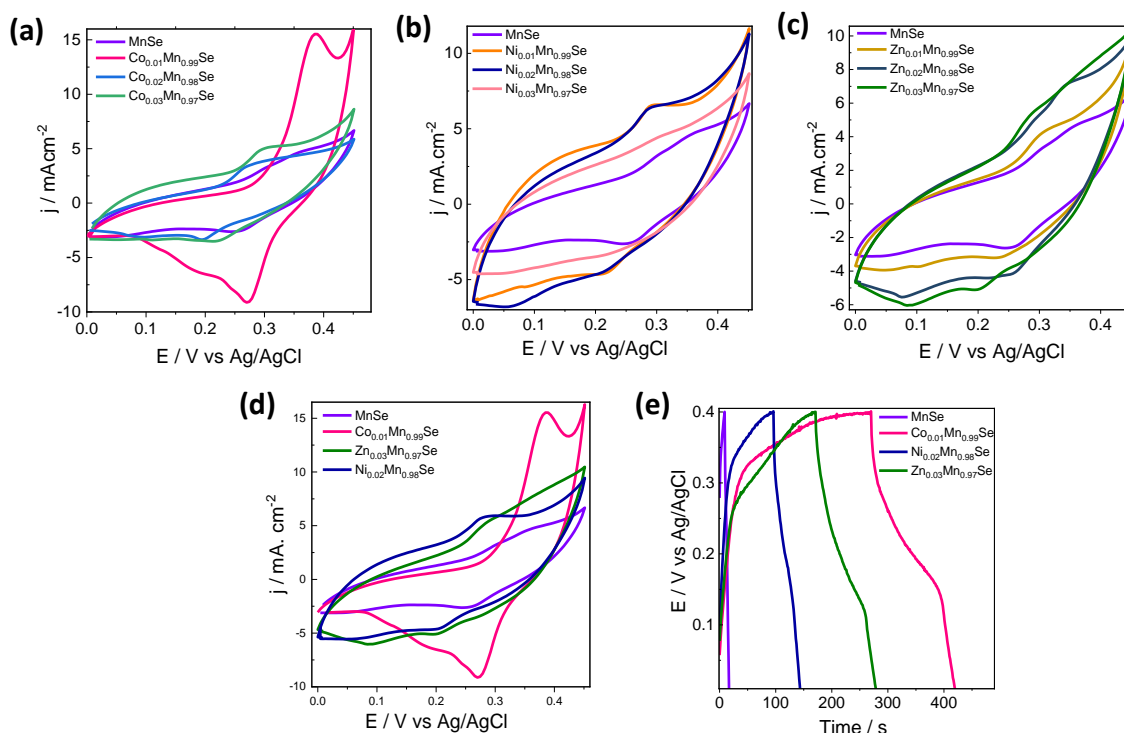


Figure 3.4. CV of (a) $\text{Co}_x\text{Mn}_{1-x}\text{Se}$ (b) $\text{Ni}_x\text{Mn}_{1-x}\text{Se}$ (c) $\text{Zn}_x\text{Mn}_{1-x}\text{Se}$ ($x = 0.0, 0.01, 0.02$ and 0.03); (d) CV of MnSe, $\text{Co}_{0.01}\text{Mn}_{0.99}\text{Se}$, $\text{Ni}_{0.02}\text{Mn}_{0.98}\text{Se}$ and $\text{Zn}_{0.03}\text{Mn}_{0.97}\text{Se}$ at 50mV/s; (e) GCD of MnSe, $\text{Co}_{0.01}\text{Mn}_{0.99}\text{Se}$, $\text{Ni}_{0.02}\text{Mn}_{0.98}\text{Se}$ and $\text{Zn}_{0.03}\text{Mn}_{0.97}\text{Se}$ at 1A/g;

The CV for $\text{M}_x\text{Mn}_{1-x}\text{Se}$ ($\text{M} = \text{Co} / \text{Ni} / \text{Zn}$, $x = 0.0, 0.01, 0.02, 0.03$) within the potential window of 0.0-0.45 V at a scan rate of 50 mV/s is shown in Figure 3.4 (a-c). This analysis reveals the most active material among each of the dopants. Specifically, $\text{Co}_{0.01}\text{Mn}_{0.99}\text{Se}$, $\text{Ni}_{0.02}\text{Mn}_{0.98}\text{Se}$, and $\text{Zn}_{0.03}\text{Mn}_{0.97}\text{Se}$ have been identified as the best performers for each respective dopant. Fig 3.4 (d&e) depicts the CV and GCD analyses of the selected materials such as MnSe, $\text{Co}_{0.01}\text{Mn}_{0.99}\text{Se}$, $\text{Ni}_{0.02}\text{Mn}_{0.98}\text{Se}$, and $\text{Zn}_{0.03}\text{Mn}_{0.97}\text{Se}$. The data reveals that the electrochemical performance of $\text{Co}_{0.01}\text{Mn}_{0.99}\text{Se}$ surpasses that of MnSe, $\text{Ni}_{0.02}\text{Mn}_{0.98}\text{Se}$, and $\text{Zn}_{0.03}\text{Mn}_{0.97}\text{Se}$. This is supported by significantly elevated anodic and cathodic peaks in $\text{Co}_{0.01}\text{Mn}_{0.99}\text{Se}$ compared to MnSe, GCD charge-discharge analysis demonstrates that $\text{Co}_{0.01}\text{Mn}_{0.99}\text{Se}$ exhibits the lengthiest discharge time relative to the other materials. The

specific capacitance calculated for MnSe, Co_{0.01}Mn_{0.99}Se, Ni_{0.02}Mn_{0.98}Se, Zn_{0.03}Mn_{0.97}Se through CV and GCD are 50 F/g, 160 F/g, 136 F/g and 73 F/g at 50 mV/s and 17, 377, 272, 120 F/g at 1 A/g respectively. The cobalt doping in Co_{0.01}Mn_{0.99}Se has contributed towards the highest surface area, lower solution resistance, and higher conductivity of the material. The high charge/discharge behaviour of Co_{0.01}Mn_{0.99}Se is well established and therefore has better electrochemical characteristics than the other electrodes.

All the selected materials such as MnSe, Co_{0.01}Mn_{0.99}Se, Ni_{0.02}Mn_{0.98}Se and Zn_{0.03}Mn_{0.97}Se were subjected to XRD analysis as shown in Fig 3.3 (d). There are no significant changes in the diffraction peak pattern of Co_{0.01}Mn_{0.99}Se, Ni_{0.02}Mn_{0.98}Se and Zn_{0.03}Mn_{0.97}Se verifying that the phase structure of the doped materials are unmodified compared to pure MnSe (Tigwere et al. 2023). The similarity of ionic radii of dopants with Mn²⁺ helps in the easy doping of dopant ions to replace the Mn²⁺ in the MnSe lattice. The identical peaks between MnSe and doped materials and the absence of CoSe peaks in the XRD highlights that cobalt, as a dopant, did not modify the crystal structure of MnSe. The XRD of the plane (200) exhibits a slight shift to the higher diffraction angle confirming doping in their respective host as shown in Fig 3.3(e).

Table 3.1. Crystalline size (D) and lattice parameters of MnSe, Co_{0.01}Mn_{0.99}Se, Ni_{0.02}Mn_{0.98}Se, Zn_{0.03}Mn_{0.97}Se.

Sample	a=b=c (Å)	D (nm)
MnSe	5.453	45.71
Co_{0.01}Mn_{0.99}Se	5.455	42.23
Ni_{0.02}Mn_{0.98}Se	5.448	57.51
Zn_{0.03}Mn_{0.97}Se	5.450	87.18

The application of the Scherrer equation revealed average crystallite sizes for MnSe, Co_{0.01}Mn_{0.99}Se, Ni_{0.02}Mn_{0.98}Se and Zn_{0.03}Mn_{0.97}Se are 45.71 nm, 42.23 nm, 57.51 nm, and 87.18 nm, respectively. Comprehensive lattice parameter calculations for the composite materials are detailed in Table 3.1.

3.3.3 Raman analysis

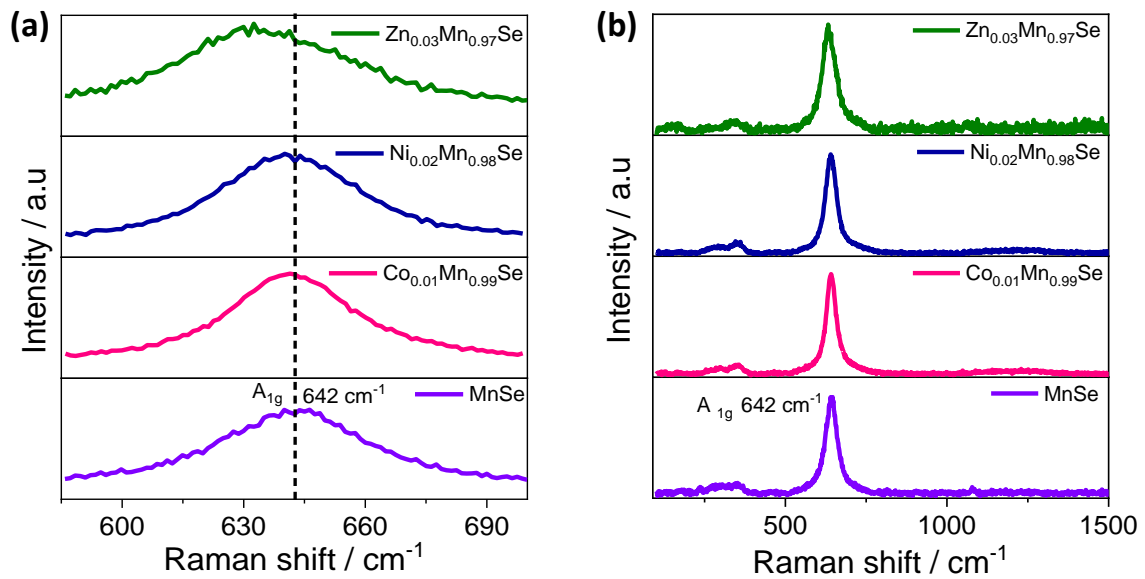


Figure 3.5 (a) Raman spectrum of MnSe, $\text{Co}_{0.01}\text{Mn}_{0.99}\text{Se}$, $\text{Ni}_{0.02}\text{Mn}_{0.98}\text{Se}$ and $\text{Zn}_{0.03}\text{Mn}_{0.97}\text{Se}$; (d) Raman peak shift with different dopants

The Raman spectra of MnSe, $\text{Co}_{0.01}\text{Mn}_{0.99}\text{Se}$, $\text{Ni}_{0.02}\text{Mn}_{0.98}\text{Se}$ and $\text{Zn}_{0.03}\text{Mn}_{0.97}\text{Se}$ composites are shown in Fig 3.5 (a). The distinctive spectral peak at 642 cm^{-1} , observed in both undoped and doped materials of MnSe, corresponds to the A_{1g} mode. This peak is ascribed to the stretching modes of MnSe (Lu et al. 2020; Vidhya et al. 2022). It can be observed that, the characteristic peak of the doped materials exhibits a slight shift to the lower diffraction angle and peak intensity is changed reporting the confirmation of doping of Co, Ni and Zn in their respective host as shown in Fig 3.5 (b).

3.3.4 ECSA and EIS analysis

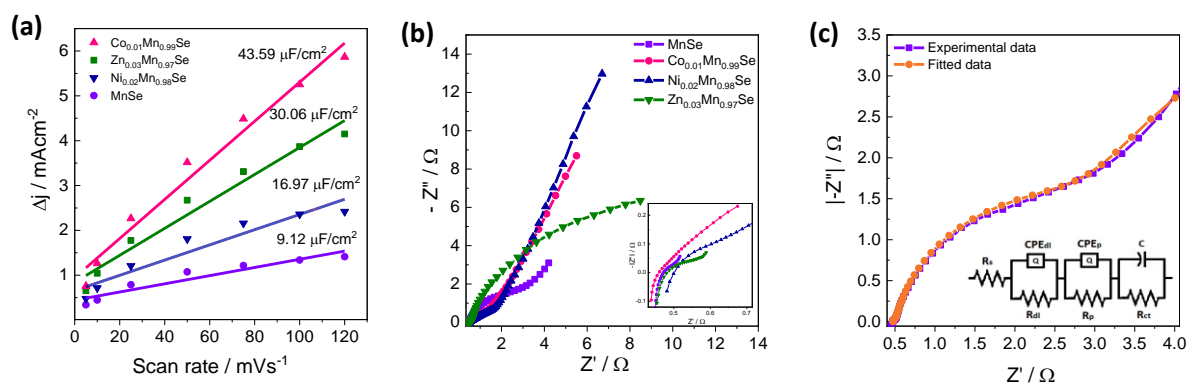


Figure 3.6. (a) ECSA of MnSe, $\text{Co}_{0.01}\text{Mn}_{0.99}\text{Se}$, $\text{Ni}_{0.02}\text{Mn}_{0.98}\text{Se}$ and $\text{Zn}_{0.03}\text{Mn}_{0.97}\text{Se}$; (b) Nyquist plot of MnSe, $\text{Co}_{0.01}\text{Mn}_{0.99}\text{Se}$, $\text{Ni}_{0.02}\text{Mn}_{0.98}\text{Se}$ and $\text{Zn}_{0.03}\text{Mn}_{0.97}\text{Se}$; (c) Nyquist plot of MnSe fitted with equivalent circuit

The activity of MnSe , $\text{Co}_{0.01}\text{Mn}_{0.99}\text{Se}$, $\text{Ni}_{0.02}\text{Mn}_{0.98}\text{Se}$, and $\text{Zn}_{0.03}\text{Mn}_{0.97}\text{Se}$ was compared through electrochemical surface area (ECSA) measurements. As shown in Fig 3.6 (a), the variations in ECSA reflect the influence of different dopants on the catalytic performance of MnSe . Unlike the BET study, this method allows complete immersion of the material in the electrolyte, allowing us to determine the surface area of the material participating in the electrochemical activity (Anantharaj et al. 2018). From Fig 3.6 (a), it is seen that C_{dl} value of MnSe , $\text{Ni}_{0.02}\text{Mn}_{0.98}\text{Se}$, $\text{Zn}_{0.03}\text{Mn}_{0.97}\text{Se}$ and $\text{Co}_{0.01}\text{Mn}_{0.99}\text{Se}$, are 4.56 $\mu\text{F/cm}^2$, 8.48 $\mu\text{F/cm}^2$, 15.03 $\mu\text{F/cm}^2$, and 21.8 $\mu\text{F/cm}^2$ respectively. The surface area was calculated to be 0.114 cm^2 , 0.212 cm^2 , 0.375 cm^2 , and 0.545 cm^2 for MnSe , $\text{Ni}_{0.02}\text{Mn}_{0.98}\text{Se}$, $\text{Zn}_{0.03}\text{Mn}_{0.97}\text{Se}$ and $\text{Co}_{0.01}\text{Mn}_{0.99}\text{Se}$ respectively. The $\text{Co}_{0.01}\text{Mn}_{0.99}\text{Se}$ produces maximum surface area due to the enhancement of the active sites in comparison to other electrodes making it optimal and leading among other materials.

Additionally, Nyquist plots for MnSe , $\text{Co}_{0.01}\text{Mn}_{0.99}\text{Se}$, $\text{Ni}_{0.02}\text{Mn}_{0.98}\text{Se}$, and $\text{Zn}_{0.03}\text{Mn}_{0.97}\text{Se}$ are illustrated in Fig 3.6 (b), highlighting the electrochemical impedance characteristics of these materials. The plots exhibit a distinctive semicircle in the high-frequency region and a subsequent straight line in the lower frequency region. These features in the Nyquist plot suggest the excellent capacitive behaviour of the material. The fitted equivalent circuit is displayed in the inset of Fig 3.6 (c).

Table 3.2. EIS parameters for the fitted circuit.

Samples	R_s (Ω)	CPE_{dl} (F)	R_{dl} (Ω)	CPE_p (F)	R_p (Ω)	CPE_{ct} (F)	R_{ct} (Ω)
MnSe	0.48	0.0018	0.028	0.006	2.82	0.05	6.862
Co_{0.01}Mn_{0.99}Se	0.42	0.0269	0.534	2.528	3×10 ⁻²⁰	0.58	0.015
Ni_{0.02}Mn_{0.98}Se	0.45	7.3×10 ⁻⁸	349	2.3×10 ⁻⁵	2.5×10 ⁴	7.15×10 ⁻⁹	333.4
Zn_{0.03}Mn_{0.97}Se	0.48	0.0003	0.073	0.009	15.83	51.95	1000

The electrochemically fitted parameters are tabulated in Table 3.2 where it can be observed that R_s of MnSe and Co_{0.01}Mn_{0.99}Se are 0.48 Ω and 0.42 Ω respectively and R_{ct} of Co_{0.01}Mn_{0.99}Se is 0.015 Ω which is lowest compared to other doped materials. The lower R_s and R_{ct} values of Co_{0.01}Mn_{0.99}Se indicates that the cobalt doping has increased the conductivity of the material (Kanade et al. 2018). Also, the reduced R_{ct} facilitates swift and efficient ion movement, leading to smooth charge transfer, which brings about several benefits such as minimized voltage drop, superior energy delivery, enhanced cycling stability, and an improved electrode-electrolyte interface (Uke et al. 2020). These factors collectively increase capacitance and overall performance of the supercapacitor. The Co_{0.01}Mn_{0.99}Se electrode shows a straight line with greater slope compared with MnSe providing a lower diffusive resistance and faster ion transmission in the electrolyte (Zhao et al. 2020). The obtained outcome claims that Co_{0.01}Mn_{0.99}Se is the best active material because it improves electron transmission and lowers internal resistance (Yang et al. 2020a).

3.3.5 FESEM analysis

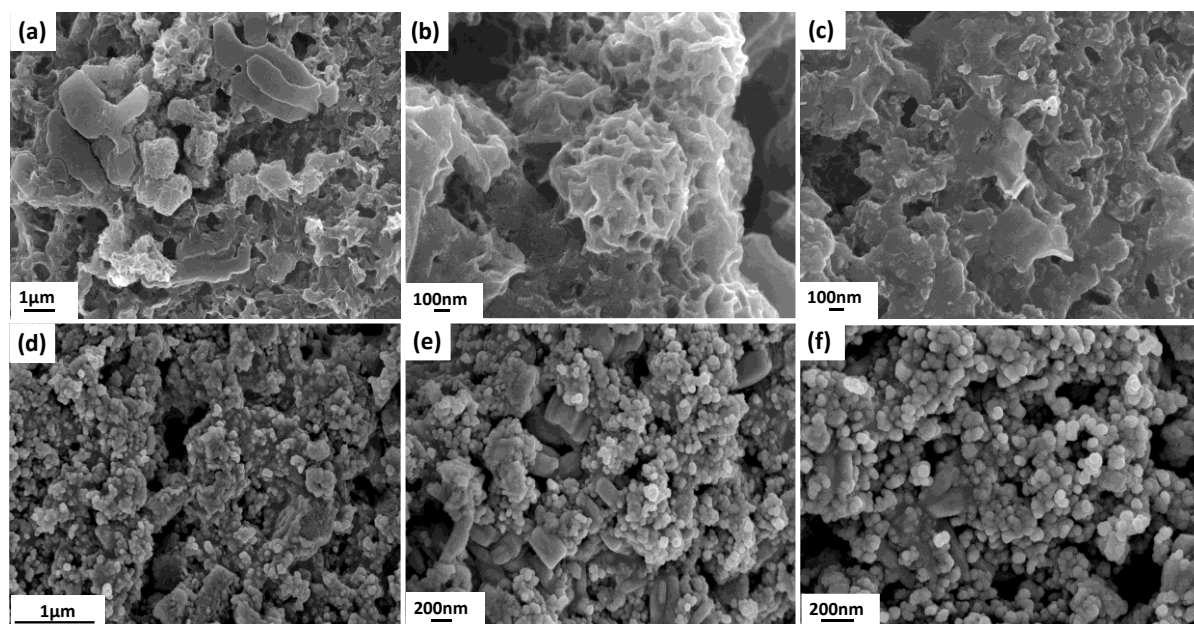


Figure 3.7. FESEM images of (a-c) MnSe; (d-f) Co_{0.01}Mn_{0.99}Se

The nanoflakes have been formed on NF and agglomeration of nanoflakes is observed at a few positions in the FESEM images of MnSe as (Fig 3.7 (a-c)). The Co_{0.01}Mn_{0.99}Se FESEM images (Fig 3.7 (d-f)) demonstrate the formation of nanoclusters that are wrapped around MnSe nanoflakes. This morphology promotes efficient electron transport at the junction between the electrode and electrolyte in Co_{0.01}Mn_{0.99}Se (Wen et al. 2017, 2019).

3.3.6 TEM analysis

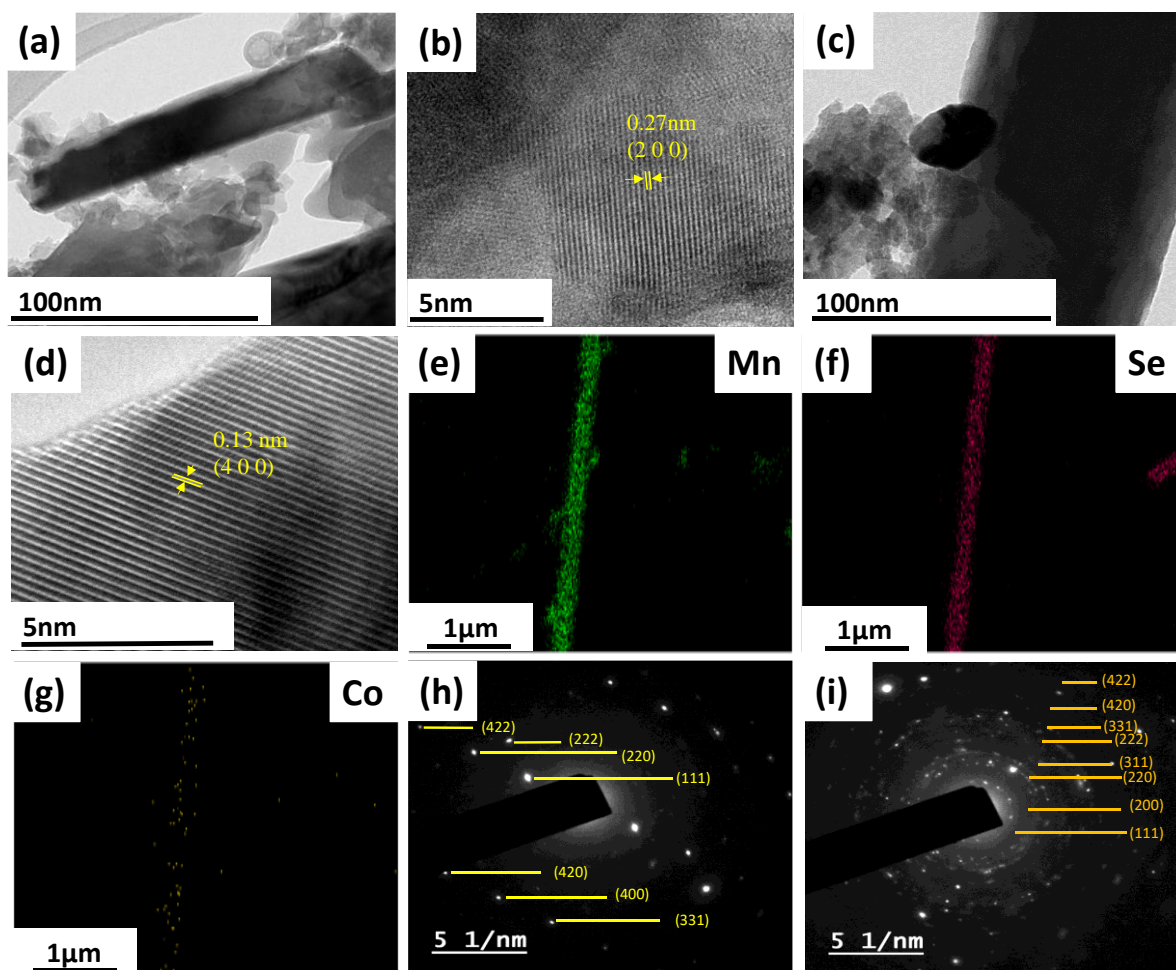


Figure 3.8. (a&c) TEM image of MnSe and $\text{Co}_{0.01}\text{Mn}_{0.99}\text{Se}$; (b&d) corresponding HRTEM images Elemental mapping of (e) Mn, (f) Se and (g) Co; SAED pattern of (h) MnSe and (i) $\text{Co}_{0.01}\text{Mn}_{0.99}\text{Se}$.

The MnSe and $\text{Co}_{0.01}\text{Mn}_{0.99}\text{Se}$ nanomaterial shows the nanoflakes and nanoclusters in the TEM images (Fig 3.8 (a&c)) which is in accordance with SEM results. The macroporous characteristics of $\text{Co}_{0.01}\text{Mn}_{0.99}\text{Se}$ are shown in Fig 3.9. It features nanoclusters of irregular shapes with diameters ranging from 38 nm to 138 nm. The (200) plane of MnSe is displayed in Fig 3.8 (b) and it represents an interplanar distance (d) of 0.27 nm, while the (400) plane of $\text{Co}_{0.01}\text{Mn}_{0.99}\text{Se}$ corresponds to an interplanar distance (d) of 0.13 nm as shown in Fig 3.8 (d), as determined from XRD results. Hence proved that the introduction of Co^{2+} ions did not change the crystal structure of MnSe.

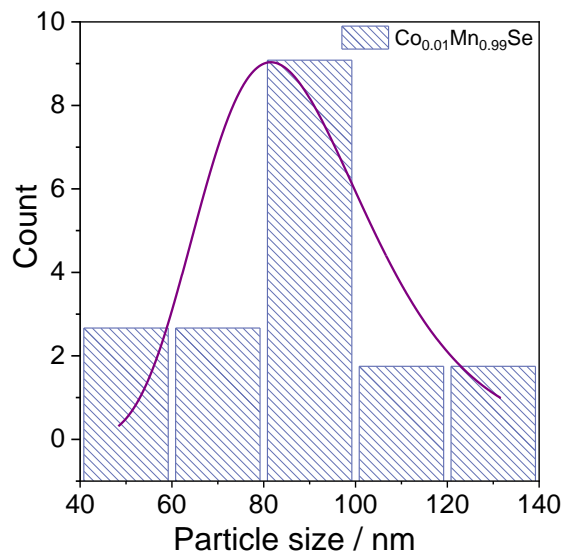


Figure 3.9 Particle size analysis of $Co_{0.01}Mn_{0.99}Se$.

The elemental color mapping of $Co_{0.01}Mn_{0.99}Se$ determined as Mn, Se, and Co presented in Fig 3.8 (e-g). These images demonstrate that the Mn, Se, and Co elements are evenly distributed across the nanomaterial. This means that the growth of the nanoclusters has been uniform, resulting in a homogeneous distribution of Mn, Co, and Se elements throughout the $Co_{0.01}Mn_{0.99}Se$ nanoclusters. This further proves that the $Co_{0.01}Mn_{0.99}Se$ samples were successfully prepared using a single hydrothermal step (Wen et al. 2017). The selected area electron diffraction (SAED) pattern of MnSe and $Co_{0.01}Mn_{0.99}Se$ is presented in Fig 3.8 (h&i), which exhibits clear diffraction spots and the concentric patterns correspond well with crystal plane features.

3.3.7 XPS analysis

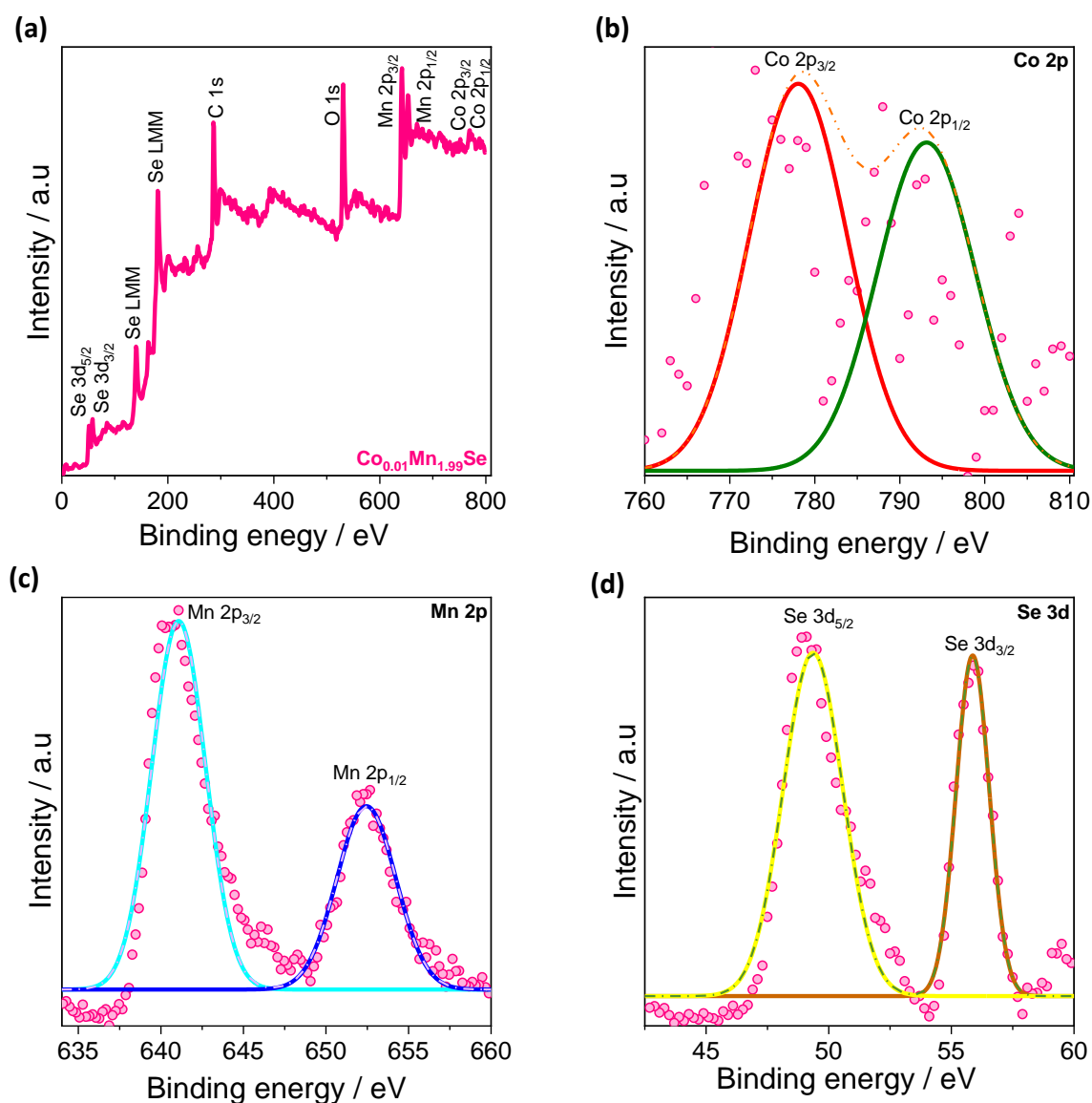


Figure 3.10. (a) XPS survey spectrum of $\text{Co}_{0.01}\text{Mn}_{0.99}\text{Se}$; XPS spectra results of (b) Co 2p; (c) Mn 2p; (d) Se 3d.

The XPS survey spectrum for $\text{Co}_{0.01}\text{Mn}_{0.99}\text{Se}$, illustrated in Fig 3.10 (a), reveals the presence of elements such as Co, Mn, and Se. Also, the observed peaks between 120 and 260 eV in the $\text{Co}_{0.01}\text{Mn}_{0.99}\text{Se}$ XPS spectrum can be attributed to Se LMM transitions. Specifically, the peaks at 140 and 180 eV are consistent with the Se LMM transitions. Fig 3.10 (b) shows the XPS spectrum of Co 2p. The two eminent peaks at 779.92 and 793.18 eV correspond to Co 2p_{3/2} and Co 2p_{1/2}, respectively, implying the presence of Co²⁺ (Ming et al. 2016). The XPS peaks at 641.02 and 652.40 eV shown in Fig 3.10 (c) coincides to Mn 2p_{3/2} and Mn 2p_{1/2}, respectively implying positive bivalent charge of Mn ion.

Compared with bare MnSe (641.8 eV/ Mn 2p_{3/2} and 654.0 eV/ Mn 2p_{1/2}) the slight downshift for Mn 2p peaks for Co_{0.01}Mn_{0.99}Se can be attributed to the partial replacement of Mn²⁺ by Co²⁺ (Liu et al. 2017; Ou et al. 2016). Fig 3.10 (d) shows the spectrum of Se where the peaks at 49.39 and 55.89 eV corresponds to Se 3d_{5/2} and Se 3d_{3/2} respectively. The minor upshift of Se 3d peaks for Co_{0.01}Mn_{0.99}Se in comparison to bare MnSe (55.3 eV/ Mn_{5/2} and 56.1 eV/ Mn_{3/2}) can be due to the stronger connection between Se and Co (Ou et al. 2016; Tang et al. 2020a).

3.3.8 Electrochemical performance of Co_{0.01}Mn_{0.99}Se

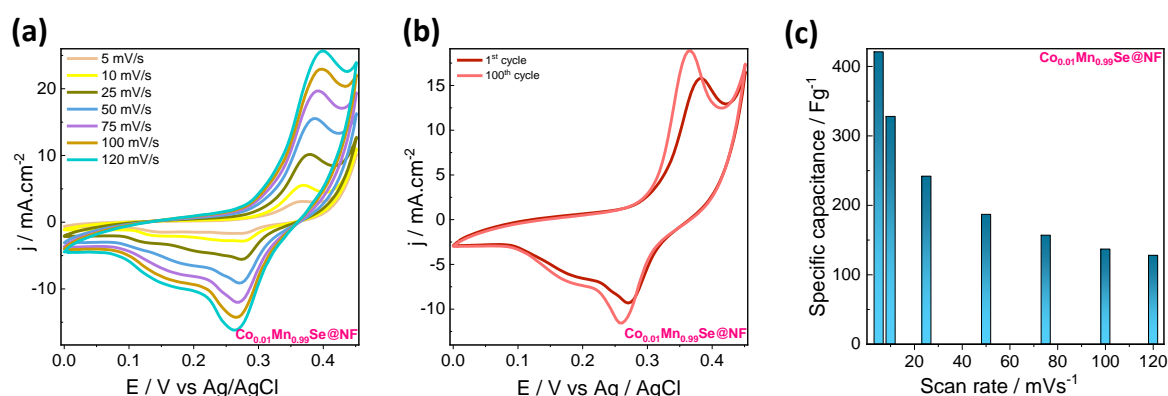


Figure 3.11. (a) CV curves of Co_{0.01}Mn_{0.99}Se at distinct scan rates; (b) CV of Co_{0.01}Mn_{0.99}Se after 100 cycles; (c) Plot of specific capacitance vs scan rate of Co_{0.01}Mn_{0.99}Se

The CV curve of Co_{0.01}Mn_{0.99}Se at different scan rates, ranging from 5 mV/s to 120 mV/s is depicted in Fig 3.11 (a). The presence of distinct redox peaks in the CV curves, across all scan rates, suggests that the energy storage capacity originates from the pseudocapacitive behaviour of the Co_{0.01}Mn_{0.99}Se material. These redox peaks can be ascribed to the specific reversible reactions (Eq. 3.2 & 3.3), defining the electrochemical processes.



The uniformity of the CV curves across all scan rates combined with corresponding redox peaks, attest to the material's superior rate capacity and stability. With the acceleration of the scan rate, the anodic peak shifted towards more positive potentials, while the cathodic peak shifted towards more negative potentials, revealing the influence of polarization effects, as illustrated in Fig 3.11 (a). Additionally, as the scan rate rises, the potential gap

between the oxidation and reduction peaks widens (Yang et al. 2020a). Despite the increase in peak current with scan rate, there is no corresponding increase in specific capacitance. The underlying reason for this phenomenon is the less probability of electrolyte ions coming into contact with a significant portion of the electrode material, resulting in partial redox processes. As a consequence, the specific capacitance exhibited a decline with increasing scan rate, as illustrated in Fig 3.11 (c) (Singu and Yoon 2019; Zhang et al. 2014c). Moreover, as illustrated in Fig 3.11 (b), after undergoing 100 cycles of cyclic voltammetry, both the anodic and cathodic current peaks show a significant increase compared to the first cycle as the material gets activated over time. (Aboutalebi et al. 2011). At scan speeds of 5–120 mV/s, the specific capacitance for $\text{Co}_{0.01}\text{Mn}_{0.99}\text{Se}$ was observed to be 421, 328, 242, 187, 157, 137, 128 F/g respectively.

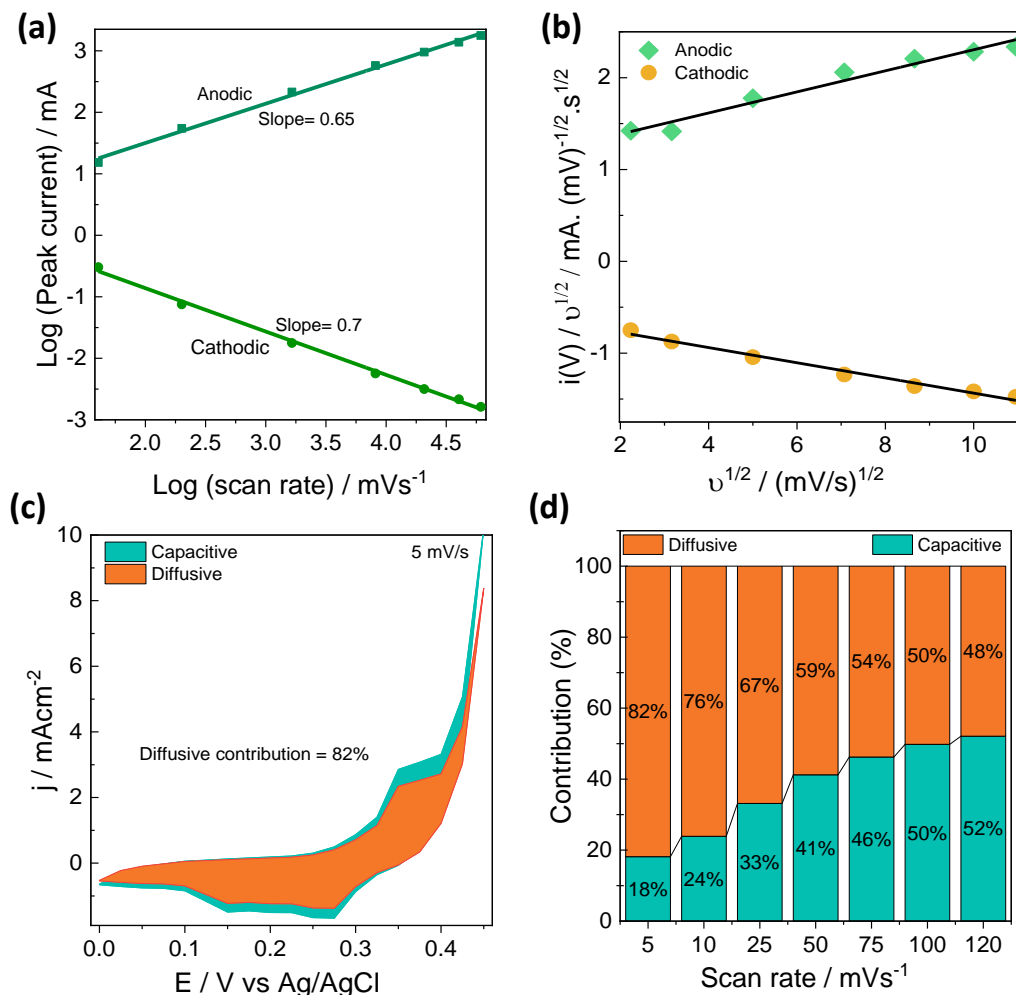


Figure 3.12 (a) Graph of Log of peak current vs Log of scan rate; (b) Relationship between $v^{1/2}$ and $i(V)/v^{1/2}$; (c) Capacitive and diffusive contributions of $\text{Co}_{0.01}\text{Mn}_{0.99}\text{Se}$ at 5 mV/s; (d) Capacitive and diffusive contribution of $\text{Co}_{0.01}\text{Mn}_{0.99}\text{Se}$ at various sweep rates

Additionally, the kinetic analysis of $\text{Co}_{0.01}\text{Mn}_{0.99}\text{Se}$ electrode was assessed by CV profiles using the Trasatti method. The following relationship between peak current (i) and scan rate (v) of CV profile obey the power law (Velayutham et al. 2021a).

$$i = av^b \quad (3.4)$$

where a and b are variables ranging between 0.5 and 1 (Balakrishna Pillai et al. 2018). The value of b is determined by the slope of the graph of $\text{Log } i$ and $\text{Log } v$ (Zardkhoshoui and Davarani 2020b). When the y value is around 0.5, it means that ions are being intercalated towards the electrode or the diffusion process takes over. On the other hand, if the y value nears 1.0, it means that the charge storage is being governed by capacitive nature of the material. In Fig 3.12 (a), it was determined that the value of b is 0.7 for the cathodic peak and 0.65 for the anodic peak. Therefore the charge storage mechanism includes the contribution from both capacitive and battery type behaviour (Augustyn et al. 2013). This method does not, however, offer convincing proof that the charge storage is diffusion or surface controlled. Hence to measure the proportion of capacitive and diffusive contributions, Dunn's technique was developed (Mondal et al. 2021). This technique decodes the contribution of current from diffusion-controlled and surface-reaction at a specific voltage using the following equation:

$$i(V) = cv + dv^{1/2} \quad (3.5)$$

Where $i(V)$ represents the potential-dependent current, the terms cv and $dv^{1/2}$ and signify the current contribution from capacitive effects and the diffusion-controlled process, respectively. The modified equation (3.6) can be utilized to compute the values of c and d . By knowing these values, we can have the portion of the current attributed to each of these contributions at specific potentials using equation (3.5) (Manikandan et al. 2021).

$$\frac{i(V)}{v^{1/2}} = cv^{1/2} + d \quad (3.6)$$

The linear fit of plot $v^{1/2}$ vs $i(V)/v^{1/2}$ is shown in Fig 3.12 (b). The slope and intercept of that graph gives the values of c and d respectively. Fig 3.12 (c) displays the contribution from diffusion-controlled and surface-controlled regions of $\text{Co}_{0.01}\text{Mn}_{0.99}\text{Se}$ electrode at 5 mV/s. The orange-coloured area represents the diffusion-controlled part, and the remaining part corresponds to the surface-controlled process. The diffusion-controlled contribution (%) of $\text{Co}_{0.01}\text{Mn}_{0.99}\text{Se}$ electrode is 82 %, 76 %, 67 %, 59 %, 54 %, 50 %, 48 % whereas the surface- controlled contribution (%) is 18 %, 24 %, 33 %, 41 %, 46 %, 50 %

and 52 % at different scan rates 5, 10, 25, 50, 75, 100 and 120 mV/s, respectively as shown Fig 3.12 (d). Most of the contribution (%) to the charge storage mechanism at lowest scan rate comes from diffusion-controlled interaction which is 85 % and a small contribution of 18 % can be obtained from surface reaction as shown in Fig 3.12 (d). In contrast to diffusion-controlled behaviour, surface-controlled behaviour is more prevalent at high scan rates. These findings support battery-like electrochemical behaviour of $\text{Co}_{0.01}\text{Mn}_{0.99}\text{Se}$.

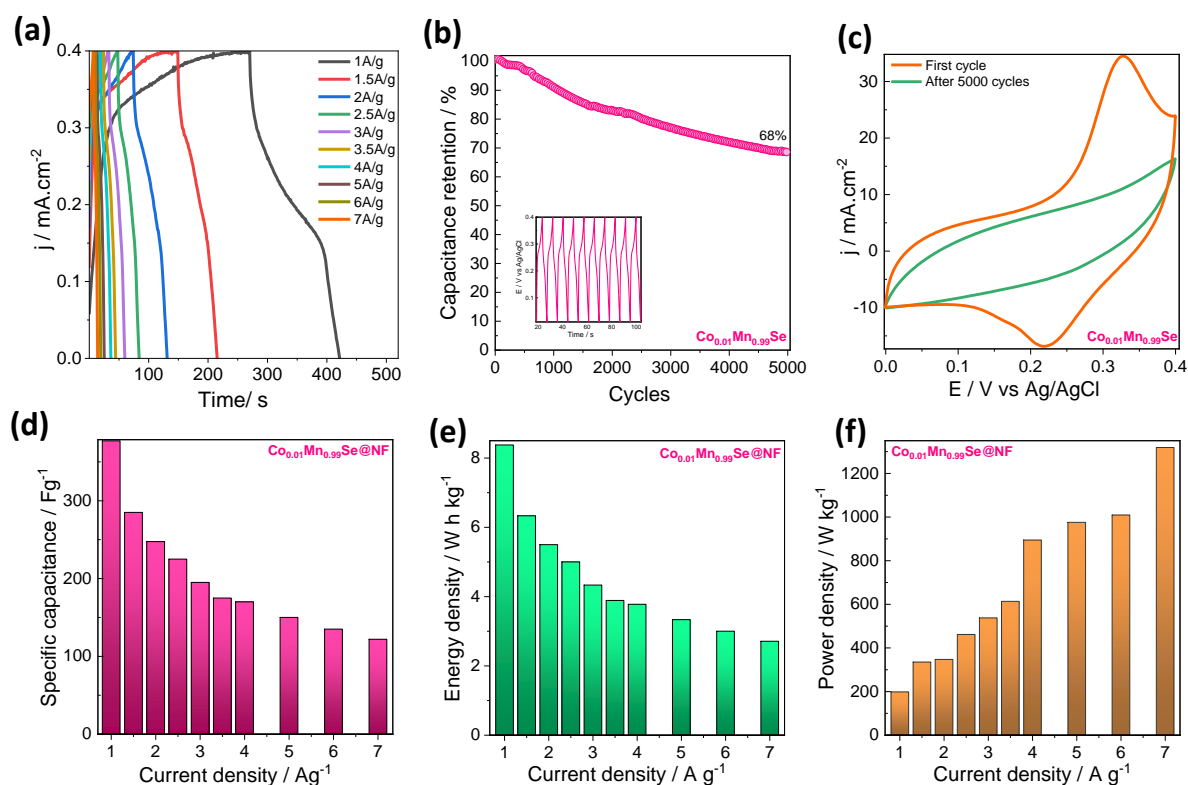


Figure 3.13. (a) GCD of $\text{Co}_{0.01}\text{Mn}_{0.99}\text{Se}$ at various current densities; (b) Cyclic stability of $\text{Co}_{0.01}\text{Mn}_{0.99}\text{Se}$ for 5000 cycles at 4 A/g; (c) CV of $\text{Co}_{0.01}\text{Mn}_{0.99}\text{Se}$ before and after 5000 cycles; (d) Plot of specific capacitance vs current density of $\text{Co}_{0.01}\text{Mn}_{0.99}\text{Se}$; (e) Plot of energy density vs current density of $\text{Co}_{0.01}\text{Mn}_{0.99}\text{Se}$; (f) Plot of power density vs current density of $\text{Co}_{0.01}\text{Mn}_{0.99}\text{Se}$.

The GCD Curves for $\text{Co}_{0.01}\text{Mn}_{0.99}\text{Se}$ at various current densities are displayed in Fig 3.13 (a). The specific capacitances measured at 1, 1.5, 2, 2.5, 3, 3.5, 4, 5, 6, 7 A/g are 377, 285, 247.5, 225, 195, 175, 170, 150, 135, 122 F/g respectively. The charging and discharging curves exhibit a voltage plateau comparable to that of the CV curve, but they do not have the perfect triangular form that emphasises the pseudocapacitive nature of the material (Li et al. 2018; Yu et al. 2017b). The fact that these curves stay symmetric at various current densities suggests the reversibility of the material (Zardkhoshoui and Davarani 2020b). The material exhibits low internal resistance and great electrical

conductivity because of the smaller iR drop (Moosavifard et al. 2021b). The CV was run for $\text{Co}_{0.01}\text{Mn}_{0.99}\text{Se}$ after 5000 cycles where we observe no redox peaks and it occupies much lesser area than the initial cycle as shown in Fig 3.13 (c). As seen in Fig 3.13 (d), the specific capacitance of $\text{Co}_{0.01}\text{Mn}_{0.99}\text{Se}$ electrode decrease with rising current density by cause of the rapid intercalation of electrolyte ions over the surface of the electrode. The energy density and power density values are determined utilizing equations (1.8) and (1.9), resulting in values of 8.37 Wh/kg and 196.5 W/kg at a current density of 1 A/g , respectively. Similarly, at a higher current density of 7 A/g, the corresponding values are 2.7 Wh/kg and 1322.25 W/kg. The calculated energy density and power density values at various current density from GCD curves are graphically given in Fig 3.13 (e&f) respectively.

3.3.9 Post-Cyclic Stability Characterization

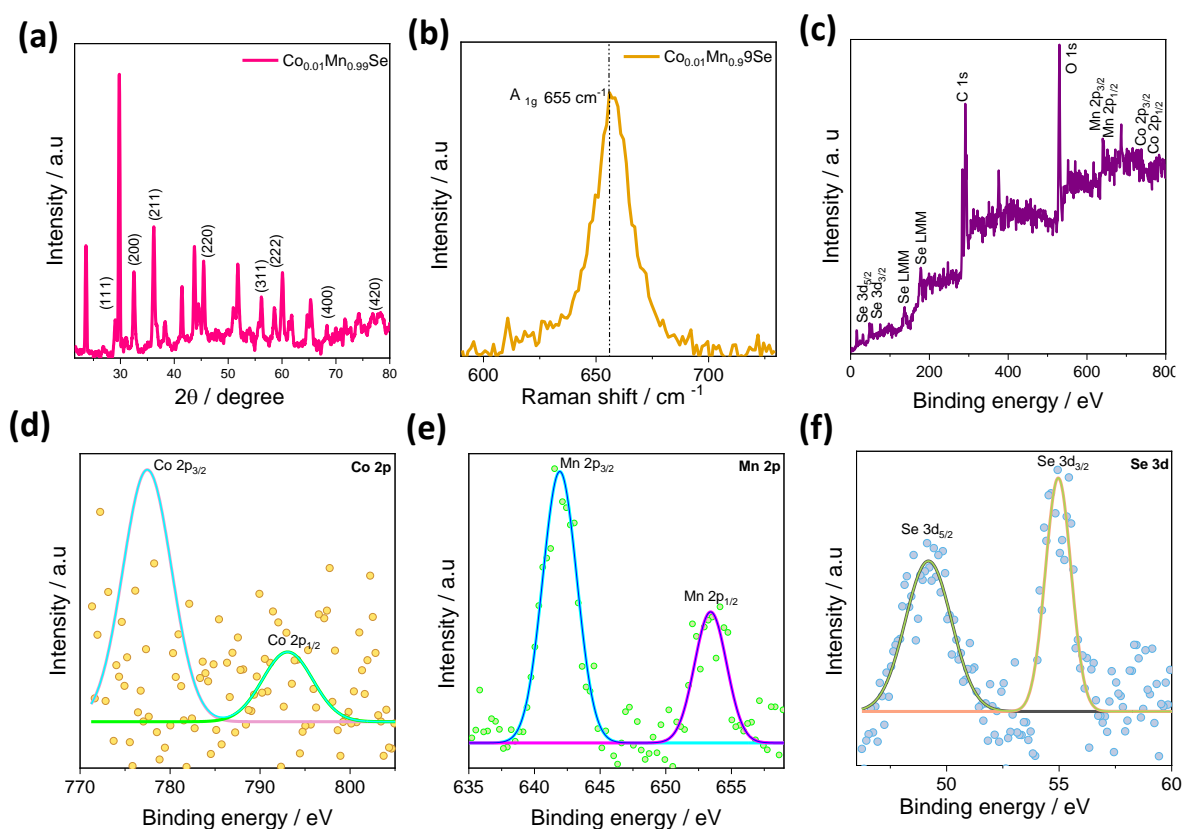


Figure 3.14. (a) XRD pattern of $\text{Co}_{0.01}\text{Mn}_{0.99}\text{Se}$; (b) Raman spectrum of $\text{Co}_{0.01}\text{Mn}_{0.99}\text{Se}$; (c) XPS survey spectrum of $\text{Co}_{0.01}\text{Mn}_{0.99}\text{Se}$; XPS spectra results of (d) Co 2p; (e) Mn 2p; (f) Se 3d after 5000 charge discharge cycles.

Cyclic stability is a crucial factor in the performance of supercapacitors. In this context, the $\text{Co}_{0.01}\text{Mn}_{0.99}\text{Se}$ electrode material underwent 5,000 cycles at a current density of 4 A/g, with 68 % of capacitance retained upon the completion of the cycles, as shown in Fig 3.13 (b) where the first ten GCD cycles are presented in the inset. Our investigation has shown that the material displays a remarkable 68 % retention of capacitance even after being subjected to 5000 charge-discharge cycles, which is a testament to its durability.

To gain a better understanding of the mechanisms of charge storage, we conducted post-cycling assessments using XPS, XRD, and Raman spectroscopy. In Fig 3.14 (a), the XRD pattern of $\text{Co}_{0.01}\text{Mn}_{0.99}\text{Se}$ remains consistent even after undergoing 5000 cycles of charge and discharge. It is noteworthy that the crystal structure remains remarkably stable with no noticeable alterations as compared to its pre-5000 cycle state as shown in Fig 3.3 (a). The XRD peaks persist unchanged and there is an absence of any additional peaks, signifying the structural integrity and resilience of the material even under the rigorous conditions of repeated cycling.

In addition, the Raman peak in the Raman spectrum (Fig 3.14 (b)) that was previously observed at 642 cm^{-1} in the Fig 3.5 (a) has undergone a slight shift to 655 cm^{-1} . This indicates that there has been a very small change in the material. However, it is important to note that this change is minimal, and the overall Raman spectrum remains largely unchanged. The similarity to the initial state remains, which confirms that the material is stable, and there are no significant differences observed.

The XPS survey reveals the presence of all anticipated elements (Fig 3.14 (c)). Further, the XPS spectra of Co 2p, Mn 2p, and Se 3d are illustrated in Fig 3.14 (d, e & f) respectively. Notably, all peaks maintain their positions at the same binding energy levels as observed in the initial XPS analysis prior to the cyclic processes (Fig 3.10). This consistency in binding energies reaffirms the elemental composition and chemical states of Mn, Co, and Se, underscoring the material's stability throughout the charge-discharge cycles. In conclusion, our comprehensive spectroscopic analyses through XPS, XRD, and Raman spectroscopy collectively support and elaborate on the experimental observations. The minimal changes observed in these characterizations contribute to our understanding of the mechanisms behind the impressive 68 % capacitance retention, affirming the robustness and stability of the $\text{Co}_{0.01}\text{Mn}_{0.99}\text{Se}$ electrode under extended cycling conditions.

Table 3.3. List of comparable electrochemical performances of the $\text{Co}_{0.01}\text{Mn}_{0.99}\text{Se}$ with the literature

Electrode material	C_s /F. g^{-1}	Scan rate / mVs^{-1}	Current density/ Ag^{-1}	Method of synthesis	Cyclic stability/ cycles	References
$\text{Co}_{0.01}\text{Mn}_{0.99}\text{Se}$	421	5	-	Hydrothermal method	68 % (5000)	This work
MnSe	184.92	-	0.1	Electrodeposition	-	(Raman et al. 2019)
α -MnSe nanoparticle	96.76	-	0.1 mA/cm^2	Hydrothermal method	103.4 % (2000)	(Sahoo et al. 2018)
α -MnSe Nanosheets	88.3 mAh/g	-	1	Hydrothermal method	-	(Miao et al. 2021)
MnSe@NF	325.6 mAh/g		2	Hydrothermal method	96.8 % (15000)	(Ameri et al. 2021)
α -MnSe nanoflowers	200		1	Solvothermal method	97.15 % (5000)	(Javed et al. 2020b)
$\text{MnSe}_2\text{-CoSe}_2$	373		1	Hydrothermal method	95.8 % (5000)	(Vidhya et al. 2021)
MnSe_2/rGO	326		1.5	Hydrothermal method	99.94 % (10000)	(Sajjad et al. 2021)

Consequently, every electrochemical analysis conducted on the $\text{Co}_{0.01}\text{Mn}_{0.99}\text{Se}$ material highlights its superiority as a material for supercapacitors, firmly establishing it as a potent candidate. Furthermore, the electrode has demonstrated commendable performance relative to the literature-reported values, as delineated in Table 3.3.

3.3.10 Electrochemical performance of symmetric supercapacitor

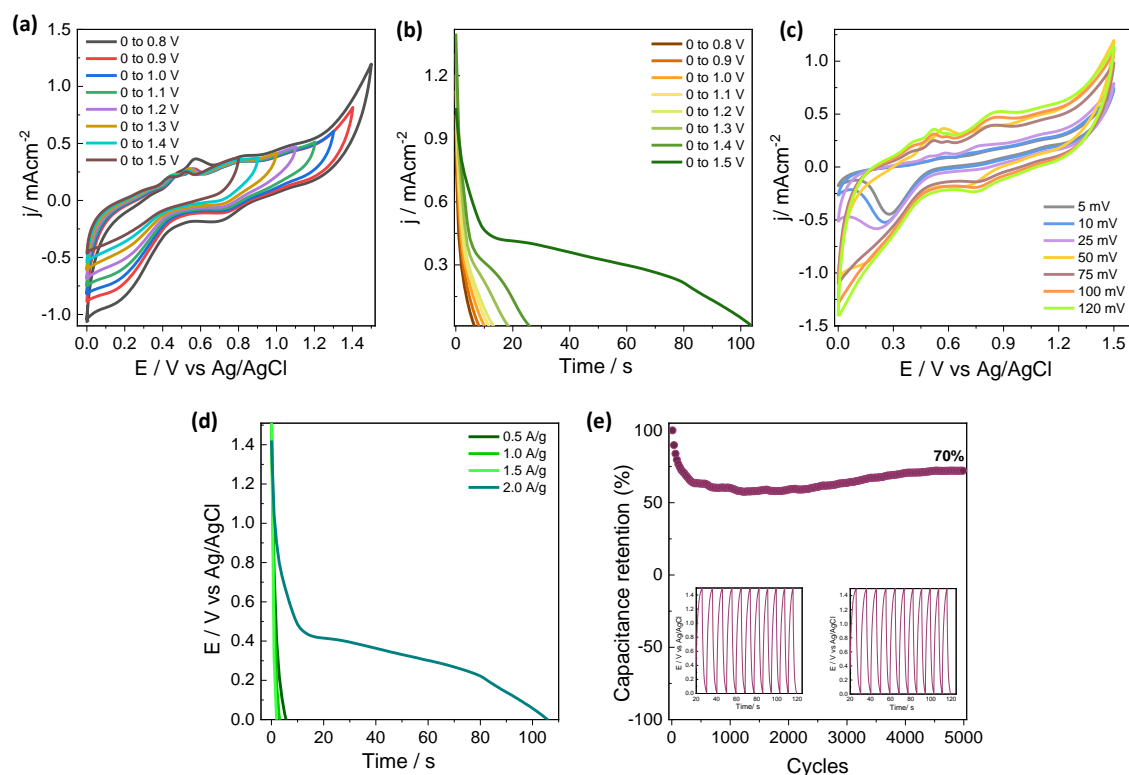


Figure 3.15. (a & b) CV and GCD of symmetric supercapacitor of $\text{Co}_{0.01}\text{Mn}_{0.99}\text{Se}$ with various potential windows. (c) CV of symmetric supercapacitor at various scan rates. (d) GCD of symmetric supercapacitor at different current densities. (e) Cyclic stability of symmetric supercapacitor after 5000 GCD cycles with the inset showing the first and the last ten GCD cycles respectively.

A two-electrode symmetric configuration was established using $\text{Co}_{0.01}\text{Mn}_{0.99}\text{Se}$ as the active material and 5 M KOH as the electrolytic solution. The optimization of the symmetric cell voltage involved CV and GCD assessments across a spectrum of cell voltages ranging from 0.8 to 1.5 V at a scan rate of 50 mV/s and a current density of 0.5 A/g (Velayutham et al. 2021b). The resultant CV and GCD profiles indicated a faradaic nature up to 1.5 V, as depicted in Fig 3.15 (a&b). Fig 3.15 (c) showcased the CV of the symmetric cell for diverse scan rates 5, 10, 25, 50, 75, 100 and 120 mV/s. The CV patterns exhibited a redox profile, confirming the prevalence of pseudocapacitance in the device. Additionally, the GCD test was conducted at different current densities 0.5, 1, 1.5, 2 A/g, revealing nearly symmetrical non triangular profiles that suggest excellent electrochemical reversibility and validate the pseudocapacitive nature of the device as shown in Fig 3.15 (d). The specific capacitance values were determined using Eq. (1.7), with the

maximum specific capacitance reaching 73 F/g at 0.5 A/g. To evaluate long-term cyclic stability, the fabricated device underwent 5,000 consecutive GCD cycles at a current density of 1 A/g, demonstrating remarkable capacitance retention of 70 % even after 5,000 cycles, as illustrated in Fig 3.15 (e). The maximum energy density found to be 20.44 Wh/kg at a power density of 700.9 W/kg and the maximum power density was calculated to be 2838 W/kg at an energy density of 2 Wh/kg. The comparative energy and power density values with similar literature is given in Table 3.4.

Table 3.4. Comparison of energy density and power density of the symmetric supercapacitor with the similar literature.

Two electrode assembly	Synthesis method	Electrolyte	Energy density (Wh/kg)	Power density (W/kg)	References
Co_{0.01}Mn_{0.99}Se //Co_{0.01}Mn_{0.99}Se	Hydrothermal method	5 M KOH	20.44	700.9	This work
MoS ₂ /GF//AEG	Hydrothermal method	6 M KOH	16	758	(Masikhwa et al. 2017)
NaMnO ₂ //AC	Ball milling	0.5 M Na ₂ SO ₄	19.5	130	(Liu et al. 2014)
TiO ₂ //CNT	Hydrothermal reaction	1 M LiPF ₆	12.5	300	(Wang et al. 2006)
MnO ₂ //Graphene hydrogel	Electro-deposition	0.5 M Na ₂ SO ₄	23.2	1000	(Gao et al. 2012)
CoS//AC	solvothermal method	PVA/KOH	5.3	1800	(Subramani et al. 2017)
Carbon spheres/MnO ₂ //Carbon spheres	Self-reaction deposition	1M Na ₂ SO ₄	22.1	100	(Lei et al. 2012)

Graphite //La ₂ Se ₃	chemical-bath deposition method	2 M KOH	2.14	265	(Patil et al. 2015)
Co _{0.85} Se//AC	Hydrothermal method	2 M KOH	17.8	3.57 k	(Zhao et al. 2017b)
Co _{0.85} Se//N- PCN	solvothermal method	2 M KOH	21.1	400	(Peng et al. 2015)

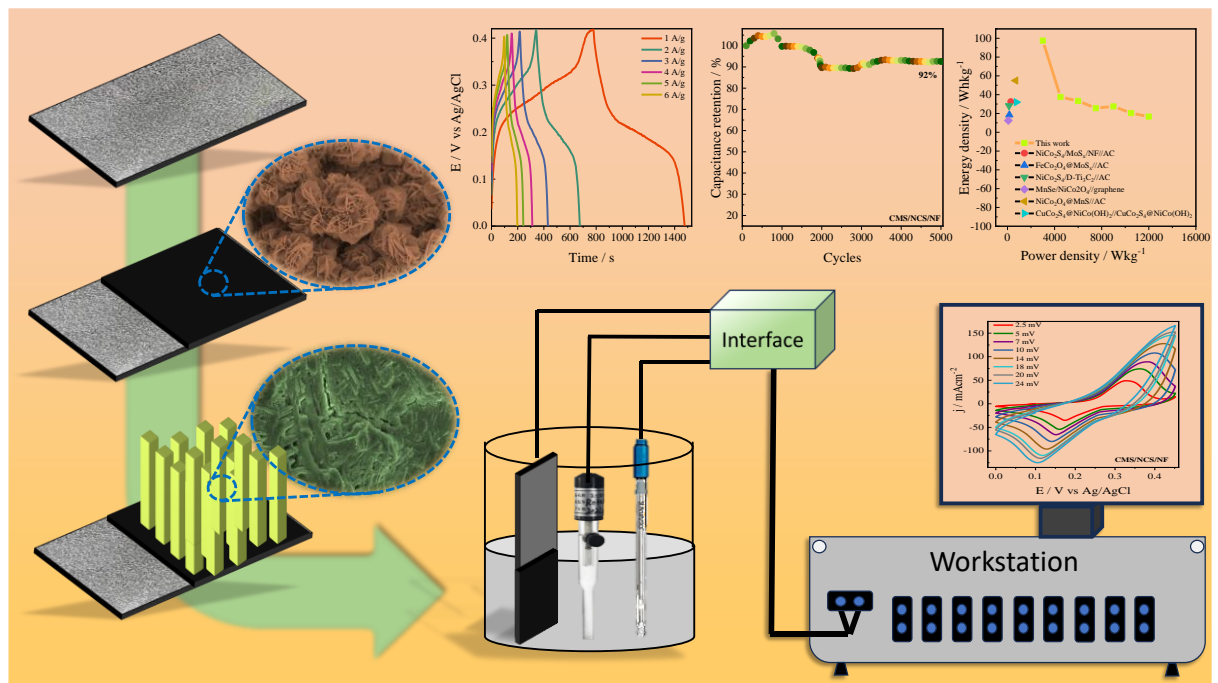
The synergistic influence of cobalt doping on MnSe has endowed Co_{0.01}Mn_{0.99}Se with an elevated specific capacitance value, heightened rate capability, and enhanced cycle stability. This substantiates the feasibility, practicality, and advantages of the employed method, affirming its potential for broader applications.

3.4 CONCLUSIONS

In summary M_xMn_{1-x}Se (M= Co / Ni / Zn, x = 0.0, 0.01, 0.02, and 0.03) were synthesized, fabricated electrodes were subjected to electrochemical studies to find the optimal active electrode. These composites have undergone in-depth characterization to elucidate their intricate structures and properties. The crystalline nature, high surface area, and lower solution and charge-transfer resistances with the unique morphology, could be the reasons for Co_{0.01}Mn_{0.99}Se to exhibit superior electrochemical properties compared to other materials. Therefore, Co_{0.01}Mn_{0.99}Se delivered maximum specific capacitance of 421 F/g at 5 mV/s and 377 F/g at 1 A/g. A two-electrode symmetric setup was developed, employing Co_{0.01}Mn_{0.99}Se as the active material in a 5 M KOH electrolyte. This configuration demonstrated a noteworthy specific capacitance of 73 F/g at 0.5 A/g. Impressively, it achieved maximum energy density and power density values of 20.44 Wh/kg and 2838 W/kg respectively. Additionally, the assembly demonstrated high capacitance retention of 70 % after 5000 charge-discharge cycles. Consequently, the acquired results shed light on the functions of transition metal doping in nano MnSe, which could be helpful for the material's future advancement in supercapacitor applications.

CHAPTER 4

TWO STEP ELECTRODEPOSITION SYNTHESIS OF $\text{CoMnS}/\text{NiCo}_2\text{S}_4$ NANOCOMPOSITE FOR HIGH PERFORMANCE SYMMETRIC SUPERCAPACITOR



***Abstract:** This chapter involves the nanocomposite CoMnS/NiCo₂S₄/NF (CMS/NCS/NF) synthesized through a two-step electrodeposition method and studies its application in supercapacitors.*

4.1 INTRODUCTION

Electrode materials with multiple oxidation states or structures capable of facilitating numerous redox reactions are particularly desirable for enhancing pseudocapacitance in supercapacitors. Transition metal chalcogenides are emerging as promising materials for the future, owing to their remarkable optical, electrical, magnetic, and transport properties (Raman et al. 2019). Consequently, transition metal chalcogenides are gaining recognition as leading candidates for high-performance energy storage devices. Among the various transition metal chalcogenides, transition metal sulfides such as MnS, MoS₂, WS₂, Ni₃S₂, CoS, and CuS stand out as superior electrode materials, boasting superior electrical conductivity compared to oxides. Their ability to accommodate multiple oxidation states enhances redox reactions, making them highly suitable for energy storage applications. Compared to metal oxides, metal sulfides have a weaker M-S bond, making them more kinetically favourable. This enhances their redox reversibility (Melkiyur et al. 2023; Zhu et al. 2018). However, single-element metallic sulfides can experience rapid capacitance decay over prolonged cycles, limiting their utility in electrochemical energy storage devices (Meng et al. 2016; Wei et al. 2022).

Composite materials such as ZnS/FeS (Javed et al. 2021), CuS/MnS (Zhai et al. 2019), CoFeS₂ (Zhang et al. 2017) typically demonstrate superior electrochemical properties compared to individual components. These composites harness the strengths of multiple materials, integrating them into a structured arrangement to mitigate the shortcomings observed in single-material configurations (Song et al. 2020). Previous studies have shown that binary Cobalt Manganese Sulfide (CoMnS) have an increased redox activity, superior mechanical and thermal stability and possess higher specific capacitance than their respective monometal sulfides. The improved electrochemical properties of CoMnS (CMS) can be attributed to their higher theoretical specific capacitance and remarkable electronic conductivity, which can reach values as high as 3.2×10^3 S/cm (Chen et al. 2016a; Tue et al. 2023; Wang et al. 2012c). Meanwhile Ni and Co, known for their plentiful valence electrons, demonstrate effective electrocatalytic activity, particularly in energy storage devices such as supercapacitors. Specifically, NiCo₂S₄ (NCS) demonstrates enhanced

faradaic behaviour compared to its monometallic sulfide counterparts like NiS and CoS (Bulakhe et al. 2016; Dai et al. 2015; Shim 2015) and exhibits superior electrical conductivity relative to the bimetallic NCS (Zhu et al. 2015).

Despite their individual merits, each of these materials possesses inherent limitations that could potentially hinder their widespread application. To address these challenges and synergize the benefits of both materials, we have synthesized a novel composite material comprising CMS and NCS. The rationale behind this composite design lies in leveraging the complementary properties of Mn and Co sulfides with the electrochemical activity of NCS to find more possible breakthroughs. This approach is supported by existing literature, where various composite materials such as NiCo₂S₄/MoS₂ (Tue et al. 2023), NiCo₂S₄/MnO₂ (Shim 2015), NiCo₂O₄/MnSe (Raman et al. 2019), and NiCo₂O₄/MnS (Liao et al. 2024) have been successfully synthesized and demonstrated enhanced electrochemical performance. These composite materials capitalize the synergistic effects of combining different metal sulfides, resulting in improved specific capacitance, cycling stability, and rate capability.

In this study, we developed a binder-free CoMnS/NiCo₂S₄ (CMS/NCS) composite through a two-step electrodeposition method. Initially, CMS was electrodeposited onto a Nickel foam (NF) substrate. Subsequently, a thin layer of NCS was electrochemically deposited over the CMS layer, to form CMS/NCS/NF. This approach aimed to enhance the surface area of the substrate, improve the specific capacitance, and enhance the material's stability. Directly growing transition metal sulfides on a NF eliminates the need for conductive additives or polymer binders. This method ensures better electrical contact with the substrate, potentially improving the electrode's performance. We assessed the potential of the CMS/NCS/NF composite as an electrode material for supercapacitors. Our findings revealed that the CMS/NCS/NF composite demonstrated an impressive specific capacitance of 1676 F/g at a current density of 1 A/g. To further understand the synergistic effects of this composite material, we fabricated a symmetric supercapacitor. Following electrochemical characterizations, we analyzed the capacitive and diffusive contributions using Dunn's model. The devices exhibited high energy and power densities along with remarkable rate capability, indicating the material as a promising electrode in the application of supercapacitors.

4.2 EXPERIMENTAL

4.2.1 Materials

Manganese chloride tetrahydrate ($\text{MnCl}_2 \cdot 4\text{H}_2\text{O}$), cobalt chloride hexahydrate ($\text{CoCl}_2 \cdot 6\text{H}_2\text{O}$), nickel nitrate hexahydrate ($\text{Ni}(\text{NO}_3)_2 \cdot 6\text{H}_2\text{O}$), thiourea were bought from Loba Chemie. NF was bought from Global Nanotech, Mumbai, India. We prepared the solutions using high-quality Ultrapure Milli-Q water to maintain solvent purity. All commercially sourced materials were of exceptional purity and used directly without the need for further purification

4.2.2 Electrodeposition of CoMnS (CMS)/NF

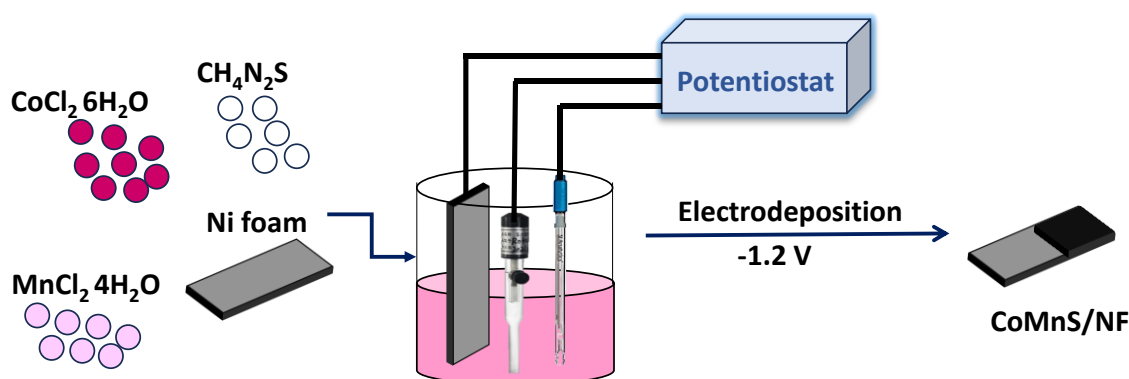


Figure 4.1. Schematic diagram for the electrodeposition of CoMnS (CMS) on Nickel foam.

At first, the NF was cleaned with Milli Q water and ethanol, then soaked in a 3 N HCl solution, sonicated, washed with Milli Q water and acetone, finally dried at 60°C for 1 h. The CoMnS (CMS) composite was synthesized through one step electrodeposition method using a freshly prepared solution. Initially, a solution was prepared by dissolving 0.025 M of $\text{CoCl}_2 \cdot 6\text{H}_2\text{O}$, 0.025 M of $\text{MnCl}_2 \cdot 4\text{H}_2\text{O}$, and 0.1 M of $\text{CH}_4\text{N}_2\text{S}$ in 300 mL of Milli Q water. The solution was rigorously stirred for ten min to ensure complete dissolution of the solutes. Electrodeposition was carried out using a three-electrode setup, wherein a cleaned NF served as the working electrode, platinum electrode acted as the counter electrode and Ag/AgCl electrode was employed as the reference electrode. Chronoamperometry was employed as the electrochemical technique with a deposition potential of -1.2 V applied for a duration of 300 s (Fig 4.1). Post-electrodeposition, the synthesized composite was thoroughly rinsed with Milli Q water and ethanol to remove any residual electrolyte and impurities. Subsequently, the material was subjected to calcination at 350°C to enhance its

crystallinity and structural integrity. The resultant CMS/NF composite was then carefully collected for further characterization and application.

4.2.3 Electrodeposition of NiCo₂S₄ (NCS) on CoMnS (CMS)/NF

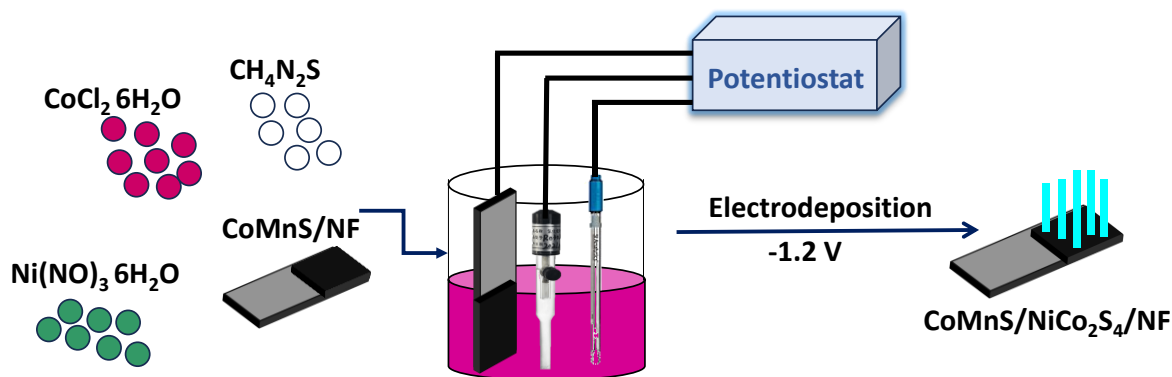


Figure 4.2 Schematic diagram for the electrodeposition of NiCo₂S₄ (NCS) on CoMnS (CMS)/NF

The NiCo₂S₄ (NCS) was electrodeposited onto the pre-synthesized CMS/NF substrate using a prepared solution. Initially, a solution was formulated by dissolving 0.025 M of Ni(NO₃)₂·6H₂O, 0.05 M of CoCl₂·6H₂O, and 0.1 M of CH₄N₂S in 100 mL of Milli-Q water. The solution was stirred rigorously to ensure complete dissolution of the constituents. Electrodeposition was carried out using the previously described three-electrode setup with CMS/NF composite served as the working electrode. Chronoamperometry was adopted as the electrochemical technique, with a deposition potential of -1.2 V applied for a duration of 300 s using the prepared solution (Fig 4.2). Following electrodeposition, the material was carefully removed from the electrode and subjected to sequential rinsing steps with Milli-Q water and ethanol to eliminate any residual electrolytes and impurities. Subsequently, the electrodeposited material underwent calcination at 250°C and collected. The coated material weighed 4.2 mg. The CMS/NF and NCS/NF were synthesized individually using the same procedure mentioned above to compare their electrochemical performance with the composite material.

4.2.4 Materials Characterization Techniques

Surface morphology and elemental composition were examined using a Jeol 7610 FPLUS field-emission scanning electron microscope. High-resolution transmission electron microscopy was conducted using a Jeol JEM 2100 Plus instrument. X-ray diffraction analyses were performed with an Empyrean 3rd Gen instrument from Malvern PANalytical,

utilizing monochromatic Cu-K α radiation with a wavelength of 0.154 nm. X-ray photoelectron spectroscopy data were acquired using a Thermo Fischer Scientific ESCALAB Xi+ with an Al K-alpha X-ray source (1486.7 eV).

4.2.5 Electrochemical characterisation

The Autolab PGSTAT204 electrochemical workstation is employed for the electrochemical properties of the prepared electrodes. Employing a sophisticated three-electrode setup, the CMS/NCS/NF act as a working electrode, a platinum electrode as a counter electrode, while Ag/AgCl serves as the reference electrode. This detailed configuration serves as the basis for precise electrochemical investigations. The CV analyses were conducted over a potential window of 0.0-0.45 V vs. Ag/AgCl, with scan rates varying from 2.5-24 mV/s. Furthermore, GCD tests were performed across different current densities ranging from 1-6 A/g, utilizing a potential range of 0.0-0.42 V. The EIS was carried out over a frequency range of 1-100 kHz at zero-bias voltage. Electrochemical Active Surface Area (ECSA) was carried out for various scan rates from 5-50 mV/s. The ECSA is calculated using the Eq.(3.1) (Junita et al. 2023; Kim et al. 2020). The specific capacitance (C_s) for the three-electrode setup was determined from the GCD measurements using the Eq. (1.6).

A symmetrical supercapacitor cell was meticulously assembled using the most promising sample via a three-electrode configuration. The electrodes were prepared following the same procedure as for the three-electrode system, resulting in an electrode mass of 5 mg. The cell was immersed in a 5 M KOH electrolyte for electrochemical analysis. To comprehensively assess the electrochemical performance of the cell, CV experiments were carried out over a potential range of 0-1.5 V at scan rates from 5-100 mV/s. Additionally, GCD studies were conducted at various current densities, spanning from 1.0-5.0 A/g, within a potential window of 0.0-1.5 V. The energy density (E (Wh/kg)) and power density (P (W/kg)) are determined using Eqns (1.8) and (1.9).

4.3 RESULTS AND DISCUSSIONS

4.3.1 XRD analysis

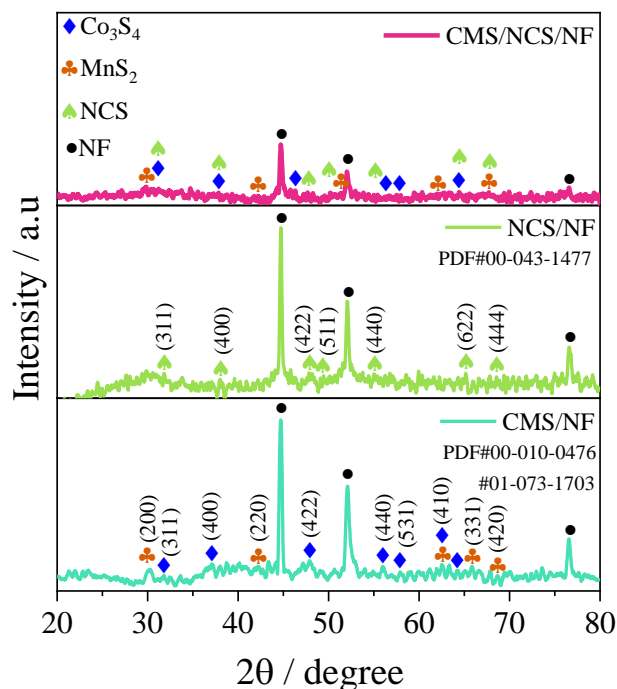


Figure 4.3. XRD of CMS/NF, NCS/NF, and CMS/NCS/NF.

The interpretation of diffraction patterns is crucial for identifying the phases present in synthesized materials and evaluating their degree of crystallinity. Displayed in Fig 4.3 are the XRD patterns of CMS/NF, NCS/NF, and their composite CMS/NCS/NF. CMS/NF exhibits moderate crystallinity, indicated by somewhat broader peaks, suggesting partially amorphous nature. The detected phases of MnS₂ and Co₃S₄ correspond to JCPDS Card Nos. 010-0476 and 073-1477, respectively. The XRD pattern of NCS/NF shows broader peaks and reduced crystallinity, aligning with the NCS phase as identified by JCPDS Card No. 043-0477. For the composite CMS/NCS/NF, the XRD pattern reveals the characteristic peaks of MnS₂, Co₃S₄, and NCS. And the peaks at 44°, 51°, 76° corresponds to the NF. This confirms the successful formation of the composite material, indicating that the individual components have been effectively combined while maintaining their crystalline characteristics.

4.3.2 ECSA and EIS analysis

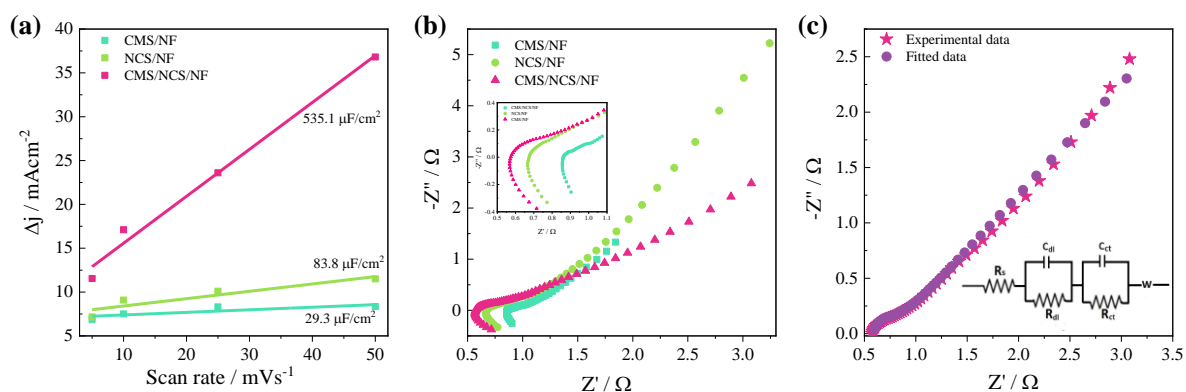


Figure 4.4. (a) ECSA of CMS/NF, NCS/NF, and CMS/NCS/NF; (b) Nyquist plot of CMS/NF, NCS/NF, and CMS/NCS/NF; (c) equivalent circuit fitted with nyquist plot of CMS/NCS/NF.

The plot in Fig 4.4 (a) shows Δj ($j_a - j_c$) plotted against the scan rate, focusing particularly on the non-faradaic region. This analysis aims to determine the electrochemically active surface area (ECSA) of the electrode. The slope of this plot provides the $2C_{dl}$ value (double layer capacitance). The C_{dl} values for CMS/NF, NC/SNF, and NCS/CMS/NF were found to be 14.65 $\mu\text{F}/\text{cm}^2$, 41.9 $\mu\text{F}/\text{cm}^2$, and 267.55 $\mu\text{F}/\text{cm}^2$ respectively. This led to corresponding real surface areas of 0.366 cm², 1.04 cm², and 6.68 cm² for CMS/NF, NCS/NF, and CMS/NCS/NF respectively. Notably, the CMS/NCS/NF combination exhibited the highest surface area at 6.68 cm², indicating a greater concentration of active sites compared to CMS/NF and NCS/NF individually (Kim et al. 2020).

The Nyquist plots depicted in Fig 4.4 (b) for CMS/NF, NCS/NF, and CMS/NCS/NF demonstrate a small semicircular pattern in the high-frequency range followed by a linear trend in the low-frequency range. The Nyquist plot of CMS/NCS/NF has been fitted with the equivalent circuit as shown in Fig 4.4 (c).

Table 4.1. EIS parameters for the fitted circuit.

Samples	R_s (Ω)	C_{dl} (F)	R_{dl} (Ω)	C_{ct} (F)	R_{ct} (Ω)	W (Ω)
CMS/NCS/NF	0.5666	0.0011	0.1249	0.0156	0.0565	0.1225
CMS/NF	0.6918	0.0056	0.2297	0.1336	6.981	0.0743
NCS/NF	0.8753	0.2345	1.649	0.0111	0.0959	0.4284

The electrochemical parameters obtained from Table 4.1 indicate that the R_s for CMS/NF, NCS/NF, and CMS/NCS/NF are 0.6918 Ω , 0.8753 Ω , and 0.5666 Ω , respectively, while the R_{ct} value for CMS/NCS/NF is 0.0565 Ω . Comparing the EIS data, it is evident that CMS/NCS/NF exhibits superior performance with the lowest R_s and R_{ct} values, indicating reduced internal resistance and improved charge transfer dynamics compared to CMS/NF and NCS/NF. This mitigates voltage drop, boosts energy delivery, and reinforces cycling endurance (Uke et al. 2020). Together, these factors may be responsible for the higher activity of CMS/NCS/NF electrode (Zhao et al. 2020).

4.3.3 CV and GCD analysis

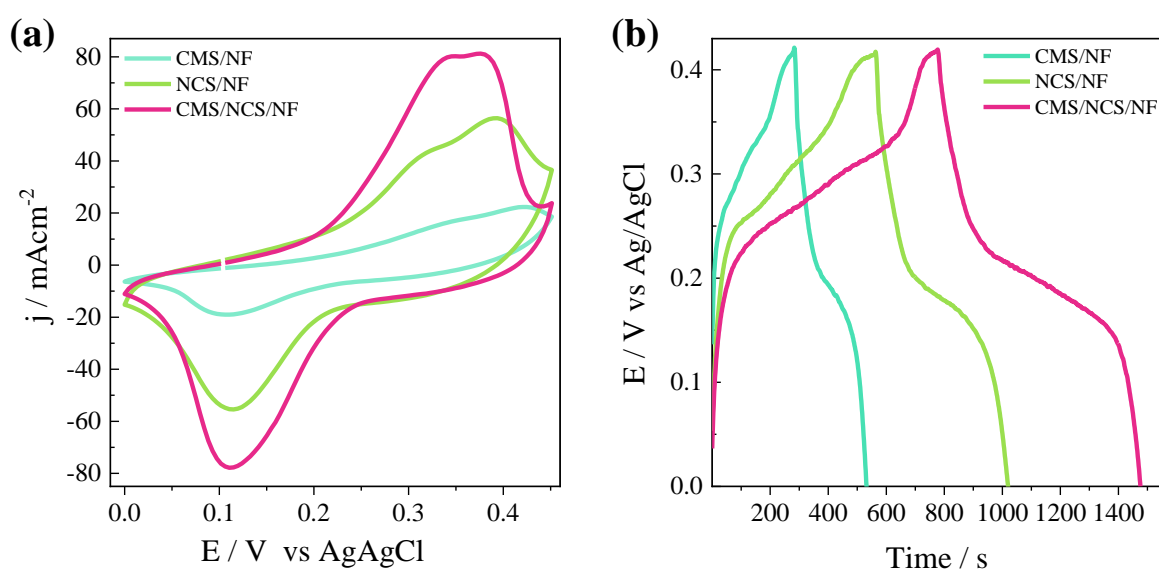


Figure 4.5. (a) CV of CMS/NF, NCS/NF, CMS/NCS/NF at 5mV/s; (b) GCD of CMS/NF, NCS/NF, CMS/NCS/NF at 1A/g.

The CV and GCD profiles of CMS/NF, NCS/NF, and CMS/NCS/NF at a scan rate of 5 mV/s and a current density of 1 A/g, respectively is shown in Fig 4.5 (a&b), facilitating a comparative electrochemical analysis. Upon comparison the CV graph, it is evident that the CMS/NCS/NF electrode exhibits a greater enclosed area under the CV curve, which indicates a greater capacity for storing charge. This suggests that the CMS/NCS/NF electrode has a higher specific capacitance compared to CMS/NF and NCS/NF electrode. The integral area enclosed by the CV curve is directly equivalent to the capacitance of the material, and in this case, it indicates that the CMS/NCS/NF electrode has superior charge storage capabilities (Vargheese et al. 2020). The CMS/NF, and NCS/NF display constrained redox peaks in contrast to the wider peaks observed in CMS/NCS/NF. This observation

suggests that the CMS/NCS/NF electrode possesses the highest specific capacity, as evidenced by its larger CV area. Additionally, Fig 4.5 (b) presents the GCD curves of CMS/NF, NCS/NF, and CMS/NCS/NF. Notably, the CMS/NCS composite demonstrates the longest discharge time, indicating its superior specific capacity. This observation aligns with the findings from the CV analysis in Fig 4.5 (a). The increase in specific capacitance for CMS/NCS/NF can be attributed to two main reasons. Firstly, the unique composite heterostructure of CMS/NF and NCS/NF augments the surface morphology of the prepared composite, consequently an increased number of sites are provided for substances to disperse and engage in the faradaic reactions. Furthermore, it facilitates the infiltration of electrolyte into the interfacial region between the electrode and other constituent materials. Secondly, the collaborative effect between NCS/NF and CMS/NF plays a significant role in enhancing the specific capacitance of the CMS/NCS/NF electrode and improving their electrical conductivity (Liao et al. 2024; Raman et al. 2019).

4.3.4 FESEM and EDS analysis

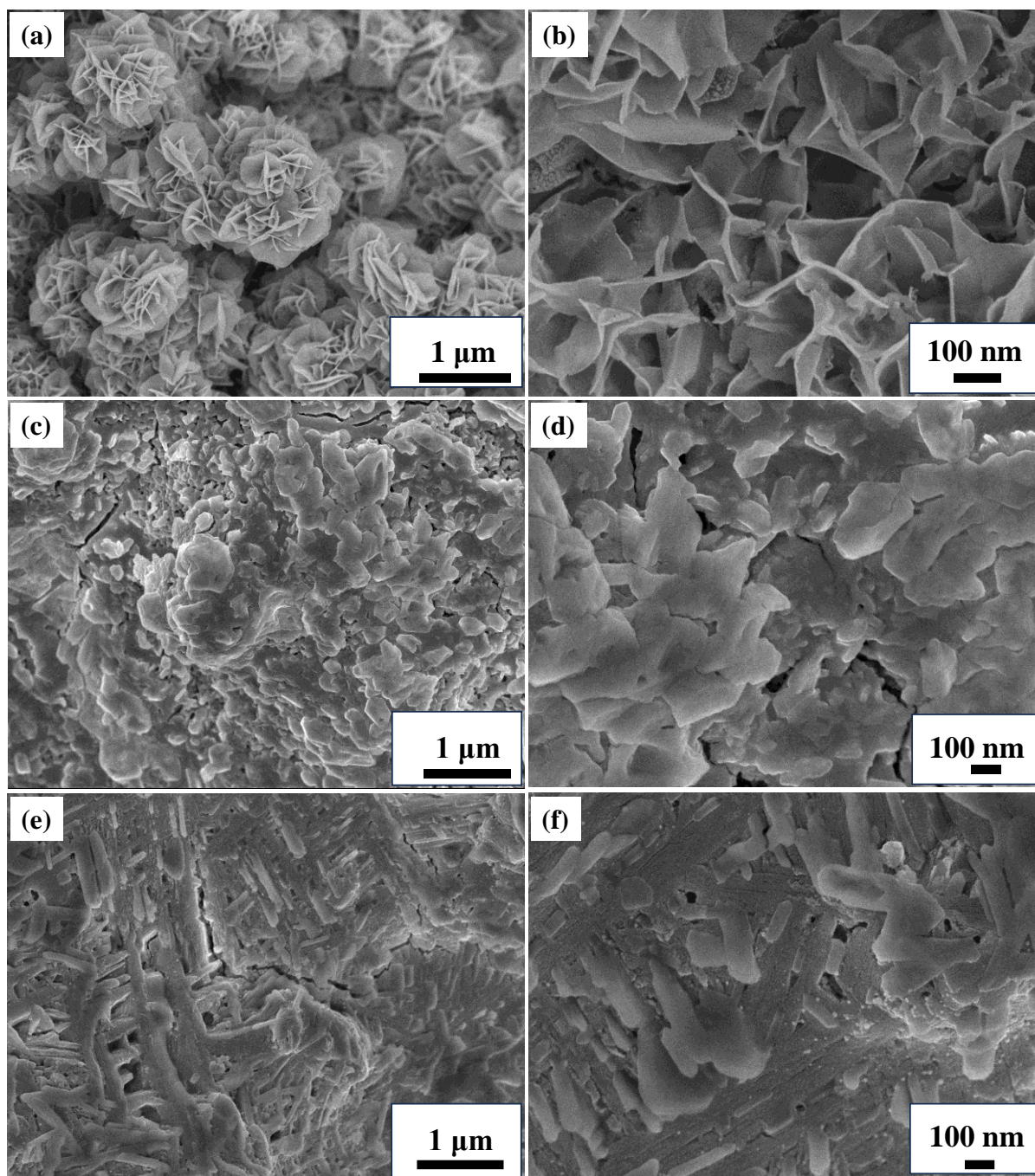


Figure 4.6. (a&b) FESEM images of CMS/NF; (c&d) FESEM images of NCS/NF; (e&f) FESEM images of CMS/NCS/NF.

The morphological characteristics of CMS/NF were obtained through FESEM images. In Fig 4.6 (a), at lower magnification, CMS/NF structures resemble intricate nanoflowers with noticeable petal-like protrusions. Upon closer scrutiny in Fig 4.6 (b), a deeper examination reveals the detailed organization of nanoflower clusters, where densely packed petals, each on the nanometre scale, intricately assemble to form the overall structure. The FESEM

images of NCS/NF (Fig 4.6 (c&d)) exhibit a markedly different morphology. They depict a random orientation of petaloid structures scattered across the surface of NCS/NF. These petaloids, appearing as irregularly shaped nanoscale features, contribute to the unique surface architecture of NCS/NF. Fig 4.6 (e&f) provide insight into the composite material, CMS/NCS/NF. The images unveil a distinct morphology characterized by nanostrip-shaped entities with irregular dimensions. These nanostrips are randomly distributed across the field of view, with instances of overlapping, indicating a complex and disordered arrangement. The presence of nanostrips in the composite structure offers several advantages for energy storage applications. Firstly, the high aspect ratio of nanostrips provides a large surface area, facilitating enhanced electrochemical reactions. Secondly, the interconnected network of nanostrips promotes efficient electron and ion transport, leading to improved charge/discharge kinetics (Lee et al. 2016). Overall, the intricate morphology of the CMS/NCS/NF composite, characterized by nanostrip structures, plays a crucial role in enhancing the energy storage performance by maximizing active material utilization and facilitating rapid charge transfer processes.

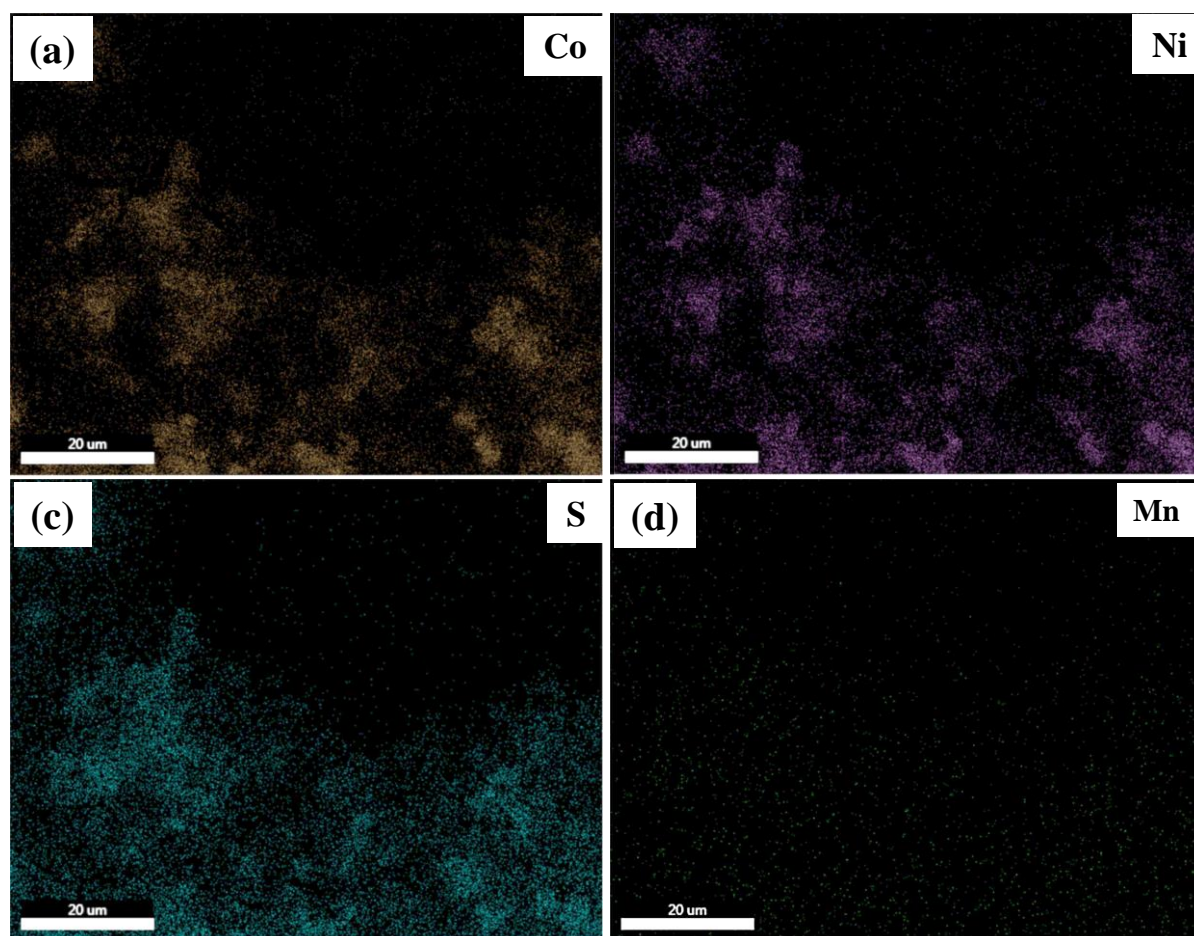


Figure 4.7. EDS mapping of CMS/NCS/NF: (a) Co; (b) Ni; (c) S; (d) Mn.

Energy Dispersive spectroscopy (EDS) proved to be an effective technique for analyzing the chemical composition of nanocomposites. The elemental distribution within CMS/NCS /NF was further examined using EDS mapping, as illustrated in Fig 4.7 (a-d). This figure revealed the existence of Co, Mn, Ni, and S elements in the sample. Also, it was confirmed that the elements Co, Mn, Ni, and S were dispersed within the heterojunction, demonstrating a close integration of CMS/NCS/NF.

4.3.5 TEM analysis

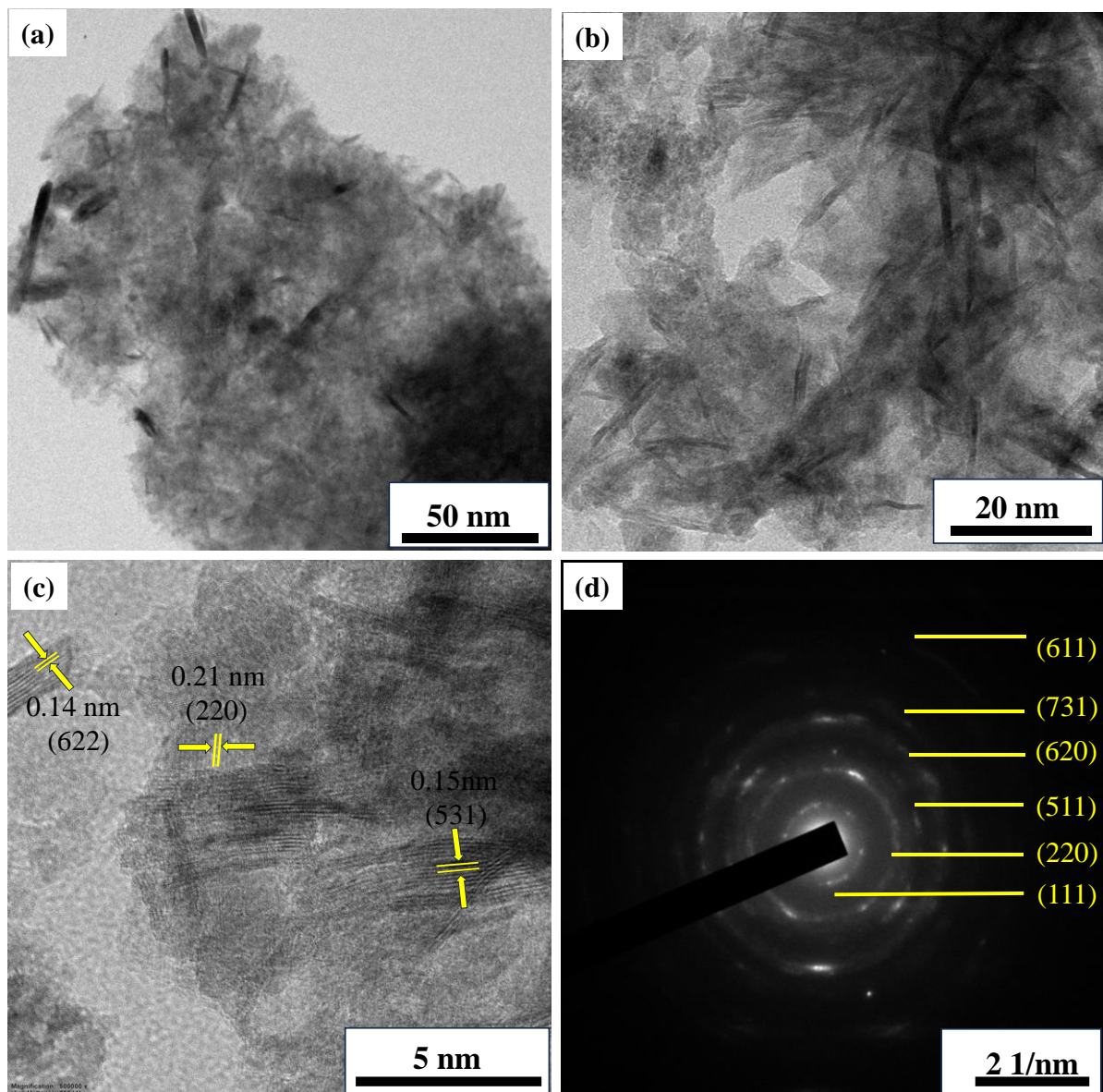


Figure 4.8. CMS/NCS: (a&b) TEM images; (c) HRTEM images; (d) SAED pattern

The TEM images depicted in the Fig 4.8 (a&b) at lower and higher magnification respectively reveal a nanostrip morphology, with various strips intertwined, forming a

network. This morphology is consistent with the results observed in the FESEM analysis (Fig 4.6 (e&f)). The average thickness of these nanostrips is measured to be 2.68 nm, indicating a mesoporous nature. The HRTEM image in Fig 4.8 (c) provides detailed lattice information. The spacing between planes for MnS_2 (220), NCS (622), and Co_3S_4 (531) are 0.21 nm, 0.14 nm, and 0.15 nm, respectively, as determined by XRD results. Furthermore, the selected area electron diffraction (SAED) pattern of CMS/NCS features diffraction rings elucidates a polycrystalline nature and correlates with the respective planes as shown in Fig 4.8 (d), corroborating the structural information obtained from XRD and HRTEM analyses.

4.3.6 XPS analysis

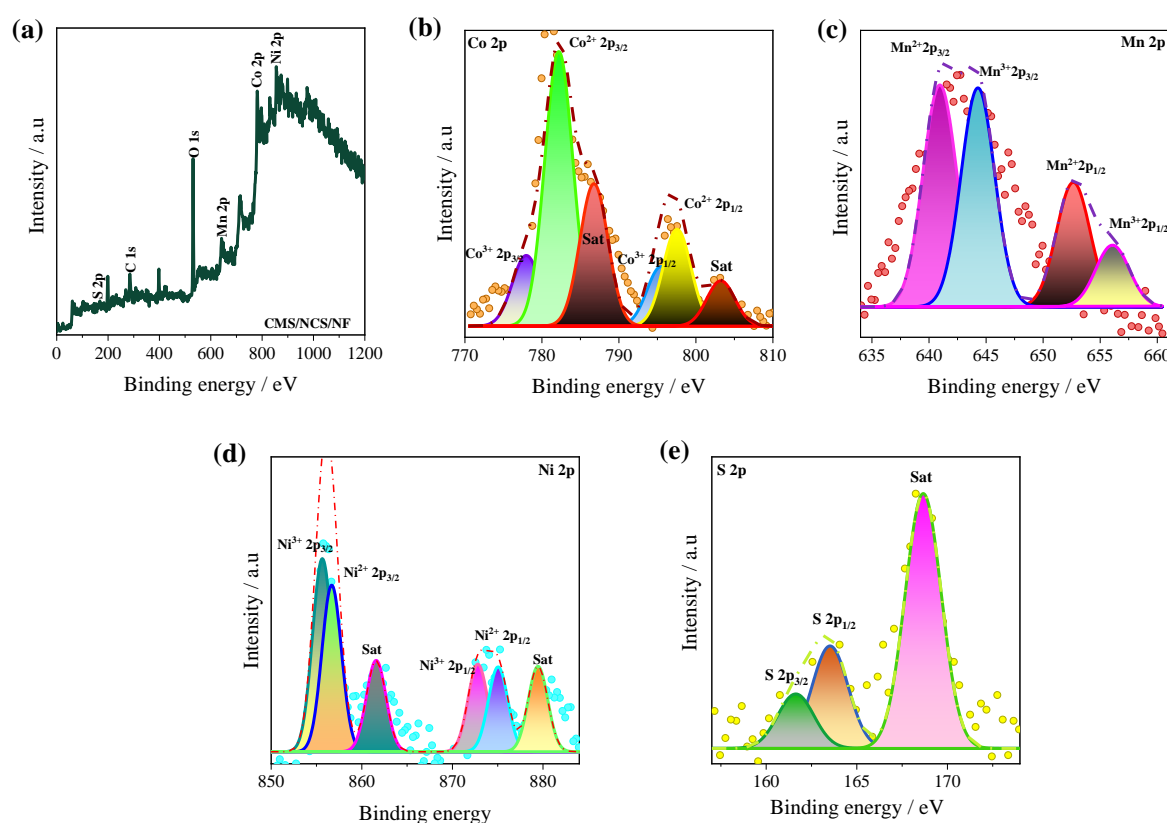


Figure 4.9. (a) XPS survey spectrum of CMS/NCS/NF; (b) XPS spectra of (b) Co 2p; (c) Mn 2p; (d) Ni 2p; (e) S 2p.

The elemental composition of CMS/NCS/NF was meticulously analyzed using XPS. The information in Fig 4.9 (a) clearly shows that the survey spectrum indicates the existence of Co 2p, Mn 2p, Ni 2p, and S 2p in the composite material. In Fig 4.9 (b), peaks corresponding to binding energies 779.9 eV and 782.2 eV, are associated with Co^{3+} $2p_{3/2}$ and Co^{2+} $2p_{3/2}$, respectively. Additionally, peaks at 795.3 eV and 797.5 eV correspond to

$\text{Co}^{3+} 2p_{1/2}$ and $\text{Co}^{2+} 2p_{1/2}$, respectively. This observation elucidates the coexistence of Co^{3+} and Co^{2+} species. The satellite peaks at 786.7 eV and 803.1 eV can be assigned to Co^{3+} and Co^{2+} respectively (Ma et al. 2020c; Wang and Zhang 2017). The Mn 2p spectrum (Fig 4.9 (c)) displays peak positions at 640.8 eV and 652.6 eV, signifying the occurrence of Mn^{2+} in the nanomaterial. Additionally, two peaks at 644.2 eV and 655.96 eV correspond to Mn^{3+} (Quan et al. 2016; Sambasivam et al. 2021). In Fig 4.9 (d), the peaks observed at 855.5 eV and 856.68 eV correspond to $\text{Ni}^{3+} 2p_{3/2}$ and $\text{Ni}^{2+} 2p_{3/2}$, respectively. Additionally, peaks at 872.6 eV and 874.9 eV are associated with $\text{Ni}^{3+} 2p_{1/2}$ and $\text{Ni}^{2+} 2p_{1/2}$, respectively. This indicates the occurrence of both Ni^{3+} and Ni^{2+} ions (Huang et al. 2019; Wu et al. 2021b). Additionally, two satellite peaks at 861.46 eV and 879.54 eV are attributed to the characteristic peaks of Ni $2p_{3/2}$ and Ni $2p_{1/2}$, respectively (Chang et al. 2018b). In Fig 4.9 (e), a peak is observed at 162.2 eV, accompanied by the leading peak at 163.4 eV, in the S 2p spectrum. These peaks are coordinating with the S $2p_{3/2}$ and S $2p_{1/2}$ orbitals, respectively. The emergence of a peak at 168.5 eV within the S 2p spectrum suggests the transition from sulfide ions to sulfate. This change is presumably due to the oxidation reaction happening at the material's surface. The XPS data additionally verifies the effective creation of CMS/NCS/NF (De et al. 2017; Huang et al. 2017; Yan et al. 2018).

4.3.7 Electrochemical performance of CMS/NCS/NF

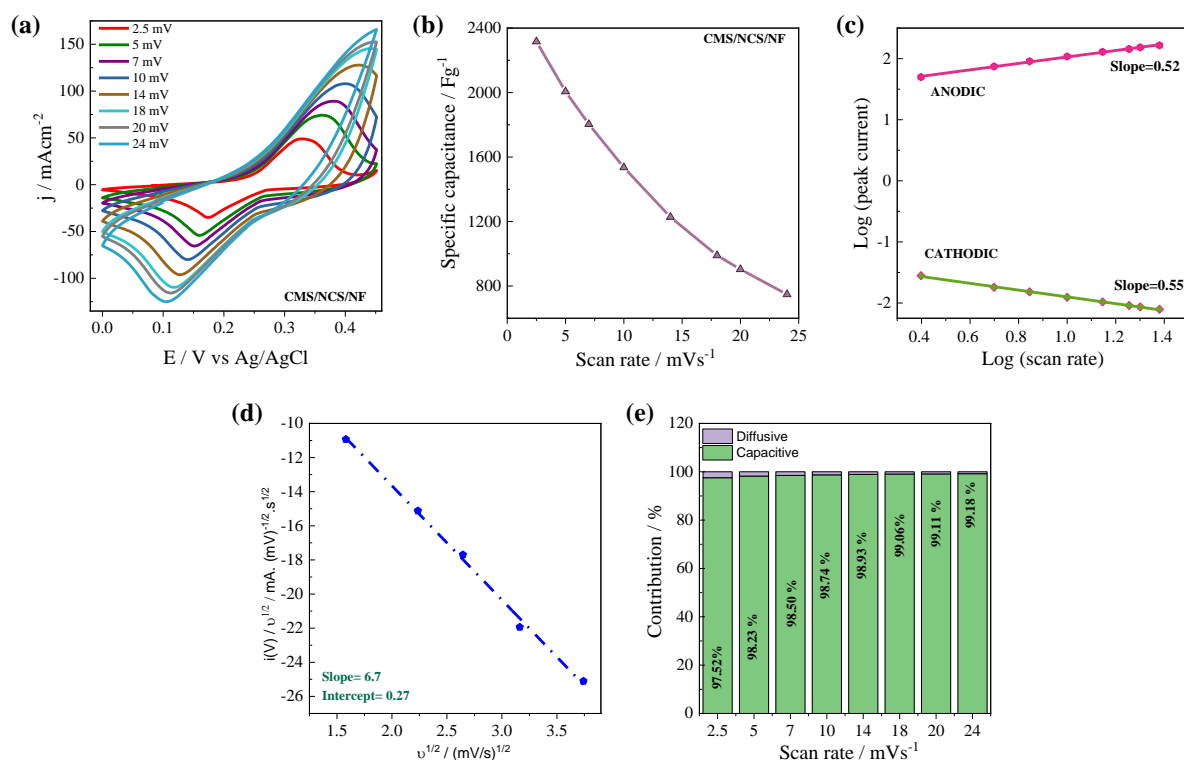
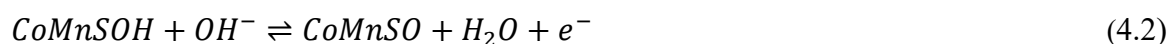


Figure 4.10. (a) CV of CMS/NCS/NF at various potential scan rates; (b) Graph of variation between specific capacitance versus scan rate of CMS/NCS/NF; (c) Plot of log (peak current) versus log(scan rate) of CMS/NCS/NF; (d) Plot of $v^{1/2}$ versus $i(V)/v^{1/2}$; (e) Capacitive and diffusive contribution of CMS/NCS/NF at various sweep rates.

When observing the CV curves of the CMS/NCS/NF electrode in a KOH solution at different scan rates (Fig 4.10 (a)), we can see a set of reversible redox peaks. These peaks are unique to the electrode and are believed to be caused by the faradaic redox reactions described by the following equations (Liao et al. 2024; Raman et al. 2019).



With an increase in scanning speed, cathodic peak of the CV moves towards a more negative voltage, whereas the anodic peak moves towards a more positive voltage. This phenomenon arises from increased polarization at higher scanning rates (Huo et al. 2014). The CV curves also illustrate a gradual increase in current density as the scan rates range

from 2.5 mV/s to 24 mV/s, maintaining a stable potential window of 0.0-0.45 V. Significantly, the system demonstrates strong stability and reversibility, as evidenced by the consistent and symmetrical CV curves, even when subjected to increased scanning speeds. This observation underscores the effectiveness of the CMS/NCS/NF structure in maintaining its performance under varying conditions. Nevertheless, despite the high current density, the specific capacitance diminishes at higher scan rates as shown in Fig 4.10 (b). This decline is attributed to the sluggish kinetics of redox reactions under increased current densities (Sahoo et al. 2017).

To deepen our comprehension of the charge storage mechanism, an extensive inquiry has been conducted into the interplay between current and potential sweep rate. In essence, the Eq. (3.4) described in the previous chapter elucidates the connection between peak current and scan rate. To determine the value of parameter “b” from the Eq. (3.4), we plotted CV data as a log i versus log v graph, which is displayed in Fig 4.10 (c). The plot slope enables the determination of the b value. If the “b” value equals 1, it indicates the current is influenced by capacitive processes, whereas a “b” value of 0.5 points to the current being directed by diffusion-limited processes.

After analyzing the graph, we found that the “b” values for the anodic peak and the cathodic peak were 0.52 and 0.55, respectively. This suggests that the system is diffusion-controlled (Zardkhoshoui and Davarani 2020a). When dealing with complex systems that have multiple charge storage mechanisms, researchers usually assume that the peak current results from both capacitive processes, such as the electrical double layer or outer surface, and diffusion-limited processes, like the inner surface (Manikandan et al. 2021) which can be explained using the equations described in the previous chapter (Eqns 3.5 and 3.6). To unveil their interplay, we plotted $i(V)/v^{1/2}$ versus $v^{1/2}$ (Fig 4.10 (d)) at a specific potential, extracting “c” from the slope and “d” from the y-intercept (Manikandan et al. 2021; Mondal et al. 2021). Across scan rates from 2.5 to 24 mV/s, the CMS/NCS/NF electrode displayed a surface-controlled contributions. At lower scan rates, only 2.4 % of charge storage occurs through diffusion, with the majority being surface-controlled. This behaviour persists across different scan rates, where surface-controlled reactions increase while the diffusive nature decreases (Fig 4.10 (e)). Therefore, the material primarily relies on surface-controlled mechanisms for charge storage, with minimal contribution from diffusive processes, even at lower scan rates (Raman et al. 2019).

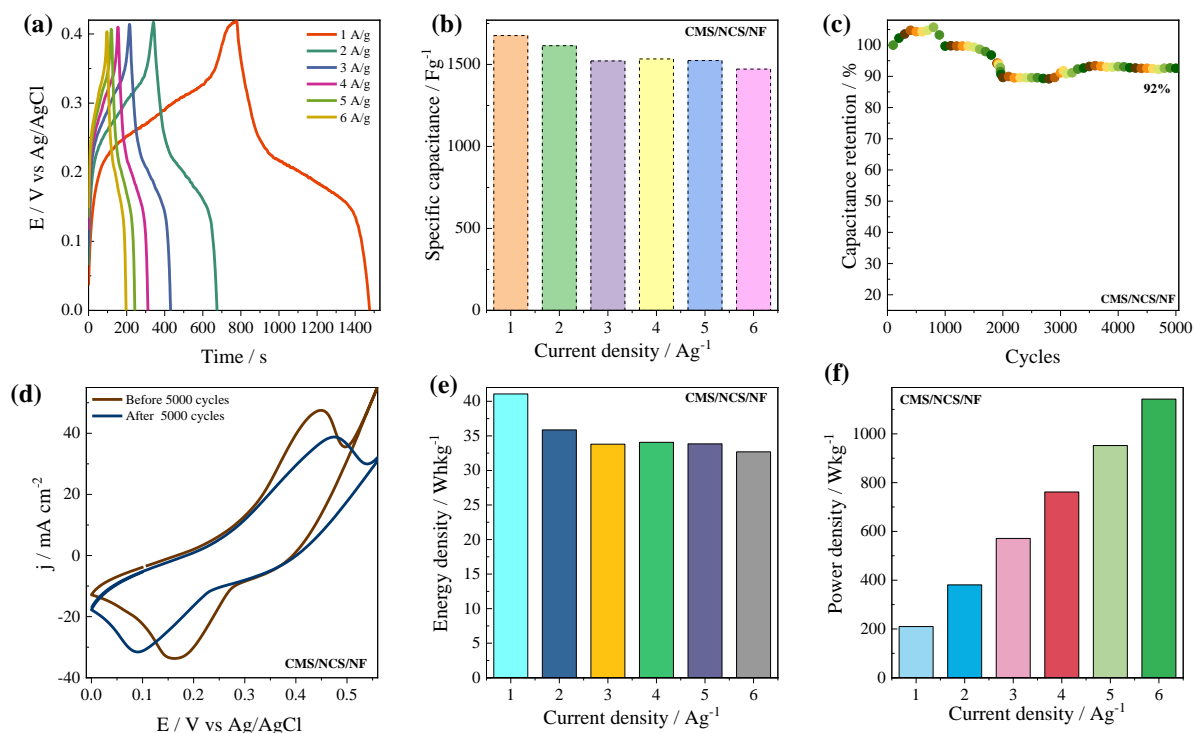


Figure 4.11. (a) GCD of CMS/NCS/NF at various current densities; (b) Variation of specific capacitance versus current density of CMS/NCS/NF; (c) Capacitance retention plot of CMS/NCS/NF; (d) CV before and after 5000 CV cycles at 5 mV/s; (e) Plot of energy density versus current density; (f) Plot of Power density versus current density.

We performed the GCD test on CMS/NCS/NF at various current densities, within a voltage limit of 0.42 V, as illustrated in Fig 4.11 (a). Examination of the GCD profile revealed that lower current densities resulted in longer discharge periods, indicating increased electrochemical efficiency. Conversely, as the current density escalated, discharge periods contracted, denoting the attainment of greater specific capacitance at diminished current densities. The array of plateaus discernible in the GCD profile attests to the electrode material CMS/NCS/NF possessing characteristics similar to battery-grade materials. The voltage plateau observed in the charging and discharging curves is similar to that seen in the CV curve (Iqbal et al. 2020a). Notably, discharge curves of CMS/NCS/NF displayed marginal IR drop, underscoring a minute internal resistance (Zhang and Mo 2014). The specific capacitance derived from the discharge curve is 1676 F/g under a current density of 1 A/g. At current densities of 2 A/g, 3 A/g, 4 A/g, 5 A/g, and 6 A/g, the specific capacitance registered are 1614 F/g, 1521 F/g, 1533 F/g, 1523 F/g, and 1471 F/g, respectively. The inverse relationship between specific capacitance and current density, as delineated in Fig 4.11 (b), arises from the behaviour where, at increased current densities,

ions mainly engage with the surface pores of the electrode, while the inner pores stay inaccessible due to inadequate interaction time, resulting in reduced specific capacitance.

Testing the stability of our composite electrode CMS/NCS/NF is crucial for evaluating its effectiveness in supercapacitors. We subjected it to 5,000 CV cycles at a scan rate of 400 mV/s to see how well it holds up over time. Remarkably, even after all those cycles, it retained 92 % of its capacity, showing it is tough and can handle long periods of use (Fig 4.11 (c)). After these cycles, we tested it again with a CV test at 5 mV/s and found hardly any changes. This means its electrochemical properties have not really changed much despite all the cycling, proving it is reliable for long-term use in supercapacitors (Fig 4.11 (d)). The specific energy and specific power values are computed utilizing Eqns (1.8) and (1.9). At a current density of 1 A/g, these metrics yield 41.06 Wh/kg and 209.9 W/kg, correspondingly. Conversely, at a maximum current density of 6 A/g, the corresponding values are 32.68 Wh/kg and 1142.52 W/kg. These calculated specific energy and specific power values across different current densities, derived from the GCD curves, are presented in Fig 4.11(e&f) as bar diagrams. Compared to the similar literature available, the electrodeposited CMS/NCS/NF exhibit superior electrochemical properties (Table 4.2).

Table 4.2 Comparison of the electrochemical performance of our work with that of other studies in the literature.

Electrode material	Specific capacitance /Fg⁻¹	Current density/ Ag⁻¹	Electrolyte	Cyclic stability (cycles)	References
CoMnS/ NiCo ₂ S ₄ /NF	1676	1	5 M KOH	92 % (5000)	This work
NiCo ₂ S ₄ / MoS _x /NF	1494	1	1 M Na ₂ SO ₄	93.03 % (1000)	(Wang et al. 2023)
MnSe(20)/ NiCo ₂ O ₄	450.75	0.1	3 M KOH	-	(Raman et al. 2019)
CuMnS	1691	10	1 M KOH	-	(Iqbal et al. 2020a)
NiCo ₂ S ₄ / rGO	1072	1	6 M KOH	-	(Abdel-Salam et al. 2022)
ZnNiSe@ NiCo ₂ S ₄	1417 C/g	1	6 M KOH	95.5 % (10000)	(Mohammadi Zardkhoshoui et al. 2020)
NiCo ₂ S ₄ @SnS ₂	329.22 mAh/g	2	KOH	76.87 % (10000)	(Reddy et al. 2022)
MnCo ₂ O ₄ /NiCo ₂ S ₄	600 C/g	0.5	3 M KOH	75 % (10000)	(Hu et al. 2021)
CuS/MnS @NF	1517	1	2 M KOH	115.6 % (3000)	(Zhai et al. 2019)
NiCo ₂ S ₄ @CoS ₂	1565	1	2 M KOH	91 % (8000)	(Govindasamy et al. 2019)
NiCo ₂ S ₄ @ MoS ₂	860	1	6 M KOH	71.9 % (1000)	(Song et al. 2019)
FeCo ₂ S ₄ - NiCo ₂ S ₄	1519	5 mAcm ⁻²	3 M KOH	95.1 % 5000	(Zhu et al. 2017)

4.3.8 Electrochemical performance of a symmetric supercapacitor

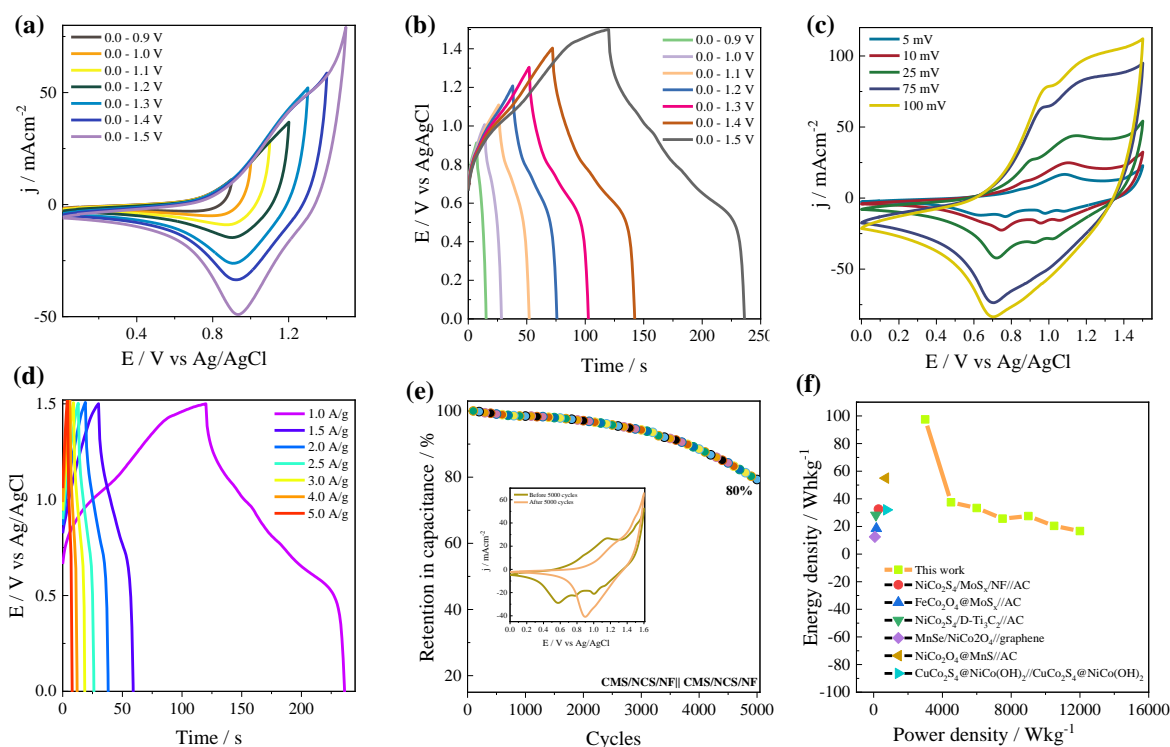


Figure 4.12 (a & b) CV and GCD of CMS/NCS/NF//CMS/NCS/NF with various potential windows and current densities; (c) CV of CMS/NCS/NF//CMS/NCS/NF at various scan rates; (d) GCD of CMS/NCS/NF//CMS/NCS/NF at different current densities; (e) Cyclic stability of CMS/NCS/NF//CMS/NCS/NF for 5000 CV cycles (f) Ragone plot of CMS/NCS/NF//CMS/NCS/NF.

To validate the potential of the synthesized CMS/NCS/NF electrode, we assembled a two-electrode symmetric cell using CMS/NCS/NF as both positive and negative electrode material in a 5 M KOH electrolyte as used in three electrode system. In our study, we focused on optimizing the voltage of cells through meticulous experimentation, specifically employing CV and GCD techniques. The experiments encompassed a voltage span from 0.9 to 1.5 V. These procedures were executed at a scanning pace of 50 mV/s and utilized a defined current of 1 A/g, respectively. The cell voltage optimization through CV and GCD tests enables the determination of the optimal operating voltage window for the supercapacitor cell ensuring optimal performance, longevity, and safety in various practical applications (Joyline et al. 2024). The CV and GCD curves, depicted in Fig 4.12 (a&b), unveiled a faradaic behaviour extending up to 1.5 V. The CV profiles (Fig 4.12 (c)) at varying sweep rates, exhibiting a redox profile consistent with pseudocapacitive behaviour. The GCD tests were executed at various specific currents ranging from 1.0 to 5.0 A/g,

displaying approximately symmetrical non-triangular curves. This suggests excellent reversibility in electrochemical processes, affirming the ability of the device to efficiently store and release energy through fast and reversible redox reactions at the electrode-electrolyte interface (Fig 4.12 (d)). We calculated specific capacitance using Eq. (1.7), yielding a highest value of 312 F/g observed at 1 A/g.

To evaluate the durability of the device over numerous cycles, it endured 5,000 CV cycles at a scan rate of 400 mV/s. Remarkably, even after this extensive cycling, 80 % detainment from the original value has been achieved, as illustrated in Fig 4.12 (e). The inset of the Fig 4.12 (e) displays the CV data before and after the cyclic stability test. It reveals that the oxidation and reduction potentials have shifted towards higher potentials and have slightly diminished in magnitude after multiple test runs, indicating some degree of electrode degradation or changes in the electrochemical behaviour. Despite undergoing 5,000 cycles, redox peaks are still observable, suggesting the persistence of some reversible electrochemical processes within the electrode material.

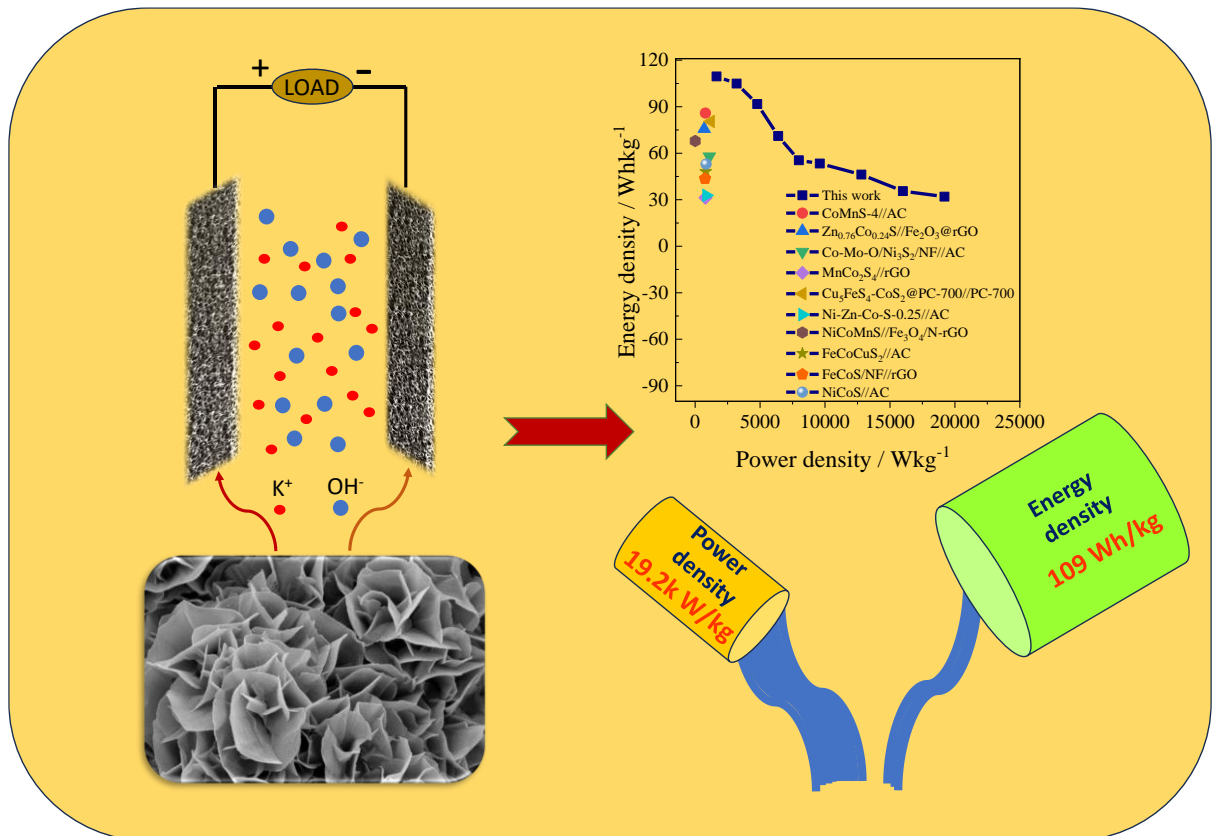
In our analysis, we found that the maximum specific energy was 97.5 Wh/kg at a specific power of 3000 W/kg. Additionally, the maximum specific power achieved was 12000 W/kg at a specific energy of 16.66 Wh/kg. Fig 4.12 (f) presents a comparative plot of specific energy and power values from this work alongside similar values from the literature. The distinctive composite between CMS and NCS, coupled with its intricate nanostrip morphology, has resulted in a notable increase in specific capacitance, improved charge-discharge performance, and enhanced durability over multiple cycles. The better surface area achieved by combining these two composites further contributes to these improvements. These discoveries underscore the practicality and promise of this approach across a spectrum of applications. This research provides crucial insights for the practical energy storage of supercapacitors, and the symmetric supercapacitor assembled in this study exhibits great promise for real-world applications.

4.4 CONCLUSIONS

In conclusion, through a facile two-step electrodeposition technique, a CoMnS/NiCo₂S₄/NF (CMS/NCS/NF) electrode material has been synthesized for the intended use in supercapacitor applications. Notably, the electrochemical performance of the CMS/NCS/NF composite outperforms that of its single-component counterparts, CMS/NF, and NCS/NF, due to significant enhancements. The unique nanostrip morphology and the synergistic effects between CMS and NCS contribute to the efficient insertion of electrolyte ions, an augmentation in electroactive sites, and an improvement in charge transport mechanisms. Consequently, the CMS/NCS/NF electrode exhibits exceptional redox kinetics, evidenced by a high specific capacitance of 1676 F/g at a current density of 1 A/g in a three-electrode setup, utilizing 5 M KOH as the electrolyte, thereby exceeding the performance of its counterparts. Additionally, the CMS/NCS/NF electrode demonstrates outstanding cyclic stability, retaining 92 % of its initial capacitance after 5000 charging-discharging cycles in supercapacitors. A symmetric supercapacitor, employing CMS/NCS/NF as both anode and cathode, was also constructed, achieving a maximum specific capacitance of 312 F/g at 1 A/g along with maximum energy density of 97.5 Wh/kg and a power density of 12000 W/kg. These findings underscore the significant potential of the CMS/NCS/NF electrode material in advancing supercapacitor technology.

CHAPTER 5

IRON DECORATED COBALT MANGANESE SULPHIDE NANOFLOWERS AS A BATTERY TYPE ELECTRODE MATERIAL FOR HIGH PERFORMANCE SUPERCAPACITOR



***Abstract:** This chapter includes the synthesis of trimetallic sulphide FeCoMnS and studying its application in supercapacitors.*

5.1 INTRODUCTION

Carbonaceous materials, conductive polymers, and transition metal oxides have undergone extensive research in recent years, emerging as the most commonly studied materials (Zheng et al. 2016). Transition metal oxides/hydroxides exhibit ten times more capacitance compared to carbon-based materials and conductive polymers. However, their widespread use is significantly hindered by their low conductivity (Hu et al. 2020a; Yu et al. 2015). Therefore developing a new type of electrode material that offers unique features, such as catalytic efficiency, a considerable surface area alongside distinctive porous structures, admirable chemical and mechanical stability, and affordability, is crucial for increasing the energy density of supercapacitors (Al Haj et al. 2019). In this context, considerable endeavours have been devoted to substituting metal oxide-based electrode materials in supercapacitors.

In general, transition metal sulfides exhibit a wide range of potential stoichiometric compositions, crystal structures, valence states, and nanocrystalline morphologies, which confer upon them heightened electrochemical activities (Yu et al. 2016). Also, transition metal sulfides emerge as a novel category of supercapacitor electrode materials, boasting intricate structures, superior physical properties, and elevated specific capacitance in comparison to traditional transition metal oxide counterparts (Balamurugan et al. 2017; Cai et al. 2017; Manuscript 2017). Moreover, the lower electronegativity of sulphur facilitates electron transport, further enhancing their appeal. Widely researched for their outstanding redox characteristics, remarkable electrical conductivity, and increased catalytic activity, transition metal sulfides present themselves as promising contenders for the advancement of supercapacitor technology (Douglas et al. 2015; Jiang et al. 2019; Liu et al. 2018d). In recent times, numerous single metal sulfide materials, including NiS (Yan et al. 2020), MnS (Li et al. 2017a), and Co₉S₈ (Zhu et al. 2019), have garnered significant attention and application as electrode materials in supercapacitors (Hu et al. 2020a). A promising strategy for enhancing the capacitive performance of individual transition metal sulfides involves leveraging multicomponent synergy to amplify their intrinsic properties (Tang et al. 2015b). Mixed transition metal sulfides, including bimetallic or trimetallic variants, exhibit superiority over single-metal sulfides due to several factors. These include enhanced

electrical conductivity, richer faradaic reactions, and synergistic effects arising from the presence of different metal ions (He et al. 2017; Li et al. 2015; Zhou et al. 2020). Particularly, when mixed metal sulfides integrate heterometal ions, they amalgamate the advantages of each transition metal ion, resulting in substantial improvements in conductivity (Chen et al. 2013a; Shen et al. 2015; Tang et al. 2016) . Additionally, the incorporation of multiple counterpart elements leads to an abundance of reaction sites, thereby enhancing electrochemical activities and resulting in higher specific capacitance (Cheng et al. 2017; Gao et al. 2019; Liu et al. 2018e; Wang et al. 2016).

For example, Sahoo et al. (Sahoo et al. 2017) developed porous Nickel Cobalt Manganese Sulfide nanomaterial through cathodic electrodeposition on nickel foam, offering a large electrochemically active surface with an ultrahigh specific capacitance of 2717 F/g at 1 A/g and exemplary retention in capacitance. Lv et al. (Lv et al. 2020) synthesized Mo–Co–Ni sulfide @ Ni–Co sulfide on carbon cloth, showcasing an impressive areal capacitance of 9.81 F/cm² with good cyclic stability. Kang et al. (Kang et al. 2022) fabricated hollow rod-like NiCoMnS from MOFs via etching/ion-exchange and sulfurization, exhibiting superior specific capacitance of 2098.2 F/g. Their asymmetric supercapacitor NiCoMnS//AC achieved high capacitance (124.5 F/g) and excellent retention (73.6 % after 6000 cycles). Sahoo et al. (Sahoo et al. 2020a) synthesized isostructural via a refluxing method which showed a specific capacitance of 1425.0 F/g at 1 A/g and delivered capacitance retention of 77.0 % after 4000 cycles. A series of Ni–Zn–Co–S nanocages were synthesized by Zhao et al. (Zhao et al. 2021) with various Zn/Co ratios. The Ni–Zn–Co–S-0.25 electrode exhibited an exceptionally high capacitance values of 1930.9 F/g at 1 A/g. Additionally, the asymmetric energy storage device with Ni–Zn–Co–S-0.25 as anode and activated carbon as cathode, achieved energy density of 32.8 Wh/kg at the power density of 864.8 W/kg alongside admirable cyclic stability. These studies investigate the capacity of Mult metallic transition metal sulfides as an electrode material for supercapacitors, owing to the existence of various oxidation states of metal ions in a diverse system.

Mixed transition metal sulfides exhibit insufficient electrochemical characteristics, particularly concerning subpar rate performance and cycle life, ascribed to slow reaction kinetics and volume fluctuations during GCD cycles. On the other hand, the morphology of electrode materials significantly influences electrochemical behaviour and interfacial charge transport kinetics. Hence, the rational design of nanostructures for transition metal sulfides emerges as a crucial approach to augment their electrochemical performance (Zhao

et al. 2021). Recent efforts have focused on crafting and examining three-dimensional (3D) hierarchical architectures constructed from low-dimensional building blocks. These structures offer an expansive surface area ideal for enhanced electrolyte diffusion, thereby facilitating heightened redox activity, efficient electron transfer, and minimized recombination dynamics. However, existing synthetic methodologies typically entail intricate procedures, reliance on toxic or costly chemicals, elevated temperatures, structure-directing templates, and prolonged growth processes. Hence, the ongoing challenge is to devise a straightforward and efficient technique for fabricating such hierarchical architectures (Kumar et al. 2019).

To address this challenge, we have introduced a simple and cost-effective method for synthesizing trimetallic FeCoMnS nanoflowers derived from bimetallic CoMnS, serving as electrode materials for supercapacitors. We extensively investigated their electrochemical properties, including interfacial charge transport kinetics, GCD profiles, and CV analysis in both three and two-electrode systems. Consequently, the FeCoMnS electrode attained an exceptionally high specific capacitance of 3200 F/g at 1 A/g. Additionally, the symmetric supercapacitor constructed with FeCoMnS exhibited remarkable energy storage capability (109 Wh/kg at 19.2k W/kg) and exceptional cycle life, enduring approximately 80.1 % of the original capacitance after 5,000 cycles.

5.2 EXPERIMENTAL

5.2.1 Materials

Manganese chloride tetrahydrate ($\text{MnCl}_2 \cdot 4\text{H}_2\text{O}$), cobalt chloride hexahydrate ($\text{CoCl}_2 \cdot 6\text{H}_2\text{O}$), ethylene glycol, N-Methyl 2-pyrrolidone (NMP), were bought from Loba Chemie. Polyvinylidene fluoride (PVDF), ferric sulfate hydrate ($\text{Fe}_2(\text{SO}_4)_3 \cdot x\text{H}_2\text{O}$), C65 conductive carbon were purchased from Sigma Aldrich. Nickel foam (NF) was bought from Global Nanotech, Mumbai, India. The solutions were prepared using Ultrapure Milli-Q water (18.2 M Ω) to ensure high solvent quality. All commercially obtained materials were of superior purity and used without purification.

5.2.2 Synthesis of CoMnS

In the synthesis process, an equimolar concentration of $\text{MnCl}_2 \cdot 4\text{H}_2\text{O}$ and $\text{CoCl}_2 \cdot 6\text{H}_2\text{O}$, each at 0.05 M, was dissolved in 60 mL of ethylene glycol through sonication for a duration of

30 min. Following this, 0.2 M thiourea was added to the solution. The resulting mixture was then transferred to an autoclave and subjected to heating at 180°C in a hot air oven for 24 h. Upon completion of the heating process, the precipitated product was carefully washed sequentially with Milli-Q water, ethanol, and acetone to ensure the removal of any residual impurities. Finally, the washed product was dried at a temperature of 60°C until it reached a constant weight and was ready for further analysis or collection. Following the same synthesis procedure described earlier, single metal ion sulfides, specifically MnS and Co₃S₄, were prepared for comparison with the bimetallic CoMnS compound in terms of their electrochemical activity.

5.2.3 Synthesis of FeCoMnS

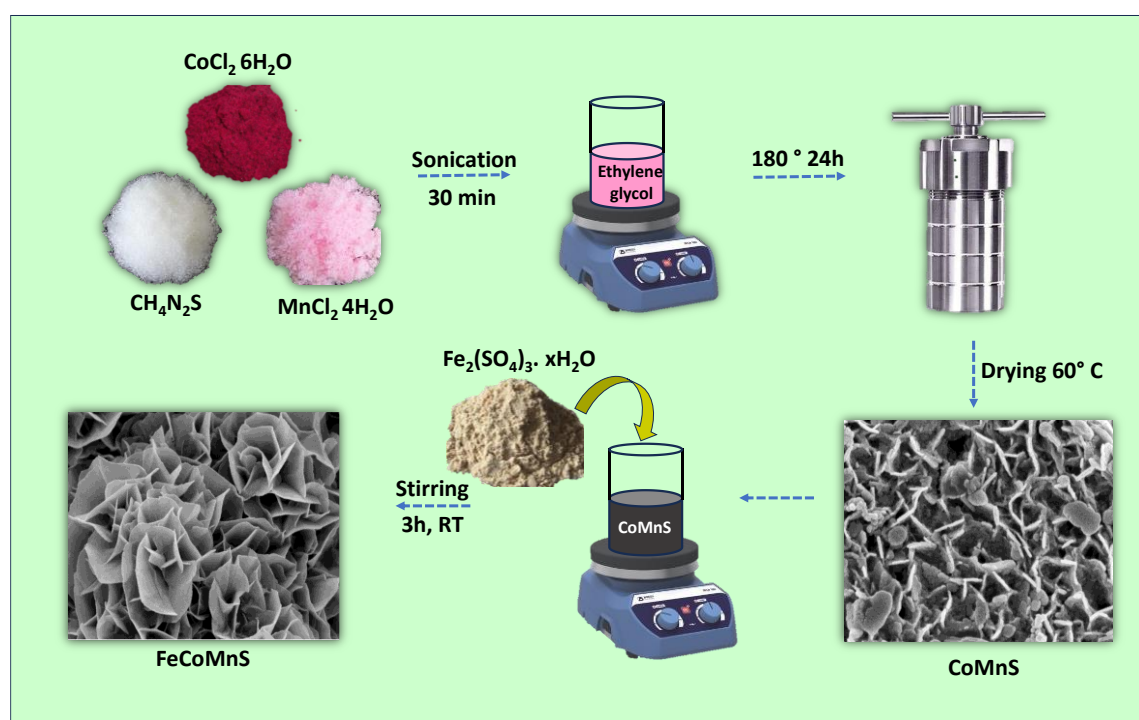


Figure 5.1. Schematic representation for the synthesis of FeCoMnS

In the synthesis of the trimetallic sulfide, 250 mg of the prepared CoMnS was dispersed in 100 mL of Milli-Q water and stirred for 10 min to ensure uniform distribution of the CoMnS nanomaterial. Subsequently, a solution of 0.05 M $\text{Fe}_2(\text{SO}_4)_3 \cdot x\text{H}_2\text{O}$ was added to the CoMnS dispersion, allowing iron to decorate the CoMnS. The mixture was then stirred for an additional 3 h. The resulting trimetallic sulfide, with iron decorated on the CoMnS, was separated from the solution by centrifugation, washed sequentially with Milli-Q water, ethanol, and acetone, and then dried at 60°C to obtain the final product for further

characterization and analysis. The schematic representation for the synthesis of FeCoMnS is given in Fig 5.1.

5.2.4 Electrode fabrication

Initially, the NF underwent a cleansing process with Milli-Q water, followed by ethanol. Subsequently, the NF was immersed in 3 N HCl and sonicated for 20 min to eliminate impurities and residues. Afterwards, it was again washed with Milli-Q water and acetone, then dried at 60°C for 1 h. Next, a homogeneous mixture was obtained by grinding together 75 wt % of active material, 20 wt % C65 as a conductive additive, and 10 wt % PVDF as a binder in a mortar. This mixture was then dispersed in NMP to form a slurry. This slurry was coated on pretreated NF possessing a coating dimension of 1×1 cm² using micropipette. The coated assembly dried at 120°C for 24 h. The analysis of the coated material showed a mass of approximately 1.2 mg.

5.2.5 Material characterisation

Surface morphology and elemental composition were examined using a GEMINI 300, Carl Zeiss HR-FESEM instrument. High-resolution transmission electron microscopy was conducted using a Jeol Model JM 2100 instrument. X-ray diffraction analyses were performed with an Empyrean 3rd Gen instrument from Malvern PANalytical, utilizing monochromatic Cu-K α radiation with a wavelength of 0.154 nm. X-ray photoelectron spectroscopy data were acquired using a Thermo Fischer Scientific ESCALAB Xi+ with an Al K-alpha X-ray source (1486.7 eV).

5.2.6 Electrochemical characterization

The electrochemical properties of the prepared electrodes were investigated using the Autolab PGSTAT204 electrochemical workstation. Employing a sophisticated three-electrode setup, in 5 M KOH as an electrolyte, the designated material coated on a NF act as a working electrode, a platinum electrode as a counter electrode, while Ag/AgCl serves as the reference electrode. This intricate arrangement forms the foundation for the meticulous execution of electrochemical studies. The CV studies encompassed a potential range of 0.0-0.45 V vs. Ag/AgCl employing diverse scan rates ranging from 5-120 mV/s. Additionally, GCD studies were executed at various current densities spanning from 1-6 A/g within the potential window of 0.0-0.4 V. The EIS study was accomplished at a frequency range of 1-100 kHz at zero-bias voltage. Electrochemical Active Surface Area

(ECSA) was carried out for different scan rates from 5-50 mV/s. The surface area is calculated using the Eq. (3.1). The specific capacitance (C_s) for the three-electrode configuration can be calculated using the equation (1.6) from the GCD studies.

A symmetrical supercapacitor cell was carefully created using the FeCoMnS as both anode and cathode material. The electrodes were coated using the same procedure used for three-electrode system. The calculated mass of the electrodes was found to be 5 mg. The cell assembly involved immersing both electrodes in a 5 M KOH electrolyte for the electrochemical analysis. To thoroughly examine the electrochemical behavior of the cell CV experiments were conducted in a potential range of 0-1.6 V at scan rates ranging from 5-120 mV/s. Additionally, GCD studies were performed at varying current densities, ranging from 0.5-6 A/g, within the potential window of 0.0-1.6 V. The specific capacitance (C_s) of the cell can be calculated using the equation (1.7). The energy density (E (Wh/kg)) and power density (P (W/kg)) are calculated using the equations (1.8) and (1.9).

5.3. RESULTS AND DISCUSSIONS

5.3.1 XRD analysis

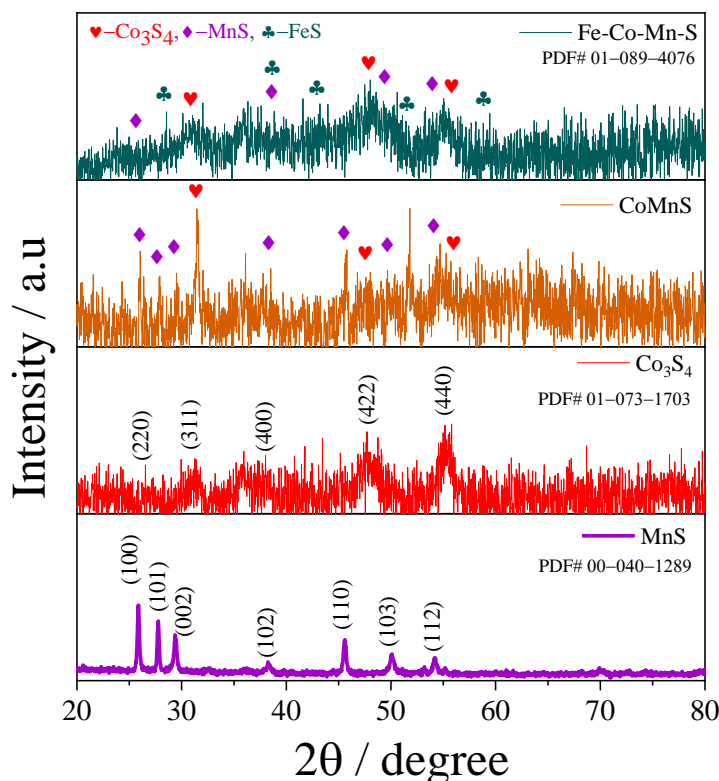


Figure 5.2. XRD of MnS, Co_3S_4 , CoMnS and FeCoMnS

The structural characterization of MnS, Co₃S₄, CoMnS, and FeCoMnS was conducted using XRD, as presented in Fig 5.2. The XRD pattern of FeCoMnS exhibits broad diffraction peaks, indicative of a structure that lies between crystalline and fully amorphous states. For MnS, discernible diffraction peaks were identified at 25.7°, 27.7°, 29.4°, 38.3°, 45.5°, 50.1°, and 54.3°, corresponding to the (100), (101), (002), (102), (110), (103), and (112) crystallographic orientations, respectively. These observations are consistent with the data retrieved from the JCPDS card no. 00-040-1289. In the case of Co₃S₄, characteristic diffraction peaks were recorded at 26.5°, 31.3°, 38.3°, 47.9°, and 55.4°, aligning with the (220), (311), (400), (422), and (440) crystallographic facets, respectively. These findings corroborate with the data provided by the JCPDS card no. 01-073-1703. The XRD pattern of the synthesized CoMnS revealed peaks characteristic of both MnS and Co₃S₄ phases, substantiating its formation. Furthermore, the trimetallic sulphide FeCoMnS displayed an additional FeS phase, as evidenced by the JCPDS card no. 01-089-4076, alongside the MnS and Co₃S₄ phases.

5.3.2 ECSA and EIS analysis

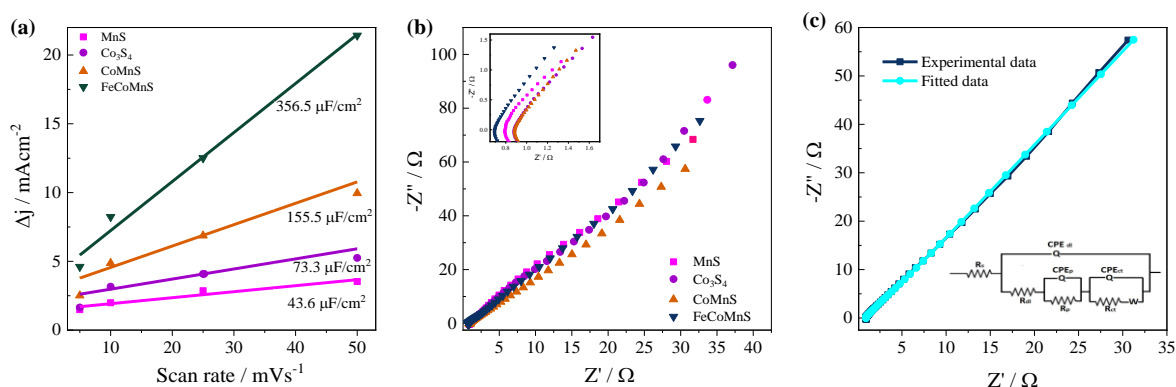


Figure 5.3. (a) ECSA of MnS, Co₃S₄, CoMnS and FeCoMnS; (b) Nyquist plot of MnS, Co₃S₄, CoMnS and FeCoMnS; (c) Nyquist plot of FeCoMnS fitted with equivalent circuit.

The non-faradaic region of the synthesized materials was analyzed at varying scan rates to assess the ECSA. The double-layer capacitance (2C_{dl}) determined from the slope of the graph is as shown in Fig 5.3 (a). The C_{dl} values for MnS, Co₃S₄, CoMnS, and FeCoMnS were measured at 21.8 $\mu\text{F/cm}^2$, 36.65 $\mu\text{F/cm}^2$, 77.75 $\mu\text{F/cm}^2$, and 178.25 $\mu\text{F/cm}^2$, respectively. The corresponding surface areas were calculated as 0.545 cm², 0.916 cm², 1.943 cm², and 4.456 cm² for MnS, Co₃S₄, CoMnS, and FeCoMnS, respectively. The notably higher C_{dl} value and ECSA of 4.456 cm² for FeCoMnS compared to the others indicate a greater concentration of active sites (Junita et al. 2023; Kim et al. 2020).

Table 5.1. EIS parameters for the fitted circuit.

Samples	R_s (Ω)	CPE_{dl} (F)	R_{dl} (Ω)	CPE_p (F)	R_p (Ω)	CPE_{ct} (F)	R_{ct} (Ω)	W (Ω)
FeCoMnS	0.76	3×10^{-4}	2.36	1.2×10^{15}	1.33	4.2×10^{-5}	0.023	1.5×10^{-13}
CoMnS	0.92	2×10^{-4}	1.12	0.0024	2.26	0.0012	16.03	8.0×10^{-5}
Co₃S₄	0.92	2×10^{-4}	1.00	1.38	3.3×10^{-11}	0.034	0.001	0.0024
MnS	0.84	3×10^{-4}	2.07	4.9×10^{-17}	0.01422	0.0002	0.014	0.0023

The Nyquist plots for MnS, Co₃S₄, CoMnS and FeCoMnS is shown in Fig 5.3 (b). The impedance data shows a small semicircle in the high-frequency region and a straight line following it in the lower frequency region. The Nyquist data of FeCoMnS is fitted with equivalent circuit (inset of Fig 5.3 (c)). It can be noticed from Table 5.1 that the R_s of CoMnS and FeCoMnS are 0.92 Ω and 0.76 Ω respectively and R_{ct} of CoMnS is 16.03 Ω and of FeCoMnS is 0.023 Ω . Moreover, the lesser R_{ct} and R_s of FeCoMnS indicates that the charge transfer efficiency is the highest. The lower R_{ct} allows rapid ion flow, resulting in smooth charge transfer. This lowers voltage drop, enhances energy delivery, and improves cycling stability (Uke et al. 2020). The FeCoMnS electrode shows a straight line with greater slope compared with CoMnS providing a lower diffusive resistance and faster ion transmission in the electrolyte (Zhao et al. 2020). Together, these factors may be responsible for the higher activity of FeCoMnS electrode.

5.3.3 CV and GCD analysis

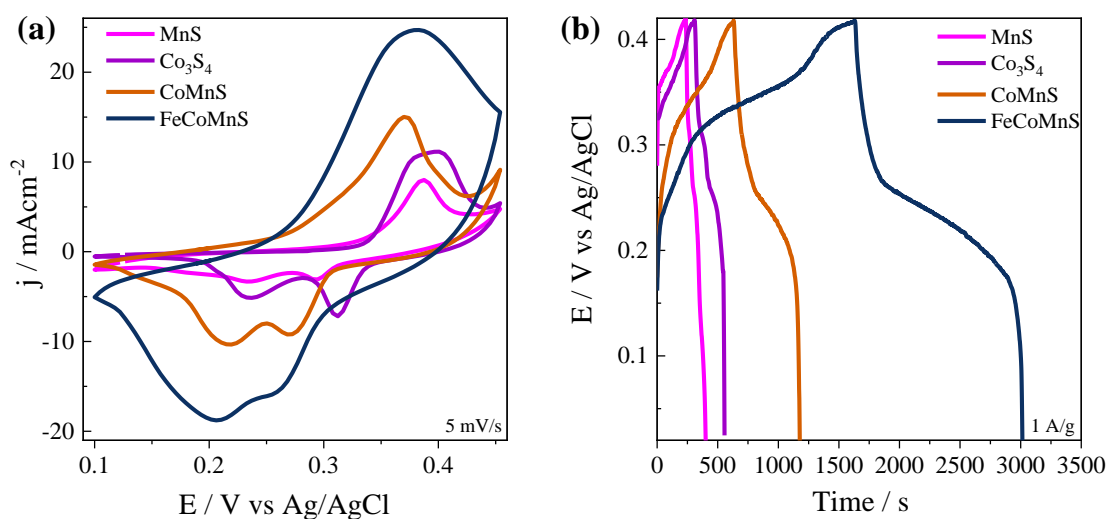


Figure 5.4. (a) CV of MnS, Co₃S₄, CoMnS and FeCoMnS at 5 mV/s; (b) GCD of MnS, Co₃S₄, CoMnS and FeCoMnS at 1A/g.

The comparison of CV and GCD analyses of MnS, Co₃S₄, CoMnS, and FeCoMnS at 5mVs and 1 A/g respectively is shown in Fig 5.4 (a&b) respectively. The experimental results elucidates that the electrochemical efficacy of FeCoMnS outperforms that of MnS, Co₃S₄, and CoMnS. This assertion is substantiated by markedly elevated anodic and cathodic peaks, delineating the greatest area encompassed by the CV curve in FeCoMnS relative to MnS, Co₃S₄, and CoMnS. This observation signifies that FeCoMnS exhibits the highest charge storage capability. Additionally, the GCD analysis reveals that FeCoMnS showcases the most prolonged discharge duration compared to the other synthesized materials. The synergistic effect of trimetallic sulphide in FeCoMnS and its flower-like morphology provides a high surface area conducive to increased electrolyte diffusion, which is beneficial for enhancing redox activity, electron transfer and responsible for the improvements in the electrochemical behaviour.

5.3.4 FESEM and EDS analysis

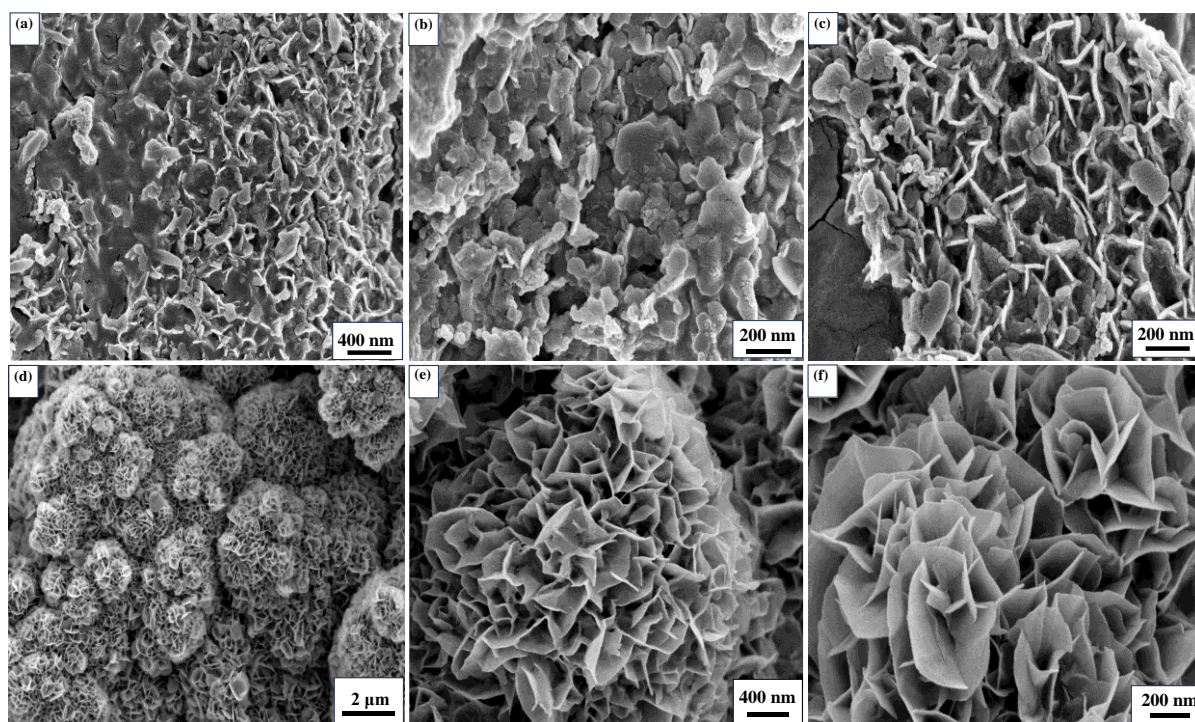


Figure 5.5. (a-c) FESEM images of CoMnS; (d-f) FESEM images of FeCoMnS.

In the FESEM analysis of CoMnS (Fig 5.5 (a-c)), a distinct cellular structure is observed, primarily constructed from side-face contacted nanosheets (Costa et al. 2009; Lin et al. 2021). This arrangement creates a network of interconnected compartments or voids, resembling a lattice-like or honeycomb pattern. While the majority of the nanosheets are oriented in a side-face contact manner (Fig 5.5 (c)), allowing for a porous and interconnected structure, there are also instances where the nanosheets make face-to-face contacts (Fig 5.5 (b)). This side-by-side arrangement provides insights into the material's morphology and surface characteristics. In contrast, FeCoMnS exhibits a distinct morphological transformation, where the nanosheets have fused together to create intricate nanoflowers (Fig 5.5 (d-f)). These nanoflowers display a flower-like structure with vertically arranged ultrathin nanosheets radiating from a central point, as revealed by FESEM analysis (Hu et al. 2020a; Miralles et al. 2023). This comparison highlights the structural differences induced by the introduction of Fe into the material, emphasizing the significant morphological variations between CoMnS and FeCoMnS at the nanoscale. The unique shape of FeCoMnS increases the active sites, leading to better electrochemical performance of the composite. The closely arranged nanoflower clusters facilitate faster electron conduction, further boosting the material's electrochemical performance.

Additionally, the connected nanosheets form uniform and orderly nanoflowers, ensuring consistent performance and stability. The aggregation of these nanoflowers enhances the material's conductivity, making it advantageous for high electrical energy storage and supply (Arunachalam et al. 2017; Murugan et al. 2021).

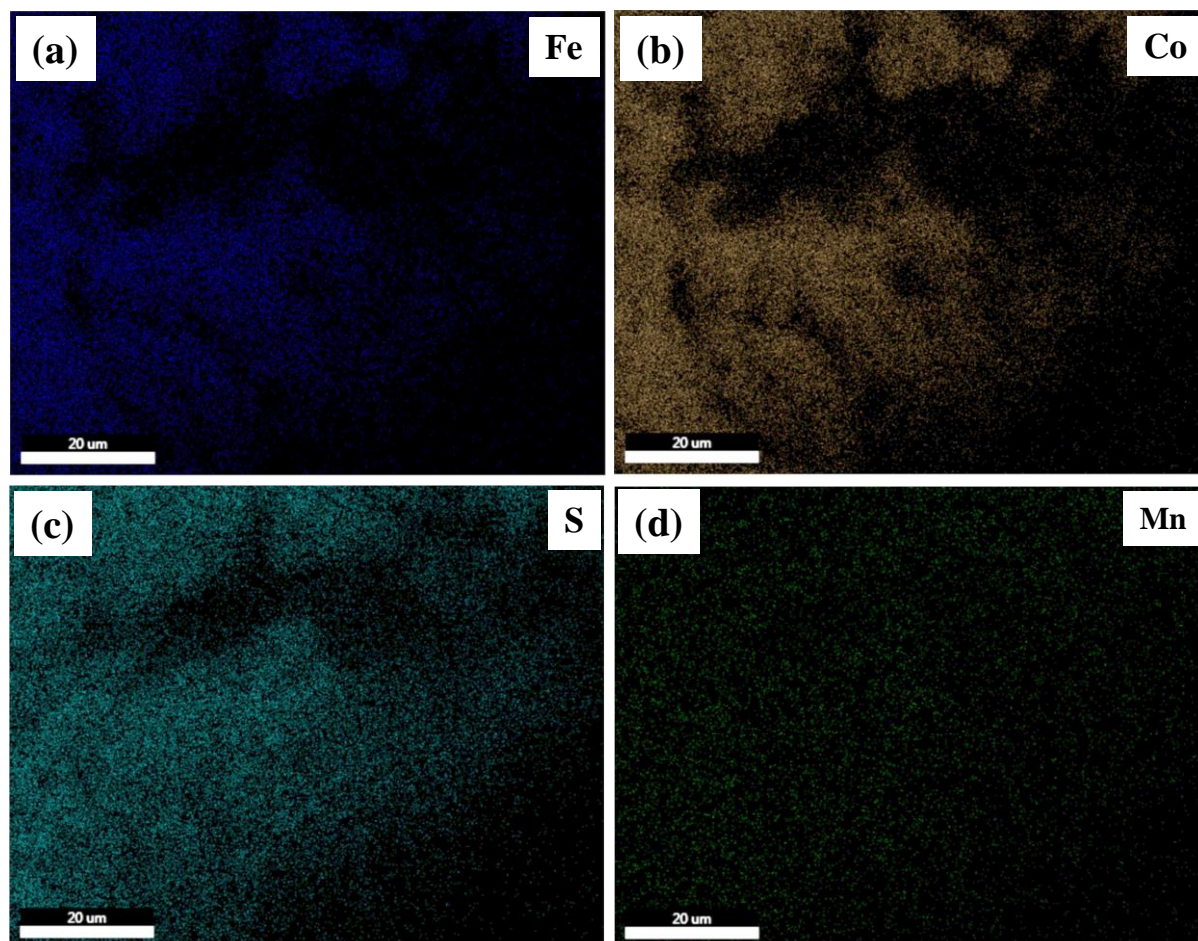


Figure 5.6. Elemental mapping images of (a) Fe; (b) Co; (c) S; (d) Mn.

The elemental color mapping of Fe, Co, Mn, and S in Fig 5.6 (a-d) illustrates that these elements are uniformly dispersed within the nanoflower arrangement. This uniform distribution suggests that the nanoflowers have grown uniformly, leading to a homogeneous spread of Fe, Co, Mn, and S elements throughout the material (Wen et al. 2017).

5.3.5 HRTEM analysis

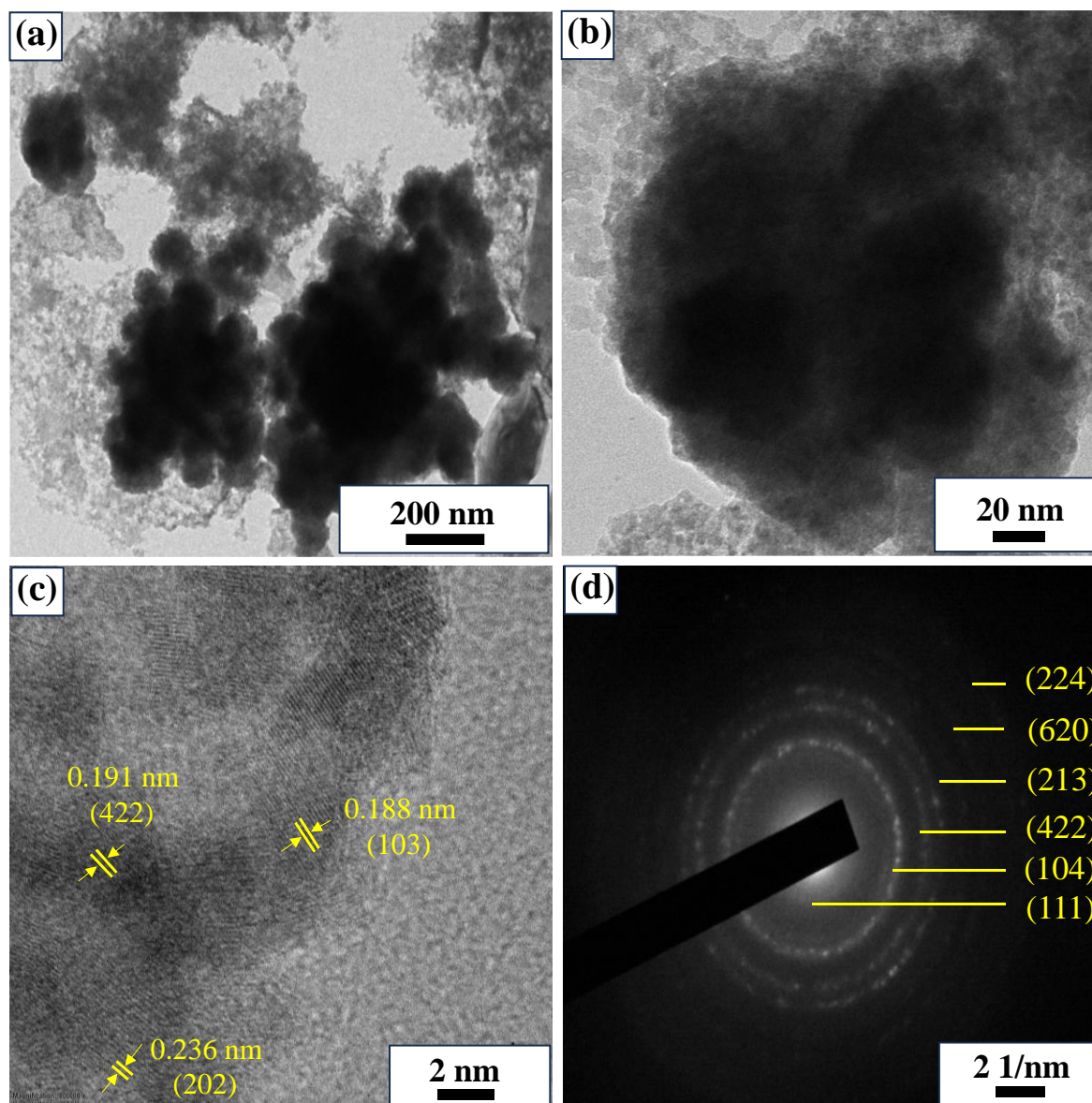


Figure 5.7. (a&b) TEM images; (c) HRTEM image; (d) SAED pattern of FeCoMnS.

The TEM images of FeCoMnS, presented in Fig 5.7 (a&b), show both higher and lower magnifications. These images clearly reveal the intricate nanoflower structure of FeCoMnS, consistent with the findings from FESEM. Additionally, the high-resolution HRTEM image in Fig 5.7 (c) provide an in-depth view of the lattice fringes and crystalline structure of FeCoMnS. The HRTEM images are particularly useful for observing the atomic arrangement and identifying the precise lattice spacings within the material. The interplanar crystal spacing for MnS is approximately 0.188 nm, while for FeS and Co₃S₄, it is approximately 0.236 nm and 1.91 nm, respectively. These spacings correspond to the (103), (202), and (422) crystal planes of FeCoMnS, offering valuable insights into

the crystallographic properties. Furthermore, the selected area electron diffraction (SAED) pattern of FeCoMnS features diffraction rings elucidates a polycrystalline nature and correlates with the respective planes as shown in Fig 5.7 (d), enhancing the structural characterization of FeCoMnS.

5.3.6 XPS analysis

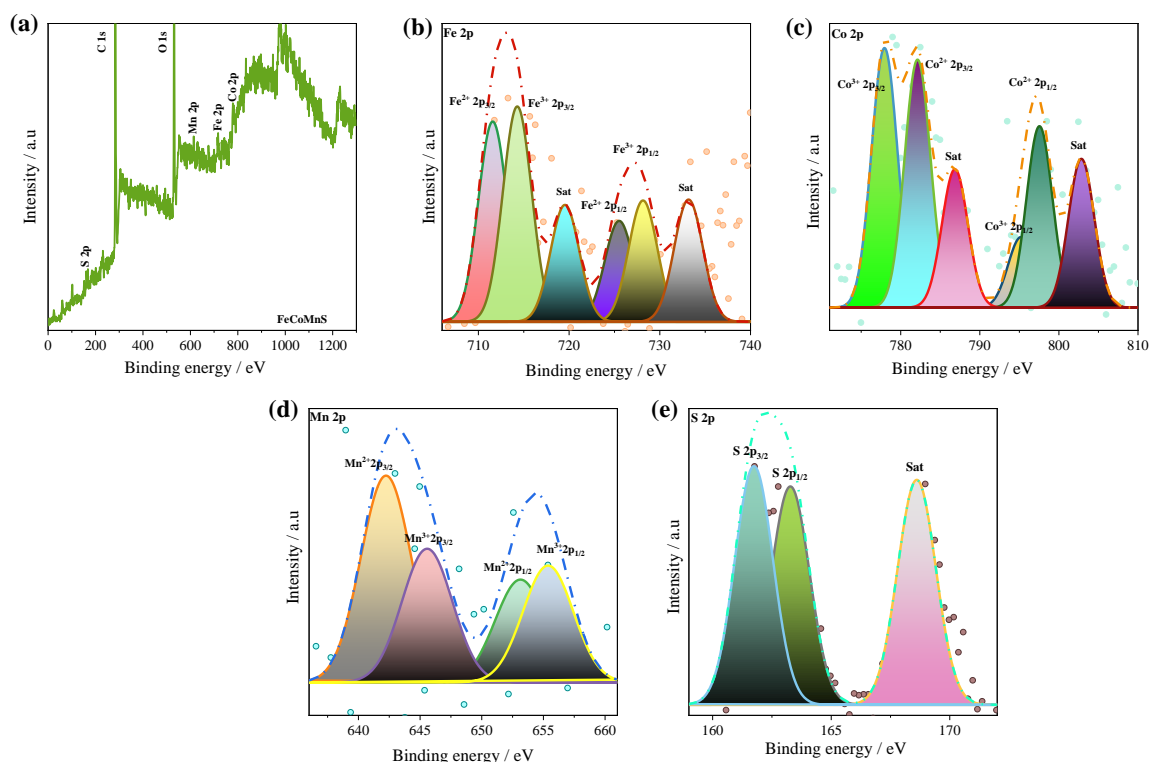


Figure 5.8. (a) XPS survey spectrum of FeCoMnS; (b) XPS spectra results of (b) Fe 2p, (c) Co 2p, (d) Mn 2p and (e) S 2p.

XPS analyses were performed on FeCoMnS to investigate its elemental composition and chemical valence states. Fig 5.8 (a) displays the XPS survey spectrum of FeCoMnS, revealing the presence of Fe 2p, Co 2p, Mn 2p, and S 2p elements. Fig 5.8 (b-e) present the typical XPS spectra for Fe, Co, Mn, and S, obtained using the Gaussian fitting method. The O 1s signal is associated with the adsorption of oxygen and the surface oxidation of the sample. The Fe 2p, Mn 2p, and Co 2p spectra each display two spin-orbit doublets (Hu et al. 2020b; Yang et al. 2016). In the Fe 2p spectrum, the core level reveals two main peaks, Fe 2p_{3/2} and Fe 2p_{1/2}, at binding energies of 713 and 727.2 eV, respectively, along with two satellite peaks at 719.4 and 733.1 eV. As explained in Fig 5.8 (b), the peaks fitted at 714.2 eV and 728.1 eV are indicative of Fe³⁺, while those at 711.6 eV and 725.4 eV are associated

with Fe^{2+} . The fitted peaks and their corresponding satellite features are consistent with the presence of Fe^{2+} and Fe^{3+} , suggesting their coexistence in FeCoMnS (Mohamed et al. 2017). In Fig 5.8 (c), we can see two main peaks at binding energy 779.8 and 797.1 eV. These are attributed to Co $2p_{3/2}$ and Co $2p_{1/2}$, along with satellite peaks at 786.8 and 802.7 eV. Further analysis showed that the peaks at 782.15 eV and 797.5 eV correspond to Co^{2+} , while the peaks at 777.9 eV and 795.1 eV are associated with Co^{3+} . The fitted peaks, along with their satellite features, suggest a mixture of Co^{2+} and Co^{3+} valence states. This indicates that they coexist in FeCoMnS (Kuang et al. 2015; Wen et al. 2017).

The Mn 2p emission spectrum (Fig 5.8 (d)), shows strong peaks at 642 eV for Mn $2p_{3/2}$ and 653.6 eV for Mn $2p_{1/2}$, indicating the presence of both Mn^{2+} and Mn^{3+} . Further analysis revealed that the peaks at 642.25 eV and 653.05 eV correspond to Mn^{2+} , while the peaks at 645.54 eV and 655.3 eV are associated with Mn^{3+} (Xu et al. 2014). The S 2p spectrum displays a primary doublet along with a shake-up satellite as shown in Fig 5.8 (e). The main doublet comprises two peaks at binding energies of 161.7 and 163.2 eV, corresponding to S $2p_{3/2}$ and S $2p_{1/2}$, respectively. The binding energy at 161.7 eV is associated with S^{2-} in a low-coordination environment on the surface, while the peak at 163.2 eV originates from sulfur-metal bonds. The satellite peak at 168.57 eV is attributed to surface sulfur species in higher oxidation states (He et al. 2017). According to the test result, the nanoflower sample contains the elements Fe, Co, Mn, and S. The main states of these elements are Co^{2+} , Co^{3+} , Fe^{2+} , Fe^{3+} , Mn^{2+} , Mn^{3+} , and S^{2-} . Compounds with multiple valence states of trimetallic cations are anticipated to have a significant impact on the performance of a high-capacity supercapacitor electrode material.

5.3.7 Electrochemical performance of FeCoMnS

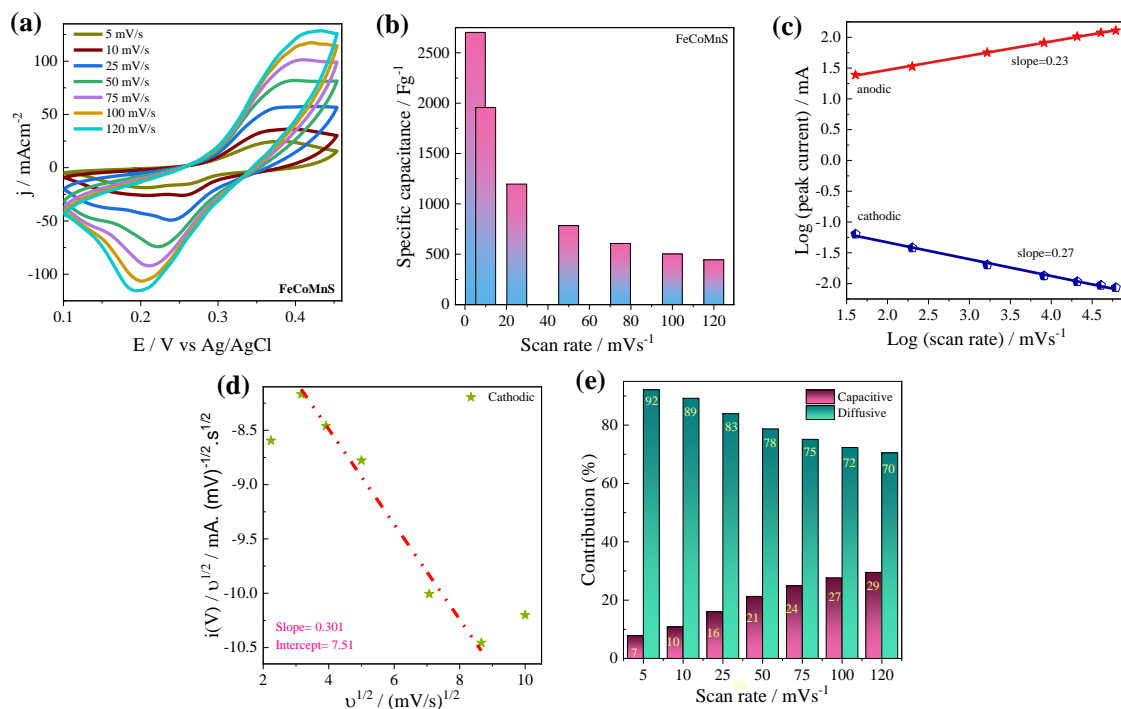


Figure 5.9. (a) CV of FeCoMnS at different scan rates; (b) Variation of specific capacitance of FeCoMnS with respect to scan rate; (c) Graph of log of peak current vs log of scan rate; (d) Relationship between $v^{1/2}$ and $i(V)/v^{1/2}$; (e) Capacitive and diffusive contribution of FeCoMnS at various sweep rates.

Fig 5.9 (a) illustrates the CV curve of FeCoMnS at different scan rates. The consistent appearance of distinct oxidation-reduction peaks in the CV curves, regardless of scan rates, suggests that the energy storage capacity originates from the pseudo capacitance behaviour of the material. These redox peaks can be attributed to specific reversible reactions (Eq. 5.1-5.5), delineating the underlying electrochemical processes associated with faradaic redox reactions driving charge storage (Hu et al. 2020a).



At a scanning rate of 120 mV/s, the material exhibits symmetrical redox peaks, highlighting its impressive high-rate capacity. The uniformity of these curves across all scan rates further confirms the superior rate capacity and stability of the material (Joyline et al. 2024). Furthermore, with increasing scan rates, there is a widening potential gap between the oxidation and reduction peaks (Yang et al. 2020a). Fig 5.9 (b) shows that as the scan rate increases, the specific capacitance decreases. This happens because the redox reactions occur more slowly at higher current densities (Sahoo et al. 2017).

To further understand the charge storage mechanism, a comprehensive investigation has been carried out on the alliance amid current and scan rate. In other words, the Eq. (3.4) from the previous chapter expresses the correlation between the peak current and the scan rate (Lindstro et al. 1997). To determine the value of parameter "b," CV data were plotted as a log i versus log v graph (Eq.(3.4)), which is shown in Fig 5.9 (c). The slope of this plot represents the "b" value. A "b" value of 1 indicates that current is driven by capacitive processes, whereas a "b" value of 0.5 suggests that diffusion-limited processes are controlling the current. From the graph, we can see that the "b" value for the anodic peak is 0.23 and cathodic peaks is 0.27. This indicates that the system is diffusion-controlled. For complex systems with various charge storage mechanisms, the peak current is believed to be a combination of capacitive processes and diffusion-limited processes (Film and Processes 1969; Forghani et al. 2018) as explained in the Eq. (3.5 and 3.6).

The constants "c" and "d" from the Eq. 3.5 are linked to capacitive and diffusion-limited processes, respectively. By plotting $i(V)/v^{1/2}$ versus $v^{1/2}$ at a specific potential, we can analyze the effects of capacitive and diffusion-limited charge storage mechanisms. The slope "c" and y-intercept "d" of this plot provide insights into these mechanisms (Manikandan et al. 2021; Mondal et al. 2021). In Fig 5.9 (d), a linear fit of the plot $i(V)/v^{1/2}$ versus $v^{1/2}$ is depicted. The FeCoMnS electrode exhibits a diffusion-controlled contribution of 92 %, 89 %, 83 %, 78 %, 75 %, 72 %, and 70 %, while the surface-controlled contribution (%) is 7 %, 10 %, 16 %, 21 %, 24 %, 27 %, and 29 % at scan rates of 5, 10, 25, 50, 75, 100, and 120 mV/s, respectively, as explained in Fig 5.9 (e). Almost at all the scan rates, the charge storage mechanism is predominantly governed by diffusion, with 92 % contribution, while a minor portion of 7 % arises from surface reactions (Fig 5.9 (e)). These findings underscore the battery-like electrochemical behaviour of FeCoMnS (Iqbal et al. 2020b).

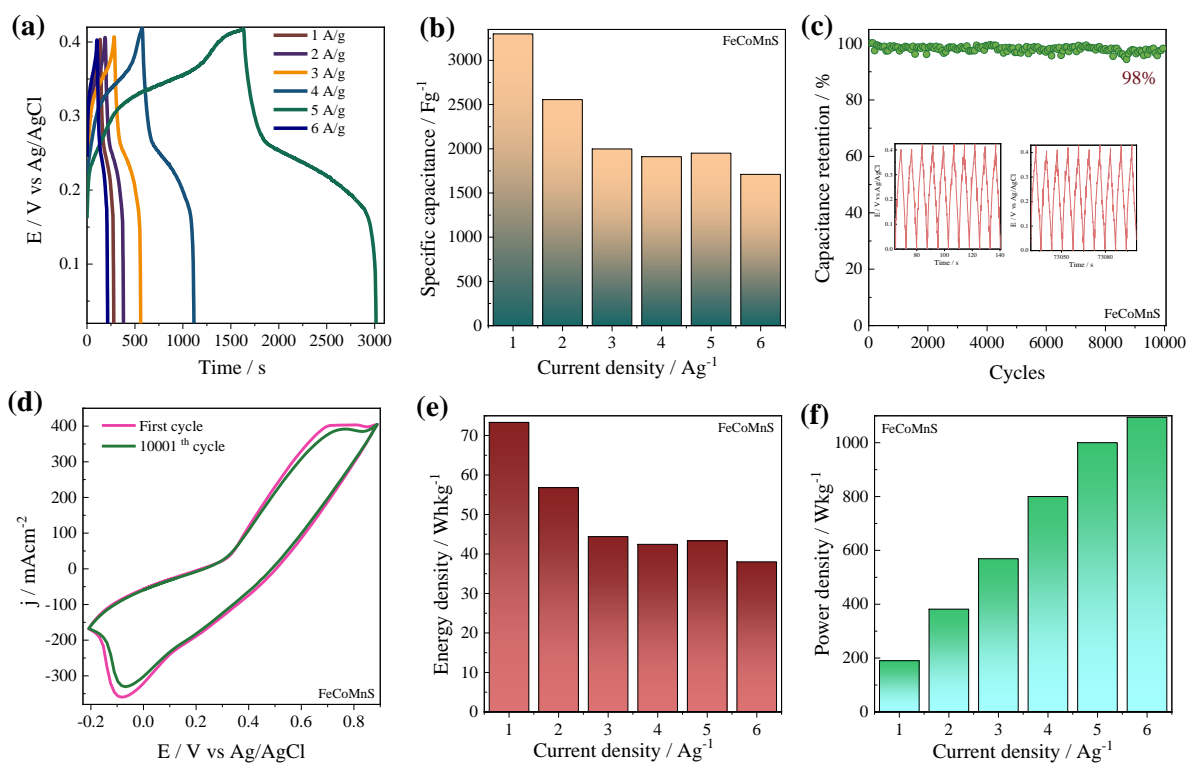


Figure 5.10. (a) CV of FeCoMnS at different scan rates; (b) Variation of specific capacitance vs current density; (c) Cyclic stability of FeCoMnS for 10,000 cycles; (d) CV of FeCoMnS before and after cyclic stability; (e) Variation of energy density with current density; (f) Variation of power density with current density.

GCD Curves for FeCoMnS is shown in Fig 5.10 (a). The charge-transfer-driven redox reaction is further validated by the non-linear nature of GCD curves plotted at various current densities ranging from 1-6 A/g as shown in Fig 5.10 (a). The voltage plateau observed in the charging and discharging curves is similar to that seen in the CV curve. The distinct plateaus observed in the GCD curves indicate the battery-like pseudocapacitive behaviour of FeCoMnS (Poudel et al. 2023). The symmetrical nature of these curves across different current densities implies the ability of the material to undergo reversible processes (Zardkhoshoui and Davarani 2020b). The maximum specific capacitance was found to be 3200 F/g at 1A/g current density. The specific capacitances measured at 2, 3, 4, 5, 6 A/g are 2556, 1998, 1910, 1950, 1710 F/g respectively. The decrease in specific capacitance (Fig 5.10 (b)) of the FeCoMnS electrode with rising current density is due to increased ion intercalation rates. This leads to incomplete ion adsorption, limited ion diffusion, and greater polarization effects, resulting in reduced charge storage capacity (Li et al. 2018). The energy density and power density values are calculated using Eqns. (1.8) and (1.9),

yielding 73.33 Wh/kg and 190.2 W/kg at 1 A/g, respectively and the analogous values at 6 A/g are 38 Wh/kg and 1094 W/kg. respectively. Fig 5.10 (e&f) showcases the variation of calculated power density and energy density with current density. Compared to the reported transition metal sulfide electrode materials, the FeCoMnS nanoflower electrode materials prepared by us exhibit superior electrochemical properties (Table 5.2).

Table 5.2 Comparison of the electrochemical performance of our work with that of other studies in the literature.

Electrode material	Specific capacitance /F/g	Current density/ A/g	Electrolyte	Cyclic stability/cycles	References
FeCoMnS	3200	1	5 M KOH	98 % (10000)	This work
MnCo ₂ S ₄	2067	1	3 M KOH	80.2 % (6000)	(Liu and Jun 2017)
CoMoS ₄ @Ni-Co-S	2208.5	1	6 M KOH	91.3 % (5000)	(Ma et al. 2020a)
NiCoMnS /Ti ₃ C ₂	347.1 C/g	1	6 M KOH	115.8 % (5000)	(Zhang et al. 2022)
Ni-Zn-Co-S	1930.9	1	2 M KOH	69.5 % (5000)	(Zhao et al. 2021)
NiCoMn-S	657.7 C/g	1	6 M KOH	97.8 % (1100)	(Zhang et al. 2021)
Cu ₂ NiSnS ₄	1496	1	2 M KOH	77 % (4000)	(Sahoo et al. 2020b)
CoNiCuS	2047	1	6 M KOH	-	(Wu et al. 2024)
Co ₃ S ₄ /NiS ₂ /Cu ₂ S	464.16 C/g	1	6 M KOH	-	(Mohapatra et al. 2024)
NiCoMnS	1885	1	3 M KOH	92.9 % (10000)	(Tamang et al. 2023)
P-Ni ₂ S ₃ /Co ₃ S ₄ /ZnS	2716	1	3 M KOH	79.7 % (5000)	(Gao et al. 2024)
Fe-Co-S-Ti ₃ C ₂ @NF	1981	1.23	3 M KOH	-	(Wang et al. 2024a)

5.3.8 Post cycling characterization

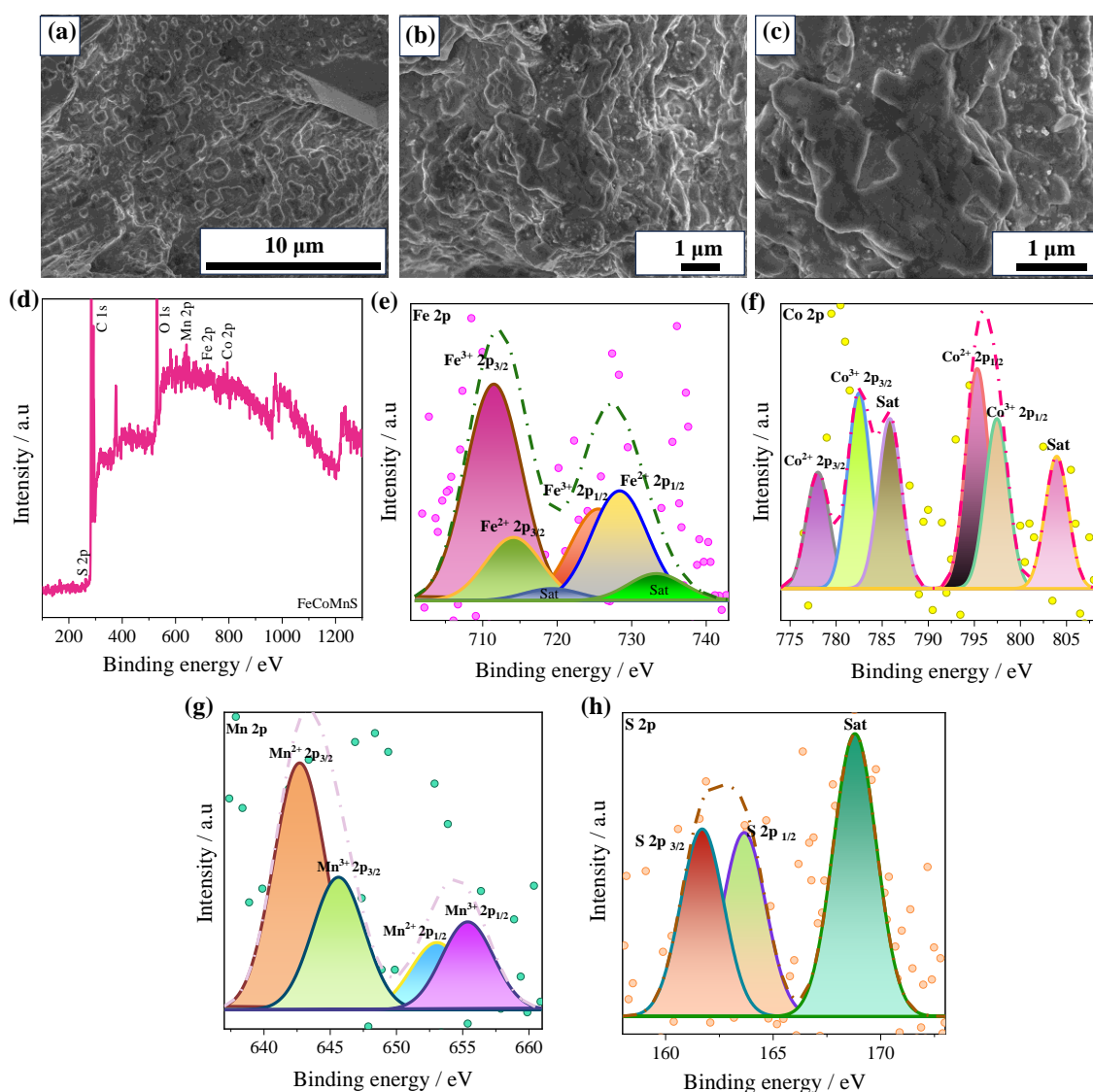


Figure 5.11. (a-c) FESEM images of FeCoMnS after 10,000 GCD cycles; (b) XPS survey spectrum of FeCoMnS ; XPS spectra results (e) Fe (f) Co (g) Mn (h) S after 10000 GCD cycles.

To test the stability of FeCoMnS, it underwent 10,000 GCD cycles at 10 A/g. The observed consistency in cyclic stability, where 98 % retention in capacity was achieved after 10,000 cycles, is indicative of the material's robustness and resilience to prolonged cycling, as shown in Fig 5.10 (c). The inset of Fig 5.10 (c) displays the first and last ten GCD cycles. When a CV test was conducted after these 10,000 charge-discharge cycles, minimal changes were observed. The lack of significant changes in the CV curve indicates that the material's electrochemical properties remain relatively unchanged despite undergoing extensive cycling, further validating its suitability for long-term supercapacitor applications as shown in Fig 5.10 (d).

To further understand the charge storage mechanisms, we conducted post-cycling analyses using FESEM and XPS characterisation. Fig 5.11(a-c) shows the FESEM images of FeCoMnS after cyclic stability. Prior to cyclic stability testing, the FESEM images revealed a well-defined nanoflowers arrangement of the material. Upon completion of the cyclic stability testing, the FESEM images exhibited a distinct morphological transformation. Although there was a remarkable retention rate of 98 %, the material displayed separated layers compared to the initial nanoflowers arrangement. The observed morphological changes can be attributed to the mechanical stress and structural rearrangements induced during the cyclic stability testing. The repeated charge-discharge cycles might have led to the delamination or separation of the layers within the material, resulting in the observed structural evolution. Despite the morphological changes, the high retention rate indicates that the fundamental structure and electrochemical properties of FeCoMnS remain largely intact under the testing conditions. The XPS survey after cyclic stability confirms the presence of expected elements, with detailed spectra for Fe 2p, Co 2p, Mn 2p, and S 2p in Fig 5.11 (e, f, g &h). All peaks maintain consistent binding energy levels as observed initially (Fig 5.8). Surprisingly, all the observed peaks remained unchanged, with no discernible shifts or new peaks emerging in the spectrum. The consistent XPS spectra before and after cyclic stability testing suggest that the surface chemistry and electronic states of FeCoMnS remain stable under the testing conditions. The absence of significant changes in the peak positions indicates that the material maintains its chemical integrity and composition, even after undergoing repeated charge-discharge cycles. This suggests that the material possesses inherent resilience against mechanical degradation, which is a desirable trait for supercapacitor applications where long-term stability and durability are crucial.

5.3.9 Electrochemical performance of FeCoMnS || FeCoMnS

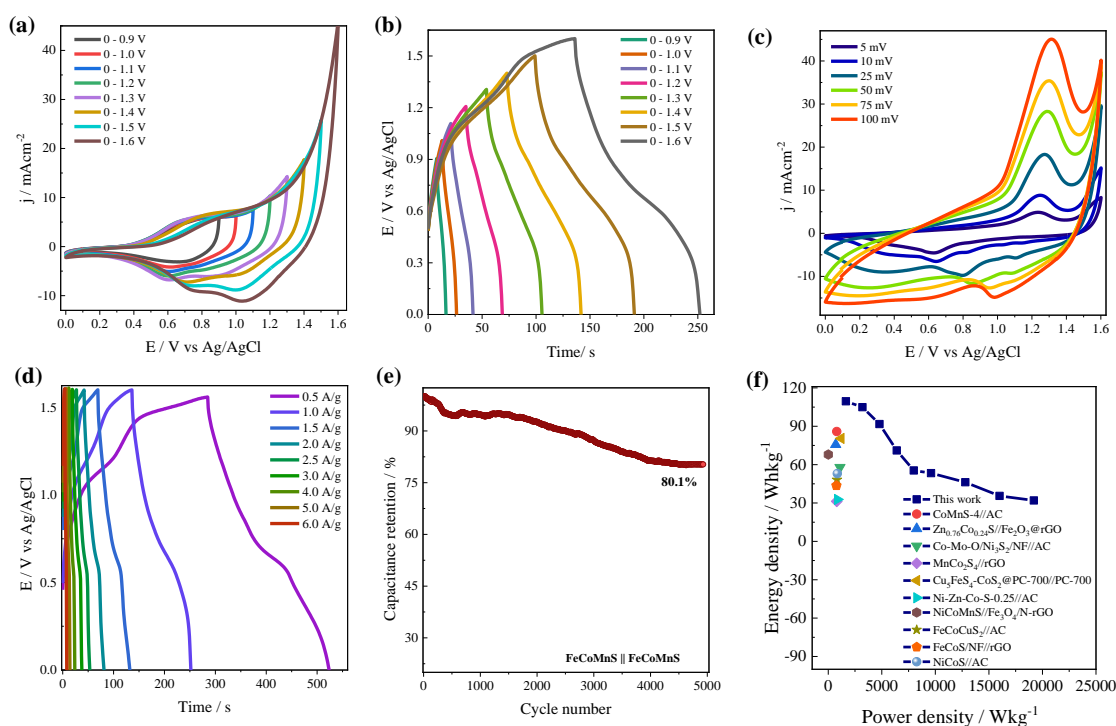


Figure 5.12 (a) CV FeCoMnS//FeCoMnS for the optimization; (b) GCD of FeCoMnS//FeCoMnS for optimization (c) CV of FeCoMnS//FeCoMnS at various scan rates; (d) GCD of FeCoMnS//FeCoMnS at different current densities; (e) Cyclic stability of FeCoMnS//FeCoMnS for 5000 GCD cycles; (f) power density vs energy density of a symmetric supercapacitor;

To validate the potential applications of the trimetallic FeCoMnS electrode material, we assembled a two-electrode symmetric cell utilizing FeCoMnS as both cathode and anode in a 5M KOH electrolyte. The cell voltage optimization was performed through CV and GCD tests over a voltage range of 0.9-1.6 V, using a scan rate of 50 mV/s and a specific current of 1 A/g. This will promise enhanced electrochemical performance with higher specific capacitance and better charge-discharge rates, and enhanced stability of electrode materials. The CV and GCD curves, shown in Fig 5.12 (a & b), revealed a faradaic behavior up to 1.6 V. Fig 5.12 (c) presents the CV curves at different scan rates, demonstrating a redox profile consistent with pseudocapacitive behaviour. Later, GCD tests were carried out at specific currents ranging from 0.5-6 A/g, displaying approximately symmetrical non-triangular curves. This suggests excellent reversibility in electrochemical processes, affirming the ability of the device to efficiently store and release energy through fast and reversible redox reactions at the electrode-electrolyte interface (Fig 5.12 (d)).

The specific capacitance was determined using Eq (1.7), yielding a peak value of 308 F/g observed at 0.5 A/g. To evaluate the durability of the device over numerous cycles, it endured 5,000 GCD cycles at 3 A/g. Remarkably, even after this extensive cycling, 80.1 % retention from the original value has been achieved, as illustrated in Fig 5.12 (e). Furthermore, the device exhibited a highest energy density of 109 Wh/kg at a corresponding power density of 1649 W/kg. Conversely, the maximum power density reached 19.2k W/kg at an energy density of 32 Wh/kg. The Ragone diagram for the FeCoMnS//FeCoMnS device is shown in Fig 5.12 (f), with previously reported trimetallic sulfide supercapacitors provided for comparison. The distinctive amalgamation of Fe, Co, and Mn within the FeCoMnS compound, coupled with its intricate nanoflower morphology, has resulted in a notable increase in specific capacitance, improved charge-discharge performance, and enhanced durability over multiple cycles. These discoveries underscore the practicality and promise of this approach across a spectrum of applications. This research provides crucial insights for the practical energy storage of supercapacitors, and the symmetric supercapacitor assembled in this study exhibits great promise for real-world applications.

5.4 CONCLUSIONS

In conclusion, trimetallic sulphide FeCoMnS nanoflowers were synthesized via a hydrothermal method, leveraging bimetallic CoMnS precursors, and employed as electrode materials for supercapacitors. The distinct nanoflower morphology of FeCoMnS amplifies the active material's surface area, facilitating swift electron and ion movement. Thus, the result is outstanding electrical performance, as evidenced by a specific capacitance of 3200 F/g at 1 A/g and a capacitance retention of 98 % after 10,000 cycles. The FeCoMnS // FeCoMnS cell attained a notable energy density of 109 Wh/kg and a power density of 19.2k W/kg. Notably, the cell demonstrates remarkable stability, retaining 80.1 % of its original capacitance after 5,000 cycles. These findings underscore the promising potential of FeCoMnS nanoflowers for practical electrochemical energy storage applications.

CHAPTER 6

SUMMARY AND CONCLUSIONS

6.1 SUMMARY

As the demand for high-performance energy storage solutions continues to rise, especially in the realm of portable electronic devices and renewable energy systems, the need for advanced materials capable of delivering superior performance becomes paramount. Supercapacitors, with their exceptional power density, rapid charge-discharge cycles, and long operational lifespans, are emerging as a pivotal technology in this field. Unlike traditional batteries, supercapacitors can store and release energy quickly, making them ideal for applications requiring bursts of power. Supercapacitors are an emerging technology that is set to play a crucial role in meeting the demands of electronic devices and systems, both now and in the future. This thesis focuses on the synthesis and characterization of various transition metal chalcogenide materials (TMCs) for potential supercapacitor applications. The primary objectives were to develop advanced electrode materials with superior electrochemical performance and to elucidate the structural and compositional factors contributing to their efficiency. The research employed meticulous synthesis techniques, including hydrothermal methods and electrodeposition, combined with comprehensive characterization to assess the structures, properties, and performance of the nanocomposites.

In the first study, Copper selenide-Graphene oxide nanocomposites were synthesized, with $\text{Cu}_2\text{Se-5GO}$ showing the best performance. The second study involved transition metal-doped manganese selenides, with $\text{Co}_{0.01}\text{Mn}_{0.99}\text{Se}$ demonstrating superior electrochemical properties. The third study fabricated a $\text{CoMnS/NiCo}_2\text{S}_4/\text{NF}$ electrode material using a two-step electrodeposition method, achieving significantly enhanced performance. Finally, trimetallic sulphide FeCoMnS nanoflowers were synthesized, exhibiting exceptional electrochemical properties. Overall, the synthesized materials showed remarkable electrochemical performance, stability, and energy storage capabilities, underscoring their potential for future energy storage technologies. These findings provide a strong foundation for further research aimed at enhancing the performance, durability, and efficiency of supercapacitor materials. By advancing our understanding of the relationship between material structure, composition, and electrochemical behaviour, this research paves the way for the development of next-generation supercapacitors with improved energy density, power density, and longevity.

6.2 CONCLUSIONS

This thesis has successfully synthesized and characterized various nanocomposite materials, demonstrating their promising potential for supercapacitor applications. Through meticulous synthesis methods and comprehensive characterization, we have been able to elucidate the structures, properties, and electrochemical performance of each composite, highlighting their suitability as advanced electrode materials.

In the first study, Copper selenide-Graphene oxide nanocomposites with varying compositions (Cu_2Se -5GO, Cu_2Se -10GO, and Cu_2Se -20GO) were synthesized via a one-step hydrothermal method. Among these, Cu_2Se -5GO exhibited superior electrochemical performance, achieving a maximum specific capacitance of 219 F/g at 5mV/s, with a high capacitance retention of 90.6 %. This indicates the synergistic effect of Cu_2Se and GO, making Cu_2Se -5GO a promising candidate for supercapacitor electrodes.

In the second study, transition metal-doped manganese selenides ($\text{M}_x\text{Mn}_{1-x}\text{Se}$, where M = Co, Ni, and Zn, and $x = 0.0, 0.01, 0.02, 0.03$) were synthesized and evaluated. $\text{Co}_{0.01}\text{Mn}_{0.99}\text{Se}$ demonstrated the best electrochemical properties, with a specific capacitance of 421 F/g at 5mV/s and 377 F/g at 1 A/g. In a two-electrode symmetric setup, $\text{Co}_{0.01}\text{Mn}_{0.99}\text{Se}$ exhibited a specific capacitance of 73 F/g at 0.5 A/g, an energy density of 20.44 Wh/kg, and a power density of 2838 W/kg, with 70 % capacitance retention after 5000 cycles. These results underscore the effectiveness of Co doping in enhancing the electrochemical performance of MnSe-based materials.

The third study involved the fabrication of a $\text{CoMnS}/\text{NiCo}_2\text{S}_4/\text{NF}$ electrode material using a two-step electrodeposition method. This composite demonstrated significantly enhanced electrochemical performance compared to its single-component counterparts. The $\text{CoMnS}/\text{NiCo}_2\text{S}_4/\text{NF}$ electrode achieved a high specific capacitance of 1676 F/g at 1 A/g and retained 92 % of its capacitance after 5000 cycles. The symmetric supercapacitor fabricated using this material showcased a maximum energy density of 97.5 Wh/kg and a power density of 12000 W/kg, highlighting its potential for high-performance supercapacitor applications.

Finally, the synthesis of trimetallic sulphide FeCoMnS nanoflowers via a hydrothermal method was explored. The unique nanoflower morphology resulted in exceptional electrochemical performance, with a specific capacitance of 3200 F/g at 1 A/g and 98 % capacitance retention. The $\text{FeCoMnS}/\text{FeCoMnS}$ cell achieved an energy density of 109

Wh/kg and a power density of 19.2 kW/kg, retaining 80.1 % of its capacitance after 5000 cycles. These findings illustrate the high potential of FeCoMnS nanoflowers for practical energy storage solutions.

Based on a thorough comparative analysis of these synthesized materials, it becomes evident that the trimetallic sulphide FeCoMnS nanoflowers exhibit the most exceptional electrochemical properties. The unique structural advantages inherent in the nanoflower morphology, coupled with the synergistic effects of the trimetallic composition, contribute to their superior performance metrics. Specifically, the FeCoMnS nanoflowers demonstrate the highest specific capacitance, outstanding rate capability, and unparalleled cyclic stability among the synthesized materials. Overall, this thesis provides significant insights into the synthesis and application of advanced transition metal chalcogenides and their nanocomposites for supercapacitors. The synthesized materials exhibit remarkable electrochemical performance, stability, and energy storage capabilities, making them promising candidates for future energy storage technologies. These studies lay a strong foundation for further research and development in the field of supercapacitor materials, aiming to achieve higher performance, durability, and efficiency in energy storage applications.

6.3 FUTURE WORK

The findings presented in this thesis pave the way for several promising avenues of future research in the field of supercapacitor materials. Firstly, exploring the scalability and reproducibility of the synthesis methods employed for the nanocomposite materials could be a critical next step. Upscaling the synthesis processes to produce these materials in larger quantities while maintaining their desired properties will be essential for their practical application in energy storage devices. Additionally, further investigations into the long-term stability and cycling performance of these materials under real-world operating conditions would provide valuable insights into their practical utility. Long-term durability studies, including accelerated aging tests and real-world application simulations, could elucidate the feasibility of integrating these materials into commercial supercapacitor devices.

Furthermore, there is considerable scope for optimizing the performance of the synthesized nanocomposite materials through structural and compositional modifications. Exploring different dopants, nanomorphologies, and composite architectures could potentially

enhance the specific capacitance, cycling stability, and rate capability of these materials. Moreover, integrating advanced characterization techniques, such as in-situ spectroscopy and microscopy, could provide deeper insights into the underlying electrochemical mechanisms governing the performance of these materials. Understanding the intricate interplay between structure, composition, and electrochemical behaviour will be crucial for designing next-generation supercapacitor materials with superior performance and energy storage capabilities. Overall, future research endeavours should focus on refining the synthesis techniques, elucidating the fundamental electrochemical processes, and optimizing the performance of nanocomposite materials to realize their full potential in energy storage applications.

REFERENCES

- Abdel-Salam, A. I., Attia, S. Y., El-Hosiny, F. I., Sadek, M. A., Mohamed, S. G., and Rashad, M. M. (2022). "Facile one-step hydrothermal method for NiCo₂S₄/rGO nanocomposite synthesis for efficient hybrid supercapacitor electrodes." *Mater. Chem. Phys.*, 277, 125554.
- Aboutalebi, S. H., Chidembo, A. T., Salari, M., Konstantinov, K., Wexler, D., Kun Liu, H., and Xue Dou, S. (2011). "Comparison of GO, GO/MWCNTs composite and MWCNTs as potential electrode materials for supercapacitors." *Energy Environ. Sci.*, 4(5), 1855–1865.
- Ahmad, S. A., Shah, M. Z. U., Arif, M., Ullah, E., ur Rahman, S., Shah, M. S. U., Eldin, S. M., Song, P., Sajjad, M., and Shah, A. (2023). "High power aqueous hybrid asymmetric supercapacitor based on zero-dimensional ZnS nanoparticles with two-dimensional nanoflakes CuSe₂ nanostructures." *Ceram. Int.*, 49(12), 20007–20016.
- Ahmadi, M., Zabihi, O., Jeon, S., Yoonessi, M., Dasari, A., Ramakrishna, S., and Naebe, M. (2020). "2D transition metal dichalcogenide nanomaterials: Advances, opportunities, and challenges in multi-functional polymer nanocomposites." *J. Mater. Chem. A*, 8(3), 845–883.
- Ai, K., Huang, J., Xiao, Z., Yang, Y., Bai, Y., and Peng, J. (2021). "Localized surface plasmon resonance properties and biomedical applications of copper selenide nanomaterials." *Mater. Today Chem.*, 20.
- Ali, A., Jamal, R., Rahman, A., Osman, Y., and Abdiryim, T. (2013). "Structure and properties of solid-state synthesized poly (3, 4-propylenedioxythiophene)/nano-ZnO composite." *Prog. Nat. Sci. Mater. Int.*, 23(6), 524–531.
- Ali, Z., Iqbal, M. Z., and Hegazy, H. H. (2023). "Recent advancements in redox-active transition metal sulfides as battery-grade electrode materials for hybrid supercapacitors." *J. Energy Storage*, 73, 108857.
- Alshammari, D. A., Ahmed, I. A., Alahmari, S. D., Abdullah, M., Aman, S., Ahmad, N., Henaish, A. M. A., Ahmad, Z., Farid, H. M. T., and El-Bahy, Z. M. (2024). "Electrochemical investigation of niobium doped nickel selenide nanostructure for supercapacitor devices." *J. Energy Storage*, 75, 109886.
- Ameri, B., Mohammadi Zardkhouei, A., and Hosseiny Davarani, S. S. (2021). "Metal-organic-framework derived hollow manganese nickel selenide spheres confined with

nanosheets on nickel foam for hybrid supercapacitors.” *Dalt. Trans.*, 50(24), 8372–8384.

Anantharaj, S., Ede, S. R., Karthick, K., Karthik, P. E., Kundu, S., Sankar, S. S., and Sangeetha, K. (2018). “Environmental Science Precision and correctness in the evaluation of electrocatalytic water splitting : revisiting activity parameters with a critical assessment.” 744–771.

Aravinda, L. S., Bhat, K. U., and Ramachandra, B. (2013a). “Nano CeO₂ / activated carbon based composite electrodes for high performance supercapacitor.” *Mater. Lett.*, 112, 158–161.

Aravinda, L. S., Bhat, U., and Ramachandra, B. (2013b). “Electrochimica Acta Binder free MoO₃ / multiwalled carbon nanotube thin film electrode for high energy density supercapacitors.” *Electrochim. Acta*, 112, 663–669.

Aravinda, L. S., Nagaraja, K. K., Nagaraja, H. S., Bhat, K. U., and Bhat, B. R. (2013c). “ZnO/carbon nanotube nanocomposite for high energy density supercapacitors.” *Electrochim. Acta*, 95, 119–124.

Aravinda, L. S., Nagaraja, K. K., Nagaraja, H. S., Bhat, K. U., and Bhat, B. R. (2016a). “Fabrication and performance evaluation of hybrid supercapacitor electrodes based on carbon nanotubes and sputtered TiO₂.” *Nanotechnology*, 27(31).

Aravinda, L. S., Nagaraja, K. K., Nagaraja, H. S., Bhat, K. U., and Bhat, B. R. (2016b). “Fabrication and performance evaluation of hybrid supercapacitor electrodes based on carbon nanotubes and sputtered TiO₂.” *Nanotechnology*, 27(31), 314001.

Armand, M., Endres, F., MacFarlane, D. R., Ohno, H., and Scrosati, B. (2009). “Ionic-liquid materials for the electrochemical challenges of the future.” *Nat. Mater.*, 8(8), 621–629.

Armaroli, N., and Balzani, V. (2011). “The legacy of fossil fuels.” *Chem. - An Asian J.*, 6(3), 768–784.

Arunachalam, P., Shaddad, M. N., Alamoudi, A. S., Ghanem, M. A., and Al-Mayouf, A. M. (2017). “Microwave-assisted synthesis of Co₃(PO₄)₂ nanospheres for electrocatalytic oxidation of methanol in alkaline media.” *Catalysts*, 7(4).

Augustyn, V., Come, J., Lowe, M. A., Kim, J. W., Taberna, P. L., Tolbert, S. H., Abruña, H. D., Simon, P., and Dunn, B. (2013). “High-rate electrochemical energy storage through Li + intercalation pseudocapacitance.” *Nat. Mater.*, 12(6), 518–522.

- Augustyn, V., Simon, P., and Dunn, B. (2014). "Pseudocapacitive oxide materials for high-rate electrochemical energy storage." *Energy Environ. Sci.*, 7(5), 1597–1614.
- Azaïs, P., Duclaux, L., Florian, P., Massiot, D., Lillo-Rodenas, M.-A., Linares-Solano, A., Peres, J.-P., Jehoulet, C., and Béguin, F. (2007). "Causes of supercapacitors ageing in organic electrolyte." *J. Power Sources*, 171(2), 1046–1053.
- Bagotsky, V. S. (2005). *Fundamentals of electrochemistry*. John Wiley & Sons.
- Balakrishna Pillai, P., Kumar, A., Song, X., and Souza, M. M. De. (2018). "Diffusion-Controlled Faradaic Charge Storage in High-Performance Solid Electrolyte-Gated Zinc Oxide Thin-Film Transistors." *ACS Appl. Mater. Interfaces*, 10(11), 9782–9791.
- Balamurugan, J., Li, C., Thanh, T. D., Park, O., Kim, N. H., and Lee, J. H. (2017). "Hierarchical design of Cu_{1-x}Ni_xS nanosheets for high-performance asymmetric solid-state supercapacitors." 19760–19772.
- Balasingam, S. K., Lee, J. S., and Jun, Y. (2016). "Molybdenum diselenide/reduced graphene oxide based hybrid nanosheets for supercapacitor applications." *Dalt. Trans.*, 45(23), 9646–9653.
- Baptista, J. M., Sagu, J. S., KG, U. W., and Lobato, K. (2019). "State-of-the-art materials for high power and high energy supercapacitors: Performance metrics and obstacles for the transition from lab to industrial scale—A critical approach." *Chem. Eng. J.*, 374, 1153–1179.
- Bard, A. J., and Faulkner, L. R. (2001). "Fundamentals and applications." *Electrochem. methods*, 2(482), 580–632.
- Beemaroo, M., Periyannan, P., and Ravichandran, K. (2023). "High-performance supercapacitor electrode obtained by directly bonding 2D materials: Hierarchical NiS₂ on reduced graphene oxide." *J. Mater. Sci. Mater. Electron.*, 34(18), 1423.
- Bhol, P., Jagdale, P. B., Jadhav, A. H., Saxena, M., and Samal, A. K. (2024). "All-Solid-State Supercapacitors Based on Cobalt Magnesium Telluride Microtubes Decorated with Tellurium Nanotubes." *ChemSusChem*, 17(7), e202301009.
- Bober, P., Gavrilov, N., Kovalcik, A., Mičušík, M., Unterweger, C., Pašti, I. A., Šeděnková, I., Acharya, U., Pflieger, J., and Filippov, S. K. (2018). "Electrochemical properties of lignin/polypyrrole composites and their carbonized analogues." *Mater. Chem. Phys.*, 213, 352–361.
- Boddula, R., Ahmer, M. F., and Asiri, A. M. (2019). *Morphology design paradigms for*

supercapacitors. CRC Press.

Bogdan, M., Brugger, D., Rosenstiel, W., and Speiser, B. (2014). “Estimation of diffusion coefficients from voltammetric signals by support vector and gaussian process regression.” *J. Cheminform.*, 6, 1–13.

Booth, T. J., Blake, P., Nair, R. R., Jiang, D., Hill, E. W., Bangert, U., Bleloch, A., Gass, M., Novoselov, K. S., and Katsnelson, M. I. (2008). “Macroscopic graphene membranes and their extraordinary stiffness.” *Nano Lett.*, 8(8), 2442–2446.

Bordun, I., Pohrebennyk, V., Sadowa, M., Ptashnyk, V., Kłos-Witkowska, A., and Martsenyuk, V. (2017). “Impedance spectroscopy of supercapacitors on the basis on modified by the ultrasound activated carbon material.” *2017 9th IEEE Int. Conf. Intell. Data Acquis. Adv. Comput. Syst. Technol. Appl.*, IEEE, 86–90.

Breitkopf, C., and Swider-Lyons, K. (2017). *Springer handbook of electrochemical energy*. Springer.

Britto, J. F., Samson, V. A. F., Bernadsha, S. B., Raj, M. V. A., Harini, S., and Madhavan, J. (2024). “A Synergistic effect of binary metal oxides NiMn₂O₄ nanocomposite decorated on rGO for energy storage supercapacitor application.” *J. Mater. Sci. Mater. Electron.*, 35(10), 703.

Brownson, D. A. C., Kampouris, D. K., and Banks, C. E. (2011). “An overview of graphene in energy production and storage applications.” *J. Power Sources*, 196(11), 4873–4885.

Bulakhe, R. N., Sahoo, S., Nguyen, T. T., Lokhande, C. D., Roh, C., Lee, Y. R., and Shim, J.-J. (2016). “Chemical synthesis of 3D copper sulfide with different morphologies for high performance supercapacitors application.” *RSC Adv.*, 6(18), 14844–14851.

Burke, A. (2007). “R&D considerations for the performance and application of electrochemical capacitors.” *Electrochim. Acta*, 53(3), 1083–1091.

Cai, P., Huang, J., Chen, J., and Wen, Z. (2017). “Oxygen-Incorporated Amorphous Cobalt Sulfide Porous Nanocubes as High-Activity Electrocatalysts for the Oxygen Evolution Reaction in an Alkaline / Neutral Medium Communications Angewandte.” 1–5.

Cameron, C. G. (2017). “Electrochemical capacitors.” *Springer Handb. Electrochem. Energy*, 563–589.

Casiraghi, C., Hartschuh, A., Lidorikis, E., Qian, H., Harutyunyan, H., Gokus, T., Novoselov, K. S., and Ferrari, A. C. (2007). “Rayleigh imaging of graphene and graphene

layers.” *Nano Lett.*, 7(9), 2711–2717.

Chakraborty, S., and N. L., M. (2022). “Review—An Overview on Supercapacitors and Its Applications.” *J. Electrochem. Soc.*, 169(2), 020552.

Chandraraj, S. S., and Xavier, J. R. (2023). “Facile synthesis of graphene based mixed metal sulphide nanocomposite for energy storage applications.” *Surfaces and Interfaces*, 36, 102515.

Chang, A., Zhang, C., Yu, Y., Yu, Y., and Zhang, B. (2018a). “Plasma-assisted synthesis of NiSe₂ ultrathin porous nanosheets with selenium vacancies for supercapacitor.” *ACS Appl. Mater. Interfaces*, 10(49), 41861–41865.

Chang, C., Zhang, L., Hsu, C.-W., Chuah, X.-F., and Lu, S.-Y. (2018b). “Mixed NiO/NiCo₂O₄ nanocrystals grown from the skeleton of a 3D porous nickel network as efficient electrocatalysts for oxygen evolution reactions.” *ACS Appl. Mater. Interfaces*, 10(1), 417–426.

Chatterjee, D. P., and Nandi, A. K. (2021). “A review on the recent advances in hybrid supercapacitors.” *J. Mater. Chem. A*, 9(29), 15880–15918.

Chen, B., Meng, Y., Sha, J., Zhong, C., Hu, W., and Zhao, N. (2018). “Preparation of MoS₂/TiO₂ based nanocomposites for photocatalysis and rechargeable batteries: progress, challenges, and perspective.” *Nanoscale*, 10(1), 34–68.

Chen, D., Li, J., and Wu, Q. (2019a). “Review of V₂O₅-based nanomaterials as electrode for supercapacitor.” *J. Nanoparticle Res.*, 21(9), 201.

Chen, H., Jiang, J., Zhang, L., Wan, H., Qi, T., and Xia, D. (2013a). “Highly conductive NiCo₂S₄ urchin-like nanostructures for high-rate pseudocapacitors.” *Nanoscale*, 5(19), 8879–8883.

Chen, J. S., Guan, C., Gui, Y., and Blackwood, D. J. (2017a). “Rational design of self-supported Ni₃S₂ nanosheets array for advanced asymmetric supercapacitor with a superior energy density.” *ACS Appl. Mater. Interfaces*, 9(1), 496–504.

Chen, J., Yao, B., Li, C., and Shi, G. (2013b). “An improved Hummers method for eco-friendly synthesis of graphene oxide.” *Carbon N. Y.*, 64, 225–229.

Chen, P. C., Shen, G., Shi, Y., Chen, H., and Zhou, C. (2010a). “Preparation and characterization of flexible asymmetric supercapacitors based on transition-metal-oxide nanowire/single-walled carbon nanotube hybrid thin-film electrodes.” *ACS Nano*, 4(8),

4403–4411.

Chen, S., Zhu, J., Wu, X., Han, Q., and Wang, X. (2010b). “Graphene oxide– MnO₂ nanocomposites for supercapacitors.” *ACS Nano*, 4(5), 2822–2830.

Chen, T., Liu, Z., Liu, Z., Tao, X., Fan, H., and Guo, L. (2019b). “Fabrication of interconnected 2D/3D NiS/Ni₃S₄ composites for high performance supercapacitor.” *Mater. Lett.*, 248, 1–4.

Chen, T., Tang, Y., Qiao, Y., Liu, Z., Guo, W., Song, J., Mu, S., Yu, S., Zhao, Y., and Gao, F. (2016a). “All-solid-state high performance asymmetric supercapacitors based on novel MnS nanocrystal and activated carbon materials.” *Sci. Rep.*, 6(1), 23289.

Chen, T., Wei, S., and Wang, Z. (2020a). “NiCo₂S₄-Based Composite Materials for Supercapacitors.” *Chempluschem*, 85(1), 43–56.

Chen, X., Paul, R., and Dai, L. (2017b). “Carbon-based supercapacitors for efficient energy storage.” *Natl. Sci. Rev.*, 4(3), 453–489.

Chen, Y. M., Yu, X. Y., Li, Z., Paik, U., and Lou, X. W. (2016b). “Hierarchical MoS₂ tubular structures internally wired by carbon nanotubes as a highly stable anode material for lithium-ion batteries.” *Sci. Adv.*, 2(7), e1600021.

Chen, Y., Muthukumar, K., Leban II, L., and Li, J. (2020b). “Microwave-assisted high-yield exfoliation of vanadium pentoxide nanoribbons for supercapacitor applications.” *Electrochim. Acta*, 330, 135200.

Cheng, F., Yang, X., Zhang, S., and Lu, W. (2020a). “Boosting the supercapacitor performances of activated carbon with carbon nanomaterials.” *J. Power Sources*, 450, 227678.

Cheng, L., Chen, S., Zhang, Q., Li, Y., Chen, J., and Lou, Y. (2020b). “Hierarchical sea-urchin-like bimetallic zinc–cobalt selenide for enhanced battery-supercapacitor hybrid device.” *J. Energy Storage*, 31, 101663.

Cheng, Q., Tang, J., Ma, J., and Zhang, H. (2011a). “Graphene and carbon nanotube composite electrodes for supercapacitors with ultra-high energy density.” 17615–17624.

Cheng, Q., Tang, J., Ma, J., Zhang, H., Shinya, N., and Qin, L.-C. (2011b). “Graphene and nanostructured MnO₂ composite electrodes for supercapacitors.” *Carbon N. Y.*, 49(9), 2917–2925.

Cheng, S., Shi, T., Chen, C., Zhong, Y., Huang, Y., Tao, X., Li, J., Liao, G., and Tang, Z.

(2017). “Construction of porous CuCo₂S₄ nanorod arrays via anion exchange for high-performance asymmetric supercapacitor.” *Sci. Rep.*, 7(1), 1–11.

Chou, S.-W., and Lin, J.-Y. (2013). “Cathodic Deposition of Flaky Nickel Sulfide Nanostructure as an Electroactive Material for High-Performance Supercapacitors.” *J. Electrochem. Soc.*, 160(4), D178–D182.

Conway, B. E., and Conway, B. E. (1999). “Capacitance behavior of films of conducting, electrochemically reactive polymers.” *Electrochem. Supercapacitors Sci. Fundam. Technol. Appl.*, 299–334.

Costa, F. R., Leuteritz, A., Wagenknecht, U., Auf der Landwehr, M., Jehnichen, D., Haeussler, L., and Heinrich, G. (2009). “Alkyl sulfonate modified LDH: Effect of alkyl chain length on intercalation behavior, particle morphology and thermal stability.” *Appl. Clay Sci.*, 44(1–2), 7–14.

Dai, Z., Zang, X., Yang, J., Sun, C., Si, W., Huang, W., and Dong, X. (2015). “Template synthesis of shape-tailorable NiS₂ hollow prisms as high-performance supercapacitor materials.” *ACS Appl. Mater. Interfaces*, 7(45), 25396–25401.

De, B., Balamurugan, J., Kim, N. H., and Lee, J. H. (2017). “Enhanced electrochemical and photocatalytic performance of core–shell CuS@ carbon quantum dots@ carbon hollow nanospheres.” *ACS Appl. Mater. Interfaces*, 9(3), 2459–2468.

Deka, B. K., Hazarika, A., Kim, J., Kim, N., Jeong, H. E., Park, Y. Bin, and Park, H. W. (2019). “Bimetallic copper cobalt selenide nanowire-anchored woven carbon fiber-based structural supercapacitors.” *Chem. Eng. J.*, 355, 551–559.

Dekrafft, K. E., Wang, C., and Lin, W. (2012). “Metal-organic framework templated synthesis of Fe₂O₃/TiO₂ nanocomposite for hydrogen production.” *Adv. Mater.*, 24(15), 2014–2018.

Devi, R., Kumar, V., Kumar, S., Bulla, M., Sharma, S., and Sharma, A. (2023). “Electrochemical analysis of MnO₂ (α , β , and γ)-based electrode for high-performance supercapacitor application.” *Appl. Sci.*, 13(13), 7907.

Dillon, A. C. (2010). “Carbon nanotubes for photoconversion and electrical energy storage.” *Chem. Rev.*, 110(11), 6856–6872.

Douglas, A., Carter, R., Oakes, L., Share, K., Cohn, A. P., Pint, C. L., and Al, D. E. T. (2015). “Ultra fine Iron Pyrite (FeS₂) Nanocrystals Improve Sodium À Sulfur and

- Lithium Sulfur Conversion Reactions for Efficient Batteries.” (11), 11156–11165.
- Dreyer, D. R., Park, S., Bielawski, C. W., and Ruoff, R. S. (2010). “The chemistry of graphene oxide.” *Chem. Soc. Rev.*
- Du, C., Yeh, J., and Pan, N. (2005). “High power density supercapacitors using locally aligned carbon nanotube electrodes.” *Nanotechnology*, 16(4), 350.
- Du, L., Du, W., Ren, H., Wang, N., Yao, Z., Shi, X., Zhang, B., Zai, J., and Qian, X. (2017). “Honeycomb-like metallic nickel selenide nanosheet arrays as binder-free electrodes for high-performance hybrid asymmetric supercapacitors.” *J. Mater. Chem. A*, 5(43), 22527–22535.
- Duan, H., Wang, S., Li, B., and Ma, S. (2023). “Hydrothermally prepared MnSe electrode as a promising pseudocapacitive material for high-performance supercapacitor.” *New J. Chem.*, 47(17), 8297–8304.
- Dubal, D. P., Chodankar, N. R., Gomez-Romero, P., and Kim, D.-H. (2017). “Fundamentals of Binary Metal Oxide-Based Supercapacitors.” *Met. oxides supercapacitors*, Elsevier, 79–98.
- Dubey, R., and Guruviah, V. (2019). “Review of carbon-based electrode materials for supercapacitor energy storage.” *Ionics (Kiel)*, 25, 1419–1445.
- Eftekhari, A. (2018a). “Surface diffusion and adsorption in supercapacitors.” ACS Publications.
- Eftekhari, A. (2018b). “The mechanism of ultrafast supercapacitors.” *J. Mater. Chem. A*, 6(7), 2866–2876.
- Endo, M., Takeda, T., Kim, Y. J., Koshiba, K., and Ishii, K. (2001). “High power electric double layer capacitor (EDLC’s); from operating principle to pore size control in advanced activated carbons.” *Carbon Lett.*, 1(3_4), 117–128.
- Fan, Y., Chen, H., Li, Y., Cui, D., Fan, Z., and Xue, C. (2021). “PANI-Co₃O₄ with excellent specific capacitance as an electrode for supercapacitors.” *Ceram. Int.*, 47(6), 8433–8440.
- Fan, Z., Yan, J., Zhi, L., Zhang, Q., Wei, T., Feng, J., Zhang, M., Qian, W., and Wei, F. (2010). “A three-dimensional carbon nanotube/graphene sandwich and its application as electrode in supercapacitors.” *Adv. Mater.*, 22(33), 3723–3728.
- Farashah, D. D., Beigloo, F., Zardkhoshoui, A. M., and Davarani, S. S. H. (2023).

“Boosting energy storage performance: An exploration of tellurium-based hollow FeNiCoTe nanocubes in hybrid supercapacitors.” *Chem. Eng. J.*, 474, 145584.

Film, O., and Processes, F. (1969). “Zinc Oxidation and Redeposition Processes in Aqueous Alkali and Carbonate Solutions.” 906–918.

Forghani, M., Donne, S. W., Soc, J. E., Cameron, A. P., Davey, S. B., and Latham, K. G. (2018). “Method Comparison for Deconvoluting Capacitive and Pseudo-Capacitive Contributions to Electrochemical Capacitor Electrode Behavior Method Comparison for Deconvoluting Capacitive and Pseudo-Capacitive Contributions to Electrochemical.”

Forouzandeh, P., Kumaravel, V., and Pillai, S. C. (2020a). “Electrode materials for supercapacitors: A review of recent advances.” *Catalysts*, 10(9), 1–73.

Forouzandeh, P., Kumaravel, V., and Pillai, S. C. (2020b). “Electrode Materials for Supercapacitors: A Review of Recent Advances.” *Catalysts*, 10(9), 969.

Galiński, M., Lewandowski, A., and Stępnik, I. (2006). “Ionic liquids as electrolytes.” *Electrochim. Acta*, 51(26), 5567–5580.

Gao, H., Xiao, F., Ching, C. B., and Duan, H. (2012). “High-performance asymmetric supercapacitor based on graphene hydrogel and nanostructured MnO₂.” *ACS Appl. Mater. Interfaces*, 4(5), 2801–2810.

Gao, M.-R., Xu, Y.-F., Jiang, J., and Yu, S.-H. (2013). “Nanostructured metal chalcogenides: synthesis, modification, and applications in energy conversion and storage devices.” *Chem. Soc. Rev.*, 42(7), 2986–3017.

Gao, S. Q., Zhang, P. P., Guo, S. H., Chen, W. Q., Li, M., Liu, F., and Cheng, J. P. (2019). “Journal of Colloid and Interface Science Synthesis of single-phase CuCo₂À x Ni x S 4 for high-performance supercapacitors.” 555, 284–293.

Gao, Y., Yue, X., Dong, Y., Zheng, Q., and Lin, D. (2024). “High-efficiency activated phosphorus-doped Ni₂S₃/Co₃S₄/ZnS nanowire/nanosheet arrays for energy storage of supercapacitors.” *J. Colloid Interface Sci.*, 658, 441–449.

Geng, P., Zheng, S., Tang, H., Zhu, R., Zhang, L., Cao, S., Xue, H., and Pang, H. (2018). “Transition metal sulfides based on graphene for electrochemical energy storage.” *Adv. Energy Mater.*, 8(15), 1703259.

Ghasemi, A. K., Ghorbani, M., Lashkenari, M. S., and Nasiri, N. (2023). “Facile synthesise of PANI/GO/CuFe₂O₄ nanocomposite material with synergistic effect for superb

performance supercapacitor.” *Electrochim. Acta*, 439, 141685.

González, A., Goikolea, E., Barrena, J. A., and Mysyk, R. (2016a). “Review on supercapacitors: Technologies and materials.” *Renew. Sustain. Energy Rev.*, 58, 1189–1206.

González, A., Goikolea, E., Barrena, J. A., and Mysyk, R. (2016b). “Review on supercapacitors: Technologies and materials.” *Renew. Sustain. energy Rev.*, 58, 1189–1206.

Goodenough, J. B., and Park, K.-S. (2013). “The Li-ion rechargeable battery: a perspective.” *J. Am. Chem. Soc.*, 135(4), 1167–1176.

Gopi, C. V. V. M., Reddy, A. E., and Kim, H.-J. (2018). “Wearable superhigh energy density supercapacitors using a hierarchical ternary metal selenide composite of CoNiSe 2 microspheres decorated with CoFe 2 Se 4 nanorods.” *J. Mater. Chem. A*, 6(17), 7439–7448.

Govindasamy, M., Shanthi, S., Elaiyappillai, E., Wang, S.-F., Johnson, P. M., Ikeda, H., Hayakawa, Y., Ponnusamy, S., and Muthamizhchelvan, C. (2019). “Fabrication of hierarchical NiCo₂S₄@ CoS₂ nanostructures on highly conductive flexible carbon cloth substrate as a hybrid electrode material for supercapacitors with enhanced electrochemical performance.” *Electrochim. Acta*, 293, 328–337.

Grishchenko, L. M., Tsapyuk, G. G., Ricco, M., Diyuk, V. E., Boldyrieva, O. Y., Mariychuk, R., Matushko, I. P., Pontiroli, D., Lisnyak, V. V, and Scaravonati, S. (2020). “Enhancing the performance of supercapacitor activated carbon electrodes by oxidation.” *2020 IEEE 40th Int. Conf. Electron. Nanotechnol.*, IEEE, 173–177.

Gu, Y., Du, W., Darrat, Y., Saleh, M., Huang, Y., Zhang, Z., and Wei, S. (2020). “In situ growth of novel nickel diselenide nanoarrays with high specific capacity as the electrode material of flexible hybrid supercapacitors.” *Appl. Nanosci.*, 10, 1591–1601.

Guo, C. X., and Li, C. M. (2011). “A self-assembled hierarchical nanostructure comprising carbon spheres and graphene nanosheets for enhanced supercapacitor performance.” *Energy Environ. Sci.*, 4(11), 4504–4507.

Guo, D., Lai, L., Cao, A., Liu, H., Dou, S., and Ma, J. (2015a). “Nanoarrays: design, preparation and supercapacitor applications.” *Rsc Adv.*, 5(69), 55856–55869.

Guo, K., Yang, F., Cui, S., Chen, W., and Mi, L. (2016). “Controlled synthesis of 3D hierarchical NiSe microspheres for high-performance supercapacitor design.” *RSC Adv.*,

6(52), 46523–46530.

Guo, T., Zheng, D., Xu, G., Ding, Y., and Liu, D. (2023). “Two birds with one stone: facile fabrication of an iron–cobalt bimetallic sulfide nanosheet-assembled nanosphere for efficient energy storage and hydrogen evolution.” *Dalt. Trans.*, 52(41), 14896–14903.

Guo, W., Sun, W., and Wang, Y. (2015b). “Multilayer CuO@ NiO hollow spheres: microwave-assisted metal–organic-framework derivation and highly reversible structure-matched stepwise lithium storage.” *ACS Nano*, 9(11), 11462–11471.

Gupta, V., and Miura, N. (2006). “High performance electrochemical supercapacitor from electrochemically synthesized nanostructured polyaniline.” *Mater. Lett.*, 60(12), 1466–1469.

Haj, Y. Al, Balamurugan, J., Kim, N. H., and Lee, J. H. (2019). “Nitrogen-doped graphene encapsulated cobalt iron sulfide as an advanced electrode for high-performance asymmetric supercapacitors.” *J. Mater. Chem. A*, 7(8), 3941–3952.

Halper, M. S., and Ellenbogen, J. C. (2006). “Supercapacitors: A brief overview.” *MITRE Corp. McLean, Virginia, USA*, 1.

Han, J. H., Kwak, M., Kim, Y., and Cheon, J. (2018). “Recent advances in the solution-based preparation of two-dimensional layered transition metal chalcogenide nanostructures.” *Chem. Rev.*, 118(13), 6151–6188.

Hao, C., Wang, X., Wu, X., Guo, Y., Zhu, L., and Wang, X. (2022). “Composite material CCO/Co-Ni-Mn LDH made from sacrifice template CCO/ ZIF-67 for high-performance supercapacitor.” *Appl. Surf. Sci.*, 572(July 2021), 151373.

He, W., Wang, C., Li, H., Deng, X., Xu, X., and Zhai, T. (2017). “Ultrathin and Porous Ni₃S₂/CoNi₂S₄ 3D-Network Structure for Superhigh Energy Density Asymmetric Supercapacitors.” *Adv. Energy Mater.*, 7(21), 1–11.

He, X., Yang, M., Ni, P., Li, Y., and Liu, Z. H. (2010). “Rapid synthesis of hollow structured MnO₂ microspheres and their capacitance.” *Colloids Surfaces A Physicochem. Eng. Asp.*, 363(1–3), 64–70.

Hegde, S. S., and Bhat, B. R. (2024a). “Sustainable energy storage: Mangifera indica leaf waste-derived activated carbon for long-life, high-performance supercapacitors.” *RSC Adv.*, 14(12), 8028–8038.

Hegde, S. S., and Bhat, B. R. (2024b). “Impact of electrolyte concentration on

electrochemical performance of Cocos nucifera Waste-Derived High-Surface carbon for green energy storage.” *Fuel*, 371, 131999.

Heinze, J. (1984). “Cyclic voltammetry—‘electrochemical spectroscopy’. New analytical methods (25).” *Angew. Chemie Int. Ed. English*, 23(11), 831–847.

Helmholtz, H. v. (1853). “VON., ober einige Gesetzeder Verarbeitung elektrischer Strijme in Kdperlichen Leitern mit Anwendung auf die theorischelektrischen Versuche.” *Ann. Phys. u. Chem*, 89, 21.

Hongtao, L., Zichen, X., Lina, Z., Zhiqiang, Z., and Li, X. (2019). “The effects of different surfactants on the morphologies and electrochemical properties of MoS₂/reduce graphene oxide composites.” *Chem. Phys. Lett.*, 716, 6–10.

Hosseini, H., and Shahrokhian, S. (2019). “Self-supported nanoporous Zn–Ni–Co/Cu selenides microball arrays for hybrid energy storage and electrocatalytic water/urea splitting.” *Chem. Eng. J.*, 375, 122090.

Hou, L., Lian, L., Zhang, L., Pang, G., Yuan, C., and Zhang, X. (2015). “Self-sacrifice template fabrication of hierarchical mesoporous Bi-Component-Active ZnO/ZnFe₂O₄ sub-microcubes as superior anode towards high-performance lithium-ion battery.” *Adv. Funct. Mater.*, 25(2), 238–246.

Hu, H., Guan, B., Xia, B., and Lou, X. W. (2015). “Designed formation of Co₃O₄/NiCo₂O₄ double-shelled nanocages with enhanced pseudocapacitive and electrocatalytic properties.” *J. Am. Chem. Soc.*, 137(16), 5590–5595.

Hu, L., Huang, Y., Zhang, F., and Chen, Q. (2013). “CuO/Cu₂O composite hollow polyhedrons fabricated from metal–organic framework templates for lithium-ion battery anodes with a long cycling life.” *Nanoscale*, 5(10), 4186–4190.

Hu, P., Liu, Y., Liu, H., Wu, X., and Liu, B. (2021). “MnCo₂O₄ nanosheet/NiCo₂S₄ nanowire heterostructures as cathode materials for capacitors.” *ACS Appl. Nano Mater.*, 4(2), 2183–2189.

Hu, X., Liu, S., Chen, Y., Jiang, J., Cong, H., Tang, J., Sun, Y., Han, S., and Lin, H. (2020a). “Rational design of flower-like cobalt-manganese-sulfide nanosheets for high performance supercapacitor electrode materials.” *New J. Chem.*, 44(27), 11786–11795.

Hu, X., Liu, S., Chen, Y., Jiang, J., Sun, Y., Wang, L., Han, S., and Lin, H. (2020b). “One-step electrodeposition fabrication of iron cobalt sulfide nanosheet arrays on Ni foam for

- high-performance asymmetric supercapacitors.” *Ionics (Kiel)*, 26(4), 2095–2106.
- Huang, G., Zhang, L., Zhang, F., and Wang, L. (2014a). “Metal–organic framework derived Fe₂O₃@NiCo₂O₄ porous nanocages as anode materials for Li-ion batteries.” *Nanoscale*, 6(10), 5509–5515.
- Huang, H., and Niederberger, M. (2019). “Towards fast-charging technologies in Li⁺/Na⁺ storage: from the perspectives of pseudocapacitive materials and non-aqueous hybrid capacitors.” *Nanoscale*, 11(41), 19225–19240.
- Huang, X., Chafi, H., Matthews II, K. L., Carmichael, O., Li, T., Miao, Q., Wang, S., and Jia, G. (2019). “Magnetic resonance elastography of the brain: A study of feasibility and reproducibility using an ergonomic pillow-like passive driver.” *Magn. Reson. Imaging*, 59, 68–76.
- Huang, X., Sun, B., Chen, S., and Wang, G. (2014b). “Self-assembling synthesis of free-standing nanoporous graphene–transition-metal oxide flexible electrodes for high-performance lithium-ion batteries and supercapacitors.” *Chem. Asian J.*, 9(1), 206–211.
- Huang, X., Zhang, Z., Li, H., Zhao, Y., Wang, H., and Ma, T. (2017). “Novel fabrication of Ni₃S₂/MnS composite as high performance supercapacitor electrode.” *J. Alloys Compd.*, 722, 662–668.
- Hui, C., Kan, C., Mak, C., and Chau, K. (2019). “Flexible energy storage system—an introductory review of textile-based flexible supercapacitors.” *Processes*, 7(12), 922.
- Hulicova-Jurcakova, D., Sereych, M., Lu, G. Q., and Bandosz, T. J. (2009). “Combined effect of nitrogen- and oxygen-containing functional groups of microporous activated carbon on its electrochemical performance in supercapacitors.” *Adv. Funct. Mater.*, 19(3), 438–447.
- Huo, H., Zhao, Y., and Xu, C. (2014). “3D Ni₃S₂ nanosheet arrays supported on Ni foam for high-performance supercapacitor and non-enzymatic glucose detection.” *J. Mater. Chem. A*, 2(36), 15111–15117.
- Hussain, I., Sahoo, S., Lamiel, C., Nguyen, T. T., Ahmed, M., Xi, C., Iqbal, S., Ali, A., Abbas, N., and Javed, M. S. (2022). “Research progress and future aspects: Metal selenides as effective electrodes.” *Energy Storage Mater.*, 47, 13–43.
- Hussain, M., Alotaibi, B. M., Alrowaily, A. W., Alyousef, H. A., Alotiby, M. F., Abdullah, M., Al-Sehemi, A. G., Henaish, A. M. A., Ahmad, Z., and Aman, S. (2024). “Synthesis of

high-performance supercapacitor electrode materials by hydrothermal route based on ZnSe/MnSe composite.” *J. Phys. Chem. Solids*, 188, 111919.

Hwang, J. Y., El-Kady, M. F., Wang, Y., Wang, L., Shao, Y., Marsh, K., Ko, J. M., and Kaner, R. B. (2015). “Direct preparation and processing of graphene/RuO₂ nanocomposite electrodes for high-performance capacitive energy storage.” *Nano Energy*, 18, 57–70.

Iqbal, M. Z., Zakar, S., Haider, S. S., Afzal, A. M., Iqbal, M. J., Kamran, M. A., and Numan, A. (2020a). “Electrodeposited CuMnS and CoMnS electrodes for high-performance asymmetric supercapacitor devices.” *Ceram. Int.*, 46(13), 21343–21350.

Iqbal, M. Z., Zakar, S., Tayyab, M., Haider, S. S., Alzaid, M., Afzal, A. M., and Aftab, S. (2020b). “Scrutinizing the charge storage mechanism in SrO based composites for asymmetric supercapacitors by diffusion-controlled process.” *Appl. Nanosci.*, 10(11), 3999–4011.

Iro, Z. S., Subramani, C., and Dash, S. S. (2016). “A brief review on electrode materials for supercapacitor.” *Int. J. Electrochem. Sci.*, 11(12), 10628–10643.

Isacfranklin, M., Rathinam, Y., Ganesan, R., and Velauthapillai, D. (2023). “Direct growth of binder-free CNTs on a nickel foam substrate for highly efficient symmetric supercapacitors.” *ACS omega*, 8(13), 11700–11708.

Javed, M. S., Najam, T., Sajjad, M., Shah, S. S. A., Hussain, I., Idrees, M., Imran, M., Assiri, M. A., and Siyal, S. H. (2021). “Design and fabrication of highly porous 2D bimetallic sulfide ZnS/FeS composite nanosheets as an advanced negative electrode material for supercapacitors.” *Energy & Fuels*, 35(18), 15185–15191.

Javed, M. S., Shah, S. S. A., Hussain, S., Tan, S., and Mai, W. (2020a). “Mesoporous manganese-selenide microflowers with enhanced electrochemical performance as a flexible symmetric 1.8 V supercapacitor.” *Chem. Eng. J.*, 382, 122814.

Javed, M. S., Shah, S. S. A., Hussain, S., Tan, S., and Mai, W. (2020b). “Mesoporous manganese-selenide microflowers with enhanced electrochemical performance as a flexible symmetric 1.8 V supercapacitor.” *Chem. Eng. J.*, 382(July 2019), 122814.

Jevtovic, V., Khan, A. U., Almarhoon, Z. M., Tahir, K., Latif, S., Abdulaziz, F., Albalawi, K., Zaki, M. E. A., and Rakic, V. (2023). “Synthesis of MnSe-Based GO Composites as Effective Photocatalyst for Environmental Remediations.” *Nanomaterials*, 13(4).

Jia, H., Wang, Z., Zheng, X., Cai, Y., Lin, J., Liang, H., Qi, J., Cao, J., Feng, J., and Fei,

- W. (2019). “Controlled synthesis of MOF-derived quadruple-shelled CoS₂ hollow dodecahedrons as enhanced electrodes for supercapacitors.” *Electrochim. Acta*, 312, 54–61.
- Jiang, J., Sun, Y., Chen, Y., Hu, X., Zhu, L., and Chen, H. (2019). “materials One-step synthesis of nickel cobalt sulfide nanostructure for high-performance supercapacitor.” *J. Mater. Sci.*, 54(18), 11936–11950.
- Jiang, Y., and Liu, J. (2019). “Definitions of pseudocapacitive materials: a brief review.” *Energy Environ. Mater.*, 2(1), 30–37.
- Jing, C., Dong, B., and Zhang, Y. (2020a). “Chemical modifications of layered double hydroxides in the supercapacitor.” *Energy Environ. Mater.*, 3(3), 346–379.
- Jing, C., Liu, X. D., Li, K., Liu, X., Dong, B., Dong, F., and Zhang, Y. (2021). “The pseudocapacitance mechanism of graphene/CoAl LDH and its derivatives: Are all the modifications beneficial?” *J. Energy Chem.*, 52, 218–227.
- Jing, C., Song, X., Li, K., Zhang, Y., Liu, X., Dong, B., Dong, F., Zhao, S., Yao, H., and Zhang, Y. (2020b). “Optimizing the rate capability of nickel cobalt phosphide nanowires on graphene oxide by the outer/inter-component synergistic effects.” *J. Mater. Chem. A*, 8(4), 1697–1708.
- Joyline, F., Rodney, J. D., Chul, B., and Bhat, R. (2024). “Significance of transition metal (Co , Ni and Zn) doping on the nano MnSe for high-performance supercapacitor electrode.” *J. Alloys Compd.*, 986(December 2023), 173957.
- Junita, J., Jayalakshmi, D., and Rodney, J. D. (2023). “Combustion-derived BaNiO₃ nanoparticles as a potential bifunctional electrocatalyst for overall water splitting.” *Int. J. Hydrogen Energy*, 48(38), 14287–14298.
- Kalair, A., Abas, N., Saleem, M. S., Kalair, A. R., and Khan, N. (2021). “Role of energy storage systems in energy transition from fossil fuels to renewables.” *Energy Storage*, 3(1).
- Kalaji, M., Murphy, P. J., and Williams, G. O. (1999). “The study of conducting polymers for use as redox supercapacitors.” *Synth. Met.*, 102(1–3), 1360–1361.
- Kanade, C., Arbu, S., Kanade, K., Kim, K. S., Yeom, G. Y., Kim, T., and Kale, B. (2018). “Hierarchical nanostructures of nitrogen-doped molybdenum sulphide for supercapacitors.” *RSC Adv.*, 8(69), 39749–39755.
- Kandula, S., Shrestha, K. R., Kim, N. H., and Lee, J. H. (2018). “Fabrication of a 3D

hierarchical sandwich Co₉S₈/α-MnS@N-C@MoS₂ nanowire architectures as advanced electrode material for high performance hybrid supercapacitors.” *Small*, 14(23), 1800291.

Kaneti, Y. V, Zakaria, Q. M. D., Zhang, Z., Chen, C., Yue, J., Liu, M., Jiang, X., and Yu, A. (2014). “Solvothermal synthesis of ZnO-decorated α-Fe₂O₃ nanorods with highly enhanced gas-sensing performance toward n-butanol.” *J. Mater. Chem. A*, 2(33), 13283–13292.

Kang, C., Ma, L., Chen, Y., Fu, L., Hu, Q., Zhou, C., and Liu, Q. (2022). “Metal-organic framework derived hollow rod-like NiCoMn ternary metal sulfide for high-performance asymmetric supercapacitors.” *Chem. Eng. J.*, 427(June 2021), 131003.

Karnan, M., Subramani, K., and Sathish, M. (2017). “Template assisted synthesis of nitrogen doped 3d-graphene for supercapacitor applications.” *Mater. Today Proc.*, 4(11), 12144–12151.

Karuppasamy, K., Vikraman, D., Hussain, S., Kumar Veerasubramani, G., Santhoshkumar, P., Lee, S. H., Bose, R., Kathalingam, A., and Kim, H. S. (2022a). “Unveiling a binary metal selenide composite of CuSe polyhedrons/CoSe₂ nanorods decorated graphene oxide as an active electrode material for high-performance hybrid supercapacitors.” *Chem. Eng. J.*, 427(July 2021), 131535.

Karuppasamy, K., Vikraman, D., Hussain, S., Veerasubramani, G. K., Santhoshkumar, P., Lee, S.-H., Bose, R., Kathalingam, A., and Kim, H.-S. (2022b). “Unveiling a binary metal selenide composite of CuSe polyhedrons/CoSe₂ nanorods decorated graphene oxide as an active electrode material for high-performance hybrid supercapacitors.” *Chem. Eng. J.*, 427, 131535.

Kaushik, P., Rastogi, C. K., Channegowda, M., Patel, A., and Gyanprakash, M. (2023). “Investigating electrochemical properties of iron oxide-carbon nanotube composite for supercapacitor application.” *Mater. Today Proc.*, 74, 324–328.

Khandelwal, M., and Kumar, A. (2015). “One-step chemically controlled wet synthesis of graphene nanoribbons from graphene oxide for high performance supercapacitor applications.” *J. Mater. Chem. A*, 3(45), 22975–22988.

Kim, B. K., Sy, S., Yu, A., and Zhang, J. (2015a). “Electrochemical supercapacitors for energy storage and conversion.” *Handb. clean energy Syst.*, 1–25.

Kim, B. K., Sy, S., Yu, A., and Zhang, J. (2015b). “Electrochemical Supercapacitors for

Energy Storage and Conversion.” *Handb. Clean Energy Syst.*, 1–25.

Kim, B. K., Sy, S., Yu, A., and Zhang, J. (2015c). “Electrochemical Supercapacitors for Energy Storage and Conversion.” *Handb. Clean Energy Syst.*, John Wiley & Sons, Ltd, 1–25.

Kim, H. W., Lee, Y., Song, D. H., Kwon, Y. K., Kim, E. J., and Cho, E. A. (2020). “Cu₃P/PAN derived N-doped carbon catalyst with non-toxic synthesis for alkaline hydrogen evolution reaction.” *Sustain. Energy Fuels*, 4(10), 5247–5253.

Kirubasankar, B., Murugadoss, V., Lin, J., Ding, T., Dong, M., Liu, H., Zhang, J., Li, T., Wang, N., and Guo, Z. (2018). “In situ grown nickel selenide on graphene nanohybrid electrodes for high energy density asymmetric supercapacitors.” *Nanoscale*, 10(43), 20414–20425.

Ko, Y. N., Choi, S. H., and Kang, Y. C. (2016). “Hollow cobalt selenide microspheres: synthesis and application as anode materials for Na-ion batteries.” *ACS Appl. Mater. Interfaces*, 8(10), 6449–6456.

Kong, W., Li, J., Gong, J., Yu, Q., Chen, G., Chen, J., Dai, Y., Pu, L., Zhang, H., and Wang, W. (2023). “Three-dimensional network structured MnCo₂S₄/NiCo₂S₄ electrode materials assembled with two-dimensional nanosheets as basic building units for asymmetric supercapacitor applications.” *J. Alloys Compd.*, 940, 168480.

Kötz, R., and Carlen, M. (2000). “Principles and applications of electrochemical capacitors.” *Electrochim. Acta*, 45(15–16), 2483–2498.

Kovalska, E., and Kocabas, C. (2016). “Organic electrolytes for graphene-based supercapacitor: Liquid, gel or solid.” *Mater. Today Commun.*, 7, 155–160.

Kuang, M., Li, T. T., Chen, H., Zhang, S. M., Zhang, L. L., and Zhang, Y. X. (2015). “Hierarchical Cu₂O/CuO/Co₃O₄ core-shell nanowires: Synthesis and electrochemical properties.” *Nanotechnology*, 26(30).

Kuilla, T., Bhadra, S., Yao, D., Kim, N. H., Bose, S., and Lee, J. H. (2010). “Recent advances in graphene based polymer composites.” *Prog. Polym. Sci.*, 35(11), 1350–1375.

Kumagai, S., Mukaiyachi, K., and Tashima, D. (2015). “Rate and cycle performances of supercapacitors with different electrode thickness using non-aqueous electrolyte.” *J. Energy Storage*, 3, 10–17.

Kumar, K. A., Pandurangan, A., Arumugam, S., and Sathiskumar, M. (2019). “Effect of

Bi-functional Hierarchical Flower-like CoS Nanostructure on its Interfacial Charge Transport Kinetics , Magnetic and Electrochemical Behaviors for Supercapacitor and DSSC Applications.” *Sci. Rep.*, (June 2018), 1–16.

Kundu, J., Khilari, S., Bhunia, K., and Pradhan, D. (2019). “Ni-Doped CuS as an efficient electrocatalyst for the oxygen evolution reaction.” *Catal. Sci. Technol.*, 9(2), 406–417.

Kunwar, R., Harilal, M., Krishnan, S. G., Pal, B., Misnon, I. I., Mariappan, C. R., Ezema, F. I., Elim, H. I., Yang, C.-C., and Jose, R. (2019). “Pseudocapacitive charge storage in thin nanobelts.” *Adv. Fiber Mater.*, 1, 205–213.

Lakshmi, K. C. S., and Vedhanarayanan, B. (2023). “High-performance supercapacitors: A comprehensive review on paradigm shift of conventional energy storage devices.” *Batteries*, 9(4), 202.

Lee, C., Wei, X., Kysar, J. W., and Hone, J. (2008). “Measurement of the elastic properties and intrinsic strength of monolayer graphene.” *Science (80-.)*, 321(5887), 385–388.

Lee, Y.-W., Kim, B.-S., Hong, J., Lee, J., Pak, S., Jang, H.-S., Whang, D., Cha, S., Sohn, J. I., and Kim, J. M. (2016). “A pseudo-capacitive chalcogenide-based electrode with dense 1-dimensional nanoarrays for enhanced energy density in asymmetric supercapacitors.” *J. Mater. Chem. A*, 4(26), 10084–10090.

Lei, Z., Zhang, J., and Zhao, X. S. (2012). “Ultrathin MnO₂ nanofibers grown on graphitic carbon spheres as high-performance asymmetric supercapacitor electrodes.” *J. Mater. Chem.*, 22(1), 153–160.

Li, C., Balamurugan, J., Kim, N. H., and Lee, J. H. (2018). “Hierarchical Zn–Co–S Nanowires as Advanced Electrodes for All Solid State Asymmetric Supercapacitors.” *Adv. Energy Mater.*, 8(8).

Li, H., Yu, K., Fu, H., Guo, B., Lei, X., and Zhu, Z. (2015). “MoS₂/graphene hybrid nanoflowers with enhanced electrochemical performances as anode for lithium-ion batteries.” *J. Phys. Chem. C*, 119(14), 7959–7968.

Li, L., Jiang, Y., Guo, C., Han, K., Cui, X., He, C., Chen, Y., and Yang, Y. (2024). “Mechanochemical production of graphene/amorphous carbon/Mn₃O₄ nanocomposites for asymmetric supercapacitor.” *Appl. Surf. Sci.*, 653, 159388.

Li, M., Liang, J., Chai, Y., Li, D., Lu, J., and Li, L. (2017a). “One-step synthesis of alpha-MnS nanosheets for supercapacitor electrode materials.” *Micro Nano Lett.*, 12(10), 735–

737.

Li, N., Tang, S., Dai, Y., and Meng, X. (2014). “The synthesis of graphene oxide nanostructures for supercapacitors: a simple route.” *J. Mater. Sci.*, 49, 2802–2809.

Li, N., Zhang, Y., Zhao, H., Liu, Z., Zhang, X., and Du, Y. (2016). “Synthesis of High-Quality α -MnSe Nanostructures with Superior Lithium Storage Properties.” *Inorg. Chem.*, 55(6), 2765–2770.

Li, X., Du, D., Zhang, Y., Xing, W., Xue, Q., and Yan, Z. (2017b). “Layered double hydroxides toward high-performance supercapacitors.” *J. Mater. Chem. A*, 5(30), 15460–15485.

Li, X., Rong, J., and Wei, B. (2010). “Electrochemical behavior of single-walled carbon nanotube supercapacitors under compressive stress.” *ACS Nano*, 4(10), 6039–6049.

Li, Z., Hu, B., Yu, R., Tian, T., Guo, Z., Mu, J., Zhang, X., Wang, G., Liu, X., and Liu, A. (2023). “Hollow cobalt selenide nanospheres wrapped with reduced graphene oxide nanosheets as electrodes for hybrid supercapacitor.” *Appl. Surf. Sci.*, 608, 155237.

Liang, J., Huang, Y., Oh, J., Kozlov, M., Sui, D., Fang, S., Baughman, R. H., Ma, Y., and Chen, Y. (2011). “Electromechanical actuators based on graphene and graphene/Fe₃O₄ hybrid paper.” *Adv. Funct. Mater.*, 21(19), 3778–3784.

Liang, J., Huang, Y., Zhang, L., Wang, Y., Ma, Y., Guo, T., and Chen, Y. (2009). “Molecular-level dispersion of graphene into poly (vinyl alcohol) and effective reinforcement of their nanocomposites.” *Adv. Funct. Mater.*, 19(14), 2297–2302.

Liao, X., Hou, X., Yi, C., Wang, G., Wang, S., Yang, Y., Chen, C., Yu, D., Liu, Y., and Zhou, X. (2024). “Construction and application of NiCo₂O₄@MnS composite with hierarchical structure for hybrid supercapacitor.” *Dalt. Trans.*

Libich, J., Máca, J., Vondrák, J., Čech, O., and Sedlaříková, M. (2018). “Supercapacitors: Properties and applications.” *J. Energy Storage*, 17(March), 224–227.

Liivand, K., Thomberg, T., Jänes, A., and Lust, E. (2015). “Separator materials influence on supercapacitors performance in viscous electrolytes.” *ECS Trans.*, 64(20), 41.

Lin, J., Zhang, Y., Zhang, Q., Shang, J., and Deng, F. (2021). “Enhanced adsorption properties of organic ZnCr-LDH synthesized by soft template method for anionic dyes.” *Environ. Sci. Pollut. Res.*, 28(35), 48236–48252.

Lindstro, H., So, S., Solbrand, A., Hjelm, J., Hagfeldt, A., and Lindquist, S. (1997). “Li +

Ion Insertion in TiO₂ (Anatase). 2 . Voltammetry on Nanoporous Films.” 2(97), 7717–7722.

Liu, B., Liu, Z., Li, D., Guo, P., Liu, D., Shang, X., Lv, M., and He, D. (2017). “Nanoscale α -MnS crystallites grown on N-S co-doped rGO as a long-life and high-capacity anode material of Li-ion batteries.” *Appl. Surf. Sci.*, 416, 858–867.

Liu, C., Yu, Z., Neff, D., Zhamu, A., and Jang, B. Z. (2010a). “Graphene-based supercapacitor with an ultrahigh energy density.” *Nano Lett.*, 10(12), 4863–4868.

Liu, G., Cai, B., Hu, Z., Gu, H., Zhou, J., Xu, R., Liu, Y., Xu, J., and Jiang, Y. (2024a). “Fe₂O₃@ FeSe₂ heterostructure as high-performance supercapacitor negative electrode material.” *J. Energy Storage*, 88, 111544.

Liu, H., Liu, Y., and Li, J. (2010b). “Ionic liquids in surface electrochemistry.” *Phys. Chem. Chem. Phys.*, 12(8), 1685–1697.

Liu, J., Wang, J., Xu, C., Jiang, H., Li, C., Zhang, L., Lin, J., and Shen, Z. X. (2018a). “Advanced Energy Storage Devices: Basic Principles, Analytical Methods, and Rational Materials Design.” *Adv. Sci.*, 5(1).

Liu, J., Wang, J., Xu, C., Jiang, H., Li, C., Zhang, L., Lin, J., and Shen, Z. X. (2018b). “Advanced energy storage devices: basic principles, analytical methods, and rational materials design.” *Adv. Sci.*, 5(1), 1700322.

Liu, K., Liu, H., Wang, J., and Shi, L. (2009a). “Synthesis and characterization of Cu₂Se prepared by hydrothermal co-reduction.” *J. Alloys Compd.*, 484(1–2), 674–676.

Liu, L., Zhao, H., and Lei, Y. (2019a). “Review on nanoarchitected current collectors for pseudocapacitors.” *Small Methods*, 3(8), 1800341.

Liu, Q., Yang, J., Luo, X., Miao, Y., Zhang, Y., Xu, W., Yang, L., Liang, Y., Weng, W., and Zhu, M. (2020a). “Fabrication of a fibrous MnO₂@ MXene/CNT electrode for high-performance flexible supercapacitor.” *Ceram. Int.*, 46(8), 11874–11881.

Liu, S., and Jun, S. C. (2017). “Hierarchical manganese cobalt sulfide core–shell nanostructures for high-performance asymmetric supercapacitors.” *J. Power Sources*, 342, 629–637.

Liu, S., Sarwar, S., Wang, J., Zhang, H., Li, T., Luo, J., and Zhang, X. (2021). “The microwave synthesis of porous CoSe₂ nanosheets for super cycling performance supercapacitors.” *J. Mater. Chem. C*, 9(1), 228–237.

- Liu, S., Yin, Y., Hui, K. S., Hui, K. N., Lee, S. C., and Jun, S. C. (2018c). “High-performance flexible quasi-solid-state supercapacitors realized by molybdenum dioxide@nitrogen-doped carbon and copper cobalt sulfide tubular nanostructures.” *Adv. Sci.*, 5(10), 1800733.
- Liu, S., Yin, Y., Hui, K. S., Hui, K. N., Lee, S. C., and Jun, S. C. (2018d). “High-Performance Flexible Quasi-Solid-State Supercapacitors Realized by Molybdenum Dioxide @ Nitrogen-Doped Carbon and Copper Cobalt Sulfide Tubular Nanostructures.” 1800733.
- Liu, S., Yin, Y., Hui, K. S., Hui, K. N., Lee, S. C., and Jun, S. C. (2018e). “High-Performance Flexible Quasi-Solid-State Supercapacitors Realized by Molybdenum Dioxide@Nitrogen-Doped Carbon and Copper Cobalt Sulfide Tubular Nanostructures.” *Adv. Sci.*, 5(10).
- Liu, S., Yin, Y., Shen, Y., Hui, K. S., Chun, Y. T., Kim, J. M., Hui, K. N., Zhang, L., and Jun, S. C. (2020b). “Phosphorus regulated cobalt oxide@nitrogen-doped carbon nanowires for flexible quasi-solid-state supercapacitors.” *Small*, 16(4), 1906458.
- Liu, W., Niu, H., Yang, J., Cheng, K., Ye, K., Zhu, K., Wang, G., Cao, D., and Yan, J. (2018f). “Ternary transition metal sulfides embedded in graphene nanosheets as both the anode and cathode for high-performance asymmetric supercapacitors.” *Chem. Mater.*, 30(3), 1055–1068.
- Liu, X., Du, J., Li, C., Han, X., Hu, X., Cheng, F., and Chen, J. (2015). “The anion effect on the oxygen reduction of MnX (X = O, S, and Se) catalysts.” *J. Mater. Chem. A*, 3(7), 3425–3431.
- Liu, X., Ma, J., Peng, P., and Zheng, W. (2009b). “Hydrothermal synthesis of cubic MnSe₂ and octahedral α -MnSe microcrystals.” *J. Cryst. Growth*, 311(5), 1359–1363.
- Liu, X., Zhang, D., Ma, Y., Li, G., Yuan, X., Huang, Y., Liu, G., Guo, M., and Zheng, W. (2024b). “M²⁺-Doped Nickel Selenide Nanoflowers (M= Co, Cu, and Zn) for Supercapacitors.” *ACS Appl. Nano Mater.*
- Liu, Y., Li, Y., Kang, H., Jin, T., and Jiao, L. (2016). “Design, synthesis, and energy-related applications of metal sulfides.” *Mater. Horizons*, 3(5), 402–421.
- Liu, Y., Zhang, B., Wang, F., Wen, Z., and Wu, Y. (2014). “Nanostructured intercalation compounds as cathode materials for supercapacitors.” *Pure Appl. Chem.*, 86(5), 593–609.

- Liu, Z., Qin, A., Yang, B., Wang, D., and Zhang, Z. (2019b). “Flower-like MoS₂ onto nitrogen-doped 3D graphene composite with active material for supercapacitor electrodes.” *Mater. Lett.*, 240, 258–261.
- Lokhande, C. D., Dubal, D. P., and Joo, O.-S. (2011). “Metal oxide thin film based supercapacitors.” *Curr. Appl. Phys.*, 11(3), 255–270.
- Lokhande, V. C., Lokhande, A. C., Lokhande, C. D., Kim, J. H., and Ji, T. (2016). “Supercapacitive composite metal oxide electrodes formed with carbon, metal oxides and conducting polymers.” *J. Alloys Compd.*, 682, 381–403.
- Lu, J., Pu, L., Wang, W., and Dai, Y. (2020). “Construction of hierarchical cobalt-molybdenum selenide hollow nanospheres architectures for high performance battery-supercapacitor hybrid devices.” *J. Colloid Interface Sci.*, 563, 435–446.
- Lu, T., Dong, S., Zhang, C., Zhang, L., and Cui, G. (2017). “Fabrication of transition metal selenides and their applications in energy storage.” *Coord. Chem. Rev.*, Elsevier B.V.
- Lv, M., Zhang, X., Wang, F., Yu, T., and Lv, H. (2020). “Flexible 3D core – shell nanoforest arrays trimetal electrode for high capacitance supercapacitor.”
- Ma, F., Dai, X., Jin, J., Tie, N., and Dai, Y. (2020a). “Hierarchical core-shell hollow CoMoS₄@ Ni–Co–S nanotubes hybrid arrays as advanced electrode material for supercapacitors.” *Electrochim. Acta*, 331, 135459.
- Ma, F., Lu, J., Pu, L., Wang, W., and Dai, Y. (2020b). “Construction of hierarchical cobalt-molybdenum selenide hollow nanospheres architectures for high performance battery-supercapacitor hybrid devices.” *J. Colloid Interface Sci.*, 563, 435–446.
- Ma, Z., Sun, Z., Jiang, H., Li, F., Wang, Q., and Qu, F. (2020c). “Nanoporous electrospun NiCo₂S₄ embedded in carbon fiber as an excellent electrode for high-rate supercapacitors.” *Appl. Surf. Sci.*, 533, 147521.
- Malavekar, D. B., Bulakhe, R. N., Kale, S. B., Patil, U. M., In, I., and Lokhande, C. D. (2021). “Synthesis of layered copper selenide on reduced graphene oxide sheets via SILAR method for flexible asymmetric solid-state supercapacitor.” *J. Alloys Compd.*, 869, 159198.
- Malavekar, D. B., Kale, S. B., Lokhande, V. C., Patil, U. M., Kim, J. H., and Lokhande, C. D. (2020). “Chemically synthesized Cu₃Se₂ film based flexible solid-state symmetric supercapacitor: effect of reaction bath temperature.” *J. Phys. Chem. C*, 124(52), 28395–28406.

Manikandan, R., Justin Raj, C., Nagaraju, G., Velayutham, R., Moulton, S. E., Puigdollers, J., and Chul Kim, B. (2021). “Selenium enriched hybrid metal chalcogenides with enhanced redox kinetics for high-energy density supercapacitors.” *Chem. Eng. J.*, 414(January), 128924.

Manuscript, A. (2017). “Materials Chemistry A.”

Marcano, D. C., Kosynkin, D. V., Berlin, J. M., Sinitskii, A., Sun, Z., Slesarev, A., Alemany, L. B., Lu, W., and Tour, J. M. (2010). “Improved synthesis of graphene oxide.” *ACS Nano*, 4(8), 4806–4814.

Mascarenhas, F. J., Rodney, J. D., Mishra, P., and Bhat, B. R. (2023). “Revolutionizing energy storage: A novel Cu₂Se-GO nanocomposite for supercapacitors.” *Inorg. Chem. Commun.*, 156(August), 111253.

Masikhwa, T. M., Madito, M. J., Bello, A., Dangbegnon, J. K., and Manyala, N. (2017). “High performance asymmetric supercapacitor based on molybdenum disulphide/graphene foam and activated carbon from expanded graphite.” *J. Colloid Interface Sci.*, 488, 155–165.

Matsumoto, H., Imaizumi, S., Konosu, Y., Ashizawa, M., Minagawa, M., Tanioka, A., Lu, W., and Tour, J. M. (2013). “Electrospun composite nanofiber yarns containing oriented graphene nanoribbons.” *ACS Appl. Mater. Interfaces*, 5(13), 6225–6231.

Mei, W., Chen, H., Sun, J., and Wang, Q. (2019). “The effect of electrode design parameters on battery performance and optimization of electrode thickness based on the electrochemical–thermal coupling model.” *Sustain. energy fuels*, 3(1), 148–165.

Melkiyur, I., Rathinam, Y., Kumar, P. S., Sankaiya, A., Pitchaiya, S., Ganesan, R., and Velauthapillai, D. (2023). “A comprehensive review on novel quaternary metal oxide and sulphide electrode materials for supercapacitor: Origin, fundamentals, present perspectives and future aspects.” *Renew. Sustain. Energy Rev.*, 173(April 2022).

Meng, Q., Cai, K., Chen, Y., and Chen, L. (2017). “Research progress on conducting polymer based supercapacitor electrode materials.” *Nano Energy*, 36, 268–285.

Meng, X., Deng, J., Zhu, J., Bi, H., Kan, E., and Wang, X. (2016). “Cobalt sulfide/graphene composite hydrogel as electrode for high-performance pseudocapacitors.” *Sci. Rep.*, 6(1), 21717.

Miah, M., Hota, P., Mondal, T. K., Chen, R., and Saha, S. K. (2023). “Mixed metal sulfides

(FeNiS₂) nanosheets decorated reduced graphene oxide for efficient electrode materials for supercapacitors.” *J. Alloys Compd.*, 933, 167648.

Miao, C., Fang, Y., Zhu, K., Zhou, C., Ye, K., Yan, J., Cao, D., Wang, G., Xu, P., and Xie, C. (2021). “Binder-free ultrathin α -MnSe nanosheets for high performance supercapacitor.” *J. Alloys Compd.*, 885.

Miao, C., Xu, P., Zhao, J., Zhu, K., Cheng, K., Ye, K., Yan, J., Cao, D., Wang, G., and Zhang, X. (2019). “Binder-Free Hierarchical Urchin-like Manganese-Cobalt Selenide with High Electrochemical Energy Storage Performance.” *ACS Appl. Energy Mater.*, 2(5), 3595–3604.

Miller, J. R. (2018). “Perspective on electrochemical capacitor energy storage.” *Appl. Surf. Sci.*, 460, 3–7.

Ming, F., Liang, H., Shi, H., Xu, X., Mei, G., and Wang, Z. (2016). “MOF-derived Co-doped nickel selenide/C electrocatalysts supported on Ni foam for overall water splitting.” *J. Mater. Chem. A*, 4(39), 15148–15155.

Miralles, C., Lana-Villarreal, T., and Gómez, R. (2023). “Unraveling the Phase Transition Behavior of MgMn₂O₄ Electrodes for Their Use in Rechargeable Magnesium Batteries.” *Materials (Basel)*, 16(15).

Mohamed, S. G., Attia, S. Y., and Hassan, H. H. (2017). “Spinel-structured FeCo₂O₄ mesoporous nanosheets as efficient electrode for supercapacitor applications.” *Microporous Mesoporous Mater.*, 251, 26–33.

Mohammadi Zardkhoshoui, A., Hayati Monjoghtapeh, R., and Hosseiny Davarani, S. S. (2020). “Zn–Ni–Se@ NiCo₂S₄ core–shell architectures: a highly efficient positive electrode for hybrid supercapacitors.” *Energy & Fuels*, 34(11), 14934–14947.

Mohapatra, S., Acharya, A., and Roy, G. S. (2012). “The role of nanomaterial for the design of supercapacitor.” *Lat. Am. J. Phys. Educ.*, 6(3), 380–384.

Mohapatra, S., Das, H. T., Chandra Tripathy, B., and Das, N. (2024). “Exploring the Bifunctionality of Co₃S₄/NiS₂/Cu₂S Heterojunction Nanocomposites for Hybrid Supercapacitors and Double Z-Scheme-Driven Dye Degradation.” *ACS Appl. Nano Mater.*

Mondal, I., and Pal, U. (2016). “Synthesis of MOF templated Cu/CuO@ TiO₂ nanocomposites for synergistic hydrogen production.” *Phys. Chem. Chem. Phys.*, 18(6), 4780–4788.

- Mondal, R., Mishra, N. K., Maiyalagan, T., Gupta, A., and Singh, P. (2021). “La_{1-x}K_xFeO_{3-δ}: An Anion Intercalative Pseudocapacitive Electrode for Supercapacitor Application.” *ACS Omega*, 6(45), 30488–30498.
- Moosavifard, S. E., Mohammadi, A., Darzi, M. E., Kariman, A., Abdi, M. M., and Karimi, G. (2021a). “A facile strategy to synthesis graphene-wrapped nanoporous copper-cobalt-selenide hollow spheres as an efficient electrode for hybrid supercapacitors.” *Chem. Eng. J.*, 415, 128662.
- Moosavifard, S. E., Mohammadi, A., Ebrahimnejad Darzi, M., Kariman, A., Abdi, M. M., and Karimi, G. (2021b). “A facile strategy to synthesis graphene-wrapped nanoporous copper-cobalt-selenide hollow spheres as an efficient electrode for hybrid supercapacitors.” *Chem. Eng. J.*, 415.
- Murugan, E., Govindaraju, S., and Santhoshkumar, S. (2021). “Hydrothermal synthesis, characterization and electrochemical behavior of NiMoO₄ nanoflower and NiMoO₄/rGO nanocomposite for high-performance supercapacitors.” *Electrochim. Acta*, 392, 138973.
- Muzaffar, A., Ahamed, M. B., Deshmukh, K., and Thirumalai, J. (2019). “A review on recent advances in hybrid supercapacitors: Design, fabrication and applications.” *Renew. Sustain. energy Rev.*, 101, 123–145.
- Niu, C., Sichel, E. K., Hoch, R., Moy, D., and Tennent, H. (1997). “High power electrochemical capacitors based on carbon nanotube electrodes.” *Appl. Phys. Lett.*, 70(11), 1480–1482.
- Ogata, C., Kurogi, R., Hatakeyama, K., Taniguchi, T., Koinuma, M., and Matsumoto, Y. (2016). “All-graphene oxide device with tunable supercapacitor and battery behaviour by the working voltage.” *Chem. Commun.*, 52(20), 3919–3922.
- Ortega, P. F. R., Santos Jr, G. A. dos, Trigueiro, J. P. C., Silva, G. G., Quintanal, N., Blanco, C., Lavall, R. L., and Santamaría, R. (2020). “Insights on the behavior of imidazolium ionic liquids as electrolytes in carbon-based supercapacitors: an applied electrochemical approach.” *J. Phys. Chem. C*, 124(29), 15818–15830.
- Ou, M., Ma, L., Xu, L., Yang, Z., and Li, H. (2016). “Hydrothermal Synthesis of Few-Layer and Edge-Rich Cobalt-Doped Molybdenum Selenide/Nitrogenated Graphene Composite and Investigation of Its Electrocatalytic Activity for Hydrogen Evolution Reaction.” *Nano*, 11(10), 1–8.

- Palaniyandy, N., Nkosi, F. P., Raju, K., and Ozoemena, K. I. (2019). “Conversion of electrolytic MnO₂ to Mn₃O₄ nanowires for high-performance anode materials for lithium-ion batteries.” *J. Electroanal. Chem.*, 833, 79–92.
- Pan, C., and Dong, L. (2024). “Synthesis and Electrochemical Performance of Flexible and Freestanding Graphene-Encapsulated PANi@ MnO₂/ECNFs Nanoscale Architectures for Electrochemical Supercapacitors.” *Russ. J. Electrochem.*, 60(4), 290–302.
- Panah, T. S., Shirvani, M., and Davarani, S. S. H. (2024). “Bimetallic NiCo₂Se₄/Fe₂CoSe₄ chrysanthemum flowers assembled by nanosheets: An efficient electrode material for hybrid supercapacitor applications.” *J. Alloys Compd.*, 978, 173496.
- Pandit, N., Singh, P., Prasad, S., Keshri, A. K., Czagany, M., Hompoth, S., Gacsi, Z., and Baumli, P. (2023). “Electrochemical behavior of GNP/CNT porous composite for supercapacitor.” *Chem. Phys. Lett.*, 827, 140695.
- Pandolfo, A. G., and Hollenkamp, A. F. (2006). “Carbon properties and their role in supercapacitors.” *J. Power Sources*, 157(1), 11–27.
- Patil, S. J., Bulakhe, R. N., and Lokhande, C. D. (2015). “Nanoflake-Modulated La₂Se₃ Thin Films Prepared for an Asymmetric Supercapacitor Device.” *Chempluschem*, 80(9), 1478–1487.
- Patil, S. S., Bhat, T. S., Teli, A. M., Beknalkar, S. A., Dhavale, S. B., Faras, M. M., Karanjkar, M. M., and Patil, P. S. (2020). “Hybrid solid state supercapacitors (HSSC’s) for high energy & power density: an overview.” *Eng. Sci.*, 12(4), 38–51.
- Patil, U. M., Nam, M. S., Kang, S., Sohn, J. S., Sim, H. B., Kang, S., and Jun, S. C. (2016). “Fabrication of ultra-high energy and power asymmetric supercapacitors based on hybrid 2D MoS₂/graphene oxide composite electrodes: A binder-free approach.” *RSC Adv.*, 6(49), 43261–43271.
- Peng, C., Jin, J., and Chen, G. Z. (2007). “A comparative study on electrochemical co-deposition and capacitance of composite films of conducting polymers and carbon nanotubes.” *Electrochim. Acta*, 53(2), 525–537.
- Peng, H., Ma, G., Sun, K., Zhang, Z., Li, J., Zhou, X., and Lei, Z. (2015). “A novel aqueous asymmetric supercapacitor based on petal-like cobalt selenide nanosheets and nitrogen-doped porous carbon networks electrodes.” *J. Power Sources*, 297, 351–358.
- Peng, H., Zhou, J., Sun, K., Ma, G., Zhang, Z., Feng, E., and Lei, Z. (2017). “High-

Performance Asymmetric Supercapacitor Designed with a Novel NiSe@MoSe₂ Nanosheet Array and Nitrogen-Doped Carbon Nanosheet.” *ACS Sustain. Chem. Eng.*, 5(7), 5951–5963.

Pham, D. T., Baboo, J. P., Song, J., Kim, S., Jo, J., Mathew, V., Alfaruqi, M. H., Sambandam, B., and Kim, J. (2018). “Facile synthesis of pyrite (FeS₂/C) nanoparticles as an electrode material for non-aqueous hybrid electrochemical capacitors.” *Nanoscale*, 10(13), 5938–5949.

Poudel, M. B., Kim, A. A., Lohani, P. C., Yoo, D. J., and Kim, H. J. (2023). “Assembling zinc cobalt hydroxide/ternary sulfides heterostructure and iron oxide nanorods on three-dimensional hollow porous carbon nanofiber as high energy density hybrid supercapacitor.” *J. Energy Storage*, 60(October 2022).

Quan, H., Cheng, B., Chen, D., Su, X., Xiao, Y., and Lei, S. (2016). “One-pot synthesis of α -MnS/nitrogen-doped reduced graphene oxide hybrid for high-performance asymmetric supercapacitors.” *Electrochim. Acta*, 210, 557–566.

Raj, F. R. M. S., Jaya, N. V., Boopathi, G., Kalpana, D., and Pandurangan, A. (2020). “S-doped activated mesoporous carbon derived from the *Borassus flabellifer* flower as active electrodes for supercapacitors.” *Mater. Chem. Phys.*, 240, 122151.

Raju, T. D., Gopalakrishnan, A., and Badhulika, S. (2020). “Facile synthesis of 3D/2D Cu₂Se cauliflower/CuS nanosheets composite as a binder-free electrode for high-performance asymmetric solid-state supercapacitors.” *J. Alloys Compd.*, 845, 156241.

Raman, V., Chinnadurai, D., Rajmohan, R., Chebrolu, V. T., Rajangam, V., and Kim, H. J. (2019). “Transition metal chalcogenide based MnSe heterostructured with NiCo₂O₄ as a new high performance electrode material for capacitive energy storage.” *New J. Chem.*, 43(32), 12630–12640.

Ramya, R., Sivasubramanian, R., and Sangaranarayanan, M. V. (2013). “Conducting polymers-based electrochemical supercapacitors—Progress and prospects.” *Electrochim. Acta*, 101, 109–129.

Rathore, H. K., Hariram, M., Ganesha, M. K., Singh, A. K., Das, D., Kumar, M., Awasthi, K., and Sarkar, D. (2022). “Charge storage mechanism in vanadium telluride/carbon nanobelts as electroactive material in an aqueous asymmetric supercapacitor.” *J. Colloid Interface Sci.*, 621, 110–118.

- Raymundo-Piñero, E., Kierzek, K., Machnikowski, J., and Béguin, F. (2006). “Relationship between the nanoporous texture of activated carbons and their capacitance properties in different electrolytes.” *Carbon N. Y.*, 44(12), 2498–2507.
- Raza, M. A., Rehman, Z. U., Tanvir, M. G., and Maqsood, M. F. (2022). “Metal oxide-conducting polymer-based composite electrodes for energy storage applications.” *Renew. Polym. Polym. Oxide Compos.*, Elsevier, 195–251.
- Raza, W., Ali, F., Raza, N., Luo, Y., Kim, K.-H., Yang, J., Kumar, S., Mehmood, A., and Kwon, E. E. (2018a). “Recent advancements in supercapacitor technology.” *Nano Energy*, 52, 441–473.
- Raza, W., Ali, F., Raza, N., Luo, Y., Kim, K. H., Yang, J., Kumar, S., Mehmood, A., and Kwon, E. E. (2018b). “Recent advancements in supercapacitor technology.” *Nano Energy*, Elsevier Ltd.
- Reddy, P. A. K., Han, H., Kim, K. C., and Bae, S. (2022). “Heterostructured NiCo₂S₄@SnS₂ hybrid for all-solid-state supercapacitor applications: delocalized charges on Co–S heterojunction improved electrochemical kinetics.” *ACS Appl. Energy Mater.*, 5(11), 13751–13762.
- Rudge, A., Davey, J., Raistrick, I., Gottesfeld, S., and Ferraris, J. P. (1994). “Conducting polymers as active materials in electrochemical capacitors.” *J. Power Sources*, 47(1–2), 89–107.
- Rui, S., Lu, J., and Chunxu, P. (2011). “A single-step process for preparing supercapacitor electrodes from carbon nanotubes.” *Soft Nanosci. Lett.*, 2011.
- Ryu, K. S., Wu, X., Lee, Y., and Chang, S. H. (2003). “Electrochemical capacitor composed of doped polyaniline and polymer electrolyte membrane.” *J. Appl. Polym. Sci.*, 89(5), 1300–1304.
- Sahoo, M. K., Gusain, M., Thangriyal, S., Nagarajan, R., and Rao, G. R. (2020a). “Journal of Solid State Chemistry Energy storage study of trimetallic Cu₂MSnS₄ (M : Fe , Co , Ni) nanomaterials prepared by sequential crystallization method.” 282(June 2019).
- Sahoo, M. K., Gusain, M., Thangriyal, S., Nagarajan, R., and Rao, G. R. (2020b). “Energy storage study of trimetallic Cu₂MSnS₄ (M: Fe, Co, Ni) nanomaterials prepared by sequential crystallization method.” *J. Solid State Chem.*, 282, 121049.
- Sahoo, S., Mondal, R., Late, D. J., and Sekhar, C. (2017). “Microporous and Mesoporous

Materials Electrodeposited Nickel Cobalt Manganese based mixed sulfide nanosheets for high performance supercapacitor application.” 244, 101–108.

Sahoo, S., Pazhamalai, P., Krishnamoorthy, K., and Kim, S. J. (2018). “Hydrothermally prepared α -MnSe nanoparticles as a new pseudocapacitive electrode material for supercapacitor.” *Electrochim. Acta*, 268, 403–410.

Sajjad, M., Iqbal, A., Shah, M. Z. U., Shah, A., Asim, S., Khan, S., Assiri, M. A., Javed, M. S., and Lu, W. (2022). “Low-temperature synthesis of 3D copper selenide microflowers for high-performance supercapacitors.” *Mater. Lett.*, 314(February), 131857.

Sajjad, M., Ismail, J., Shah, A., Mahmood, A., Shah, M. Z. U., Rahman, S. ur, and Lu, W. (2021). “Fabrication of 1.6V hybrid supercapacitor developed using MnSe₂/rGO positive electrode and phosphine based covalent organic frameworks as a negative electrode enables superb stability up to 28,000 cycles.” *J. Energy Storage*, 44(PA), 103318.

Sambasivam, S., Gopi, C. V. V. M., Arbi, H. M., Kumar, Y. A., Kim, H.-J., Zahmi, S. Al, and Obaidat, I. M. (2021). “Binder-free hierarchical core-shell-like CoMn₂O₄@ MnS nanowire arrays on nickel foam as a battery-type electrode material for high-performance supercapacitors.” *J. Energy Storage*, 36, 102377.

Sangeetha Vidhya, M., Yuvakkumar, R., Senthil Kumar, P., Ravi, G., Velauthapillai, D., and Bijad, M. (2022). “Recent progression of flower like ZnSe@ MoSe₂ designed as an electrocatalyst for enhanced supercapacitor performance.” *Top. Catal.*, 65(5), 684–693.

Santhoshkumar, P., Nagaraju, G., Shaji, N., Sim, G. S., Nanthagopal, M., Sekhar, S. C., Yu, J. S., and Lee, C. W. (2020). “Hierarchical iron selenide nanoarchitecture as an advanced anode material for high-performance energy storage devices.” *Electrochim. Acta*, 356, 136833.

Shabangoli, Y., Rahmanifar, M. S., Noori, A., El-Kady, M. F., Kaner, R. B., and Mousavi, M. F. (2019). “Nile blue functionalized graphene aerogel as a pseudocapacitive negative electrode material across the full pH range.” *ACS Nano*, 13(11), 12567–12576.

Shafiee, S., and Topal, E. (2009). “When will fossil fuel reserves be diminished?” *Energy Policy*, 37(1), 181–189.

Shah, M. Z. U., Sajjad, M., Shah, M. S., Rahim, M., Rahman, S. ur, Hou, H., Khan, A. U., and Shah, A. (2023). “Wet-chemical assisted synthesis of MnSe/ZnO nanostructures as low-resistance robust novel cathode material for advanced hybrid supercapacitors.” *New J.*

Chem., 8002–8012.

Shahabuddin, S., Gaur, R., Mukherjee, N., Chandra, P., and Khanam, R. (2022). “Conducting polymers-based nanocomposites: Innovative materials for waste water treatment and energy storage.” *Mater. Today Proc.*, 62, 6950–6955.

Shao, Y., El-Kady, M. F., Sun, J., Li, Y., Zhang, Q., Zhu, M., Wang, H., Dunn, B., and Kaner, R. B. (2018). “Design and mechanisms of asymmetric supercapacitors.” *Chem. Rev.*, 118(18), 9233–9280.

Sharma, P., and Bhatti, T. S. (2010). “A review on electrochemical double-layer capacitors.” *Energy Convers. Manag.*, 51(12), 2901–2912.

Sharma, P., and Kumar, V. (2020). “Current technology of supercapacitors: a review.” *J. Electron. Mater.*, 49(6), 3520–3532.

Sharma, R. K., Rastogi, A. C., and Desu, S. B. (2008). “Manganese oxide embedded polypyrrole nanocomposites for electrochemical supercapacitor.” *Electrochim. Acta*, 53(26), 7690–7695.

Shehzad, H., Chen, J., Shuang, M. T., Liu, Z., Zhou, L., Wang, Y., Farooqi, Z. H., Ahmed, E., Sharif, A., and Irfan, A. (2024). “Evaluation of templated N/P co-doped hierarchical mesoporous biocarbon/2D-molybdenum disulfide/polypyrrole composite as a supercapacitor electrode for U (VI) electrosorption.” *Sep. Purif. Technol.*, 329, 125226.

Shen, J., Wang, Q., Zhang, K., Wang, S., Li, L., Dong, S., Zhao, S., Chen, J., Sun, R., and Wang, Y. (2019). “Flexible carbon cloth based solid-state supercapacitor from hierarchical holothurian-morphological NiCo₂O₄@ NiMoO₄/PANI.” *Electrochim. Acta*, 320, 134578.

Shen, L., Yu, L., Wu, H. Bin, Yu, X. Y., Zhang, X., and Lou, X. W. (2015). “Formation of nickel cobalt sulfide ball-in-ball hollow spheres with enhanced electrochemical pseudocapacitive properties.” *Nat. Commun.*, 6, 1–8.

Sheng, P., Ye, R., Wu, D., Zhang, L., An, X., Tao, S., Qian, B., and Chu, P. K. (2021). “Morphological modulation of cobalt selenide on carbon cloth by Ni doping for high-performance electrodes in supercapacitors.” *Colloids Surfaces A Physicochem. Eng. Asp.*, 624(May), 126818.

Shi, C., Yang, Q., Chen, S., Xue, Y., Hao, Y., and Yan, Y. (2022a). “Granular nanosheets made of interconnected NiTe₂-CoTe₂ nanoparticles on carbon fibers for high-performance hybrid supercapacitors.” *ACS Appl. Energy Mater.*, 5(3), 2817–2825.

- Shi, C., Yang, Q., Chen, S., Xue, Y., Hao, Y., and Yan, Y. (2022b). “Granular Nanosheets Made of Interconnected NiTe₂-CoTe₂Nanoparticles on Carbon Fibers for High-Performance Hybrid Supercapacitors.” *ACS Appl. Energy Mater.*, 5(3), 2817–2825.
- Shim, J.-J. (2015). “In situ growth of hierarchical mesoporous NiCo₂S₄@ MnO₂ arrays on nickel foam for high-performance supercapacitors.” *Electrochim. Acta*, 166, 302–309.
- Shinde, S. K., Ghodake, G. S., Dubal, D. P., Patel, R. V., Saratale, R. G., Kim, D. Y., Maile, N. C., Koli, R. R., Dhaygude, H. D., and Fulari, V. J. (2017). “Electrochemical synthesis: Monoclinic Cu₂Se nano-dendrites with high performance for supercapacitors.” *J. Taiwan Inst. Chem. Eng.*, 75, 271–279.
- Shinde, S. K., Ramesh, S., Bathula, C., Ghodake, G. S., Kim, D.-Y., Jagadale, A. D., Kadam, A. A., Waghmode, D. P., Sreekanth, T. V. M., and Kim, H. S. (2019). “Novel approach to synthesize NiCo₂S₄ composite for high-performance supercapacitor application with different molar ratio of Ni and Co.” *Sci. Rep.*, 9(1), 13717.
- Shirakawa, H., Louis, E. J., MacDiarmid, A. G., Chiang, C. K., and Heeger, A. J. (1977). “Synthesis of electrically conducting organic polymers: halogen derivatives of polyacetylene,(CH)_x.” *J. Chem. Soc. Chem. Commun.*, (16), 578–580.
- Shown, I., Ganguly, A., Chen, L., and Chen, K. (2015). “Conducting polymer-based flexible supercapacitor.” *Energy Sci. Eng.*, 3(1), 2–26.
- Simon, P., and Burke, A. (2008). “Nanostructured carbons: double-layer capacitance and more.” *Electrochem. Soc. interface*, 17(1), 38.
- Simon, P., and Gogotsi, Y. (2008). “Materials for electrochemical capacitors.” *Nat. Mater.*, 7(11), 845–854.
- Singu, B. S., and Yoon, K. R. (2019). “Exfoliated graphene-manganese oxide nanocomposite electrode materials for supercapacitor.” *J. Alloys Compd.*, 770, 1189–1199.
- Sivanantham, A., and Shanmugam, S. (2017). “Nickel selenide supported on nickel foam as an efficient and durable non-precious electrocatalyst for the alkaline water electrolysis.” *Appl. Catal. B Environ.*, 203, 485–493.
- Sivaraman, P., Thakur, A., Kushwaha, R. K., Ratna, D., and Samui, A. B. (2006). “Poly (3-methyl thiophene)-activated carbon hybrid supercapacitor based on gel polymer electrolyte.” *Electrochem. solid-state Lett.*, 9(9), A435.
- Snook, G. A., Kao, P., and Best, A. S. (2011). “Conducting-polymer-based supercapacitor

devices and electrodes.” *J. Power Sources*, 196(1), 1–12.

Snook, G. A., Wilson, G. J., and Pandolfo, A. G. (2009). “Mathematical functions for optimisation of conducting polymer/activated carbon asymmetric supercapacitors.” *J. Power Sources*, 186(1), 216–223.

Song, K., Wang, X., Li, J., Zhang, B., Yang, R., Liu, P., and Wang, J. (2020). “3D hierarchical CoFe₂O₄/CoOOH nanowire arrays on Ni-Sponge for high-performance flexible supercapacitors.” *Electrochim. Acta*, 340, 135892.

Song, X.-Z., Sun, F.-F., Meng, Y.-L., Wang, Z.-W., Su, Q.-F., and Tan, Z. (2019). “Hollow core-shell NiCo₂S₄@MoS₂ dodecahedrons with enhanced performance for supercapacitors and hydrogen evolution reaction.” *New J. Chem.*, 43(8), 3601–3608.

Sreehari, M. S., Vijayan, A. K., Kour, S., Dastider, S. G., Mondal, K., and Sharma, A. L. (2024). “Electronic structure and quantum capacitance analysis of transition metal doped cobalt diselenide for supercapacitors.” *J. Phys. Chem. Solids*, 188, 111885.

Srinivasan, V., and Weidner, J. W. (2000). “Studies on the capacitance of nickel oxide films: effect of heating temperature and electrolyte concentration.” *J. Electrochem. Soc.*, 147(3), 880.

Stankovich, S., Dikin, D. A., Dommett, G. H. B., Kohlhaas, K. M., Zimney, E. J., Stach, E. A., Piner, R. D., Nguyen, S. B. T., and Ruoff, R. S. (2006). “Graphene-based composite materials.” *Nature*, 442(7100), 282–286.

Stoller, M. D., Park, S., Zhu, Y., An, J., and Ruoff, R. S. (2008). “Graphene-based ultracapacitors.” *Nano Lett.*, 8(10), 3498–3502.

Su, Y.-Z., Mathankumar, M., Lee, W.-Y., Hasin, P., Subramanian, B., Hsieh, C.-K., and Lin, J.-Y. (2024). “Phase-controllable synthesis of nickel selenide nanostructures decorated on carbon nanotubes as efficient binder-free cathodes for hybrid supercapacitors.” *J. Energy Storage*, 89, 111728.

Subhadarshini, S., Pavitra, E., Rama Raju, G. S., Chodankar, N. R., Goswami, D. K., Han, Y.-K., Huh, Y. S., and Das, N. C. (2020). “One-dimensional NiSe–Se hollow nanotubular architecture as a binder-free cathode with enhanced redox reactions for high-performance hybrid supercapacitors.” *ACS Appl. Mater. Interfaces*, 12(26), 29302–29315.

Subramani, K., Sudhan, N., Divya, R., and Sathish, M. (2017). “All-solid-state asymmetric supercapacitors based on cobalt hexacyanoferrate-derived CoS and activated carbon.” *RSC*

Adv., 7(11), 6648–6659.

SUN, X.-Z., Zhang, X., Huang, B., and MA, Y.-W. (2014). “Effects of separator on the electrochemical performance of electrical double-layer capacitor and hybrid battery-supercapacitor.” *Acta Physico-Chimica Sin.*, 30(3), 485–491.

Sun, Z., Yang, X., Lin, H., Zhang, F., Wang, Q., and Qu, F. (2019). “Bifunctional iron disulfide nanoellipsoids for high energy density supercapacitor and electrocatalytic oxygen evolution applications.” *Inorg. Chem. Front.*, 6(3), 659–670.

Syarif, N., Tribidasari, A., and Wibowo, W. (2012). “Direct synthesis carbon/Metal oxide composites for electrochemical capacitors electrode.” *Int. Trans. J. Eng. Manag. Appl. Sci. Technol.*, 3, 21–34.

Tamang, T. L., Sahoo, S., and Shim, J.-J. (2023). “Triple-shelled nickel-cobalt-manganese sulfides hollow spheres for advanced hybrid supercapacitors.” *J. Power Sources*, 572, 233107.

Tang, C., Pu, Z., Liu, Q., Asiri, A. M., Sun, X., Luo, Y., and He, Y. (2015a). “In situ growth of nise nanowire film on nickel foam as an electrode for high-performance supercapacitors.” *ChemElectroChem*, 2(12), 1903–1907.

Tang, H., Lu, X., Zhu, H., Tian, Y., Khatoon, R., Zhu, Z., Zeng, Y. J., Zhang, Q., and Lu, J. (2020a). “Hydrothermally synthesized MnSe as high cycle stability anode material for lithium-ion battery.” *Ionics (Kiel)*, 26(1), 43–49.

Tang, J., Ge, Y., Shen, J., and Ye, M. (2016). “Facile synthesis of CuCo₂S₄ as a novel electrode material for ultrahigh supercapacitor performance.” *Chem. Commun.*, 52(7), 1509–1512.

Tang, K., Ma, H., Tian, Y., Liu, Z., Jin, H., Hou, S., Zhou, K., and Tian, X. (2020b). “3D printed hybrid-dimensional electrodes for flexible micro-supercapacitors with superior electrochemical behaviours.” *Virtual Phys. Prototyp.*, 15(sup1), 511–519.

Tang, Y., Chen, T., Yu, S., Qiao, Y., Mu, S., Zhang, S., Zhao, Y., Hou, L., Huang, W., and Gao, F. (2015b). “A highly electronic conductive cobalt nickel sulphide dendrite/quasi-spherical nanocomposite for a supercapacitor electrode with ultrahigh areal specific capacitance.” *J. Power Sources*, 295, 314–322.

Theerthagiri, J., Karuppasamy, K., Durai, G., Rana, A., Arunachalam, P., Sangeetha, K., Kuppasami, P., and Kim, H.-S. (2018a). “Recent Advances in Metal Chalcogenides (MX;

X = S, Se) Nanostructures for Electrochemical Supercapacitor Applications: A Brief Review.” *Nanomaterials*, 8(4), 256.

Theerthagiri, J., Karuppasamy, K., Durai, G., Rana, A. ul H. S., Arunachalam, P., Sangeetha, K., Kuppasami, P., and Kim, H. S. (2018b). “Recent advances in metal chalcogenides (MX; X = S, Se) nanostructures for electrochemical supercapacitor applications: A brief review.” *Nanomaterials*, MDPI AG.

Theerthagiri, J., Sudha, R., Premnath, K., Arunachalam, P., Madhavan, J., and Al-Mayouf, A. M. (2017). “Growth of iron diselenide nanorods on graphene oxide nanosheets as advanced electrocatalyst for hydrogen evolution reaction.” *Int. J. Hydrogen Energy*, 42(18), 13020–13030.

Thillaikkarasi, D., Karthikeyan, S., Ramesh, R., Sengodan, P., Malarvizhi, M., Kavitha, D., and Nirmala, V. (2023). “Facile synthesis of activated carbon and multiwalled carbon nanotubes and comparative performance of various AC-MWCNTs supercapacitor electrodes.” *J. Mater. Sci. Mater. Electron.*, 34(5), 353.

Tigwera, G. A., Khan, M. D., Nyamen, L. D., Souza, F. M. de, Lin, W., Gupta, R. K., Revaprasadu, N., and Ndifon, P. T. (2023). “Transition metal (Ni, Cu and Fe) doped MnS nanostructures: Effect of doping on supercapacitance and water splitting.” *Mater. Sci. Semicond. Process.*, 158(November 2022), 107365.

Torrise, L., Silipigni, L., Cutroneo, M., and Torrise, A. (2020). “Graphene oxide as a radiation sensitive material for XPS dosimetry.” *Vacuum*, 173(January), 109175.

Toupin, M., Brousse, T., and Bélanger, D. (2004). “Charge storage mechanism of MnO₂ electrode used in aqueous electrochemical capacitor.” *Chem. Mater.*, 16(16), 3184–3190.

Tue, L. N. M., Sahoo, S., Dhakal, G., Nguyen, V. H., Lee, J., Lee, Y. R., and Shim, J. J. (2023). “NiCo₂S₄/MoS₂ Nanocomposites for Long-Life High-Performance Hybrid Supercapacitors.” *Nanomaterials*, 13(4).

Tundwal, A., Kumar, H., Binoj, B. J., Sharma, R., Kumar, G., Kumari, R., Dhayal, A., Yadav, A., Singh, D., and Kumar, P. (2024). “Developments in conducting polymer-, metal oxide-, and carbon nanotube-based composite electrode materials for supercapacitors: a review.” *RSC Adv.*, 14(14), 9406–9439.

Uke, S. J., Mardikar, S. P., Bambole, D. R., Kumar, Y., and Chaudhari, G. N. (2020). “Sol-gel citrate synthesized Zn doped MgFe₂O₄ nanocrystals: A promising supercapacitor

electrode material.” *Mater. Sci. Energy Technol.*, 3(April), 446–455.

Ul Hoque, M. I., Donne, S. W., and Holze, R. (2024). “Graphene Nanocomposite Materials for Supercapacitor Electrodes.” *Encyclopedia*, 4(1), 101–116.

Vangari, M., Pryor, T., and Jiang, L. (2013). “Supercapacitors: Review of Materials and Fabrication Methods.” *J. Energy Eng.*, 139(2), 72–79.

Vargheese, S., Muthu, D., Pattappan, D., Kavaya, K. V., Kumar, R. T. R., and Haldorai, Y. (2020). “Hierarchical flower-like MnO₂@ nitrogen-doped porous carbon composite for symmetric supercapacitor: Constructing a 9.0 V symmetric supercapacitor cell.” *Electrochim. Acta*, 364, 137291.

Velayutham, R., Manikandan, R., Justin Raj, C., Dennyson Savariraj, A., Cho, W. J., Jang, H. M., and Chul Kim, B. (2021a). “Rationally designed metal–organic framework templated iron-molybdenum sulfide for high energy density hybrid supercapacitors.” *Appl. Surf. Sci.*, 570(June), 151051.

Velayutham, R., Manikandan, R., Raj, C. J., Kale, A. M., Kaya, C., Palanisamy, K., and Kim, B. C. (2021b). “Electrodeposition of vanadium pentoxide on carbon fiber cloth as a binder-free electrode for high-performance asymmetric supercapacitor.” *J. Alloys Compd.*, 863, 158332.

Vidhya, M. S., Yuvakkumar, R., Kumar, P. S., Ravi, G., and Velauthapillai, D. (2022). “Hydrothermal Synthesis of Flower Like MnSe₂@MoSe₂ Electrode for Supercapacitor Applications.” *Top. Catal.*, 65(5–6), 615–622.

Vidhya, M. S., Yuvakkumar, R., Ravi, G., Babu, E. S., Saravanakumar, B., Nasif, O., Alharbi, S. A., and Velauthapillai, D. (2021). “Demonstration of 1.5 V asymmetric supercapacitor developed using MnSe₂-CoSe₂ metal composite.” *Ceram. Int.*, 47(8), 11786–11792.

Vinoth, S., Subramani, K., Ong, W. J., Sathish, M., and Pandikumar, A. (2021). “CoS₂ engulfed ultra-thin S-doped g-C₃N₄ and its enhanced electrochemical performance in hybrid asymmetric supercapacitor.” *J. Colloid Interface Sci.*, 584, 204–215.

Wang, C. M., Wen, C. Y., Che, Y. C., Chang, J.-Y., Ho, C. H., Kao, K.-S., Shih, W. C., Chiu, C.-M., and Shen, Y. A. (2015a). “The influence of specific surface area on the capacitance of the carbon electrodes supercapacitor.” *Proc. Second Int. Conf. Ind. Appl. Eng.*, 439–442.

Wang, D.-W., Li, F., Zhao, J., Ren, W., Chen, Z.-G., Tan, J., Wu, Z.-S., Gentle, I., Lu, G. Q., and Cheng, H.-M. (2009). "Fabrication of graphene/polyaniline composite paper via in situ anodic electropolymerization for high-performance flexible electrode." *ACS Nano*, 3(7), 1745–1752.

Wang, G., Sun, X., Lu, F., Sun, H., Yu, M., Jiang, W., Liu, C., and Lian, J. (2012a). "Flexible pillared graphene-paper electrodes for high-performance electrochemical supercapacitors." *Small*, 8(3), 452–459.

Wang, G., Zhang, L., and Zhang, J. (2012b). "A review of electrode materials for electrochemical supercapacitors." *Chem. Soc. Rev.*, 41(2), 797–828.

Wang, H.-W., Hu, Z.-A., Chang, Y.-Q., Chen, Y.-L., Wu, H.-Y., Zhang, Z.-Y., and Yang, Y.-Y. (2011a). "Design and synthesis of NiCo₂O₄-reduced graphene oxide composites for high performance supercapacitors." *J. Mater. Chem.*, 21(28), 10504–10511.

Wang, H., Tian, L., Ali, M., Zhao, X., Han, S., and Xing, Z. (2023). "Two-step electrodeposition synthesis of NiCo₂S₄/MoS_x composite on nickel foam as electrodes for supercapacitors." *J. Alloys Compd.*, 932, 167628.

Wang, H. W., Hu, Z. A., Chang, Y. Q., Chen, Y. L., Zhang, Z. Y., Yang, Y. Y., and Wu, H. Y. (2011b). "Preparation of reduced graphene oxide/cobalt oxide composites and their enhanced capacitive behaviors by homogeneous incorporation of reduced graphene oxide sheets in cobalt oxide matrix." *Mater. Chem. Phys.*, 130(1–2), 672–679.

Wang, J.-G., Kang, F., and Wei, B. (2015b). "Engineering of MnO₂-based nanocomposites for high-performance supercapacitors." *Prog. Mater. Sci.*, 74, 51–124.

Wang, J. G., Zhou, R., Jin, D., Xie, K., and Wei, B. (2016). "Controlled synthesis of NiCo₂S₄ nanostructures on nickel foams for high-performance supercapacitors." *Energy Storage Mater.*, 2, 1–7.

Wang, J., Liu, B., Miao, N., Zhou, J., and Sun, Z. (2019a). "I-doped Cu₂Se nanocrystals for high-performance thermoelectric applications." *J. Alloys Compd.*, 772, 366–370.

Wang, K., Huang, J., and Wei, Z. (2010). "Conducting polyaniline nanowire arrays for high performance supercapacitors." *J. Phys. Chem. C*, 114(17), 8062–8067.

Wang, L., Wang, S., Cao, J., Zhou, Y.-H., and Chen, W. (2024a). "Three dimensional nanonetwork structured Fe-Co-S/Ti₃C₂@ nickel foam integrated electrode for enhanced energy density supercapacitors." *Mater. Res. Bull.*, 112733.

- Wang, L., Zhang, X., Ma, Y., Yang, M., and Qi, Y. (2017a). “Supercapacitor performances of the MoS₂/CoS₂ nanotube arrays in situ grown on Ti plate.” *J. Phys. Chem. C*, 121(17), 9089–9095.
- Wang, M., and Zhang, X. (2017). “Three-Dimensional Co₃O₄@ NiCo₂S₄ Core/Shell Nanoflower Array with Enhanced Electrochemical Performance.” *ChemistrySelect*, 2(29), 9537–9545.
- Wang, Q., Jiao, L., Du, H., Si, Y., Wang, Y., and Yuan, H. (2012c). “Co₃S₄ hollow nanospheres grown on graphene as advanced electrode materials for supercapacitors.” *J. Mater. Chem.*, 22(40), 21387–21391.
- Wang, Q., Wen, Z., and Li, J. (2006). “A hybrid supercapacitor fabricated with a carbon nanotube cathode and a TiO₂-B nanowire anode.” *Adv. Funct. Mater.*, 16(16), 2141–2146.
- Wang, S., Li, W., Xin, L., Wu, M., Long, Y., Huang, H., and Lou, X. (2017b). “Facile synthesis of truncated cube-like NiSe₂ single crystals for high-performance asymmetric supercapacitors.” *Chem. Eng. J.*, 330(May), 1334–1341.
- Wang, T., Xiong, C., Zhang, Y., Wang, B., Xiong, Q., Zhao, M., and Ni, Y. (2024b). “Multi-layer hierarchical cellulose nanofibers/carbon nanotubes/vinasse activated carbon composite materials for supercapacitors and electromagnetic interference shielding.” *Nano Res.*, 17(3), 904–912.
- Wang, X., Hao, C., Zhang, J., Ni, C., Wang, X., and Shen, Y. (2022a). “Reasonable design and synthesis of nickel manganese sulfide nanoparticles derived from metal organic frameworks as electrode materials for supercapacitors.” *J. Power Sources*, 539(May), 231594.
- Wang, X., Pan, Y., Wang, X., Guo, Y., Ni, C., Wu, J., and Hao, C. (2022b). “Industrial Crops & Products High performance hybrid supercapacitors assembled with multi-cavity nickel cobalt sulfide hollow microspheres as cathode and porous typha-derived carbon as anode.” *Ind. Crop. Prod.*, 189(October), 115863.
- Wang, Y., Ding, Y., Guo, X., and Yu, G. (2019b). “Conductive polymers for stretchable supercapacitors.” *Nano Res.*, 12, 1978–1987.
- Wang, Y., Guo, J., Wang, T., Shao, J., Wang, D., and Yang, Y. W. (2015c). “Mesoporous transition metal oxides for supercapacitors.” *Nanomaterials*, 5(4), 1667–1689.
- Wang, Y., Zhang, M., Ma, T., Pan, D., Li, Y., Xie, J., and Shao, S. (2018). “A high-

performance flexible supercapacitor electrode material based on nano-flowers-like FeS₂/NSG hybrid nanocomposites.” *Mater. Lett.*, 218, 10–13.

Wang, Y., Zhang, W., Guo, X., Jin, K., Chen, Z., Liu, Y., Yin, L., Li, L., Yin, K., and Sun, L. (2019c). “Ni–Co selenide nanosheet/3D graphene/nickel foam binder-free electrode for high-performance supercapacitor.” *ACS Appl. Mater. Interfaces*, 11(8), 7946–7953.

Wang, Z., Tammela, P., Strømme, M., and Nyholm, L. (2015d). “Nanocellulose coupled flexible polypyrrole@ graphene oxide composite paper electrodes with high volumetric capacitance.” *Nanoscale*, 7(8), 3418–3423.

Wei, W., Guo, Z., Xu, J., Fang, Z., Zhang, J., Jia, Y., and Mi, L. (2022). “Novel Ni₃S₄/NiS/NC composite with multiple heterojunctions synthesized through space-confined effect for high-performance supercapacitors.” *Int. J. Extrem. Manuf.*, 5(1), 15504.

Wen, Y., Liu, Y., Dang, S., Tian, S., Li, H., Wang, Z., He, D., Wu, Z. S., Cao, G., and Peng, S. (2019). “High mass loading Ni-decorated Co₉S₈ with enhanced electrochemical performance for flexible quasi-solid-state asymmetric supercapacitors.” *J. Power Sources*, 423(March), 106–114.

Wen, Y., Peng, S., Wang, Z., Hao, J., Qin, T., Lu, S., Zhang, J., He, D., Fan, X., and Cao, G. (2017). “Facile synthesis of ultrathin NiCo₂S₄ nano-petals inspired by blooming buds for high-performance supercapacitors.” *J. Mater. Chem. A*, 5(15), 7144–7152.

Wiston, B. R., and Ashok, M. (2019). “Microwave-assisted synthesis of cobalt-manganese oxide for supercapacitor electrodes.” *Mater. Sci. Semicond. Process.*, 103, 104607.

Wu, H.-C., Lin, Y.-P., Lee, E., Lin, W.-T., Hu, J.-K., Chen, H.-C., and Wu, N.-L. (2009). “High-performance carbon-based supercapacitors using Al current-collector with conformal carbon coating.” *Mater. Chem. Phys.*, 117(1), 294–300.

Wu, H., Zhu, J., Wang, G., Min, Q., Ai, B., Liang, P., Yuan, R., and Fang, D. (2024). “Ion etching modulates the synthesis of CoNiCu sulfide for high-performance supercapacitors.” *Sustain. Energy Fuels*, 8(8), 1663–1668.

Wu, S., Hu, Q., Wu, L., Li, J., Peng, H., and Yang, Q. (2019). “One-step solvothermal synthesis of nickel selenide nanoparticles as the electrode for high-performance supercapacitors.” *J. Alloys Compd.*, 784, 347–353.

Wu, S., Xue, Y., Yang, Q., Hu, Q., Cui, T., Su, Q., Yin, F., Wang, Y., and Zhan, H. (2021a). “Conductive carbon spheres-supported nickel-cobalt selenide nanoparticles as a high-

performance and long-life electrode for supercapacitors.” *Diam. Relat. Mater.*, 111, 108187.

Wu, W., Zhao, C., Wang, C., Liu, T., Wang, L., and Zhu, J. (2021b). “Hierarchical structure of Self-Supported NiCo₂S₄ Nanoflowers@ NiCo₂S₄ nanosheets as high rate-capability and cycling-stability electrodes for advanced supercapacitor.” *Appl. Surf. Sci.*, 563, 150324.

Wu, Z.-S., Zhou, G., Yin, L.-C., Ren, W., Li, F., and Cheng, H.-M. (2012). “Graphene/metal oxide composite electrode materials for energy storage.” *Nano Energy*, 1(1), 107–131.

Xia, J., Chen, F., Li, J., and Tao, N. (2009). “Measurement of the quantum capacitance of graphene.” *Nat. Nanotechnol.*, 4(8), 505–509.

Xie, S., Gou, J., Liu, B., and Liu, C. (2018). “Synthesis of cobalt-doped nickel sulfide nanomaterials with rich edge sites as high-performance supercapacitor electrode materials.” *Inorg. Chem. Front.*, 5(5), 1218–1225.

Xu, J., Zhang, W., Yang, Z., Ding, S., Zeng, C., Chen, L., Wang, Q., and Yang, S. (2009). “Large-scale synthesis of long crystalline Cu_{2-x}Se nanowire bundles by water-evaporation-induced self-assembly and their application in gas sensing.” *Adv. Funct. Mater.*, 19(11), 1759–1766.

Xu, T., Wang, Y., Liu, K., Zhao, Q., Liang, Q., Zhang, M., and Si, C. (2023). “Ultralight MXene/carbon nanotube composite aerogel for high-performance flexible supercapacitor.” *Adv. Compos. Hybrid Mater.*, 6(3), 108.

Xu, Y., Wang, X., An, C., Wang, Y., Jiao, L., and Yuan, H. (2014). “CoMn₂O₄ nanowires and their excellent electrochemical properties in supercapacitors.” 16480–16488.

Xuan, H., Zhang, G., Han, X., Wang, R., Liang, X., Li, Y., and Han, P. (2021a). “Construction of MnSe₂/CoSe₂/reduced graphene oxide composites with enhanced electrochemical performance as the battery-like electrode for hybrid supercapacitors.” *J. Alloys Compd.*, 863, 158751.

Xuan, H., Zhang, G., Han, X., Wang, R., Liang, X., Li, Y., and Han, P. (2021b). “Construction of MnSe₂/CoSe₂/reduced graphene oxide composites with enhanced electrochemical performance as the battery-like electrode for hybrid supercapacitors.” *J. Alloys Compd.*, 863, 158751.

Yan, H., Zhu, K., Liu, X., Wang, Y., Wang, Y., Zhang, D., Lu, Y., Peng, T., Liu, Y., and

- Luo, Y. (2020). “Ultra-thin NiS nanosheets as advanced electrode for high energy density supercapacitors.” *RSC Adv.*, 10(15), 8760–8765.
- Yan, Z. S., Long, J. Y., Zhou, Q. F., Gong, Y., and Lin, J. H. (2018). “One-step synthesis of MnS/MoS₂/C through the calcination and sulfurization of a bi-metal–organic framework for a high-performance supercapacitor and its photocurrent investigation.” *Dalt. Trans.*, 47(15), 5390–5405.
- Yang, J., Yu, C., Fan, X., Liang, S., Li, S., Huang, H., Ling, Z., Hao, C., and Qiu, J. (2016). “Electroactive edge site-enriched nickel-cobalt sulfide into graphene frameworks for high-performance asymmetric supercapacitors.” *Energy Environ. Sci.*, 9(4), 1299–1307.
- Yang, X., Xiang, C., Zou, Y., Liang, J., Zhang, H., Yan, E., Xu, F., Hu, X., Cheng, Q., and Sun, L. (2020a). “Low-temperature synthesis of sea urchin-like Co-Ni oxide on graphene oxide for supercapacitor electrodes.” *J. Mater. Sci. Technol.*, 55, 223–230.
- Yang, X., Xue, H., Yang, Q., Yuan, R., Kang, W., and Lee, C.-S. (2017). “Preparation of porous ZnO/ZnFe₂O₄ composite from metal organic frameworks and its applications for lithium ion batteries.” *Chem. Eng. J.*, 308, 340–346.
- Yang, Y. Y., Hu, Z. A., Zhang, Z. Y., Zhang, F. H., Zhang, Y. J., Liang, P. J., Zhang, H. Y., and Wu, H. Y. (2012). “Reduced graphene oxide-nickel oxide composites with high electrochemical capacitive performance.” *Mater. Chem. Phys.*, 133(1), 363–368.
- Yang, Z., Shi, D., Dong, W., and Chen, M. (2020b). “Self-Standing Hydrogels Composed of Conducting Polymers for All-Hydrogel-State Supercapacitors.” *Chem. Eur. J.*, 26(8), 1846–1855.
- Yao, B., Huang, L., Zhang, J., Gao, X., Wu, J., Cheng, Y., Xiao, X., Wang, B., Li, Y., and Zhou, J. (2016). “Flexible transparent molybdenum trioxide nanopaper for energy storage.” *Adv. Mater.*, 28(30), 6353–6358.
- Yoshimura, M., and Byrappa, K. (2008). “Hydrothermal processing of materials: Past, present and future.” *J. Mater. Sci.*, 2085–2103.
- Younas, W., Naveed, M., Cao, C., Zhu, Y., Du, C., Ma, X., Mushtaq, N., Tahir, M., and Naeem, M. (2022). “Facile One-Step Microwave-Assisted Method to Synthesize Nickel Selenide Nanosheets for High-Performance Hybrid Supercapacitor.” *J. Colloid Interface Sci.*, 608, 1005–1014.
- Yu, D., Li, Z., Zhao, G., Zhang, H., Aslan, H., Li, J., Sun, F., Zhu, L., Du, B., and Yang,

- B. (2020). "Porous ultrathin NiSe nanosheet networks on nickel foam for high-performance hybrid supercapacitors." *ChemSusChem*, 13(1), 260–266.
- Yu, G., Xie, X., Pan, L., Bao, Z., and Cui, Y. (2013). "Hybrid nanostructured materials for high-performance electrochemical capacitors." *Nano Energy*, 2(2), 213–234.
- Yu, M., Li, X., Ma, Y., Liu, R., Liu, J., and Li, S. (2017a). "Nanohoneycomb-like manganese cobalt sulfide/three dimensional graphene-nickel foam hybrid electrodes for high-rate capability supercapacitors." *Appl. Surf. Sci.*, 396, 1816–1824.
- Yu, M., Li, X., Ma, Y., Liu, R., Liu, J., and Li, S. (2017b). "Nanohoneycomb-like manganese cobalt sulfide/three dimensional graphene-nickel foam hybrid electrodes for high-rate capability supercapacitors." *Appl. Surf. Sci.*, 396, 1816–1824.
- Yu, S., Ng, V. M. H., Wang, F., Xiao, Z., Li, C., Kong, L. B., Que, W., and Zhou, K. (2018). "Synthesis and application of iron-based nanomaterials as anodes of lithium-ion batteries and supercapacitors." *J. Mater. Chem. A*, 6(20), 9332–9367.
- Yu, X. Y., and Lou, X. W. (2018). "Mixed metal sulfides for electrochemical energy storage and conversion." *Adv. Energy Mater.*, 8(3), 1701592.
- Yu, X., Yu, L., Wen, X., and Lou, D. (2016). "Metal Sulfide Hollow Nanostructures for Electrochemical Energy Storage." 1–14.
- Yu, Z., Tetard, L., Zhai, L., and Thomas, J. (2015). "Supercapacitor electrode materials: Nanostructures from 0 to 3 dimensions." *Energy Environ. Sci.*, 8(3), 702–730.
- Zardkhoshoui, A. M., and Davarani, S. S. H. (2020a). "Construction of complex copper-cobalt selenide hollow structures as an attractive battery-type electrode material for hybrid supercapacitors." *Chem. Eng. J.*, 402, 126241.
- Zardkhoshoui, A. M., and Davarani, S. S. H. (2020b). "Construction of complex copper-cobalt selenide hollow structures as an attractive battery-type electrode material for hybrid supercapacitors." *Chem. Eng. J.*, 402.
- Zardkhoshoui, A. M., Davarani, S. S. H., and Asgharinezhad, A. A. (2019). "Designing graphene-wrapped NiCo₂Se₄ microspheres with petal-like FeS₂ toward flexible asymmetric all-solid-state supercapacitors." *Dalt. Trans.*, 48(13), 4274–4282.
- Zhai, M., Cheng, Y., Jin, Y., and Hu, J. (2019). "Solvothermal synthesis of flower-like structure Cu-Mn bimetallic sulfide on Ni-foam for high-performance symmetric supercapacitors." *Int. J. Hydrogen Energy*, 44(26), 13456–13465.

- Zhai, S., Jin, K., Zhou, M., Fan, Z., Zhao, H., Li, X., Zhao, Y., Ge, F., and Cai, Z. (2020). “A novel high performance flexible supercapacitor based on porous carbonized cotton/ZnO nanoparticle/CuS micro-sphere.” *Colloids Surfaces A Physicochem. Eng. Asp.*, 584, 124025.
- Zhai, Z.-B., Huang, K.-J., and Wu, X. (2018). “Superior mixed Co-Cd selenide nanorods for high performance alkaline battery-supercapacitor hybrid energy storage.” *Nano Energy*, 47, 89–95.
- Zhang, H., Wang, Z., and Liu, D. (2014a). “A comprehensive review of stability analysis of continuous-time recurrent neural networks.” *IEEE Trans. Neural Networks Learn. Syst.*, 25(7), 1229–1262.
- Zhang, J., Li, C., Fan, M., Ma, T., Chen, H., and Wang, H. (2021). “Two-dimensional nanosheets constituted trimetal Ni-Co-Mn sulfide nanoflower-like structure for high-performance hybrid supercapacitors.” *Appl. Surf. Sci.*, 565, 150482.
- Zhang, J., Wang, K., Guo, S., Wang, S., Liang, Z., Chen, Z., Fu, J., and Xu, Q. (2014b). “One-step carbonization synthesis of hollow carbon nanococoons with multimodal pores and their enhanced electrochemical performance for supercapacitors.” *ACS Appl. Mater. Interfaces*, 6(3), 2192–2198.
- Zhang, J., Yao, Z., Zou, W., Shen, Q., Fan, M., and Ma, T. (2022). “Trimetal NiCoMn sulfides cooperated with two-dimensional Ti₃C₂ for high performance hybrid supercapacitor.” *J. Solid State Chem.*, 308, 122909.
- Zhang, J., Yu, J., Zhang, Y., Li, Q., and Gong, J. R. (2011). “Visible light photocatalytic H₂-production activity of CuS/ZnS porous nanosheets based on photoinduced interfacial charge transfer.” *Nano Lett.*, 11(11), 4774–4779.
- Zhang, K., Chen, H., Wang, X., Guo, D., Hu, C., Wang, S., Sun, J., and Leng, Q. (2014c). “Synthesis and structure determination of potassium copper selenide nanowires and solid-state supercapacitor application.” *J. Power Sources*, 268, 522–532.
- Zhang, L., Hu, X., Wang, Z., Sun, F., and Dorrell, D. G. (2018). “A review of supercapacitor modeling, estimation, and applications: A control/management perspective.” *Renew. Sustain. Energy Rev.*, 81, 1868–1878.
- Zhang, L. L., and Zhao, X. S. (2009). “Carbon-based materials as supercapacitor electrodes.” *Chem. Soc. Rev.*, 38(9), 2520–2531.

- Zhang, M., Cheng, J., Zhang, L., Li, Y., Chen, M., Chen, Y., and Shen, Z. (2020a). "Activated carbon by one-step calcination of deoxygenated agar for high voltage lithium ion supercapacitor." *ACS Sustain. Chem. Eng.*, 8(9), 3637–3643.
- Zhang, M., Zai, J., Liu, J., Chen, M., Wang, Z., Li, G., Qian, X., Qian, L., and Yu, X. (2017). "A hierarchical CoFeS₂/reduced graphene oxide composite for highly efficient counter electrodes in dye-sensitized solar cells." *Dalt. Trans.*, 46(29), 9511–9516.
- Zhang, Y., Ma, Q., Feng, K., Guo, J., Wei, X., Shao, Y., Zhuang, J., and Lin, T. (2020b). "Effects of microstructure and electrochemical properties of Ti/IrO₂–SnO₂–Ta₂O₅ as anodes on binder-free asymmetric supercapacitors with Ti/RuO₂–NiO as cathodes." *Ceram. Int.*, 46(11), 17640–17650.
- Zhang, Y., and Mo, Y. (2014). "Preparation of MnO₂ electrodes coated by Sb-doped SnO₂ and their effect on electrochemical performance for supercapacitor." *Electrochim. Acta*, 142, 76–83.
- Zhao, W., Guo, C., and Li, C. M. (2017a). "Lychee-like FeS₂@ FeSe₂ core-shell microspheres anode in sodium ion batteries for large capacity and ultralong cycle life." *J. Mater. Chem. A*, 5(36), 19195–19202.
- Zhao, X., Bi, Q., Yang, C., Tao, K., and Han, L. (2021). "Design of trimetallic sulfide hollow nanocages from metal-organic frameworks as electrode materials for supercapacitors." *Dalt. Trans.*, 50(42), 15260–15266.
- Zhao, X., Li, X., Zhao, Y., Su, Z., zhang, Y., and Wang, R. (2017b). "Facile synthesis of Tremelliform Co_{0.85}Se nanosheets for supercapacitor." *J. Alloys Compd.*, 697, 124–131.
- Zhao, Y., Guo, J., Liu, A., and Ma, T. (2020). "2D heterostructure comprised of Ni₃S₂/d-Ti₃C₂ supported on Ni foam as binder-free electrode for hybrid supercapacitor." *J. Alloys Compd.*, 814, 152271.
- Zhao, Y., Luo, Y., Sun, B., Li, T., Han, S., Dong, Z., and Lin, H. (2022). "Rational construction of reduced NiCo₂S₄@ CuCo₂S₄ composites with sulfur vacancies as high-performance supercapacitor electrode for enhancing electrochemical energy storage." *Compos. Part B Eng.*, 243, 110088.
- Zheng, D., Zhao, F., Li, Y., Qin, C., Zhu, J., Hu, Q., Wang, Z., and Inoue, A. (2019a). "Flexible NiO micro-rods/nanoporous Ni/metallic glass electrode with sandwich structure for high performance supercapacitors." *Electrochim. Acta*, 297, 767–777.

- Zheng, J., Zhang, R., Cheng, K., Xu, Z., Yu, P., Wang, X., and Niu, S. (2019b). "Research on the high-performance electrochemical energy storage of a NiO@ZnO (NZO) hybrid based on growth time." *Crystals*, 9(1), 1–14.
- Zheng, K., Li, G., and Xu, C. (2019c). "Advanced battery-supercapacitor hybrid device based on Co/Ni-ZIFs-derived NiCo₂S₄ ultrathin nanosheets electrode with high performance." *Appl. Surf. Sci.*, 490(June), 137–144.
- Zheng, X., Ye, Y., Yang, Q., Geng, B., and Zhang, X. (2016). "Hierarchical structures composed of MnCo₂O₄@MnO₂ core-shell nanowire arrays with enhanced supercapacitor properties." *Dalt. Trans.*, 45(2), 572–578.
- Zhi, M., Xiang, C., Li, J., Li, M., and Wu, N. (2013). "Nanostructured carbon–metal oxide composite electrodes for supercapacitors: a review." *Nanoscale*, 5(1), 72–88.
- Zhong, C., Deng, Y., Hu, W., Qiao, J., Zhang, L., and Zhang, J. (2015). "A review of electrolyte materials and compositions for electrochemical supercapacitors." *Chem. Soc. Rev.*, 44(21), 7484–7539.
- Zhou, X., Dai, H., Huang, X., Ren, Y., Wang, Q., Wang, W., Huang, W., and Dong, X. (2020). "Porous trimetallic fluoride Ni–Co–M (M = Mn, Fe, Cu, Zn) nanoprisms as electrodes for asymmetric supercapacitors." *Mater. Today Energy*, 17, 1–8.
- Zhou, X., Li, X., Sun, H., Sun, P., Liang, X., Liu, F., Hu, X., and Lu, G. (2015). "Nanosheet-assembled ZnFe₂O₄ hollow microspheres for high-sensitive acetone sensor." *ACS Appl. Mater. Interfaces*, 7(28), 15414–15421.
- Zhu, J., Shi, W., Xiao, N., Rui, X., Tan, H., Lu, X., Hng, H. H., Ma, J., and Yan, Q. (2012). "Oxidation-etching preparation of MnO₂ tubular nanostructures for high-performance supercapacitors." *ACS Appl. Mater. Interfaces*, 4(5), 2769–2774.
- Zhu, J., Tang, S., Wu, J., Shi, X., Zhu, B., and Meng, X. (2017). "Wearable high-performance supercapacitors based on silver-sputtered textiles with FeCo₂S₄–NiCo₂S₄ composite nanotube-built multitripod architectures as advanced flexible electrodes." *Adv. Energy Mater.*, 7(2), 1601234.
- Zhu, X., Liu, D., Zheng, D., Wang, G., Huang, X., Harris, J., Qu, D., and Qu, D. (2018). "Dual carbon-protected metal sulfides and their application to sodium-ion battery anodes." *J. Mater. Chem. A*, 6(27), 13294–13301.
- Zhu, Y., Wu, Z., Jing, M., Yang, X., Song, W., and Ji, X. (2015). "Mesoporous NiCo₂S₄

nanoparticles as high-performance electrode materials for supercapacitors.” *J. Power Sources*, 273, 584–590.

Zhu, Z., Lin, J., Li, N., Zhang, R., Zhang, K., Zhao, C., Chen, G., and Zhao, C. (2019). “Porous Co₉S₈ nanosheet arrays@ Co foam electrode via in situ sulfidation at room temperature for superior supercapacitors.” *J. Phys. Chem. C*, 124(1), 83–91.

Zhu, Z., Wang, G., Sun, M., Li, X., and Li, C. (2011). “Fabrication and electrochemical characterization of polyaniline nanorods modified with sulfonated carbon nanotubes for supercapacitor applications.” *Electrochim. Acta*, 56(3), 1366–1372.

Zou, X., and Zhang, Y. (2015). “Noble metal-free hydrogen evolution catalysts for water splitting.” *Chem. Soc. Rev.*, 44(15), 5148–5180.

LIST OF PUBLICATIONS

1. **Mascarenhas, F.J.**, Rodney, J.D., Mishra, P., Bhat, B.R. (2023). “ Revolutionizing energy storage: A novel Cu₂Se-GO nanocomposite for supercapacitors.” *Inorg. Chem. Commun.*, 156, 111253; DOI: 10.1016/j.inoche.2023.111253.
2. **Mascarenhas, F.J.**, Hegde, S.S., Bhat, B.R.(2023). “Supercapattery: An Electrochemical Energy Storage Device.” *Sustain. Mater. Electrochem. Capacit.* 279-290. DOI: 10.1002/9781394167104.ch11.
3. **Mascarenhas, F.J.**, Rodney, J.D., Kim, B.C., Bhat, B.R. (2024). “ Significance of transition metal (Co , Ni and Zn) doping on the nano MnSe for high-performance supercapacitor electrode.” *J. Alloys Compd.* 986, 173957.
DOI: 10.1016/j.jallcom.2024.173957
4. **Mascarenhas, F.J.**, Bhat, B.R. (2024). “ Enhancing Supercapacitor performance with Zinc-doped MnSe nanomaterial.” *J Mater Sci: Mater Electron.* 35, 1249
DOI: 10.1007/s10854-024-13032-2
5. **Mascarenhas, F.J.**, Rodney, J.D., Rao, L., Kim, B.C., Bhat, B.R. (2024). “Electrodeposited CoMnS/NiCo₂S₄ nanocomposite for high performance supercapacitors.” *Electrochimica Acta.* 507,145133;
DOI: 10.1016/j.electacta.2024.145133
6. **Mascarenhas, F.J.**, Rodney, J.D., Rao, Lavanya., Kim, B.C., Bhat, B.R. (2024). “Iron decorated Cobalt Manganese Sulphide nanoflowers as a battery type electrode material for high performance supercapacitor” (Submitted to Journal of Power Sources).

LIST OF CONFERENCES AND WORKSHOPS

1. Fiona Joyline Mascarenhas and B Ramachandra Bhat (2023). “Enhancing Supercapacitor Performance with Zinc doped MnSe Nanomaterial” International Conference on Condensed Matter and Device Physics (ICCMDP 2023). 27-29 September 2023, Department of Physics, School of Energy Technology (SoET), Pandit Deendayal Energy University (PDEU), Gandhinagar, Gujarat, India.
2. Fiona Joyline Mascarenhas and B Ramachandra Bhat (2023). “Iron doping for enhancing the electrochemical performance of NiCo₂S₄ for the supercapacitor electrode” Condensed Matter Physics and Applications (CMPA 2023). 15-16 December 2023, Department of Physics, MIT Manipal, India.

3. Five-Day National E-Workshop on “Advanced Materials for Energy Storage and Conversion devices” 28-29 February 2020, CSIR – Advanced Materials And Process Research Institute (AMPRI), Bhopal, India

CURRICULUM VITAE

FIONA JOYLINE MASCARENHAS

☎ +91-9481957580

✉ fionajoymas@gmail.com

linkedin.com/in/fionajoyline

Scopus ID: 58553642800

WOS Research ID: KPY-3393-2024

Address: Kodijal, Puttur post

PIN-574201, D.K, Karnataka

SUMMARY

A dedicated researcher specializing in energy storage devices, with a strong commitment to sustainability and energy conservation. Thriving on continuous learning and innovation, research focuses on developing efficient and sustainable energy storage solutions, aiming to contribute significantly to the advancement of green technologies and the reduction of global energy consumption. Driven by a passion for sustainability, aspires to create a more energy-efficient and environmentally friendly future.

EDUCATION

- **National Institute of Technology Karnataka (NITK), Surathkal** **2019-2024**
Ph.D. Chemistry
- **National Institute of Technology Karnataka (NITK), Surathkal** **2017**
Postgraduate: Master of Science, Chemistry CGPA: **8.05**
- **St. Philomena College, Puttur, Karnataka** **2015**
Undergraduate: Bachelor of Science (Phy, Chem, Math) Percentage: **96.62%**
- **St. Philomena Pre-University College, Puttur, Karnataka** **2012**
Karnataka State Pre-University Examination (Class 12) Percentage: **89.83%**

RESEARCH EXPERIENCE

- **IISc Bengaluru** **May-July 2016**
Research Intern
- **JNCASR, Bengaluru** **July-October 2017**
Research Intern
- **NITK, Surathkal** **January- May 2017**
Major Project

PUBLICATIONS

- **Mascarenhas, F.J.**, Rodney, J.D., Mishra, P., Bhat, B.R. (2023). “ Revolutionizing energy storage: A novel Cu₂Se-GO nanocomposite for supercapacitors.” *Inorg. Chem. Commun.*, 156, 111253; DOI: 10.1016/j.inoche.2023.111253.
- **Mascarenhas, F.J.**, Hegde, S.S., Bhat, B.R.(2023). “Supercapattery: An Electrochemical Energy Storage Device.” *Sustain. Mater. Electrochem. Capacit.* 279-290. DOI: 10.1002/9781394167104.ch11.
- **Mascarenhas, F.J.**, Rodney, J.D., Kim, B.C., Bhat, B.R. (2024). “ Significance of transition metal (Co , Ni and Zn) doping on the nano MnSe for high-performance supercapacitor electrode.” *J. Alloys Compd.* 986, 173957. DOI: 10.1016/j.jallcom.2024.173957
- **Mascarenhas, F.J.**, Bhat, B.R. (2024). “ Enhancing Supercapacitor performance with Zinc-doped MnSe nanomaterial.” *J Mater Sci: Mater Electron.* 35, 1249 DOI: 10.1007/s10854-024-13032-2
- **Mascarenhas, F.J.**, Rodney, J.D., Rao, L., Kim, B.C., Bhat, B.R. (2024). “Electrodeposited CoMnS/NiCo₂S₄ nanocomposite for high performance supercapacitors.” *Electrochimica Acta.* 507,145133; DOI: 10.1016/j.electacta.2024.145133
- Rao, L., Rodney, J.D., Joy, A., Nileshbhai. C.S., James, A., Sushmitha, S., **Mascarenhas, F.J.**, Udayashankar, N.K., Anjukandi, P., Kim, B.C., Bhat, B.R (2024). “Cerium-Modulated Zinc oxide for enhanced photoelectrochemical Non-Enzymatic biosensing of Cholesterol: An experimental and first Principle analysis.” *Chemical Engineering Journal.* 156639. DOI: 10.1016/j.cej.2024.156639.

CONFERENCES

- Fiona Joyline Mascarenhas and B Ramachandra Bhat (2023). “Enhancing Supercapacitor Performance with Zinc doped MnSe Nanomaterial” International Conference on Condensed Matter and Device Physics (ICCMDP 2023). 27-29 September 2023, Department of Physics, School of Energy Technology (SoET), Pandit Deendayal Energy University (PDEU), Gandhinagar, Gujarat, India.
- Fiona Joyline Mascarenhas and B Ramachandra Bhat (2023). “Iron doping for enhancing the electrochemical performance of NiCo₂S₄ for the supercapacitor electrode” Condensed Matter Physics and Applications (CMPA 2023). 15-16 December 2023, Department of Physics, MIT Manipal, India.

- Five-Day National E-Workshop on “Advanced Materials for Energy Storage and Conversion devices” 28-29 February 2020, CSIR – Advanced Materials and Process Research Institute (AMPRI), Bhopal, India

RESEARCH INTERESTS

- Transition metal oxide, chalcogenides and carbon-based nanomaterials and their applications.
- Environmentally sustainable materials development.
- Energy Storage and conversion devices, Biosensors and Water splitting.

RESEARCH SKILLS

- Skilled in synthesizing various nanomaterials using hydrothermal, electrodeposition, and sol-gel methods for energy storage devices.
- Hands-on experience with electrochemical workstations such as Autolab PGSTAT204.
- Proficient in material characterization techniques like XRD, FESEM, HRTEM FTIR, and XPS spectroscopic techniques.
- Skilled in electrochemical techniques including Electrochemical Impedance Spectroscopy, Cyclic Voltammetry, Chronopotentiometry, Potentiostatic, and Galvanostatic methods.
- Proficient in academic software applications like MS Office, OriginPro, Xpert Highscore, and ZsimpWin.
- Experienced in preparing scientific reports, abstracts, and PowerPoint presentations.

SCHOLARSHIPS

- | | |
|--|-----------|
| • Karnataka Science and Technology Scholarship | 2012-2015 |
| • Sir.C.V.Raman Scholarship | 2012-2015 |
| • Science Academies’ Summer Research Fellowship Program for Students and Teachers (IAS fellowship) | 2016 |

ACHIEVEMENTS AND AWARDS

- Third rank holder in Bachelor of Science under Mangalore University comprising of 65 colleges during the academic year 2012-2015.
- Awarded first prize for oral presentation at the Condensed Matter Physics and Applications (CMPA 2023) conference, held at MIT Manipal, India.

DECLARATION

- I hereby declare that all the information given above is true to the best of my knowledge.
